

**MODELING METHODS IN UNDERSTANDING AND
AMELIORATING CENTRAL NERVOUS SYSTEM INJURY**

by

SAGAR SINGH

A dissertation submitted to the

Graduate School-New Brunswick

Rutgers, The State University of New Jersey

and

The Graduate School of Biomedical Sciences

In partial fulfillment of the requirements

For the degree of

Doctor of Philosophy

Graduate Program in Biomedical Engineering

Written under the direction of

Dr. David I. Shreiber

And approved by

New Brunswick, New Jersey

OCTOBER, 2016

© 2016

Sagar Singh

ALL RIGHTS RESERVED

ABSTRACT OF THE DISSERTATION

Modeling Methods in Understanding and Ameliorating Central Nervous System Injury

By SAGAR SINGH

Dissertation Director:

David I. Shreiber, PhD

To improve the quality of life for victims of traumatic spinal cord and brain injury, a better understanding of how microstructural mechanical behavior influences bulk tissue and vice versa is necessary. Two aspects that warrant attention in this matter are primary injury and neural electrode-tissue interactions. While their respective biomechanics are measurable at the macroscopic level, it is difficult to measure microscopic deformations during injury in situ and in vivo experimentally. To overcome this limitation, we develop experimentally validated computational approaches to predict the multiscale translations involved in white matter tissue injury, and probe-tissue interfaces.

In the first part of this dissertation, we developed approaches to model primary injury at the axon level. First we developed 3-D axon kinematic models to infer axonal strain as a function of tissue-level stretch. Embryonic chick spinal cord tissue was exposed to controlled stretch and axon tortuosity and kinematics were characterized in 3-dimensions. We determined that greater proportions of axons are predicted to behave with affine, composite-like kinematics. Next, we identified and evaluated contactin-associated protein (Caspr) for use as a fiducial marker in estimating axonal strain and

axonal failure thresholds. Spinal cord tissue was exposed to controlled stretch, and displacements of immunostained Caspr proteins were measured. Changes in Caspr displacements reflected the applied macroscopic stretch directly at earlier stages of development but this trend deviated with further development. This shift in trend correlated with observations of axon failure at later stages of development, and we predicted axon failure thresholds to decrease with development.

In the second part of this dissertation, we developed approaches to model multiscale mechanics in neural probe and tissue interactions. Finite element simulations were developed and experimentally validated to determine insertion and buckling forces for different coating and probe designs. Parameter sweeps of these features determined that probe length and coating thickness had the biggest impact on insertion forces. Next, we used the model to simulate the probe-tissue interface in order to correlate interfacial stress and tissue strain to chronic injury. Stress and strain predictions were made for a variety of probe designs and results were validated with parallel experiments using agarose tissue phantoms. We correlated predictions to gliosis through an in vitro model where astrocytes cultured in collagen gels were cast around a probe and exposed to micromotion. We determined that probe stiffness has a greater effect on chronic injury than size. We were also able to predict minimum strain thresholds for inducing astrocyte activation.

The findings in this work help elucidate multiscale transfers in white matter injury and probe-tissue interfaces. These results can be applied to the design of better preventative measures for brain and spinal cord injury (sports and military equipment), as well as neural probes for long-term signal acquisition/stimulation in brain-to-computer interfaces.

Acknowledgements:

This thesis is the culmination of five and a half years of work. I would say the often used phrase of “blood, sweat, and tears” went into designing, executing, and writing the work presented herein, but the last thing I need is an inquiry from Rutgers Environmental Health & Safety.

Levity aside, this work contributes to the field of central nervous system injury and rehabilitation by extending the understanding regarding the multiscale transfer of macroscopic deformations to microscale effects. I tackle the problem from two directions: 1) developing approaches to better understand and measure the translation of tissue-levels of deformation to the microscopic components in white matter primary injury; and 2) design of a tool to assess the effects of probe geometry and material on acute and chronic injury in brain tissue. When reading this thesis, try to consider the idea of how can we better understand what we can’t visualize- and how the models we develop and validate fill in this gap of knowledge. I can wax poetic here about the intricacies of this concept but there’s the rest of the thesis for that. I first want to acknowledge everyone who has influenced my journey in one way or another.

The first person I want to thank is my advisor, boss, and mentor, David Shreiber. When I first joined Dr. Shreiber’s group in September 2010, I was admittedly the furthest thing from a researcher when I set foot in his office. I was bad at coming up with good questions; worse at coming up with ways to answer said questions; and had a tendency to take any data at face value. Through six years of guidance, Dr. Shreiber has taught me to focus less on data (though its importance is still recognized) and more on good science:

that doing things the right way is paramount, and validation is equally as important as the results. When people ask at conferences what group I work in, I'm always proud to say it is David Shreiber's group. So thank you for your mentorship, guidance, and convincing me that academia is the right field for me. It took a while to take the steps back but I can finally see the forest.

Next, I want to thank my committee for all the support and feedback they have offered me throughout this process. Dr. Mina Pelegri for her guidance in the white matter multiscale modeling work; Dr. Noshir Langrana for his wisdom and input into the finite element simulations for validating the axon kinematic model; Dr. Hilton Kaplan for his feedback and potential lines of inquiry regarding the probe modeling project, and Dr. Bonnie Firestein for her input on some of the larger scale implications of the injury and probe work. This thesis is a much stronger body of work thanks to their help.

To the people of Shreiber Lab; you were always friends first and colleagues after. First I want to thank Dr. Shirley Masand, Dr. Ian Gaudet, and Dr. Aaron Carlson (even though he was technically part of Prabhas Moghe's lab) for their kindness, patience, and welcoming nature when I started my project in the fall of 2010. Next, many thanks to Dr. Ijaz Ahmed, who taught me everything I know about immunohistochemistry, histology, and cryosectioning, as well as providing me a steady supply of primary rat astrocytes. The work in chapter 5 would not be possible without his generous help.

I especially want to thank Kathryn Drzewiecki and Christopher Lowe for their assistance, support, and friendship. Whether it was in lab, or in organizing some social event, or drafting an email to a potential postdoc advisor, they never hesitated to let me know what they sincerely thought and were always ready to help. Even though I started

one to two years before them, I have learned a lot from them, and hopefully the feeling is mutual. I give special thanks to Kathryn, who housed me after Hurricane Sandy, and that other time I locked myself out of my apartment without my phone on a Saturday night. May the tripod remain structurally sound.

A special thanks to Jean Lo, a frequent collaborator, especially in the probe studies outlined in this thesis. I also want to thank the numerous undergraduates I had the pleasure of mentoring during my graduate studies. Vivak Patel, currently doing his graduate work in statistics at UChicago, taught me everything I know about dissecting the embryonic chick spinal cord. Joshua Strohl, currently at the Feinstein Institute, helped develop the in vitro model I discuss in chapter 5, and Karanvir Kals, who will continue some of the axonal strain studies in Chapter 3. Their assistance during my time here was invaluable, and where they are now is a testament to their hard work and aptitude for research.

To the faculty in the Biomedical Engineering department at Rutgers: my sincerest thanks for all the input over the years. Dr. Li Cai for his input on my qualifier. Dr. Prabhas Moghe for the opportunities he gave me during my teaching assistantship, Dr. Troy Shinbrot for giving me the pedagogical opportunity to transcribe and design the modeling methods in math course for the online format, Dr. Jeffrey Zahn for his insight and input on the probe project, and Dr. Tim Maguire, who has not only been a wonderful mentor and supporter of my sometimes ambitious ideas, but has also been a dear friend.

A heartfelt thank you to the BME staff as well: Robin Yarrow, Lawrence Stromberg, Linda Johnson, and Stratos Loukidis for tackling RU bureaucracy and making sure this building is functional. I also have to acknowledge all the friends I have made in

the Biomedical Engineering department and at Rutgers in general. When the road of research got bumpy at times, there was always someone here at all hours of the day or night I could commiserate with. I specifically have to acknowledge Jack Zheng. The two of us started at the same time and under the same circumstances, and I can't think of a better person than him to have travelled this road with. We will make a collaboration happen some day!

To my closest and dearest friends, through all my struggles maneuvering the labyrinthine nature of academia, you were always there to pull me out of the maze every now and then, with skype sessions, ski-trips, weddings (three of them!), newborns, and outings in Philadelphia, New York, and Denver. More importantly, whenever there was doubt about my choice of path, you guys were always there to sit me down and tell me how proud you were of me for doing what I do. It still surprises me how we've remained such close friends, despite the time, and physical and professional distance. So thank you: Jacqueline Yu, Daming Chung, Michael Kaplan, Zenaida Shepelin, Viktor Shepelin, Lorna Huang, Kim Beaumund, Brian Beaumund, Brian Quimby, and Jude Kersaint; thank you all for everything you've done and everything you mean to me.

And lastly, and furthest away from least, I want to thank my family from the bottom of my heart. My younger brother, Saurubh, for being as weird as me; my cousins: Vasundhara Singh, Dhruv Sharma, and Digvijay Singh, for housing me and feeding me on weekends. Finally, the greatest thanks to my parents, Namrata and Narendra Singh: thank you for making me the person that I am today, and will be tomorrow. In essence, this is their thesis as much as it is mine.

Table of Contents

Abstract of Dissertation:	ii
Foreword and Acknowledgments:	iv
Table of Contents	viii
List of Tables	xi
List of Figures	xii
Chapter 1: Introduction	1
Thesis Overview:.....	1
Defining central nervous system injury:	1
Primary axonal injury:.....	3
Designing approaches to overcoming functional damage in CNS injury:	5
Role and Significance of Modeling:.....	8
Applying modeling to predict primary and neural electrode induced injury in CNS tissue:	9
Dissertation Summary:	10
References:	13
Figures:.....	18
Chapter 2: Characterizing the 3-dimensional kinematic behavior of axons as a function of macroscopic stretch and development in white matter tissue	21
Abstract:	21
Background & Significance:	23

Methods:.....	26
Results:	38
Discussion:	43
Conclusions:	51
References:	52
Figures:.....	55
Chapter 3: Estimating axonal strain as a function of tissue-level stretch using contactin-associated protein as a fiducial marker.....	75
Abstract:	75
Background & Significance:	77
Methods:.....	80
Results:	85
Discussion:	90
Conclusions:	101
References:	103
Figures:.....	106
Chapter 4: Modeling the insertion mechanics of coated flexible neural probes for optimizing probe performance	122
Abstract:	122
Background & Significance:	124
Materials and Methods:	128
Results	135

Discussion	141
References	149
Figures:.....	152
Chapter 5: An <i>in vitro</i> approach to correlating <i>in silico</i> predictions regarding the long term performance of flexible neural implants	167
Abstract:	167
Introduction:	169
Methods:.....	172
Results	178
Discussion	183
Conclusions:	189
References:	190
Figures:.....	193
Chapter 6: Thesis Discussion and Concluding Remarks:	209
The necessity of modeling:	211
Novelty:.....	213
Philosophy of Engineering:.....	214
Future Work:	216
References:	219

List of Tables

Table 2-1: In situ lengths for spinal cord sections	72
Table 2-2: Mean 3-D tortuosity decreases with stretch	73
Table 2-3: FEM results for axons modeled with varying tortuosities.....	74
Table 3-1: Predicted parameters for axonal failure strain probability distributions for four distributions tested	120
Table 3-2: Predicted parameters for breaking strain classified by predicted kinematics	121
Table 4-1: Cohorts of probes tested in <i>ex vivo</i> chick embryonic brain tissue	164
Table 4-2: Cohorts of probes tested in <i>ex vivo</i> rat brain tissue	165
Table 4-3: Multi-variable regression results for modeled probe designs.....	166
Table 5-1: Mean concentrations of TNF- determined by ELISA analysis	208

List of Figures

Figure 1-1: Schematic for multiscale modeling methodologies	19
Figure 1-2: Depiction of the ideal probe in the design space for neural electrodes	20
Figure 1-3: Schematic of process flow in CNS primary injury and neural probe implantation.....	21
Figure 2-1: Schematic of microstretch device for applying quasistatic stretch to spinal cord tissue.....	56
Figure 2-2: Comparison of longitudinal and transverse sections of spinal cord	57
Figure 2-3: Visual schematic of image processing algorithm for 3-D tortuosity measurement	58
Figure 2-4: Test results for MATLAB image processing algorithm.....	59
Figure 2-5: Histogram comparisons of 2-D hand traced tortuosities and algorithm measurements.....	62
Figure 2-6: FEA screenshots for validating 3-D kinematic equations.....	63
Figure 2-7: Color images of transverse sections for E12 and E18 spinal cords.....	64
Figure 2-8: Representative images of microtome sections stained with OsO ₄	65
Figure 2-9: Representative images of neurofilament and MBP staining for E12 and E18 sections.....	66
Figure 2-10: Mean 2-D and 3-D tortuosity decreases with stretch level	67
Figure 2-11: Histograms of tortuosity distributions for spinal cords not exposed to pre-stretch...	69
Figure 2-12: Cumulative frequency distributions for 3-D axon tortuosity with development and stretch	70
Figure 2-13: Transition tortuosities and interpretation of parameters	71
Figure 3-1: Schematic of internodal/paranodal length measurement methods	107

Figure 3-2: Bar graphs of average internodal end-to-end, pathlength, and paranodal lengths	108
Figure 3-3: Plots of percentage length changes for 20µm thick slices	109
Figure 3-4: Histograms of internodal end-to-end lengths for E12 and E18 cords	110
Figure 3-5: Schematic and plot of thicker slices and improvement in trends	111
Figure 3-6: Percentage change in internodal length compared to change in tissue length	112
Figure 3-7: End-to-end length distributions comparing E12 and E16 proportions.....	113
Figure 3-8: Proportion of broken segments measured from 40µm thick slices	114
Figure 3-9: Model predictions of axonal failure for E12 and E18 specimens	115
Figure 3-10: Proportions of broken axons for different developmental stages classified by kinematics	116
Figure 3-11: Kinematic parameters derived from complete distributions and failed axons omitted.....	117
Figure 3-12: Histograms of length distributions predicted by simulation results	118
Figure 3-13: Segment failures classified by region of spinal cord in E18 samples	119
Figure 3-14: Representative images and failure profiles for full length spinal cords	120
Figure 4-1: Schematic of mechanical testing setup to determine insertion and buckling forces .	153
Figure 4-2: Bending profiles for SU-8 and parylene to determine bending modulus.....	154
Figure 4-3: Screenshots of FE simulation for coated probe insertion.....	155
Figure 4-4: Convergence study results to determine ideal mesh sizing	157
Figure 4-5: Force profiles for insertion phase compared between simulation and experiment ...	158
Figure 4-6: Model accuracy and validation results for buckling and insertion forces.....	159
Figure 4-7: Empirical probability of insertion as a function of safety factor.....	160

Figure 4-8: Color maps of probability of successful insertion of coated probes	161
Figure 4-9: Color maps of probability of successful insertion of uncoated probes	162
Figure 4-10: Color maps of probability of successful insertion for varying probe lengths	163
Figure 4-11: Simulation results for coated probes containing assymetrical coating thickness....	164
Figure 5-1: Schematic of FE simulations for embedded probe model.....	194
Figure 5-2: Experimental setup for validating strain predictions from FE simulations	195
Figure 5-3: Top-view screenshots of model executions and contour maps	196
Figure 5-4: Side-view screenshots of model executions and contour maps	197
Figure 5-5: Plots of predicted strain and radius of effect as a function of probe width.....	198
Figure 5-6: Represenative outputs of 2-D normalized strain profiles as a function of probe material	199
Figure 5-7: Model executions of beveled microwires	200
Figure 5-8: Simulation of beads embedded in agarose system during motion	201
Figure 5-9: Cell viability results from live-dead stains performed in 1-5 day samples	202
Figure 5-10: Composite plots of TNF- concentration from ELISA results	203
Figure 5-11: Representative images of immunostained astrocytes in stationary samples	204
Figure 5-12: GFAP and simulation profile for stationary samples	205
Figure 5-13: GFAP and simulation profile for moving samples.....	206
Figure 5-14: GFAP intensity plotted against predicted strain to predict activation thresholds ...	208

Chapter 1: Introduction

Thesis Overview:

This work utilizes computational modeling and experimental validation to develop augmented approaches to understand how macroscale effects in white matter injury and neural electrode implantation influence the microscale, or individual cellular effects. The findings from these models are then applied to estimate axonal injury thresholds, and provide insights for optimizing neural probe designs.

Defining central nervous system injury:

Central nervous system (CNS) injuries are among the leading causes of morbidity and death in the United States, with over 1.7 million new incidences of a traumatic brain injury (TBI) or spinal cord injury (SCI) occurring annually (CDC.gov, 2012). Financial costs associated with the diagnosis and treatment of CNS injuries is over 90 billion USD per year. This is in addition to the personal costs and difficulties experienced by victims and their families. An intrinsic trait of CNS injuries is its difficulty in diagnosis, as detection capabilities are limited, and most deleterious effects do not occur until weeks or months following the initial event (LaPlaca et al., 2005; Smith and Meaney, 2000). The salient issue remains that complete functional and morphological recovery is limited by the inability for CNS tissue to regenerate fully following traumatic injury (Maikos et al., 2008; Werner and Engelhard, 2007).

CNS injuries results from primary, followed by secondary events. The primary injury delineates the initial mechanical insult, caused by mechanical loading of the brain

or spinal cord (Hao and Shreiber, 2007; Smith and Meaney, 2000). Depending on the severity of loading, this can cause cellular, axonal, and/or blood-brain barrier (BBB) damage, or complete tissue damage and cell death (Johnson et al., 2013). Secondary injury refers to the subsequent damage resulting from inflammation, biochemical signal cascades, and cell death following the primary insult (Fitch and Silver, 2008). Unlike primary injury which occurs immediately during trauma at the millisecond level, secondary damage, and many of the functional deficits associated with CNS injuries may not manifest until hours, days, or weeks after the traumatic event (Hao and Shreiber, 2007; LaPlaca et al., 2007; Werner and Engelhard, 2007).

In addition to the biochemical cascades that induce cell damage and death following traumatic CNS injury, restoration is hindered by the formation of lesion cavities and scar tissue (glial scar) at the injury site (Yiu and He, 2006). The glial scar is characterized by a localized region of stiffness, caused by astrocyte activation (Saxena et al., 2012; Siebert et al., 2014). Glial scarring is a double-edged sword. While scar formation is useful for sequestering inflammatory effects and preventing further damage to healthy neurons, scarring also serves to inhibit axonal regeneration following injury (Lu et al., 2011; Rolls et al., 2008; Wanner et al., 2013) through a combination of mechanical (Lu et al., 2011; Saxena et al., 2012) and chemical cues (Aurand et al., 2012; Lee et al., 2010; Rolls et al., 2008). Evidence has been put forward that the extent of scarring is correlated with the severity of primary injury (Fitch and Silver, 2008; Silver and Miller, 2004). *By better understanding the mechanisms of primary injury, clinicians are better equipped to diagnose and treat CNS injury to prevent subsequent damage from secondary mechanisms* (Wright and Ramesh, 2012).

Primary axonal injury:

Primary axonal injury via stretch is a proximal cause of functional deficits following CNS injury (Bain et al., 2000; Hao and Shreiber, 2007; Smith and Meaney, 2000). Axonal stretch can occur when white matter tissue experiences deformation. Given enough stretch, axons can experience irrevocable damage and failure, which leads to further damage from subsequent secondary injury cascades (Fitch and Silver, 2008; Werner and Engelhard, 2007). A key metric used in predicting and assessing axonal injury is the strain individual axons can tolerate before experiencing injury (Wright and Ramesh, 2012). These strain thresholds have been characterized for *in vitro* preparations of axons (Johnson et al., 2013; Smith et al., 1999), and *in vivo* preparations in the guinea pig optic nerve (Bain et al., 2000). Depending on the type of preparation, injury thresholds can vary significantly from over 75% in *in vitro* preparations (Tang-Schomer et al., 2010), to 14% in *in vivo* conditions (Bain et al., 2000). This vast discrepancy in outcomes prevents clear definition in determining if and when axonal damage due to stretch has occurred.

One hypothesis for the wide range of injury thresholds is the differences in microstructural properties in CNS tissue preparations studied *in vivo*, *ex vivo*, and *in vitro*. It is generally accepted that features at the microscale, such as how axons are arranged or degree of myelination, directly influence the bulk tissue mechanical properties (Cloots et al., 2013a; Meaney, 2003). For instance, axons in white matter tracts are oriented, and as a result, white matter displays anisotropic or direction-dependent material properties (Prange and Margulies, 2002). In studies of the chick embryonic

spinal cord, demyelinated spinal cords had significantly less stiffness and lower ultimate tensile strength than myelinated cords (Shreiber et al., 2009). It follows that microstructure can potentially influence how axons behave, and potentially fail, as a function of tissue-scale or macroscopic stretch (Bain et al., 2003).

During trauma, the tissue-scale deformation is transferred to the cellular-scale constituents that make up the white matter tracts. There is no clear translation between the stresses experienced by the tissue to those that are experienced by axons (Cloots et al., 2013a; Meaney, 2015). Properties of axons can influence this transfer (Arbogast and Margulies 1999; Bain, Shreiber, and Meaney 2003; Cloots et al. 2013; Hao and Shreiber 2007; Shreiber, Hao, and Elias 2009), which can help explain region-dependent mechanics in brain and spinal cord deformation. These axonal features include components such as: axon morphology; axon orientation with respect to the white matter tract; degree of myelination; kinematic behavior; and connectivity to surrounding axons (Figure 1-1). Characterizing these attributes in different regions of white matter tissue allows inferences to be made regarding stresses and strains experienced by individual axons, and can potentially explain why such discrepancies regarding injury thresholds have been observed.

One limitation to inferring axonal strain from characterizing microstructural features is that there are few methods of validation, due to no clear means of directly observing how much stress or strain is being applied to axons. In many cases, the strain criterion for ascertaining axonal injury is beyond the capability of many imaging methods (Carlsen and Daphalapurkar, 2015). Finite element simulations can provide some insight into axonal behavior and can help make predictions for axonal strains and their propensity for

injury (El Sayed et al., 2008; Karami et al., 2009; Pan et al., 2013), though these models are still difficult to experimentally validate. *It is imperative to understand this multi-scale transfer to better predict axonal injury.* Improved predictive measures can help improve quality of life; by addressing these approaches for victims who have already suffered CNS injury.

Designing approaches to overcoming functional damage in CNS injury:

Following CNS injury, numerous approaches can be taken to ameliorate damage, and restore partial function. Ultimately they can be classified into regenerative and rehabilitative approaches. Regenerative approaches seek to restore injured neurons or induce the growth and development of new neurons to replace and restore failed connections that were affected by trauma. This can be accomplished by introducing soluble factors to encourage recovery (Azari et al., 2010), introducing biomaterials that provide an amenable substrate for neurons to grow (Aurang et al., 2012; Zhu, 2010), or transplanting neural stem cells or precursor cells focally to the injury site (Fitch and Silver, 2008; Xu et al., 2011).

The focus of this portion of the thesis is the other approach – rehabilitative techniques and technologies. In contrast to regeneration, rehabilitative methods make use of the post-injury architecture in an attempt to extract and utilize signals from surviving neurons (Nicolas-Alonso and Gomez-Gil, 2012). This includes devices to measure neuronal activity from surviving neurons (Lo et al., 2015; Mak and Wolpaw, 2009), or conditioning and reprogramming intact connections to restore damaged functions (Patel et al., 2011; Tan and Waxman, 2012; Xu et al., 2011). One example of this approach is

brain-to-computer interface (BCI) devices. BCI devices can aid in re-establishing functional connections following axonal injury. BCIs work by acquiring a volition signal and translating the processed signal into a proportionate response in an extra-corporeal device. Volition signals can be obtained from different sources with varying degrees of accuracy and invasiveness. The ideal device provides long-term capability to rapidly acquire and translate signals with precision.

Single-unit recordings (SURs) or neural electrodes provide the greatest accuracy and resolution in acquiring volition signal, as they can obtain signals from individual neurons (Hoogerwerf and Wise, 1994). SURs are also the most invasive, often requiring surgical implantation. Consequently these implants result in a foreign body response which serves to reduce performance and long-term efficacy (Aregueta-Robles et al., 2014; Biran et al., 2005; Karumbaiah et al., 2013). In addition to the initial damage caused by implantation, chronic injury resulting from material mismatch between surrounding tissue and electrode serves to encapsulate the electrode, preventing signal acquisition (Aregueta-Robles et al., 2014; Subbaroyan et al., 2005) in the long run.

Approaches have been taken to understand how to modulate the chronic response.

Current hypotheses for the direct cause of gliosis and subsequent electrode failure suggest a cause-effect relationship between localized strains experienced in the tissue adjacent to the electrode (Subbaroyan et al., 2005). Karumbaiah et al. (2012) demonstrated that glial cells exposed to low strain, cyclical loading lead to the overexpression of reactive markers GFAP and neurocan (Karumbaiah et al., 2012). Stiffer, larger probes have been posited to increase the localized strains in a number of models (Polanco et al., 2014; Shen

et al., 2015; Subbaroyan et al., 2005), supporting the *idea that gliosis is related to stresses and strains at the probe-tissue interface.*

Smaller and flexible probes have been shown to reduce the chronic injury response, but are appreciably more difficult to insert into tissue than stiffer, larger probes (Cheung, 2007; D. Lewitus et al., 2011; Lo et al., 2015). This leads to a balancing act between long-term efficacy and mechanical viability. An ideal probe is small and flexible enough to mitigate the chronic response, yet large enough to maximize signal acquisition, and mechanically stiff enough to implant successfully (Lo et al., 2015; Polikov et al., 2005) (Figure 1-2). Design parameters such as probe geometry, material properties, sacrificial coatings, and region-dependent tissue properties can vary considerably from design to design and implantation scenario, and can influence initial injury and the chronic response. Introducing more complex geometries or accounting for defects in fabrication serve to further complicate the problem. *Given the wide variation in design parameters to consider, there is a need for a systematic approach to determining what features matter most in developing neural electrodes suited for long-term signal acquisition.*

Role and Significance of Modeling:

Biological systems, the CNS included, are exceptionally complex systems. Signal cascades, feedback loops, and interactivity with other physiological systems are issues to consider when understanding and developing clinical interventions. Considering the degree of complexity, it behooves us to deconstruct systems by focusing on the fundamental elements that interact. This can be achieved using computational models that incorporate accurate reproductions of the macroscopic and microscopic features.

Models can be analytical, predictive, or a combination of both. Models are built on assumptions, based on fundamental principles and empirical observations. Ultimately, a model's usefulness in predicting what occurs during injury or insertion is dependent on its veracity in reflecting what physically happens. As a result, models need to be refined and validated experimentally, before any predictions on the system can be analyzed and understood. Once a validated model has been generated, researchers can probe individual features and predict the effects on the system.

In addition to improving our understanding of how a system works, modeling is a cost-effective means of simulating experiments, which augments design-of-experiments, minimizes monetary and time costs, and potentially reduces numbers of experiments, or animals to be employed. This is especially useful for processes which are iterative, for instance, testing tolerance thresholds for a beam made of different materials. Another valuable use of modeling is in predicting outcomes for experimental conditions that cannot be easily replicated, or characterized *in situ* or *in vivo*.

Applying modeling to predict primary and neural electrode induced injury in CNS tissue:

Primary CNS injury and optimal neural probe design are two distinct systems which feed into the overarching issue of understanding and treating TBI and SCI (Figure 1-3). The overarching concern in each of these systems is the inability to experimentally characterize the effects that macroscopic mechanics have on the microscale. By utilizing experimentally validated models, we can obtain a clearer link between multiple scales in CNS primary injury and electrode-induced damage. Improving our understanding in both

these realms would improve diagnostic and treatment capabilities for the debilitating pathologies associated with these injuries.

In the case of primary injury, the inherent limitation in models is the inability to experimentally validate predictions being generated. A variety of modeling studies provide keen insight into this multiscale problem. Cloots et al. (2013) employed computational simulations to determine axonal strains as a function of mechanical load at the macroscopic head level by modeling critical volume elements (Cloots et al., 2013a). Pan et al. (2013) developed a similar treatment by modeling axons as representative volume elements, and introducing kinematic coupling between axons (Pan et al., 2013) to reflect previous observations of 2-dimensional (2-D) axon kinematic behavior in myelinated (Hao and Shreiber, 2007) and demyelinated tissue (Shreiber et al., 2009). Characterizing 2-D axon kinematic behavior provided a useful metric for modeling multiscale transfer as changes in kinematics reflected changes in features of the microstructure (Hao and Shreiber, 2007; Pan et al., 2013; Shreiber et al., 2009). *Ultimately, knowledge in how axons physically behave as a function of tissue-level stretch is still incomplete, and the inability of current imaging modalities to probe these behaviors makes experimental validation difficult.*

In probe-tissue mechanics, interfacial stresses and strains between the probe and brain tissue cannot be experimentally quantified (Subbaroyan et al., 2005). While models have predictive power in this regard, there is still an unclear quantitative relationship between mechanical stresses and strains generated by probes during and after insertion, and the biological effects at the cellular and tissue level. Computational modeling of neural electrode mechanical performance is not a novel concept on its own as groups

have modeled both insertion mechanics (Bjornsson et al., 2006), and the effects of material properties on interfacial stresses (N. Hamzavi et al., 2013; Subbaroyan et al., 2005). *There is still a need to develop a validated framework for predicting probe-tissue mechanical performance and to design an all-encompassing approach in correlating biomechanical metrics to biological response.* Neural electrodes designers armed with this information can be made cognizant of design features that influence the chronic response caused by implanted electrodes, and can fabricate better electrodes to improve the long-term efficacy of neural probes.

Dissertation Summary:

This research thesis focuses on further elucidating the multiscale biomechanics of primary CNS injury, and neural electrode-tissue interaction. We accomplish this by: 1) characterizing and modeling axon kinematics and axonal strains as a function of tissue-level stretch and 2) computationally and experimentally correlating the mechanical performance of neural electrodes during and after insertion to tissue and cell damage for the purpose of optimizing BCI devices. In both scenarios, we build a model from basic principles, and validate model predictions through parallel experiments. We then use our models to predict axon failure thresholds, and probe mechanical performance and tissue behavior, respectively.

The remainder of this thesis is organized as follows. Chapters 2 & 3 focus on modeling and improving understanding of primary white matter injury to help answer: “*What causes axons in white matter tracts to fail and can we predict when failure happens based on deformations we apply to the tissue?*” In chapter 2, we extend axon kinematic

models used in inferring the transfer of macroscopic to microscopic stretch from 2-dimensions to 3-dimensions. In a chick embryo model, we excise spinal cords, characterize axon morphology and tortuosity, and demonstrate that kinematic trends exhibit the same trends in 3-D. In chapter 3, we develop a method to estimate axonal strain due to macroscopic stretch *in situ* by utilizing Caspr, an axo-glial protein expressed at the nodes of Ranvier, as a fiduciary marker. We characterize average axonal strain and proportions of broken axons in the spinal cord as a function of macroscopic stretch and developmental stage. We then adopt features from our kinematic model in chapter 2, and employ the model's methodology to estimate strain thresholds for axonal failure.

In chapters 4 & 5, we transition to modeling rehabilitative approaches, namely, designs of neural probes. Overall, we proceed to answer: "*Can we model the mechanical performance of coated flexible neural electrodes during and after insertion, and can we use this model to optimize their design for long-term implantation?*" Chapter 4 focuses on modeling the insertion mechanics of a variety of coated neural probe designs. We develop a finite element simulation that predicts insertion and buckling forces of coated neural probes penetrating brain tissue. The ratio of buckling force to insertion force is used as a metric and correlated to probability of insertion based on empirical data from validating insertion experiments for select probe designs. Chapter 5 extends this model to understanding how probe design affects the chronic response. Adapting our finite element simulation from Chapter 4, we predict interfacial stresses generated by micromotions and correlate stress magnitude to gliosis and astrocyte activation garnered from parallel *in vitro* and *in vivo* experiments. Ultimately, we utilize the information gleaned from chapters 4 & 5 to ascertain the most important requirements for neural electrode design.

Finally, we discuss overall results, and the implications of our findings in Chapter 6. A thorough treatment of how these two disparate models link to each other and their clinical significance is also addressed. *Ultimately, the contribution of this thesis is an extension of the philosophies of biological and computational modeling and their utilization in elucidating the multi-scale phenomenon in primary axonal injury and probe-tissue mechanics to improve the quality of life of CNS injury victims.*

References:

- Arbogast, K.B., Margulies, S.S., 1999. A fiber-reinforced composite model of the viscoelastic behavior of the brainstem in shear. *J. Biomech.* 32, 865–70.
- Aregueta-Robles, U. a, Woolley, A.J., Poole-Warren, L. a, Lovell, N.H., Green, R. a, 2014. Organic electrode coatings for next-generation neural interfaces. *Front. Neuroeng.* 7, 15. doi:10.3389/fneng.2014.00015
- Aurand, E.R., Wagner, J., Lanning, C., Bjugstad, K.B., 2012. Building biocompatible hydrogels for tissue engineering of the brain and spinal cord. *J. Funct. Biomater.* 3, 839–63. doi:10.3390/jfb3040839
- Azari, M.F., Mathias, L., Ozturk, E., Cram, D.S., Boyd, R.L., Petratos, S., 2010. Mesenchymal stem cells for treatment of CNS injury. *Curr. Neuropharmacol.* 8, 316–23. doi:10.2174/157015910793358204
- Bain, A.C., Meaney, D.F., Hall, H., 2000. Tissue-Level Thresholds for Axonal Damage in an Nervous System White Matter Injury 122.
- Bain, A.C., Shreiber, D.I., Meaney, D.F., 2003. Modeling of Microstructural Kinematics During Simple Elongation of Central Nervous System Tissue. *J. Biomech. Eng.* 125, 798. doi:10.1115/1.1632627
- Biran, R., Martin, D.C., Tresco, P. a, 2005. Neuronal cell loss accompanies the brain tissue response to chronically implanted silicon microelectrode arrays. *Exp. Neurol.* 195, 115–26. doi:10.1016/j.expneurol.2005.04.020
- Bjornsson, C.S., Oh, S.J., Al-Kofahi, Y. a, Lim, Y.J., Smith, K.L., Turner, J.N., De, S., Roysam, B., Shain, W., Kim, S.J., 2006. Effects of insertion conditions on tissue strain and vascular damage during neuroprosthetic device insertion. *J. Neural Eng.* 3, 196–207. doi:10.1088/1741-2560/3/3/002
- Carlsen, R.W., Daphalapurkar, N.P., 2015. The importance of structural anisotropy in computational models of traumatic brain injury. *Front. Neurol.* 6, 28. doi:10.3389/fneur.2015.00028
- Cheung, K.C., 2007. Implantable microscale neural interfaces. *Biomed. Microdevices* 9, 923–38. doi:10.1007/s10544-006-9045-z
- Cloots, R.J.H., van Dommelen, J. a W., Kleiven, S., Geers, M.G.D., 2013. Multi-scale mechanics of traumatic brain injury: predicting axonal strains from head loads. *Biomech. Model. Mechanobiol.* 12, 137–50. doi:10.1007/s10237-012-0387-6
- El Sayed, T., Mota, A., Fraternali, F., Ortiz, M., 2008. Biomechanics of traumatic brain injury. *Comput. Methods Appl. Mech. Eng.* 197, 4692–4701. doi:10.1016/j.cma.2008.06.006

- Fitch, M., Silver, J., 2008. CNS injury, glial scars, and inflammation: Inhibitory extracellular matrices and regeneration failure. *Exp. Neurol.* 209, 294–301.
- Hamzavi, N., Tsang, W.M., Shim, V.P.W., 2013. Nonlinear elastic brain tissue model for neural probe-tissue mechanical interaction. 2013 6th Int. IEEE/EMBS Conf. Neural Eng. 1119–1122. doi:10.1109/NER.2013.6696134
- Hao, H., Shreiber, D.I., 2007. Axon kinematics change during growth and development. *J. Biomech. Eng.* 129, 511–22. doi:10.1115/1.2746372
- Hoogerwerf, a C., Wise, K.D., 1994. A three-dimensional microelectrode array for chronic neural recording. *IEEE Trans. Biomed. Eng.* 41, 1136–46. doi:10.1109/10.335862
- Johnson, V.E., Stewart, W., Smith, D.H., 2013. Axonal pathology in traumatic brain injury. *Exp. Neurol.* 246, 35–43. doi:10.1016/j.expneurol.2012.01.013
- Karami, G., Grundman, N., Abolfathi, N., Naik, a, Ziejewski, M., 2009. A micromechanical hyperelastic modeling of brain white matter under large deformation. *J. Mech. Behav. Biomed. Mater.* 2, 243–54. doi:10.1016/j.jmbbm.2008.08.003
- Karumbaiah, L., Norman, S.E., Rajan, N.B., Anand, S., Saxena, T., Betancur, M., Patkar, R., Bellamkonda, R. V, 2012. The upregulation of specific interleukin (IL) receptor antagonists and paradoxical enhancement of neuronal apoptosis due to electrode induced strain and brain micromotion. *Biomaterials* 33, 5983–96. doi:10.1016/j.biomaterials.2012.05.021
- Karumbaiah, L., Saxena, T., Carlson, D., Patil, K., Patkar, R., Gaupp, E. a, Betancur, M., Stanley, G.B., Carin, L., Bellamkonda, R. V, 2013. Relationship between intracortical electrode design and chronic recording function. *Biomaterials* 34, 8061–74. doi:10.1016/j.biomaterials.2013.07.016
- LaPlaca, M.C., Cullen, D.K., McLoughlin, J.J., Cargill, R.S., 2005. High rate shear strain of three-dimensional neural cell cultures: a new in vitro traumatic brain injury model. *J. Biomech.* 38, 1093–105. doi:10.1016/j.jbiomech.2004.05.032
- LaPlaca, M.C., Simon, C.M., Prado, G.R., Cullen, D.K., 2007. CNS injury biomechanics and experimental models. *Prog. Brain Res.* 161, 13–26. doi:10.1016/S0079-6123(06)61002-9
- Lee, H., McKeon, R.J., Bellamkonda, R. V, 2010. Sustained delivery of thermostabilized chABC enhances axonal sprouting and functional recovery after spinal cord injury. *Proc. Natl. Acad. Sci. U. S. A.* 107, 3340–5. doi:10.1073/pnas.0905437106
- Lewitus, D., Smith, K.L., Shain, W., Kohn, J., 2011. Ultrafast resorbing polymers for use as carriers for cortical neural probes. *Acta Biomater.* 7, 2483–91. doi:10.1016/j.actbio.2011.02.027
- Lo, M., Wang, S., Singh, S., Damodaran, V.B., Kaplan, H.M., Kohn, J., Shreiber, D.I., Zahn, J.D., 2015. Coating flexible probes with an ultra fast degrading polymer to aid in tissue insertion. *Biomed. Microdevices* 17, 34. doi:10.1007/s10544-015-9927-z

Lu, Y.-B., Iandiev, I., Hollborn, M., Körber, N., Ulbricht, E., Hirrlinger, P.G., Pannicke, T., Wei, E.-Q., Bringmann, A., Wolburg, H., Wilhelmsson, U., Pekny, M., Wiedemann, P., Reichenbach, A., Käs, J. a, 2011. Reactive glial cells: increased stiffness correlates with increased intermediate filament expression. *FASEB J.* 25, 624–31. doi:10.1096/fj.10-163790

Maikos, J.T., Qian, Z., Metaxas, D., Shreiber, D.I., 2008. Finite element analysis of spinal cord injury in the rat. *J. Neurotrauma* 25, 795–816. doi:10.1089/neu.2007.0423

Mak, J., Wolpaw, J., 2009. Clinical applications of brain-computer interfaces: current state and future prospects. *Biomed. Eng. IEEE Rev.* ... 187–199. doi:10.1109/RBME.2009.2035356.Clinical

Meaney, D.F., 2003. Relationship between structural modeling and hyperelastic material behavior: application to CNS white matter. *Biomech. Model. Mechanobiol.* 1, 279–93. doi:10.1007/s10237-002-0020-1

Nicolas-Alonso, L.F., Gomez-Gil, J., 2012. Brain computer interfaces, a review. *Sensors (Basel)*. 12, 1211–79. doi:10.3390/s120201211

Pan, Y., Sullivan, D., Shreiber, D.I., Pelegri, A. a, 2013. Finite Element Modeling of CNS White Matter Kinematics: Use of a 3D RVE to Determine Material Properties. *Front. Bioeng. Biotechnol.* 1, 19. doi:10.3389/fbioe.2013.00019

Patel, T.P., Ventre, S.C., Meaney, D.F., 2011. Dynamic Changes in Neural Circuit Topology Following Mild Mechanical Injury In Vitro. *Ann. Biomed. Eng.* 40, 23–36. doi:10.1007/s10439-011-0390-6

Polanco, M., Yoon, H., Bawab, S., 2014. Micromotion-induced dynamic effects from a neural probe and brain tissue interface. *J. Micro/Nanolithography, MEMS, MOEMS* 13, 023009. doi:10.1117/1.JMM.13.2.023009

Polikov, V.S., Tresco, P. a, Reichert, W.M., 2005. Response of brain tissue to chronically implanted neural electrodes. *J. Neurosci. Methods* 148, 1–18. doi:10.1016/j.jneumeth.2005.08.015

Prange, M.T., Margulies, S.S., 2002. Regional, Directional, and Age-Dependent Properties of the Brain Undergoing Large Deformation. *J. Biomech. Eng.* 124, 244. doi:10.1115/1.1449907

Rolls, A., Shechter, R., London, A., Segev, Y., Jacob-Hirsch, J., Amariglio, N., Rechavi, G., Schwartz, M., 2008. Two faces of chondroitin sulfate proteoglycan in spinal cord repair: a role in microglia/macrophage activation. *PLoS Med.* 5, e171. doi:10.1371/journal.pmed.0050171

Saxena, T., Gilbert, J., Stelzner, D., Hasenwinkel, J., 2012. Mechanical characterization of the injured spinal cord after lateral spinal hemisection injury in the rat. *J. Neurotrauma* 29, 1747–57. doi:10.1089/neu.2011.1818

Shen, W., Karumbaiah, L., Liu, X., Saxena, T., Chen, S., Patkar, R., Bellamkonda, R. V., Allen, M.G., 2015. Extracellular matrix-based intracortical microelectrodes: Toward a microfabricated

neural interface based on natural materials. *Microsystems Nanoeng.* 1, 15010. doi:10.1038/micronano.2015.10

Shreiber, D.I., Hao, H., Elias, R. a I., 2009. Probing the influence of myelin and glia on the tensile properties of the spinal cord. *Biomech. Model. Mechanobiol.* 8, 311–21. doi:10.1007/s10237-008-0137-y

Siebert, J.R., Conta Steencken, A., Osterhout, D.J., 2014. Chondroitin sulfate proteoglycans in the nervous system: inhibitors to repair. *Biomed Res. Int.* 2014, 845323. doi:10.1155/2014/845323

Silver, J., Miller, J.H., 2004. Regeneration beyond the glial scar. *Nat. Rev. Neurosci.* 5, 146–56. doi:10.1038/nrn1326

Smith, D.H., Meaney, D.F., 2000. Axonal Damage in Traumatic Brain Injury. *Neurosci.* 6, 483–495. doi:10.1177/107385840000600611

Smith, D.H., Wolf, J. a, Lusardi, T. a, Lee, V.M., Meaney, D.F., 1999. High tolerance and delayed elastic response of cultured axons to dynamic stretch injury. *J. Neurosci.* 19, 4263–9.

Subbaroyan, J., Martin, D.C., Kipke, D.R., 2005. A finite-element model of the mechanical effects of implantable microelectrodes in the cerebral cortex. *J. Neural Eng.* 2, 103–13. doi:10.1088/1741-2560/2/4/006

Tan, A.M., Waxman, S.G., 2012. Spinal cord injury, dendritic spine remodeling, and spinal memory mechanisms. *Exp. Neurol.* 235, 142–51. doi:10.1016/j.expneurol.2011.08.026

Tang-Schomer, M.D., Patel, A.R., Baas, P.W., Smith, D.H., 2010. Mechanical breaking of microtubules in axons during dynamic stretch injury underlies delayed elasticity, microtubule disassembly, and axon degeneration. *FASEB J.* 24, 1401–10. doi:10.1096/fj.09-142844

Wanner, I.B., Anderson, M. a, Song, B., Levine, J., Fernandez, A., Gray-Thompson, Z., Ao, Y., Sofroniew, M. V, 2013. Glial scar borders are formed by newly proliferated, elongated astrocytes that interact to corral inflammatory and fibrotic cells via STAT3-dependent mechanisms after spinal cord injury. *J. Neurosci.* 33, 12870–86. doi:10.1523/JNEUROSCI.2121-13.2013

Werner, C., Engelhard, K., 2007. Pathophysiology of traumatic brain injury. *Br. J. Anaesth.* 99, 4–9. doi:10.1093/bja/aem131

Wright, R.M., Ramesh, K.T., 2012. An axonal strain injury criterion for traumatic brain injury. *Biomech. Model. Mechanobiol.* 11, 245–60. doi:10.1007/s10237-011-0307-1

Xu, X., Warrington, A.E., Bieber, A.J., Rodriguez, M., 2011. Enhancing CNS Repair in Neurological Disease Rewiring of the Network 25, 555–573.

Yiu, G., He, Z., 2006. Glial inhibition of CNS axon regeneration. *Nat. Rev. Neurosci.* 7, 617–627. doi:10.1038/nrn1956.Glial

Zhu, J., 2010. Bioactive modification of poly (ethylene glycol) hydrogels for tissue engineering. *Biomaterials* 31, 4639–4656. doi:10.1016/j.biomaterials.2010.02.044.Bioactive

Figures:

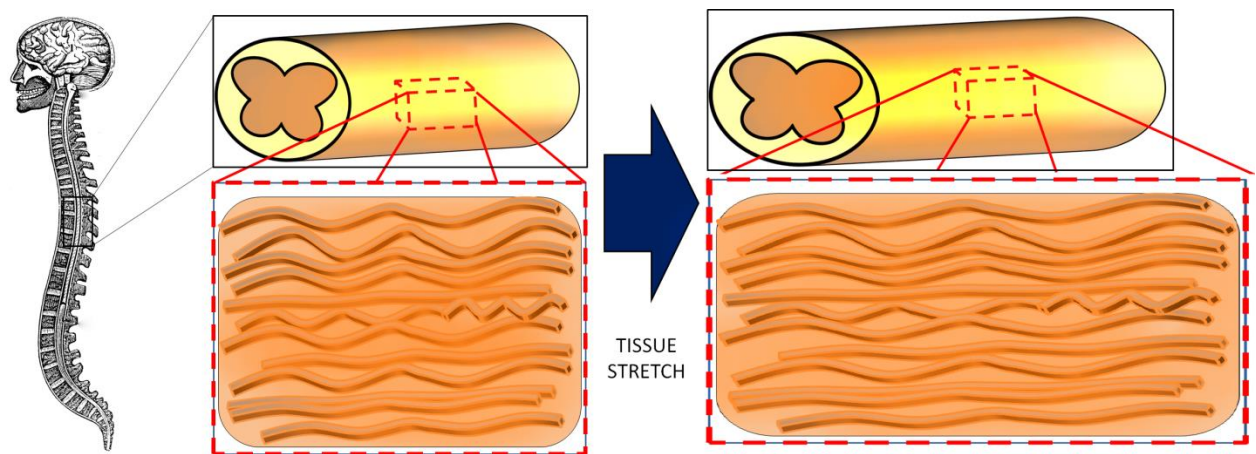


Figure 1-1: A schematic describing multiscale modeling of the spinal cord. Spinal cord tissue (macroscopic level) undergoes tissue-level stretch which causes deformation to axons (microscopic elements). Evidence from previous studies (Bain et al., 2003; Hao and Shreiber, 2007) strongly imply that this translation is not 1:1 and is dictated by microstructural components.

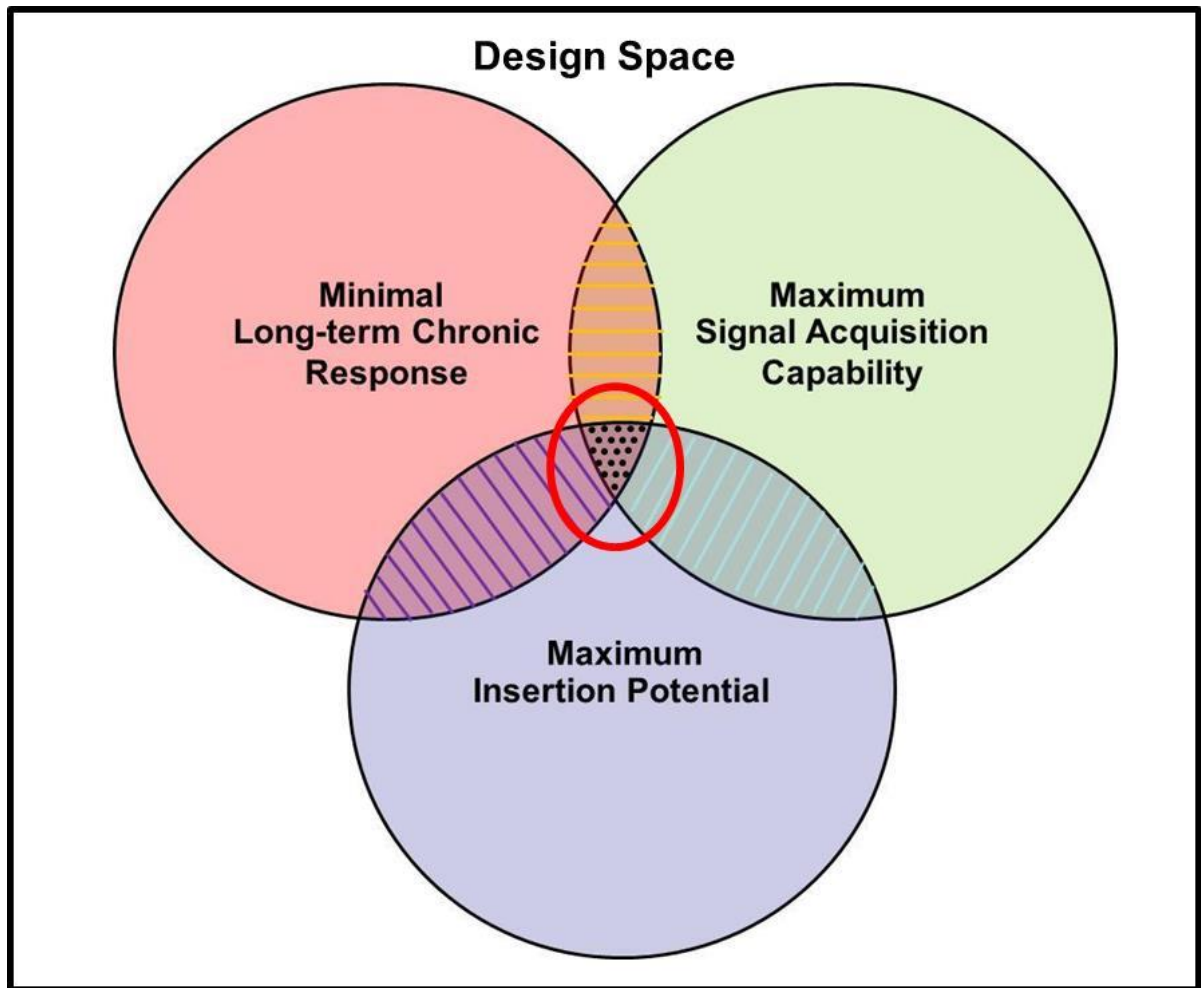


Figure 1-2: Depiction of the ideal probe in design space for neural electrodes. Ideal probes would mitigate the long-term chronic response, while being large enough to maximize space for conductive tracings (for fidelity in signal acquisition), and stiff enough for successful insertion into tissue. Unfortunately, the latter two features are in direct opposition to the first: larger, stiffer probes exacerbate the chronic response.

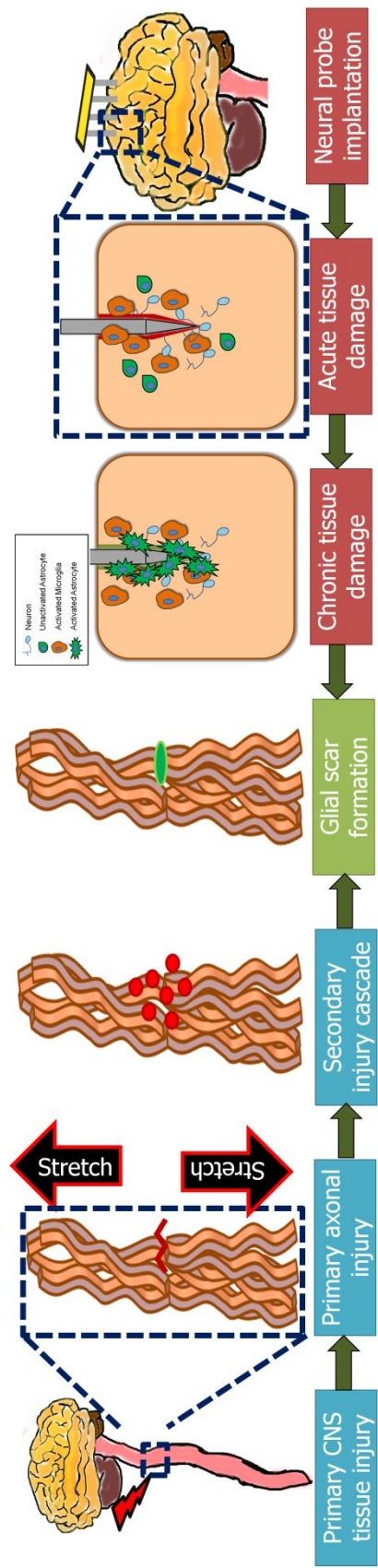


Figure 1-3: A schematic demonstrating the process flow of CNS primary injury and neural probe implantation. In both scenarios, there is a disconnect between stages in the macroscopic scale (primary CNS tissue injury via stretch/probe implantation into tissue) quantitatively translate to the microscale effects.

Chapter 2: Characterizing the 3-dimensional kinematic behavior of axons as a function of macroscopic stretch and development in white matter tissue

Major sections of this chapter have been excerpted from the following publication: Singh

S., Pelegri A.A., Shreiber D.I., 2015. “*Characterization of the three-dimensional kinematic behavior of axons in central nervous system white matter*”, Biomech. Model.

Mechanobiol.

1303–1315. I have received permission from the publishers to utilize this and all the work

presented herein is my own.

Abstract:

Axonal injury via stretch is the proximal cause of functional damage in traumatic brain and spinal cord injury. During injury, the stresses and strains experienced by the tissue are transferred to the microscopic axons. How this transfer occurs and the constituents which direct this multiscale translation is unclear, though it is accepted that axon tortuosity and kinematics exhibited by the microstructure influence transfer.

Previous studies have characterized axon tortuosity and kinematics in 2-dimensions (2-D), where axons were modeled to exhibit non-affine (discrete), affine (composite-like), and switching behavior. In this chapter, I outline the studies performed and their results in characterizing axon tortuosity and kinematic behavior in 3-dimensions (3-D), as a means to infer the macroscopic to microscopic transfer of stretch. Embryonic chick spinal cords at various developmental stages were exposed to controlled levels of stretch. Cords were fixed, transversely sectioned, and imaged via epifluorescent confocal microscopy. 3-D axon trajectory was traced through image stacks using a custom-built MATLAB script. 2-

D kinematic models previously described in Bain et al. (2003) were extended, re-derived, and validated for the 3-D case. Results showed 3-D tortuosity decreases with stretch, exhibiting similar trends with changes in development as observed in the 2-D case.

Kinematic behavior followed similar trends, where axons are predicted to exhibit more affine behavior with development. In comparison to 2-D, capturing the additional plane decreases the proportion of axons predicted to display non-affine behavior. The data and kinematic models presented in this chapter can be incorporated into current multi-scale approaches to modeling CNS injury, which can advance the accuracy of predictions and assist in gleaning more accurate axonal injury thresholds.

Background & Significance:

Traumatic injury to axons in white matter of the brain and spinal cord is one of the major causes of functional damage following primary injury (Smith and Meaney, 2000). Injury is often due to excessive tensile stretch experienced by CNS tissue (Bain and Meaney, 2000). During an injury event, strain is transferred from the tissue level to individual axons. Understandably, the properties of this transfer from macroscopic to microscopic levels are likely dictated by the features of the white matter microstructure (Meaney, 2003). In CNS white matter tissue, there is a heterogeneous population of components comprised of axons, myelin, oligodendrocytes, astrocytes, etc. Each of these components and their respective properties can contribute to the bulk material properties of the tissue as well as microscopic strain experienced by individual components. For instance, while axons are predominantly oriented in CNS tissue, they are not perfectly straight, but instead follow an undulated, tortuous path. This tortuosity, which we have defined as the ratio of the axon's pathlength to its end-to-end length, can influence the transfer of strain from the macroscale to the microscale.

Axon tortuosity has been characterized in 2-dimensions (2-D) in the chick embryo spinal cord, as well as the guinea pig optic nerve, in control tissue as well as tissue exposed to quasistatic (non-rate dependent) stretch (Bain et al., 2003; Hao and Shreiber, 2007). When excised white matter tissue is exposed to stretch, axons become progressively straighter and axon tortuosity decreases. However, the manner in which axons straighten and tortuosity changes is non-uniform, and dependent on the degree of macroscopic stretch, as well as developmental stage. Constituents of white matter, like other composite or composite-like materials, can demonstrate different degrees of

coupling with surrounding features, which serve to change kinematic behavior (Meaney, 2015; Pan et al., 2011; Shreiber et al., 2009). In 2-D characterizations, it was demonstrated that axon kinematics varied with stretch and development. Axons were theorized to exhibit one of three types of kinematic behavior: non-affine, affine, and switching (Hao and Shreiber, 2007).

In non-affine kinematic models, axons are assumed to be completely uncoupled, and straighten independently of one another with a given macroscopic stretch, acting in a manner akin to discrete elements. A consequence of this behavior is that an axon does not experience physical stretch until it has fully straightened, where the inherent tortuosity provides the axon extra slack in resisting macroscopic stretch and delaying its onset. At the opposite end of the spectrum, axons can be fully coupled to each other, exhibiting affine kinematics. Under this kinematic mode, axons behave like a composite, and experience the same geometric transformation as the tissue. As a result, axons are exposed to stretch even whilst undulated. The third type of behavior: switching, models an axon as a dynamic entity. Each axon has a unique switching threshold of tortuosity which dictates when the axon switches from non-affine to affine kinematics. As the tissue experiences stretch and axons straighten, axons eventually reach their individual threshold that causes kinematic behavior to vary. Previous studies suggest the propensity of affine behavior is a function of myelination and development. This is corroborated by studies of 2-D axon kinematics in the developing chick embryonic spinal cord (Hao and Shreiber, 2007), and by characterizations of experimentally demyelinated chick embryonic spinal cords, in which more developed, and myelinated cords were predicted to have axons with affine behavior (Shreiber et al., 2009).

Of course, axons traverse a 3-dimensions (3-D) trajectory. While we hypothesize that the kinematic trends observed for the 2-D case will carry forward in the 3-D case, it is likely that the degree of tortuosity and kinematic parameters for switching behavior will vary substantially, as information on the additional spatial plane would capture additional kinematic behavior which might have been disregarded in 2-D. Several studies have attempted to model the axon in 3-dimensions, either as a fascicle of hexagonally-arranged straight cylinders (Bas and Erdogmus, 2010), or as a helical coil (Nilsson et al., 2012), though neither study explored microstructure behavior due to stretch. Karami et al. used finite element modeling to simulate axon kinematics due to tissue-level stretch (Karami et al., 2009). However, the study relied on 2-D tortuosity and kinematic data to generate 3-D predictions and assumed pure affine behavior. More recently, Pan et al. (2013) modeled axons in a “pseudo 3-D” representative volume element (RVEs) that incorporated 2-D coupling behavior (Pan et al., 2013). However, model predictions have not been validated in 3-D. Characterizing and modeling axon kinematics in 3-dimensions will improve the predictive capabilities of CNS primary injury models, particularly in predicting axonal injury strain thresholds. In this work, we experimentally characterize the axon tortuosity in 3-D in the embryonic chick spinal cord as a function of tissue-level stretch. We then extend the model developed by Bain (Bain et al., 2003) and fitting procedures used in our previous study (Hao and Shreiber, 2007) to describe axon kinematic behavior in 3-D. We hypothesize that axon tortuosity in 3-D will be greater than 2-D, but that kinematic changes with development will be similar.

Methods:

Chick embryo spinal cord isolation: Fresh fertile chicken eggs (Charles River Laboratories, North Franklin CT) were incubated to specific development stages (Embryonic Day (E) – E12, E14, E16, and E18). The intact spinal cord was excised from the embryo by cutting along the length of the spinal column and removing the dorsal portion of the vertebrae. The full length of the spinal cord from the first cervical vertebrae (C1) to the eleventh lumbar vertebrae was measured three times with digital calipers and averaged. This measurement was designated the in situ length of the spinal cord. Pieces of reflective plastic (or glitter) were carefully placed onto the cord at the C3, C8, T4 (fourth thoracic vertebrae), and L4 (fourth lumbar vertebrae) regions using the spinal column as a visual guide. The distance between glitter markers was measured in situ, and the ventral portions of the vertebrae were removed, freeing the spinal cord from the column. The spinal cord was then pinned on each end of a custom-built microstretch device composed of two rapid-prototype platforms, and a 75mm x 30mm well immersed in 37°C phosphate buffered saline (PBS) solution (Figure 2-1). Distances between the reflective plastic pieces on the spinal cord were measured three times and averaged. The spinal cord was then stretched back to its in situ length, prior to being quasistatically stretched to a stretch ratio (λ) of 1 (unstretched control), 1.05, 1.10, 1.15, 1.2, or 1.25 defined as:

$$\lambda = \frac{\text{Final length of spinal cord}}{\text{Initial length of spinal cord}} \quad (\text{Eq 2-1})$$

Following stretch, spinal cords were photographed, and distances between the reflective plastic pieces were measured in their stretched state to confirm that macroscopic stretch was uniformly applied. Saline in the well of the microstretch device was replaced with 4% paraformaldehyde (Sigma-Aldrich, St. Louis MO) to fix tissue in its stretched state. Previous studies demonstrated that paraformaldehyde fixation does not affect the undulation or morphological appearance of axons in white matter tissue (Bain et al., 2003). Spinal cords were fixed in their stretched state for 15 minutes, carefully removed from the microstretch device, and re-measured to ensure length did not change during fixation. Afterwards, spinal cords were transferred to a fresh solution of 4% paraformaldehyde and stored overnight at 4°C, before being transferred to a cryoprotectant 20% sucrose-saline solution for at least 24 hours before sectioning and staining.

Immunohistochemistry: Spinal cords were removed from cryoprotectant solution and divided into cervical, thoracic, and lumbar regions with a razor blade. Each of these sections was divided again for coronal ([Figure 2-2A](#)) or transverse ([Figure 2-2C](#)) sectioning. Regions were embedded in Optimal Cutting Temperature (OCT) compound (Electron Microscopy Services). Frozen transverse or longitudinal sections (30µm thick) were cut on a cryostat (Thermo Electron) and placed on pre-treated glass slides (Fisher). Transverse sections were used for imaging in 3-D. Longitudinal sections were used to image the 2-D tortuosity for measuring by hand to validate our image processing algorithm (described below) and directly compare 2-D tortuosity measurements to our previous study (Hao and Shreiber, 2007). Sections were rinsed four times in immunobuffer (1% bovine serum albumin, and 0.5% Triton X-100 in phosphate buffered

saline) for 5 minutes each, and then incubated in a 10% goat serum blocking buffer for 1 hour. Sections were incubated overnight at 4°C with a primary antibody mixture of a 1:1000 dilution of mouse monoclonal α -Neurofilament-200 (Sigma) and a 1:500 dilution of rat monoclonal α -Myelin Basic Protein (MBP) (Invitrogen). Sections were again washed with immunobuffer four times for 15 minutes each and then incubated in a 1:400 dilution of Alexa 568 goat-anti-mouse secondary antibody and a 1:400 dilution of Alexa 488 goat-anti-rat secondary antibody for 1 hour. Sections were washed a final time with immunobuffer four more times for 15 minutes each and allowed to air-dry in the dark. Slides were then coverslipped with mounting solution (Vector Labs).

Histology: To quantify the degree of myelination, three spinal cords from each stage of development were fixed and stained with osmium tetroxide (OsO₄, Electron Microscopy Services). Stained spinal cords were embedded in epoxy resin, sectioned into 1- μ m thick slices with a microtome, counter-stained with toluidine blue (Electron Microscopy Services, Hatfield PA), and coverslipped.

Imaging: Confocal images of immunostained spinal cord sections were captured with an Olympus IX81 inverted epifluorescent microscope equipped with a spinning disk confocal unit and a Hamamatsu ImagEM digital camera (Middlesex NJ). Images were taken at 100x with filters at 488nm and at 568nm to visualize the different secondary antibody labeling. Images of 100 optical sections at increments of 0.3 μ m were captured through the thickness of each slice. Both the ventral funiculus and lateral funiculus were selected for imaging. Immunolabeling was observed to be qualitatively the most consistent in the ventral funiculus. The lateral funiculus was also imaged to provide side-by-side comparison with our previous study (Hao and Shreiber, 2007).

For longitudinal sections, the paths of 20 to 40 axons per image were traced using ImageJ. Tortuosity in 2-D was calculated by dividing the path length of the tracing by the end-to-end length. To examine the degree of myelination, osmium tetroxide-stained cross-sections were imaged using a 100x oil immersion objective under bright-field. Myelination was quantified by counting the number of myelinated fibers in images of each region. G-ratio was calculated for each myelinated axon, and was defined as the ratio of inner axonal diameter to outer diameter for each myelinated fiber (Chomiak and Hu, 2009).

Image Processing for 3-D Tortuosity Extraction: Image stacks were processed using a custom MATLAB script (Figure 2-3). Localized thresholding within an image was accomplished by dividing each image into a grid of 64x64 pixel sub-regions and operating on each sub-region separately. The median intensity in each sub-region was selected as the threshold intensity, based on preliminary findings where the mean intensity, and Otsu's method were used and found to be not as effective at cleaning images when compared to hand-based tracing results (Otsu, 1975). The processed regions were stitched back together to reconstruct the full image. Isolated, unconnected pixels were cleaned out so that the algorithm would not confuse these pixels for axons. The centroids of individual axons were identified in the first image of the stack. A 50x50 pixel region around each axon was cropped. Using a nearest neighbors approach, the next image of the stack was processed within the same 50x50 pixel region, and the Euclidian distance of the axon's centroid between the two images was calculated (Figure 2-3D). If more than one axon was present in the search area, the axon with the smallest distance was considered the correct one. This process was repeated for each image in the stack,

and the centerpoint displacements were stored and summed to determine the total path length that the axon has traveled. The tortuosity of the axon was then calculated. This process was repeated for each axon in the original image. Histograms of 3-D axon tortuosity were produced for each stretch level and development stage. Histograms for 2-D axon tortuosity for x-z and y-z longitudinal planes were also produced. The automated tracking algorithm was validated against 2-D and 3-D tortuosities measured by hand from test I images ([Figure 2-4](#)) and stained images of unstretched spinal cords ([Figure 2-5](#)).

Mathematical Model: Axon kinematics were modeled with MATLAB scripts modified from our previous study (Hao and Shreiber, 2007) that predicted tortuosity distributions at various stretch levels in the pure affine or non-affine states. The experimental distributions were first compared to idealized non-affine and affine distributions. The 3-D tortuosity data for unstretched specimens was used as input for the scripts. Expressions for the dependence of tortuosity on tissue-level stretch ratio (λ) in 3-dimensions were derived for non-affine and affine states. These derivations are provided below:

Non-affine model: In 2-dimensions, the microstructural transformation was calculated from the initial tortuosity, T_0 , and macroscopic stretch ratio, λ (Bain et al., 2003):

$$T_{2D} = \frac{1}{\lambda} T_0 \text{ for } \lambda < T_0 \quad (\text{Eq 2-2})$$

When the stretch ratio is equivalent to the initial tortuosity, the axon has completely straightened. If the stretch ratio continues to increase, the axon begins to stretch, but remains completely straight; mathematically this can be expressed as:

$$T_{2D} = 1 \text{ for } \lambda \geq T_0 \quad (\text{Eq 2-3})$$

In principle, this should apply to the tortuosity in 3-dimensions; axons when uncoupled will straighten according to the level of stretch, regardless of the additional plane of undulation. Additionally, once the axon has straightened, its tortuosity will remain at 1. Mathematically, this can be written as:

$$T_{3D} = \frac{1}{\lambda} T_0 \text{ for } \lambda < T_0 \quad (\text{Eq 2-4})$$

$$T_{3D} = 1 \text{ for } \lambda \geq T_0 \quad (\text{Eq 2-5})$$

Affine Model: The objective was to derive an analytical model for affine kinematics which predicted the axon's new tortuosity based on initial tortuosity and stretch.

In 2-dimensions, the undulated axon was modeled as a cosine wave with amplitude A_0 and period P_0 . There is no closed form solution for the pathlength. A solution was approximated using a simplification applicable for tortuosity values close to 1, producing the following transformation linking initial tortuosity and stretch ratio for 2-dimensional axons under an affine regime (Bain et al. 2003):

$$T_{2D} = T_0 \left[\frac{1}{\lambda^3} + \frac{1}{T_0^2} \left(1 - \frac{1}{\lambda^3} \right) \right]^{1/2} \quad (\text{Eq 2-6})$$

In adapting the kinematic model for 3-dimensional use, the 3-D axon is modeled as a helical coil, using two parametric periodic functions to describe the undeformed axon's path in each plane:

$$y(z) = A_{yz} \cos\left(\frac{2\pi z}{P_{yz}}\right) \quad \frac{dy(z)}{dz} = -\frac{2\pi A_{yz}}{P_{yz}} \sin\left(\frac{2\pi z}{P_{yz}}\right) \quad (\text{Eq 2-7})$$

$$x(z) = A_{xz} \sin\left(\frac{2\pi z}{P_{xz}}\right) \quad \frac{dx(z)}{dz} = \frac{2\pi A_{xz}}{P_{xz}} \cos\left(\frac{2\pi z}{P_{xz}}\right) \quad (\text{Eq 2-8})$$

By assuming incompressibility and isotropy, the axon's new amplitude and periodicity for a given stretch ratio, can be described as:

$$A_{new} = A_0 \left(\lambda^{-\frac{1}{3}}\right) \quad P_{new} = P_0(\lambda) \quad (\text{Eq 2-9})$$

Applying the transformations described in (Eq 2-9) to equations (Eq 2-7) and (Eq 2-8) gives the following equations for the deformed axon:

$$y'(z) = \frac{A_{yz}}{\sqrt[3]{\lambda}} \cos\left(\frac{2\pi z}{\lambda P_{yz}}\right) \quad (\text{Eq 2-10})$$

$$(\text{Eq 2-11})$$

$$x'(z) = \frac{A_{xz}}{\sqrt[3]{\lambda}} \sin\left(\frac{2\pi z}{\lambda P_{xz}}\right)$$

Differentiating equations (Eq 2-10) and (Eq 2-11) generates the following:

$$\frac{dy'(z)}{dz} = -\frac{2\pi A_{yz}}{\lambda^{4/3} P_{yz}} \sin\left(\frac{2\pi z}{\lambda P_{yz}}\right) \quad (\text{Eq 2-12})$$

$$\frac{dx'(z)}{dz} = \frac{2\pi A_{xz}}{\lambda^{4/3} P_{xz}} \cos\left(\frac{2\pi z}{\lambda P_{xz}}\right) \quad (\text{Eq 2-13})$$

The pathlength can be found by using (Eq 2-12) and (Eq 2-13) and integrating along the incremental path of the axon. Thus, the tortuosity of the stretched axon can be described as:

$$T_t = \frac{1}{L_e} \int_0^{L_e} \sqrt{1 + \left(-\frac{2\pi A_{yz}}{\lambda^{4/3} P_{yz}} \sin\left(\frac{2\pi z}{\lambda P_{yz}}\right)\right)^2 + \left(\frac{2\pi A_{xz}}{\lambda^{4/3} P_{xz}} \cos\left(\frac{2\pi z}{\lambda P_{xz}}\right)\right)^2} dz \quad (\text{Eq 2-14})$$

There is no analytical solution to the integral above. However, it is possible to approximate the solution for tortuosity by using the formula for the arc length of a helical coil:

$$s = 2\pi \sqrt{r^2 + P_0^2} \quad (\text{Eq 2-15})$$

where s is the arc length, r is the radius of the helix, and P_0 is the helix periodicity.

Experimental evidence from preliminary studies in unstretched chick embryo spinal cords and literature (Butt et al. 1994) supports the idea that the periodicity is the same in both x-z and y-z directions. This makes the equation above for arc length applicable, where the end-to-end length of a period of the helical axon is given by $2\pi P_{yz}P_{xz}$. Substituting (Eq 2-4) and (Eq 2-5) into (Eq 2-15) and dividing by the end-to-end length provides the following equation for initial undulation of the 3-D helical axon:

$$T_0 = \sqrt{1 + \frac{(A_{yz}^2 + A_{xz}^2)}{4} + 2\pi \left(\frac{A_{yz}}{P_{xz}} \times \frac{A_{xz}}{P_{yz}} \right)} \quad (\text{Eq 2-16})$$

Rearranging the above gives us:

$$T_0^2 - 1 - 2\pi \left(\frac{A_{yz}}{P_{xz}} \times \frac{A_{xz}}{P_{yz}} \right) = \frac{(A_{yz}^2 + A_{xz}^2)}{4} \quad (\text{Eq 2-17})$$

To simplify, we denote the product cross-ratio, $(A_{yz}/P_{xz} * A_{xz}/P_{yz})$ as a single variable, k .

Replacing instances of this product cross-ratio with k in (Eq 2-17), rearranging (Eq 2-17) in terms of T_0^2 , and substituting equations (Eq 2-12) and (Eq 2-13) into the arc length equation (Eq 2-15) generates expressions for the pathlength of the deformed axon.

Further rearranging gives an equation which links the transformed tortuosity to initial tortuosity and stretched ratio for axons in 3-D exhibiting affine behavior:

$$T_{3D} = T_0 \sqrt{\left\{ \frac{1}{\lambda^{8/3}} + \frac{1}{T_0^2} \left[1 - \frac{2\pi}{(2\pi + k^2)\lambda^{8/3}} \left(\frac{1}{k^2} + \frac{1}{2\pi} \right) \right] \right\}} \quad (\text{Eq 2-18})$$

Switching Model: The switching model incorporates both modalities where axons initially begin by exhibiting non-affine kinematics, and as the axon straightens (and

tortuosity decreases) there is a unique threshold after which the axon exhibits affine behavior. Mathematically, this is described by the following:

$$\begin{aligned}
 \text{Affine:} \quad & T < T_1 \\
 \text{Non-affine:} \quad & T > T_2 \\
 \text{Switching:} \quad & T_1 \leq T \leq T_2
 \end{aligned}
 \tag{Eq 2-19}$$

An axon with switching tortuosity, T , which falls in the purely affine regime demonstrates complete coupling with neighboring axons. Conversely, if T is sufficiently large (larger than T_2), the axon follows non-affine behavior. In the switching circumstance, each axon has a unique transition point, T which falls between T_1 and T_2 , where the axon switches from a non-affine to affine modality. At low levels of stretch, axons exhibit non-affine behavior. As tissue-level stretch increases, the axon straightens non-affinely and its tortuosity decreases until it reaches transition tortuosity, T , and its behavior switches to affine. The transition tortuosity is picked randomly from a uniform distribution for developmental stage with lower bound T_1 , and upper bound T_2 of the corresponding uniform distribution.

The computational model (presented in Bain et al. 2003) attempts to reconcile this mathematical framework with experimental results. Each axon in the distribution is assigned a unique tortuosity value at which it switches (based on the unstretched data). The unique switching value is picked from a uniform distribution. The distribution of axon tortuosities is then artificially stretched, and the new tortuosity values are calculated and compared to the conditions of the switching model. Axons with tortuosities above their switching value have their new tortuosity calculated via the non-affine modality. Once its tortuosity reaches the switching value, the new tortuosity is calculated using the

affine modality. The resultant distribution of tortuosities is then compared to the experimental data for that particular stretch level, and goodness-of-fit tests measure the extent to which the model agrees with the experimental data. The model then picks new values for the upper (T_2) and lower (T_1) bounds and reiterates until a convergence is reached for T_1 and T_2 . Using this scheme, the bounds of the uniform distribution that describes the transition tortuosity can be interpreted as a measure of the propensity for affine or non-affine behavior. The model was executed 100 times for each case, from which the mean values, standard deviation, and regression coefficients for each fit were determined. In our previous study, the fitting procedure uniformly resulted in the lower bound $T_1 < 1$ and the upper bound $T_2 > 1$. With these conditions, a fraction of the transition tortuosities $[(1-T_1)/(T_2-T_1)]$ will be less than 1. For this fraction of axons, because the minimum value for actual tortuosity is 1, the transition tortuosity is never reached, and the axons will exhibit non-affine behavior permanently.

Equation validation: Finite element analysis (FEA) was used to validate the 3-D kinematic model equations. These models were developed using the ABAQUS software suite (Simulia). A population of seven axons (Stiffness, $E = 0.29\text{kPa}$, Poisson's Ratio, $\nu = 0.49$, Density, $\rho = 1250\text{kg/m}^3$) (Magdesian et al., 2012; Ouyang et al., 2013), with varying tortuosities were generated (Figure 2-6). A MATLAB script was employed to extract the nodal positions and calculate the original and final tortuosities. Non affine axons were modeled as single helical coils and stretched either 10% or 20% of the original end-to-end. Affine axons were modeled as the same helical coils embedded in a solid matrix. Tie constraints were incorporated between axons and the surrounding matrix

to simulate complete coupling. The 10% or 20% stretch was then applied to the solid matrix.

Results:

Growth and morphological features of spinal cords: Figures 2-7A and 2-7B show representative images of stained transverse sections of spinal cords from E12 and E18 respectively (Figure 2-7). Spinal cords at later stages of development showed the tell-tale ‘butterfly’ profile when stained for myelin basic protein. The average *in situ* length of the spinal cord increased from 14.1 ± 1.6 mm at E12 ($N = 22$) to 24.2 ± 2.8 mm at E18 ($N = 24$), similar to results from our previous study. Lengths of the semi-major axis for spinal cord cross-sections increased from 884 ± 122 μ m at E12 to 2290 ± 274 μ m at E18. Following excision, spinal cords were observed to shrink about 4.8% in length compared to their *in situ* length. This was consistent across all developmental stages (Table 2-1, $P_{\min} = 0.12$). We determined the percentage of myelinated fibers at each development stage for both the lateral funiculus and ventral funiculus (Figure 2-8 and Figure 2-9C) using osmium tetroxide staining. More myelinated fibers were found in the ventral funiculus from E12-E16. At E18, the percentages of myelinated fibers are equal in both regions. This trend is consistent with previous findings (Chung K, 1983). Myelination followed a sigmoidal relationship in both regions, where the largest increase was seen between E14-E16. We also examined the G-ratio, which is a measure of the amount of myelin around an axon. Differences in the G-ratio between the ventral and lateral funiculus for each stage of development were evaluated with a Kruskal-Wallis (K-W) non-parametric test and were not statistically significant ($P_{\min} = 0.227$). Average axon diameter also increased with development, increasing from 0.7 ± 0.6 μ m at E12 to 1.2 ± 0.7 μ m at E18. Distributions of axon tortuosity in the lateral and ventral funiculus were compared at 0% and at 10% stretch at each developmental stage. Histograms of 3-D axon tortuosity for

unstretched E12 and E18 specimens at each region are shown in Figures 2-5D to 2-5G (Figure 2-5). The only statistically significant difference between the two regions was observed in E14 spinal cords exposed to 10% stretch ($P = 0.049$). Tortuosity significantly decreased as stretch level increased.

2-D and 3-D Tortuosity Measures: Mean 3-D tortuosity decreased with increasing stretch for each developmental stage (Table 2-2). For example, in E18 specimens tortuosity decreased from 1.146 to 1.042 as stretch increased from 0% to 20%. The largest decrease in average tortuosity was observed in E12 samples (1.158 to 1.018). K-W tests were used to evaluate the differences between the x-z and y-z tortuosities extracted from confocal stacks of transverse sections and 2-D tortuosities measured by hand from longitudinal sections. No statistical significance was found in either x-z or y-z orientations ($P_{min} = 0.094$), and these data were subsequently combined for our microkinematic analyses. Mean 3-D tortuosity was consistently higher than 2-D tortuosity for all given development and stretch levels (Figure 2-10A). For both 2-D and 3-D, tortuosities in unstretched samples decreased with development, but increased with development at higher stretch levels. Tortuosity was also compared across the three regions of the spinal cord. Two-tailed K-W tests were done among the distributions generated for the cervical (C3-C8), thoracic (C8-T4), and lumbar regions (T5-L4) at each age and stretch level. No statistically significant differences were found ($P_{min} = 0.071$), and the regional distributions were pooled into a single distribution per age group and stretch level. The distributions of tortuosity with stretch (Figure 2-10B) demonstrate some important trends. For example, in all age groups, axons are the straightest at the highest stretch level. However, the percentage of axons that can be classified as “perfectly straight”

(tortuosity of 1) decreased with increasing age, which indicates a shift to affine kinematics with development and myelination. In particular, a significant drop in straight axons was observed from E14 to E16, where the percentage of perfectly straight axons fell from 50% to 35%. We compared distributions across development stages for a given stretch using pairwise two-tailed K-S tests ($P < 0.01$) and found significant changes in the tortuosity distribution in control samples ($P_{max} = 0.004$), 10% stretch level ($P_{max} = 0.001$), and 20% stretch level ($P_{max} < 0.001$).

As mentioned above, spinal cord *ex vivo* lengths were on average 4.7% less than the *in situ* lengths. We characterized tortuosities in spinal cords not exposed to pre-stretch to determine whether axons become more undulated with adjustments to their natural state. Mean tortuosity slightly increased in all cases (Figure 2-11). Distributions shifted slightly to the right for cords not exposed to pre-stretch when compared to cords stretched to their *in situ* length. This shift was statistically significant ($P_{max} = 0.04$). These differences justified the application of pre-stretch in determining morphology changes with stretch.

Microkinematic Behavior: We extended previously developed models to characterize the 3-D microkinematic behavior for axons. At each developmental stage, distributions for unstretched axons were used as the input data. The kinematic models were used to predict the response assuming pure affine and non-affine behaviors. The equations for these idealized models and predicted results for tortuosity as a function of macroscopic stretch were first validated against a finite element model. In the purely affine case, axons did not completely straighten. The kinematic model results and finite element simulations agreed to within 0.6% axon stretch (or 3.4% engineering strain) ([Table 2-3](#)).

To determine the switching behavior, the bounds of the transition tortuosity distribution, T_1 and T_2 , were computationally iterated to allow an axon to move from non-affine to affine behavior until the predicted tortuosity distributions at the four different stretch levels converged against the experimental distributions. This was performed for all developmental stages, to determine how kinematics varied with morphological changes in the spinal cord.

Using our unstretched tortuosity data as input, we calculated “idealized” distributions of tortuosity at different stretch levels when axons exhibit pure affine and non-affine behaviors. Neither the pure affine nor non-affine models matched the experimental data for a given tissue-level stretch at any developmental stage when we evaluated cumulative frequency distributions of experimental data and predicted results (Figure 2-12).

Allowing axons to transition from non-affine to affine kinematics according to the switching model improved the agreement between the model results and experimental data, based on K-W test statistics ($P < 0.001$). Similar to the 2-D study, we found that more developed spinal cords showed more affine-like behavior. For example, there was an 11% decrease in the percentage of perfectly straight axons from E12 profile to E18 at 10% stretch. As shown in Figure 2-13A, T_1 increased with developmental stage, whereas T_2 values remained relatively constant (Figure 2-13). This trend was also seen in 2-D distributions, though no statistically significant differences were found between 2-D and 3-D lower bound (T_l) transition parameters ($P_{min} = 0.114$). These values were used to estimate the percentage of axons that follow purely non-affine kinematics. As shown in Figure 2-9C, the percentage of axons predicted to behave purely non-affinely decreased during development from ~50% at E12 to ~20% at E18. The predicted percentage of non-

affine axons was also consistently lower from the 3-D data than from the 2-D data at all developmental stages ($P < 0.005$).

Another set of tests were executed where one of the transition points (T_1 , T_2) was held fixed while the second point was iteratively transformed. Mechanically speaking, as T_1 decreases below 1, holding T_2 constant, a greater percentage of axons will demonstrate permanently non-affine behavior regardless of any macroscopic stretch these axons experience. Conversely, when T_1 is held constant at the average value of 0.921 and T_2 is increased, a smaller percentage of axons demonstrate non-affine behavior. In our simulations where T_1 was held constant, we observed that there were statistically significant changes to the cumulative distribution functions when compared to their respective control cases. When T_2 was held constant at 1.122, (average value across all 4 developmental stages) the model predicted no significant difference in cumulative distribution functions for the non-affine and affine distributions when compared with the two-parameter model. These findings are similar to the predictions made by the 2-D model where changes to the lower-bound tortuosity caused the biggest variation in kinematic predictions.

Discussion:

In this chapter, we present a quantitative characterization of CNS axon tortuosity in 3-dimensions using a novel image processing algorithm to extract axon positions from confocal images of spinal cord cross-sections. Using a nearest-neighbors methodology, we tracked single axon trajectories through cross-sections of spinal cord slices. The algorithm finds axons and measures and sums the displacement of their center points to determine tortuosity. We also stained for myelin basic protein as an indicator of spinal cord myelination, as well as to ensure that our characterizations targeted white matter axons. There was excellent agreement between 2-D data extracted from the 3-D characterization of transverse cross-sections and the 2-D data previously acquired from longitudinal slices (Hao and Shreiber, 2007) and from longitudinal sections processed in parallel in this study, which validated our image processing algorithm.

We then used tortuosity as a metric to evaluate axonal kinematics during controlled stretch of white matter. We found that our results in 3-D follow the same general kinematic trends as those found in 2-D with some consistent differences in the magnitude of the response. Previously, we estimated an 8.3% increase in tortuosity in unstretched axons by projecting 2-D results to 3-D by assuming that an axon resembles a coil with amplitude that is 10% of the axon's periodicity (Hao and Shreiber, 2007). This predicted increase in the path length of the axon is consistent with our more direct comparison in this work, where the average tortuosity in unstretched samples was 5.3% greater when measured in 3-D vs. 2-D. The 3-D tortuosity of axons within unstretched tissue decreased with development stage for the chick spinal cord, with axons becoming straighter with age and growth, and also decreased after the tissue was exposed to quasistatic stretch.

When the 3-D tortuosity data across all developmental stages and stretch levels is considered, similar trends to our previous 2-D characterization were observed, where mean tortuosity demonstrates a downward trend with development stage at low stretch levels, which reverses at higher levels of stretch ([Figure 2-10A](#)) (Hao and Shreiber, 2007).

As a result of physical growth of the spinal cord, the tortuosity of unstretched axons decreased with increasing development. The axial length of the spinal cord increased with development by almost 104% between E12 and E18 specimens, with a large spurt in growth seen between E12-E14 and E14-E16 (~23% increase between each period), and the two-fold increase in cord diameter in the same timeframe. It is possible that due to this growth-induced tension, the proportion of axons with a tortuosity of 1 increased with development. With the two-fold increase in length between E12 and E18, we would expect mean tortuosity to decrease more dramatically, as those axons in E12 should completely straighten due to growth-induced tension. This was not the case and we hypothesize that the genesis of new axons, that are inherently tortuous, contribute to this finding. Alternatively, kinematic coupling could be occurring at earlier stages, which would explain why we observed a much smaller proportion of perfectly straight axons than expected.

Results of the kinematic characterization in 3-dimensions were similar to those found in the 2-D characterization (Bain et al., 2003; Hao and Shreiber, 2007). These previous studies implied that the kinematic transition from non-affine to affine behavior is primarily driven by myelination, and not natural straightening of axons due to growth-induced tension. Axons in 3-D followed a model that allows transition from non-affine to

affine kinematics. In general, the value of the lower (T_1) and upper (T_2) bounds of the transition tortuosity distribution were larger for the 3-D characterization than the 2-D (Figure 2-13A). However, these differences were consistently significant only for the upper bound across embryonic stages ($P_{\max} = 0.037$ for E16). Figure 2-13B provides a graphical interpretation of the transition tortuosity results. An axon initially behaves with non-affine kinematics as it is stretched until its tortuosity reaches T_2 . From this point, the probability that the axon switches to affine kinematics is based on a uniform distribution with lower bound T_1 and upper bound T_2 . Thus, when a population of axons is considered, the intercept of the sloped line from this distribution with the line $T=1$ (red line in Figure 2-13B) represents the fraction of axons which are predicted to exhibit purely non-affine kinematics regardless of stretch because the actual tortuosity cannot decrease below 1. Lower values of T_1 and of T_2 will decrease the percentage of non-affine axons. Therefore, as development progresses from E12 to E18 and T_1 increases in value while T_2 remains constant, the intercept increases, which implies that a smaller proportion of axons will remain permanently non-affine. Figure 2-13B also demonstrates how the larger T_2 value for 3-D vs. 2-D behavior indicates a propensity for more affine behavior. Figure 2-13C depicts the percentage of permanently non-affine axons as a function of development stage. As with our previous 2-D study, this percentage decreased with development stage, falling about 31% from E12-E18 compared to 34% from our previous 2-D results (Hao and Shreiber, 2007). Collectively, these results support the hypothesis that increased myelination and glial presence is linked to coupling behavior and that these features influence 3-D kinematic behavior in a similar fashion to 2-D. Furthermore, we

surmise a contributing cause for the larger T_2 values predicted is the implicit capture of the extra plane in which myelination and coupling occurs.

We characterized both the ventral and lateral funiculus regions of the spinal cord. In preliminary experiments, we observed the highest amount of immunofluorescence and best image quality in the ventral funiculus. We also examined the lateral funiculus to provide direct comparisons to our previous study (Hao and Shreiber, 2007). We found that tortuosity is similar in both regions (Figure 2-9 D-G), but the profile of myelination during development was different particularly at E14, where more myelinated fibers were present in the ventral funiculus. This generally agrees with previous studies that identified the ventral funiculus as one of the first to myelinate (Anderson et al., 2000). When the tortuosity data for the two regions was fit to our kinematic model, more affine-like behavior was predicted for the ventral funiculus than the lateral funiculus, which supports the role myelin plays in inducing kinematic coupling behavior. By E18, myelination in the ventral and lateral funiculi was not significantly different ($P = 0.21$). We modeled axons using sinusoidal parametric equations, enabling us to construct an analytical solution for describing how axon tortuosity changes with stretch in the affine case. Morphologically, axons exhibit periodicity in their trajectory, which supports the use of these equations in modeling kinematic behavior. Our models used a product cross-ratio of amplitude-to-periodicity ($'k'$) of 1 in calculations. Our 2-D characterizations showed amplitude and periodicity was independent of axon orientation in the spinal cord, justifying our selection of $k = 1$. Varying our parameter, k , could theoretically allow us to model axon kinematics in different regions of white matter tissue. Black et al.

demonstrated axon morphology, including myelination and undulation, was heterogeneous and varied by region.

To validate our kinematic equations, we used finite element modeling to simulate axons undergoing stretch in the two extremes of kinematics. The disagreement between the FEM and experimental results stems from the differences in axo-glial linkages that individual axons can have. Our finite element model generated axons which are assumed to be completely untied or 100% tied to the glial matrix. Previous studies hypothesize the differences in transition tortuosities between non-affine to affine behavior is likely to be dependent on the quantity of axo-glial linkages for that given segment of an axon. For instance, an axon segment populated with more axo-glial linkages would exhibit more affine behavior, and hence, have a lower value for T_2 , than that with fewer linkages. More accurate finite element simulation would generate axons with a random localization and degree of linkages to the surrounding matrix to reflect the unique transition points between non-affine to affine behaviors. Our FEM, however, did closely match and validate the predictions made by the derived equations for purely non-affine and affine behaviors.

The rationale in characterizing and modeling axon kinematics is to provide a means of inferring axon-level strain as a function of tissue-level stretch. Our results here and in our previous study (Hao and Shreiber, 2007) imply that tortuosity and kinematic behavior can influence axonal injury thresholds. Under a non-affine framework, we assume that the microstructure does not experience strain until the axon has unfolded and fully straightened, contrasting with affine kinematics, in which strain is immediately transferred to axons with tissue-level stretch. The higher tortuosities observed in 3-D

versus 2-D suggest that axons exhibiting purely non-affine kinematics have a greater threshold of macroscopic stretch than axons that switch or are already behaving with affine kinematics. When we examine this in the context of switching kinematics, our T_2 parameter increases by 3.7% when comparing 2-D and 3-D, which is less than the increase in mean tortuosity, suggesting that macroscopic injury thresholds when the 3-D path is accounted for will be greater at earlier stages of development where a larger proportion of axons are non-affine.

Although this characterization of axon kinematics is in 3-D, the consistency of the results and trends between 2-D and 3-D and between two different tissue types and species (developing chick spinal cord and adult guinea pig optic nerve) (Bain et al., 2003), especially for “fully myelinated” tissue, suggests that the approach can be incorporated into computational models of traumatic brain injury and spinal cord injury, and white matter injury in general. This may be best accomplished using a multi-scale framework that employs representative volume elements of white matter (Cloots et al., 2011; Karami et al., 2009; Pan et al., 2013, 2011). Multi-scale models have the potential to capture the evolution of anisotropic tissue properties as the microstructure mechanically responds to applied loads. These models may also translate the macro-scale response to the micro-scale, where individual entities can be explicitly defined, to predict injury to individual cellular or tissue components. For axonal injury, this latter aspect is particularly important, given the large discrepancy between strain injury thresholds determined from in vivo models at the tissue level (Bain and Meaney, 2000) and those found from in vitro preparations of individual axons (D. H. Smith et al. 1999; Tang-Schomer et al. 2010; Wright & Ramesh 2012).

We have previously developed RVEs based on the “switching” kinematic framework described herein that have accurately predicted the evolution of tortuosity with stretch and the resultant tissue-level mechanical properties for axial loading of spinal cord tissue (Pan et al., 2013). For this RVE approach to be adopted for models of brain injury, however, the tortuosity of different regions of white matter must be characterized, which is a burdensome and difficult chore. Rapid advances in imaging techniques may enable non-invasive determination of white matter microstructure (Meaney, 2003). For example, diffusion tensor imaging (DTI) is a potential method for characterizing both the tortuosity and the myelination of axons. Nilsson et al. modeled water diffusion within undulated axons, and concluded that the tortuosity increases the diffusion time parameter to the equivalent of doubling axon diameter, confining the space in which water molecules can diffuse (Nilsson et al., 2012). Their study also represented axons as helical coils. Although the axon path can be modeled as a persistent random walk (Katz, 1985), which may more closely resemble the actual path, the regular geometry associated with the helical coil model enabled an analytical solution for the affine kinematic behavior and simplified modeling of diffusion as well. Stochasticity can then be introduced to a population of axons. Our models used a product cross-ratio of amplitude-to-periodicity (k) of 1 in calculations. The cross-ratio can be adjusted to account for differences in axon morphology in different regions of white matter. Axon orientation is another important feature that models should capture, as it varies in different regions of CNS, conferring isotropy in some regions, and anisotropy in others. It is clear that axon orientation influences strains experienced by these microstructural elements. Cloots et al. reported that maximum axonal strain relative to applied stress was modeled to occur

when the tissue-loading direction is 45° of the main axonal direction (Cloots et al., 2011), though the study omits the effects of undulation and kinematic behavior. Studies on randomly oriented collagen fiber networks showed that both orientation and kinematics influenced the strains experienced by individual fibers (Chandran and Barocas, 2006). Axon orientation would particularly influence straightening, and rotation of non-affine axons if, for example, the direction of tissue-level stretch was parallel to the axon's main orientation. Other work highlights experimental differences in straight vs. undulated axon fibers (Assaf et al., 2000), and in myelinated vs. unmyelinated fibers (Kunz et al., 2014). Extracting such information would allow development of RVEs for many in vivo models of TBI as well as simulations of clinical cases of TBI.

Conclusions:

In this chapter, we characterized the 3-dimensional kinematic behavior of axons to better infer the transfer of macroscopic to microscopic stretch. Similar to Hao's 2007 study (Hao and Shreiber, 2007), chick embryonic spinal cords at various stages of development were excised and exposed to controlled stretch. Axon morphology was then characterized and tortuosity was used as a metric to predict how kinematic behavior varied as a function of stretch and development stage. From this, we extended 2-dimensional models of axon kinematic behavior by re-deriving the characteristic equations used to calculate axon tortuosity as a function of macroscopic stretch

The rationale for characterizing kinematics is that it enabled simultaneous characterization of other microstructural features in white matter. As mentioned earlier, microstructural features are responsible for tissue-level stretch affecting axonal strain. In this chapter, we characterized 3-D axon tortuosity, axon diameter, and myelination. These properties were then examined to predict how axon kinematic behavior would change for given degrees of macroscopic, tissue-level stretch.

A limitation to this treatment is while our approach enables inferences to be made on the transfer of strain to the population of axons as a whole; we have little quantitative insight on the extent to which macroscopic stretch is being transferred to individual axons. The kinematic parameters we derived from our model for instance, can estimate proportions of axons expected to behave non-affinely and experience no strain until straightened, but these same parameters fail to indicate how individual axons behave with macroscopic stretch. To elucidate this behavior would require a means of measuring axonal strain *in situ*; the primary focus of the next chapter in this thesis.

References:

- Anderson, E.S., Bjartmar, C., Hildebrand, C., 2000. Myelination of prospective large fibres in chicken ventral funiculus. *J. Neurocytol.* 29, 755–64.
- Assaf, Y., Mayk, A., Cohen, Y., 2000. Displacement imaging of spinal cord using q-space diffusion weighted MRI. *Magn. Reson. Med.* 722, 713–722.
- Bain, A., Meaney, D., 2000. Tissue-level thresholds for axonal damage in an experimental model of central nervous system white matter injury. *J. Biomech. Eng.* 122, 615–22.
- Bain, A.C., Shreiber, D.I., Meaney, D.F., 2003. Modeling of Microstructural Kinematics During Simple Elongation of Central Nervous System Tissue. *J. Biomech. Eng.* 125, 798. doi:10.1115/1.1632627
- Bas, E., Erdogmus, D., 2010. Piecewise linear cylinder models for 3-dimensional axon segmentation in brainbow imagery. *Biomed. Imaging From Nano to Macro, ...* 1297–1300.
- Chandran, P.L., Barocas, V.H., 2006. Affine versus non-affine fibril kinematics in collagen networks: theoretical studies of network behavior. *J. Biomech. Eng.* 128, 259–70. doi:10.1115/1.2165699
- Chomiak, T., Hu, B., 2009. What is the optimal value of the g-ratio for myelinated fibers in the rat CNS? A theoretical approach. *PLoS One* 4, e7754. doi:10.1371/journal.pone.0007754
- Chung K, C.R., 1983. Numbers of axons in lateral and ventral funiculi of rat sacral spinal cord. *J Comp Neurol.* 10, 72–8.
- Cloots, R.J.H., van Dommelen, J. a W., Nyberg, T., Kleiven, S., Geers, M.G.D., 2011. Micromechanics of diffuse axonal injury: influence of axonal orientation and anisotropy. *Biomech. Model. Mechanobiol.* 10, 413–22. doi:10.1007/s10237-010-0243-5
- Hao, H., Shreiber, D.I., 2007. Axon kinematics change during growth and development. *J. Biomech. Eng.* 129, 511–22. doi:10.1115/1.2746372
- Johnson, V.E., Stewart, W., Smith, D.H., 2013. Axonal pathology in traumatic brain injury. *Exp. Neurol.* 246, 35–43. doi:10.1016/j.expneurol.2012.01.013
- Karami, G., Grundman, N., Abolfathi, N., Naik, a, Ziejewski, M., 2009. A micromechanical hyperelastic modeling of brain white matter under large deformation. *J. Mech. Behav. Biomed. Mater.* 2, 243–54. doi:10.1016/j.jmbbm.2008.08.003
- Katz, M.J., 1985. How straight do axons grow? *J. Neurosci.* 5, 589–95.

- Kunz, N., Zhang, H., Vasung, L., O'Brien, K.R., Assaf, Y., Lazeyras, F., Alexander, D.C., Hüppi, P.S., 2014. Assessing white matter microstructure of the newborn with multi-shell diffusion MRI and biophysical compartment models. *Neuroimage* 96, 288–99. doi:10.1016/j.neuroimage.2014.03.057
- Magdesian, M.H., Sanchez, F.S., Lopez, M., Thstrup, P., Durisic, N., Belkaid, W., Liazoghli, D., Grütter, P., Colman, D.R., 2012. Atomic force microscopy reveals important differences in axonal resistance to injury. *Biophys. J.* 103, 405–14. doi:10.1016/j.bpj.2012.07.003
- Meaney, D.F., 2015. Accidental Injury. doi:10.1007/978-1-4939-1732-7
- Meaney, D.F., 2003. Relationship between structural modeling and hyperelastic material behavior: application to CNS white matter. *Biomech. Model. Mechanobiol.* 1, 279–93. doi:10.1007/s10237-002-0020-1
- Nilsson, M., Lätt, J., Ståhlberg, F., van Westen, D., Hagslätt, H., 2012. The importance of axonal undulation in diffusion MR measurements: a Monte Carlo simulation study. *NMR Biomed.* 25, 795–805. doi:10.1002/nbm.1795
- Otsu, N., 1975. A threshold selection method from gray-level histograms. *Automatica C*, 62–66.
- Ouyang, H., Nauman, E., Shi, R., 2013. Contribution of cytoskeletal elements to the axonal mechanical properties. *J. Biol. Eng.* 7, 21. doi:10.1186/1754-1611-7-21
- Pan, Y., Shreiber, D.I., Pelegri, A. a, 2011. A transition model for finite element simulation of kinematics of central nervous system white matter. *IEEE Trans. Biomed. Eng.* 58, 3443–6. doi:10.1109/TBME.2011.2163189
- Pan, Y., Sullivan, D., Shreiber, D.I., Pelegri, A. a, 2013. Finite Element Modeling of CNS White Matter Kinematics: Use of a 3D RVE to Determine Material Properties. *Front. Bioeng. Biotechnol.* 1, 19. doi:10.3389/fbioe.2013.00019
- Shreiber, D.I., Hao, H., Elias, R. a I., 2009. Probing the influence of myelin and glia on the tensile properties of the spinal cord. *Biomech. Model. Mechanobiol.* 8, 311–21. doi:10.1007/s10237-008-0137-y
- Smith, D.H., Meaney, D.F., 2000. Axonal Damage in Traumatic Brain Injury. *Neurosci.* 6, 483–495. doi:10.1177/107385840000600611
- Smith, D.H., Wolf, J. a, Lusardi, T. a, Lee, V.M., Meaney, D.F., 1999. High tolerance and delayed elastic response of cultured axons to dynamic stretch injury. *J. Neurosci.* 19, 4263–9.
- Tang-Schomer, M.D., Johnson, V.E., Baas, P.W., Stewart, W., Smith, D.H., 2012. Partial interruption of axonal transport due to microtubule breakage accounts for the formation of periodic varicosities after traumatic axonal injury. *Exp. Neurol.* 233, 364–72. doi:10.1016/j.expneurol.2011.10.030

Tang-Schomer, M.D., Patel, A.R., Baas, P.W., Smith, D.H., 2010. Mechanical breaking of microtubules in axons during dynamic stretch injury underlies delayed elasticity, microtubule disassembly, and axon degeneration. *FASEB J.* 24, 1401–10. doi:10.1096/fj.09-142844

Wright, R.M., Ramesh, K.T., 2012. An axonal strain injury criterion for traumatic brain injury. *Biomech. Model. Mechanobiol.* 11, 245–60. doi:10.1007/s10237-011-0307-1

Figures:

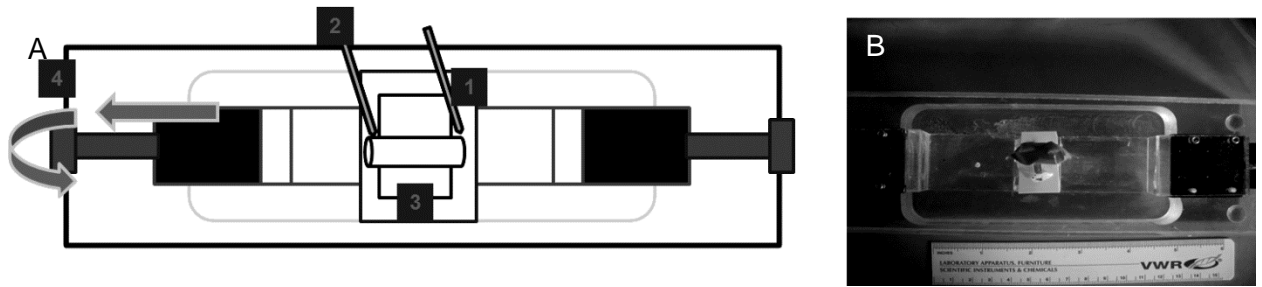


Figure 2-1: (A) Schematic of microstretch device used to apply quasistatic stretch to spinal cord tissue specimens composed of 4 components: (1) Thin plastic pieces were cut to hold tissue in place; (2) Pinning needle to hold thin plastic (1) and fix it to rapid prototype pieces; (3) Tissue specimens were then glued on each end using a cyanoacrylate glue; (4) A crank allows for controlled application of stretch.

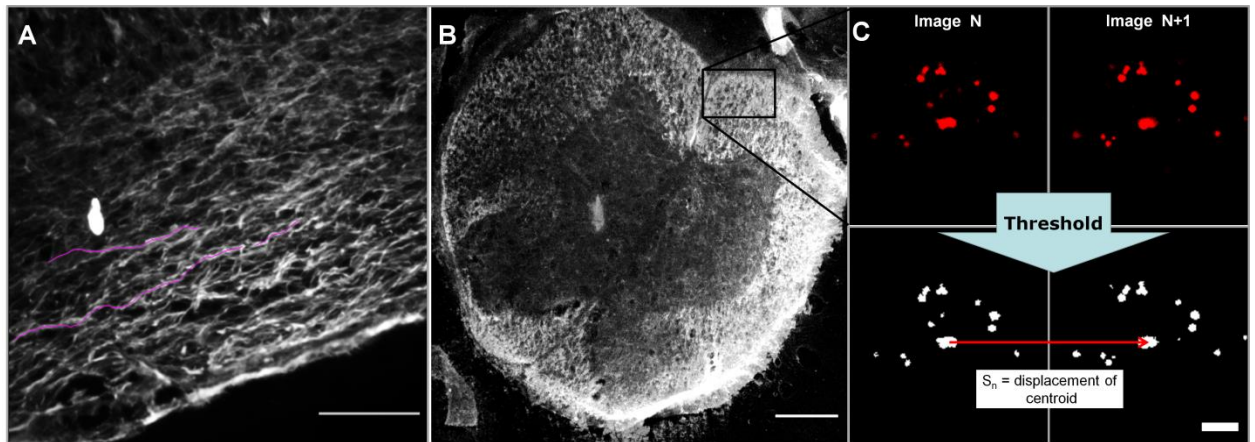


Figure 2-2: (A) Longitudinal sections of spinal cord tissue were stained for neurofilament-200kD to track 2-D tortuosity. These results were then compared with the x-z and y-z results from our custom-built image processing algorithm for validation (Scale Bar = 100 μ m). (B) Transverse sections were stained for neurofilament-200kD and MBP (Scale Bar = 200 μ m). The composite images showed the tell-tale “butterfly” signifying the location of white matter in spinal cords. (C) Zoomed-in white matter region of the cross-section. Images confocally taken with 100x oil-immersion objective were thresholded. Displacement of each axon’s centroid (S_n) from image, N, to image, N+1, was then summed through the image stack to calculate axon path length, and tortuosity. (Scale Bar = 2 μ m).

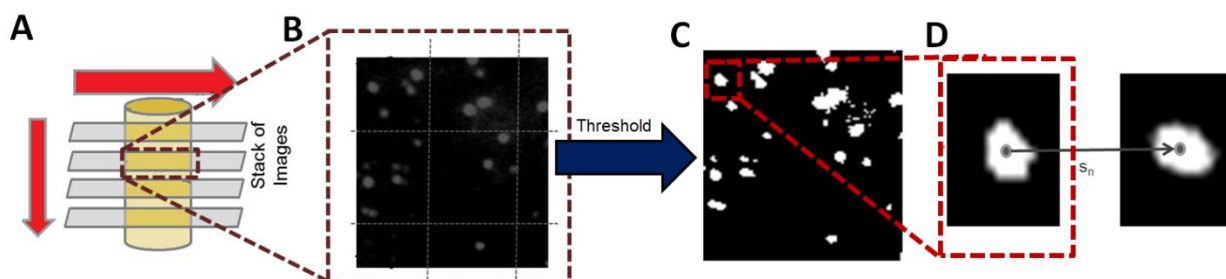
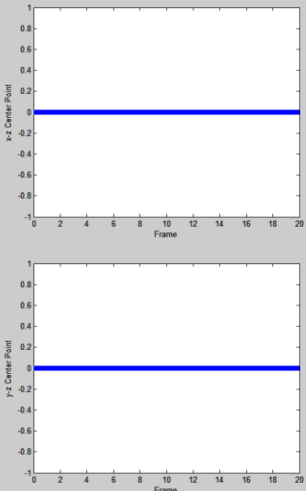
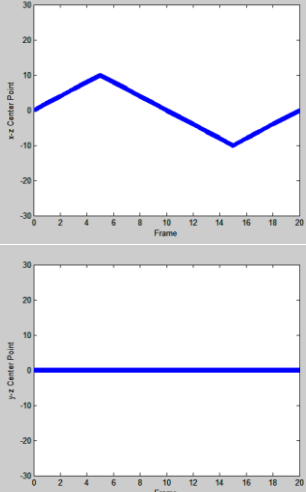
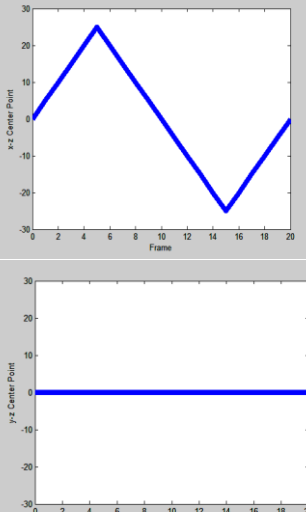


Figure 2-3: A visual schematic outlining the operations in the image processing algorithm. (A) A stack of 100 images are taken as an input. Each image in the stack (B) is segmented into a 64x64 pixel region that is separately thresholded. Processed segments are then combined to recreate the original image, albeit thresholded (C). Connected objects were then counted and each object was separated into a 50x50 pixel region (D), and the displacement of the centroid was measured through the stack of images.

Test Scenario	Description	Plot/Result
1	x-z: No displacement y-z: No displacement No change in area/	
2	x-z: Small displacement (periodic) y-z: No displacement No change in area	
3	x-z: Large displacement (periodic) y-z: No displacement No change in area	

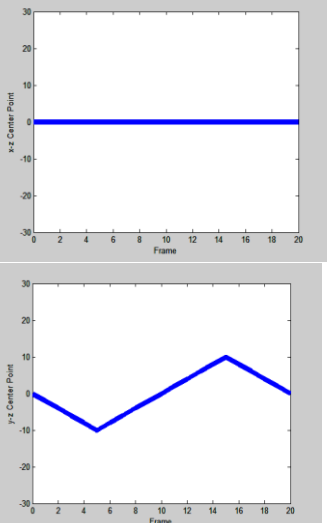
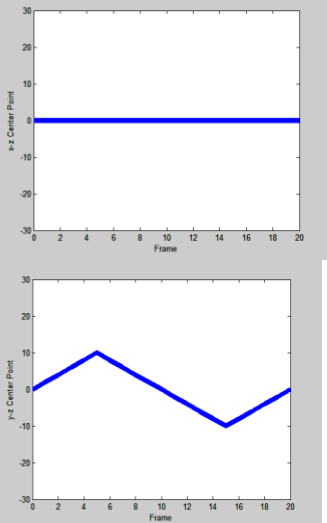
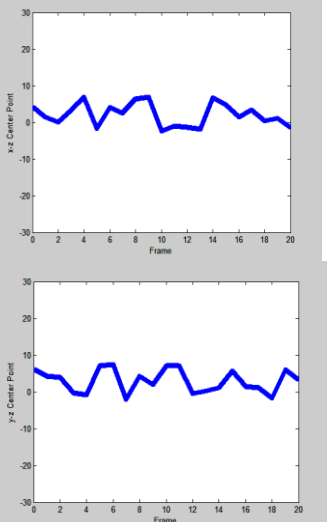
4	<p>x-z: No displacement y-z: Small displacement (periodic) No change in area</p>	
5	<p>x-z: No displacement y-z: Small displacement (periodic) Random change in area</p>	
6	<p>x-z: Small displacement (random) y-z: Small displacement (random) No change in area/shape</p>	

Figure 2-4: The custom-built MATLAB script for tracking was tested for accuracy through the following: a stack of 50 images, each image containing a single circle of constant or varying area was displaced from image to image. The script was executed to track the center point of the circle through the stack of images. Plots of displacement in the x-z and y-z direction were produced and compared to the known displacements in each image. Tracking was accurate, irrespective of changes to shape and area of the circle.

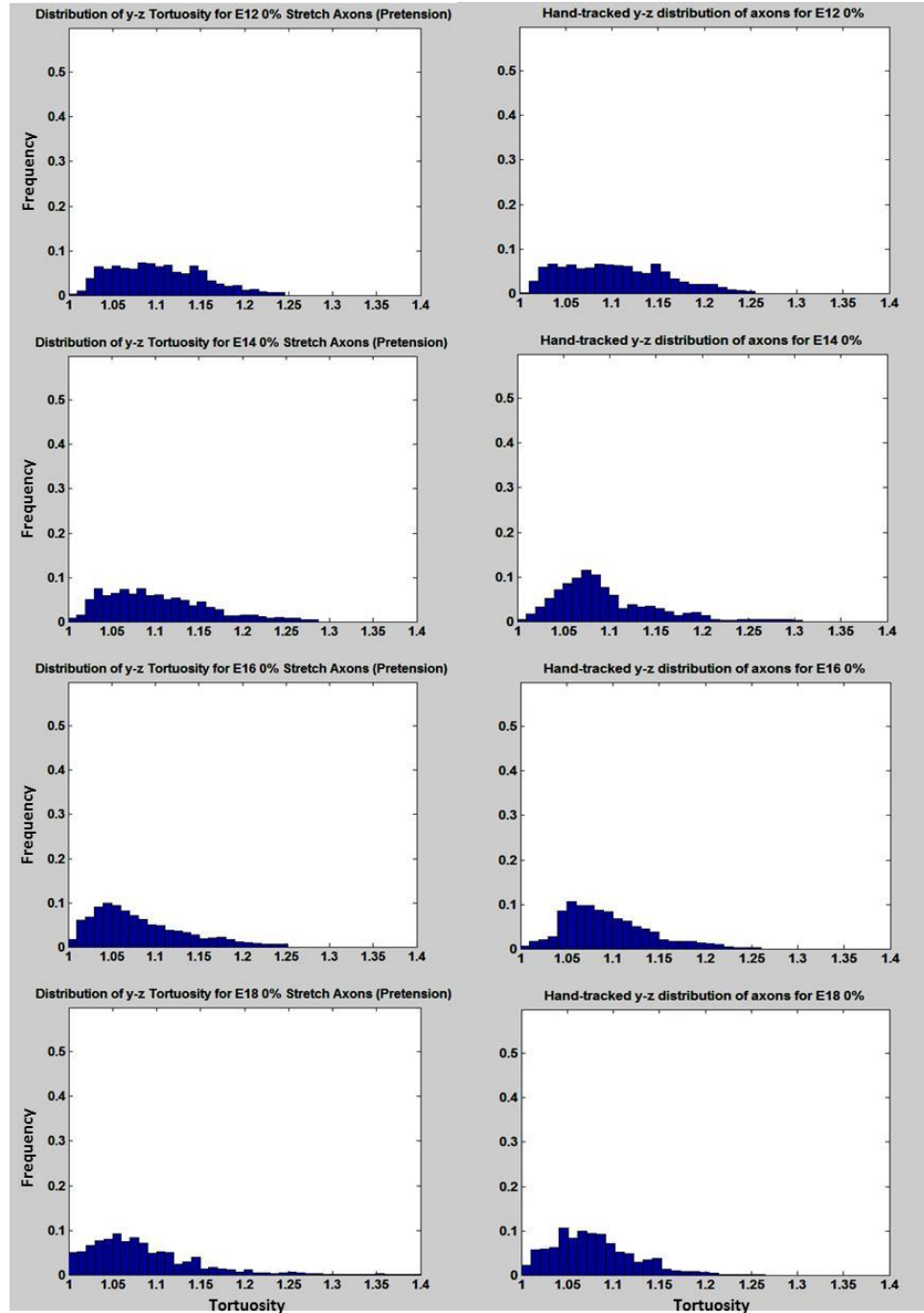


Figure 2-5: To test algorithm accuracy, distributions generated by the algorithm were compared to 2-D hand-traced distributions of tortuosity in unstretched (prestretched to *in situ* length) spinal cords. No statistically significant differences were found when tested using K-W tests ($P_{\min} = 0.09$)

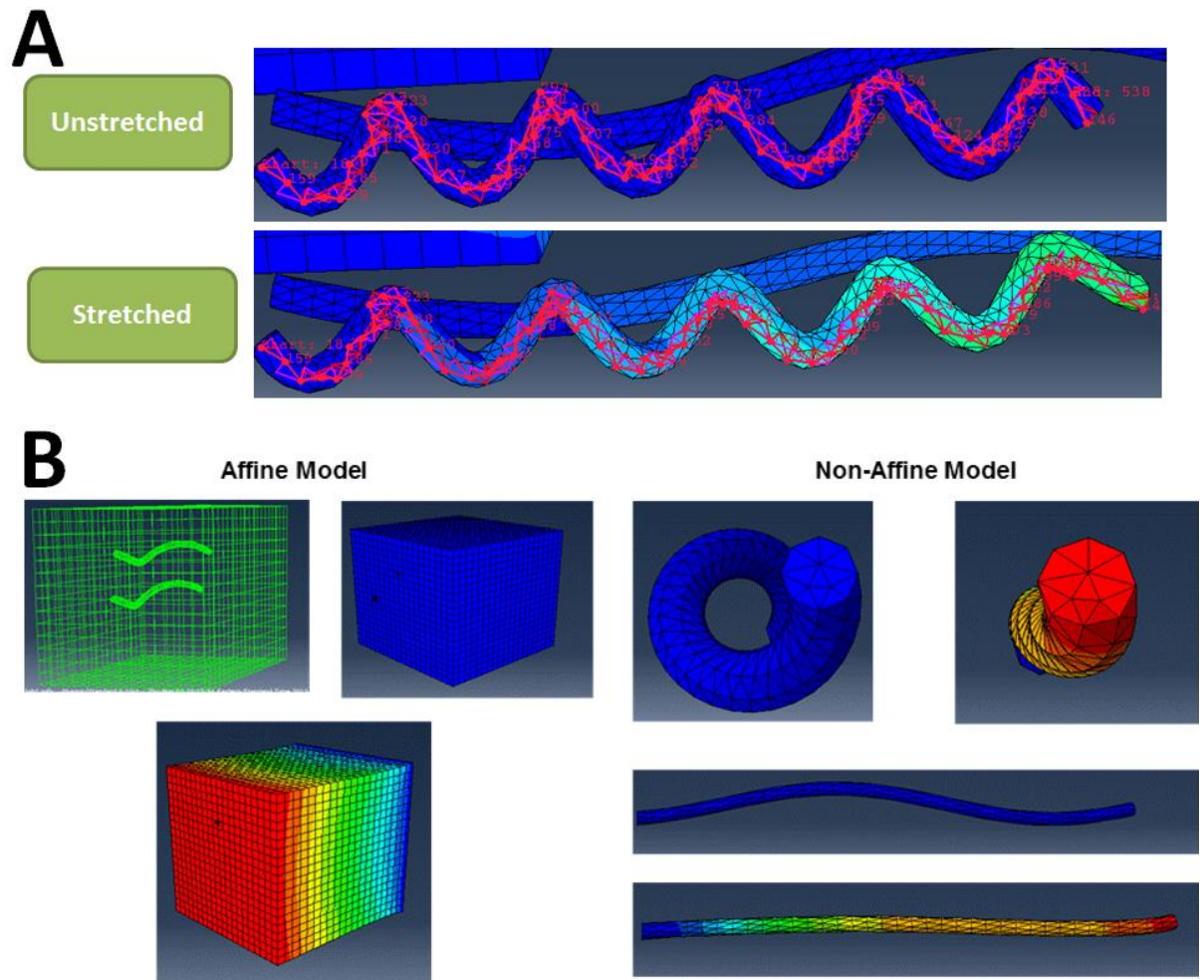


Figure 2-6: Finite element analysis was performed to validate the 3-D kinematic equations we derived. (A) Instances of coiled coils meant to represent axons were simulated using finite element analyses. Node positions were used to calculate pathlengths, and initial and final tortuosities. (B) Purely affine (100% coupled axons) and non-affine (no coupling) behavior was modeled and tortuosities were calculated from simulations before being compared to analytically obtained results from our derived equations (Table 2-3).

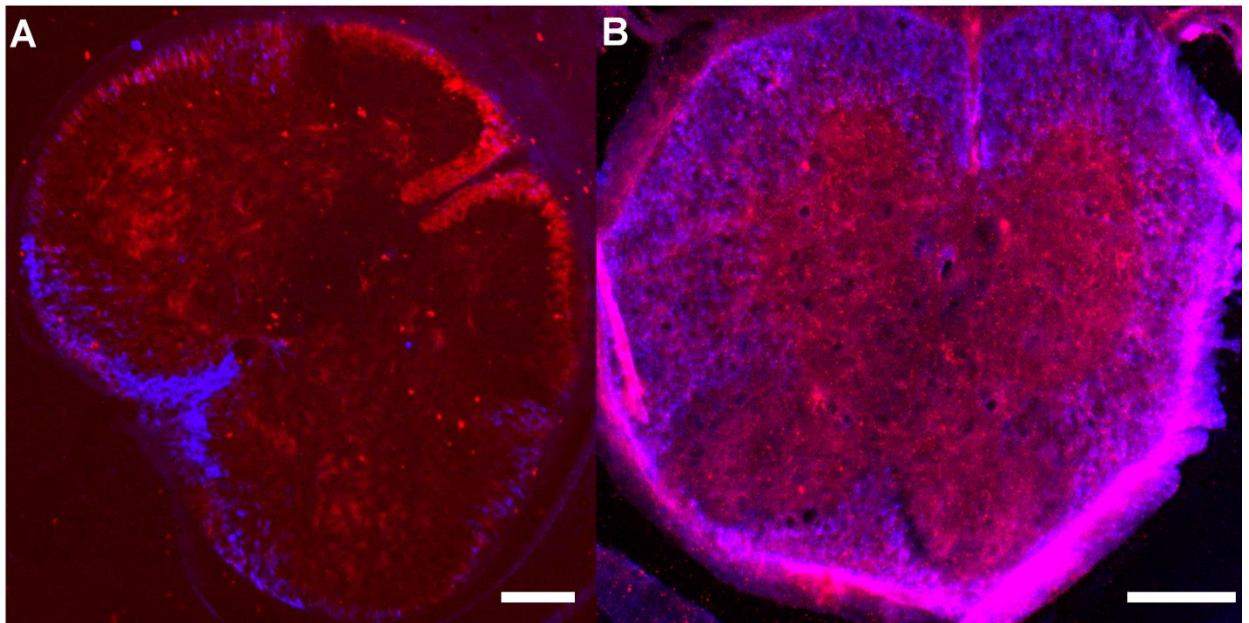


Figure 2-7: Color images of transverse sections of chick embryonic spinal cords to distinguish neurofilament (red) from Myelin Basic Protein (blue) for (A) E12 (Scale Bar = 100 μ m), and (B) E18 (Scale Bar = 200 μ m). Signal from myelin basic protein was seen to progressively increase with development.

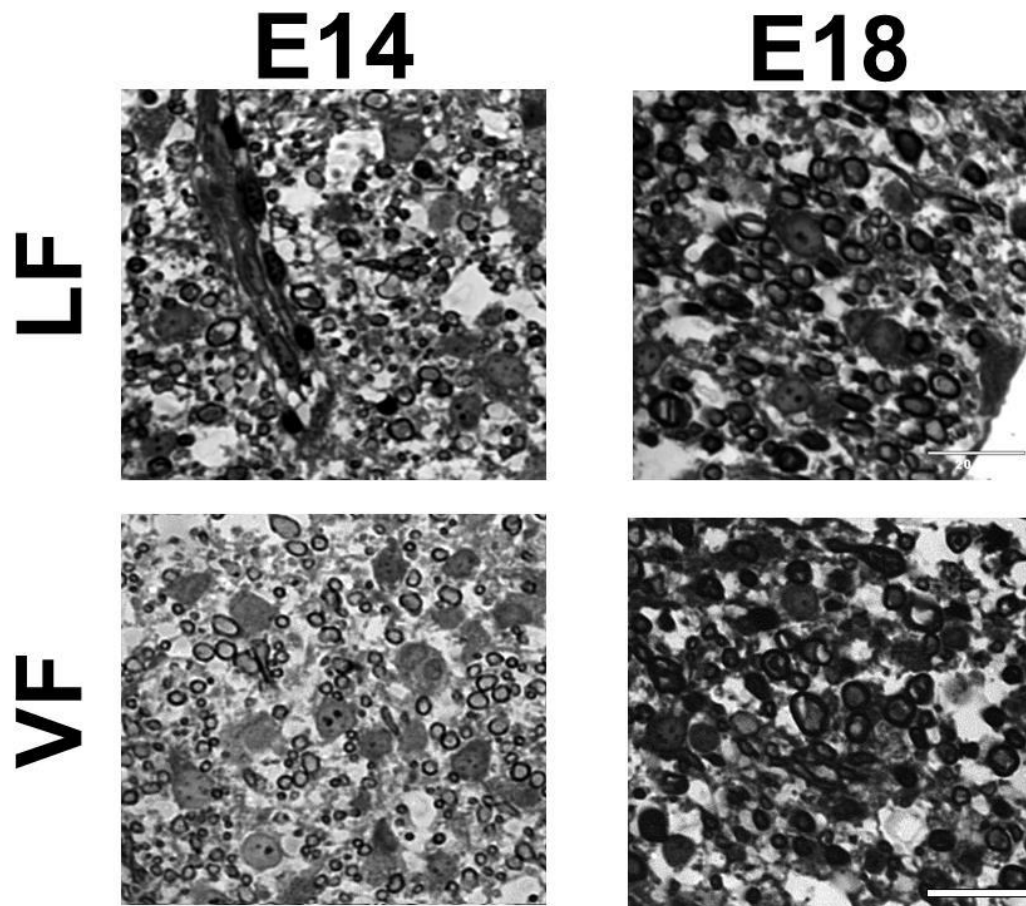


Figure 2-8: Representative images taken at 100x objective of spinal cords stained with Osmium Tetroxide (OsO_4) and counterstained with Toluidine Blue to characterize myelination and axon diameter in the lateral funiculus (LF) and ventral funiculus (VF). More myelination was found in the ventral funiculus at earlier stages, though by E18, there were equal proportions of myelinated axons in both regions. Myelination was characterized as a metric for coupling kinematic behavior. (Scale Bar = $20\mu\text{m}$)

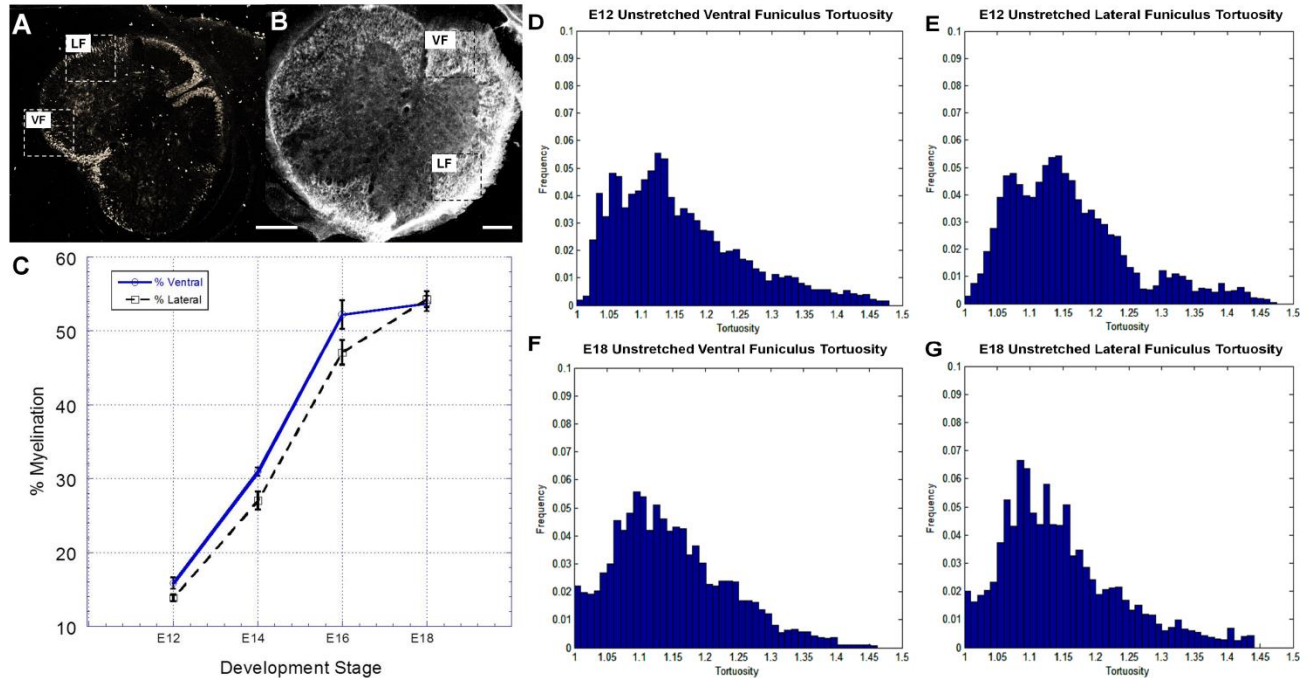


Figure 2-9: (A) Representative image of neurofilament and Myelin Basic Protein immunolabeled (A) E12, and (B) E18 spinal cord transverse section. (Scale Bar = 200 μ m). Axons were characterized in the ventral funiculus (VF) and lateral funiculus (LF). (C) Percentage of myelinated fibers in unstretched spinal cords at each development stage (N = 3 cords). Myelinated axons were counted in osmium tetroxide-stained sections. Error bars = standard error of the mean. (D & E) Histograms for 3-D tortuosity for ventral funiculus (N = 887) and lateral funiculus (N = 775) for E12 unstretched cords, and (F & G) E18 unstretched cords. No statistical significance was seen between ventral and lateral distributions at E12 ($P = 0.087$), E18 ($P = 0.092$), or for any other development stages ($P_{\min} = 0.081$).

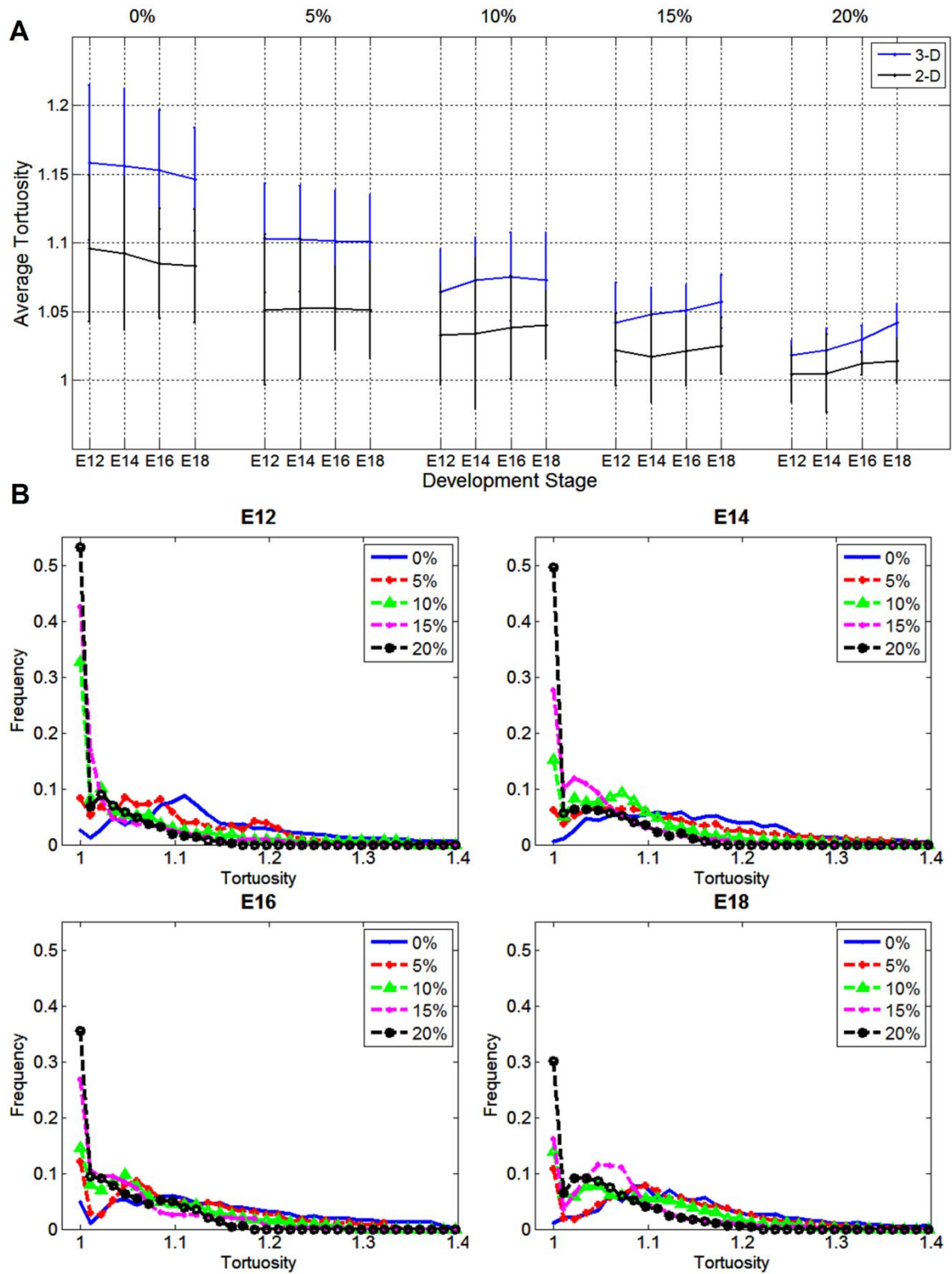


Figure 2-10: (A) Mean 3-D and 2-D tortuosity decreases with stretch level. 2-D tortuosity was extracted from tracings made from longitudinal slices of spinal cord.

Similar trends are observed in the 2-D and 3-D case: 1) Average tortuosity decreases with stretch; 2) In unstretched tissue, tortuosity decreases with development. However, as stretch increases, the trend reverses and tortuosity increases with development. Error bars = standard deviation. (B) Normalized frequency distributions for 3-D tortuosity for each chick embryo development stage. As the spinal cord embryo develops, there is a shift towards affine behavior, demonstrated by the decrease of perfectly straight axons from ~55% at E12, to ~30% at E18

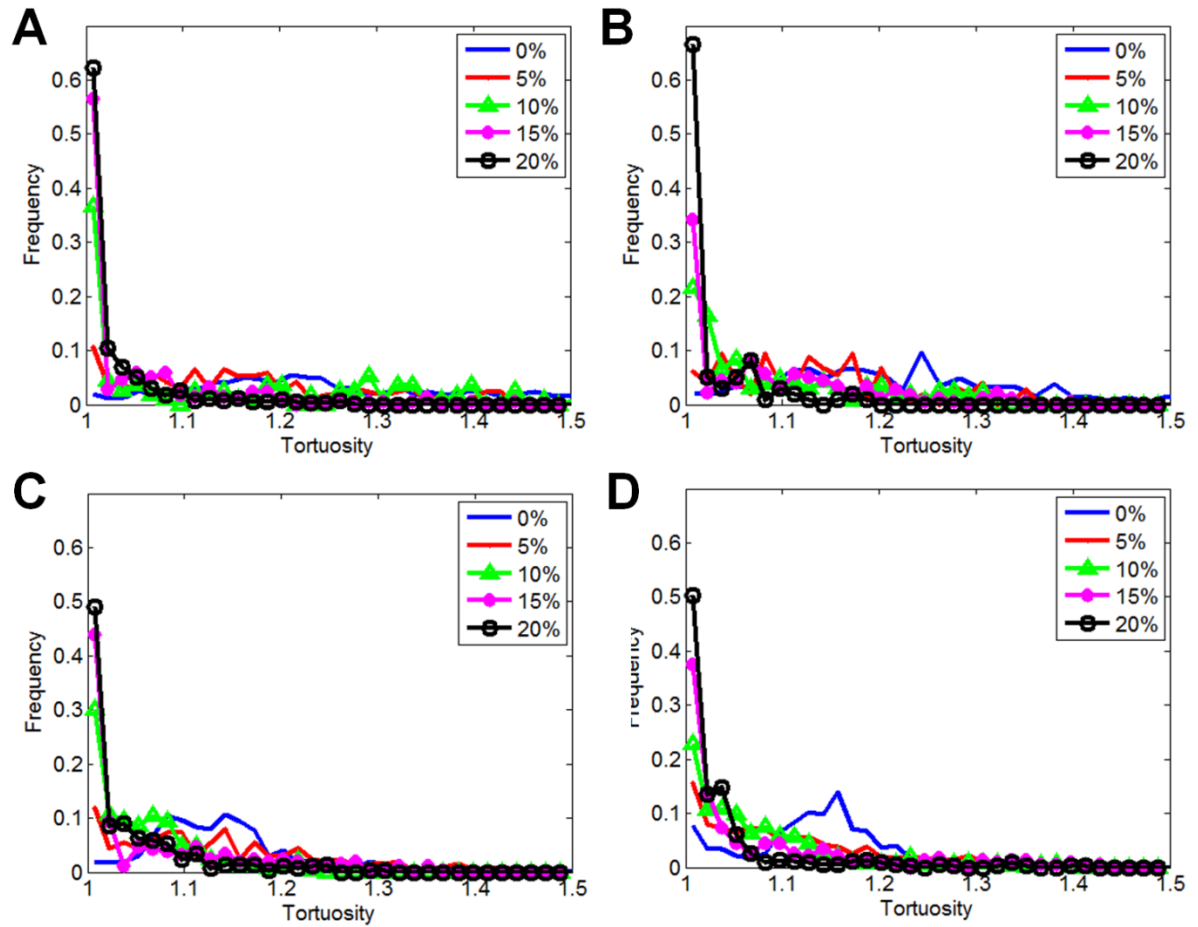


Figure 2-11: Histograms of tortuosity distributions for spinal cords that were not exposed to pre-stretch prior to deformation. When compared to the distributions in Figure 2-9B, distributions shifted significantly ($P_{\max} = 0.04$) to the right.

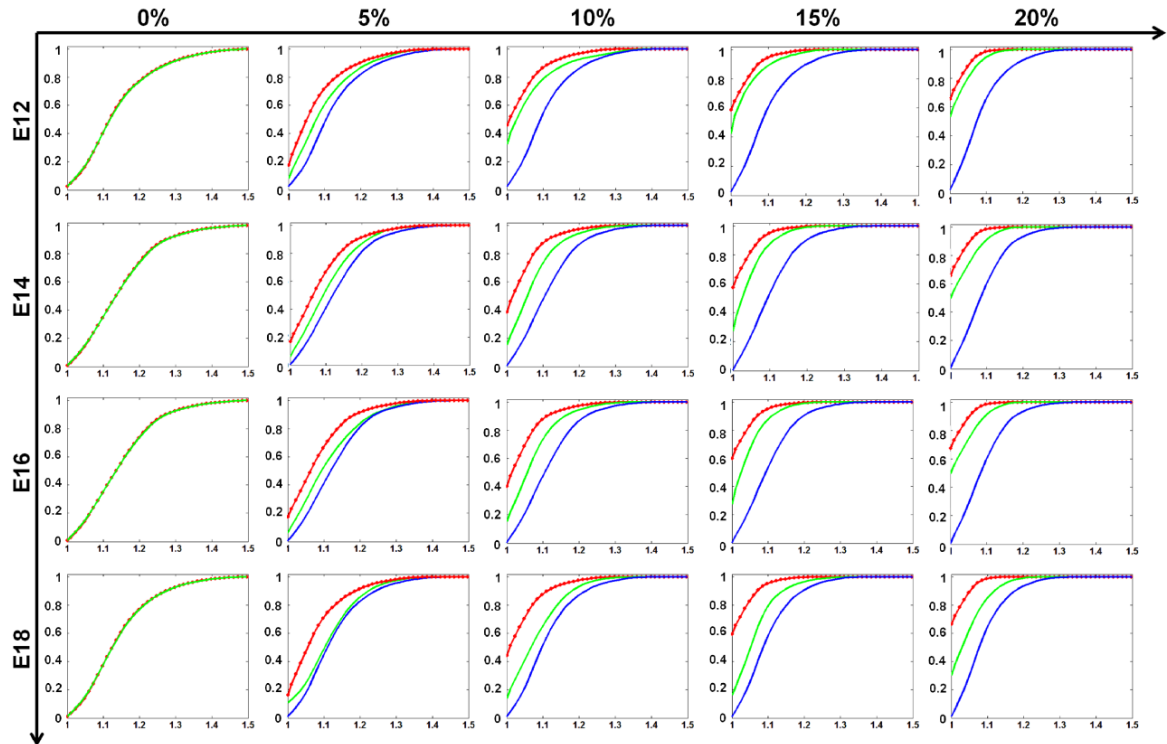


Figure 2-12: Cumulative Frequency Distribution plots of 3-D axon tortuosity for experimentally characterized distribution of axons (green), axons predicted to behave ideally non-affine (red), and axons predicted to behave ideally affine (blue) at different stretch levels and stages of development. There is a trend for the experimental distribution to move closer to the idealized affine curve with age for a given stretch level. In all cases, neither idealized distribution fit the experimental distribution perfectly. Average goodness-of-fit was 0.842.

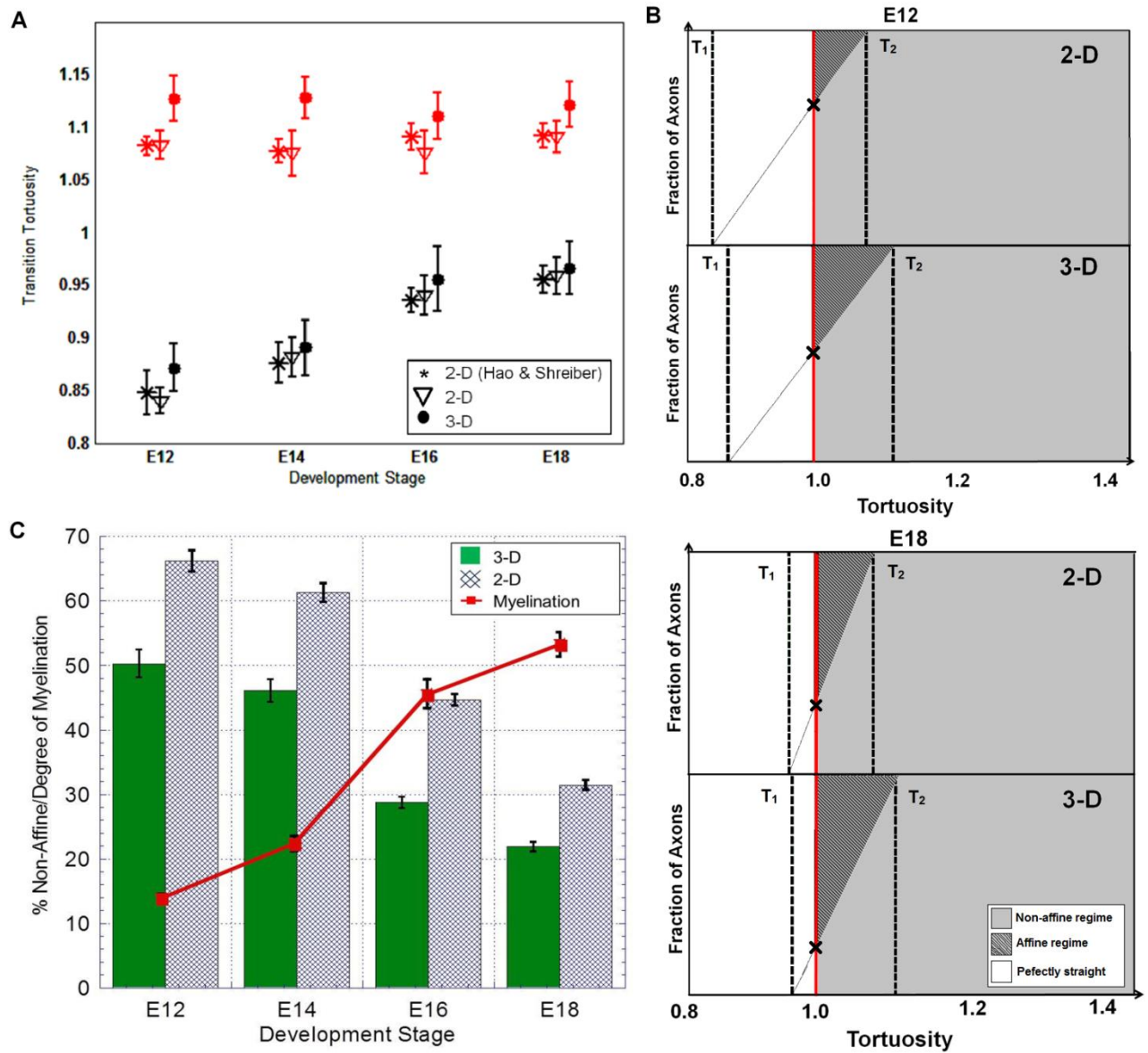


Figure 2-13: Transition tortuosity results and interpretation. (A) Lower (T_1 , black) and upper (T_2 , red) bound transition tortuosity as a function of development stage. T_1 consistently increased with age. T_2 remained roughly constant with development stage in both 2-D and 3-D. However, T_2 values for 3-D distributions were consistently higher than 2-D. (B) Graphical representation of non-affine (grey) and affine regimes (hashed) of 2-D and 3-D axons for E12 and E18. The bold dashed lines correspond to the transition parameters from Figure 4A. The diagonal line corresponds to the cumulative uniform

distribution on the interval $[T_1, T_2]$ of switching tortuosities. The intersection of the uniform distribution and the line $T=1$ (red line) is marked with an X and represents the percentage of axons that are predicted to permanently exhibit non-affine kinematics. The values of T_1 and T_2 dictate this percentage. The increase in T_1 from E12 to E18 shifts the intercept down, which corresponds to an increase in affine behavior. The increase in T_2 from the 2-D characterization to the 3-D characterization also shifts the intercept down and indicates more affine behavior. (C) Predicted percentage of purely non-affine axons as a function of development stage. Myelination also increases with development, with the biggest drop in non-affine axons coinciding with the greatest increase in myelination between E14 and E16 (Error bars = standard error of mean).

DAY	In Situ			Ex Vivo		
	C3-T2	T3-L2	L2-L13	C3-T2	T3-L2	L2-L13
E12 (N=10)	4.29 (1.12)	4.79 (0.99)	5.04 (1.32)	4.07 (0.98)	4.54 (1.05)	4.75 (1.18)
E14 (N=10)	5.12 (1.14)	5.69 (1.22)	4.23 (0.85)	4.82 (1.05)	5.44 (1.31)	4.04 (1.15)
E16 (N=10)	6.88 (2.02)	6.41 (1.75)	6.32 (2.13)	6.53 (1.87)	6.21 (1.55)	5.95 (1.63)
E18 (N=10)	7.84 (2.35)	7.79 (2.78)	7.81 (2.54)	7.48 (2.15)	7.40 (2.45)	7.57 (2.10)

Table 2-1: In situ lengths for spinal cord sections provided in mm. The ex vivo length for each segment of the cord, decreased by 4.77%, on average.

DAY	0%	5%	10%	15%	20%
E12	1.156 ± 0.075	1.106 ± 0.051	1.087 ± 0.029	1.051 ± 0.028	1.018 ± 0.040
E14	1.151 ± 0.086	1.109 ± 0.029	1.084 ± 0.033	1.056 ± 0.027	1.021 ± 0.020
E16	1.149 ± 0.067	1.118 ± 0.052	1.091 ± 0.044	1.077 ± 0.039	1.034 ± 0.029
E18	1.143 ± 0.071	1.113 ± 0.059	1.099 ± 0.060	1.073 ± 0.042	1.038 ± 0.031

Table 2-2: Mean 3-D tortuosity decreases with stretch. Slight decreases in mean tortuosity were measured with increasing development, though these changes were not statistically significant. In all cases, 3-D tortuosity was greater than the respective 2-D tortuosity.

Stretch Level	Initial				Stretched							
					Affine				Non Affine			
	Equation		Model		Equation		Model		Equation		Model	
	Mean	SD	Mean	SD	Mean	SD	Mean	SD	Mean	SD	Mean	SD
10%	1.148	0.074	1.148	0.074	1.108	0.042	1.109	0.048	1.044	0.039	1.046	0.038
15%	1.148	0.074	1.148	0.074	1.097	0.037	1.100	0.035	1.000	0.012	1.000	0.011
20%	1.148	0.074	1.148	0.074	1.086	0.025	1.085	0.036	1.000	0.006	1.000	0.009

Table 2-3: Results from FEM for axons (N=7) modeled with varying initial tortuosities.

Axons were either completely tied (Affine) to surrounding matrix or untied (Non-affine).

Equation and model values agreed within 0.6%, or 3.4% with regards to engineering strain.

Chapter 3: Estimating axonal strain as a function of tissue-level stretch using contactin-associated protein as a fiducial marker

Abstract:

Axonal injury is a proximal cause of functional deficits following primary central nervous system injury. During the injury event, tissue-scale loads are transferred to individual axons, leading to varying degrees of functional and physical damage including physical failure. Computational models have been developed to understand this transfer and better predict the circumstances that cause injury. However, the value of these studies is often limited by a lack of validating experimental work examining the mechanics of axons in their natural, in situ state. In the previous chapter of this thesis, we modeled 3-D axon kinematics to infer the multi-scale transfer to axons. To further corroborate these findings, we use contactin-associated protein (Caspr) as a fiduciary marker of axonal stretch. Caspr is expressed on axons at nodes of Ranvier and is important in the formation and maintenance of myelin. We measured changes in the distance between immunolabeled Caspr pairs along axons as a function of tissue-level stretch in chick embryo spinal cords harvested from different developmental periods. We then identified and characterized broken axons and adapted a kinematic model published previously by our group (Singh et al., 2015) to estimate average strain thresholds for axon mechanical failure. The distance between Caspr pairs, which defined the internodal length, increased with stretch, though not as much as predicted by simple continuum mechanics. For the same level of tissue stretch, greater numbers of broken axons were found at later stages of development. In adapting our kinematic model to predict a breaking threshold strain, we found that

breaking thresholds decrease with development stage, corresponding with the elevated numbers of broken axons we found. When thresholds were split and classified based on kinematic behavior, non-affine, uncoupled axons had much greater thresholds than affine, coupled axons, corroborating thresholds predicted in similar *in vitro* and *in vivo* preparations. The data provided herein along with the breaking parameters we glean provide useful information for generating more accurate multi-scale models in primary central nervous system injury.

Background & Significance:

Primary axonal injury in white matter is the leading cause of functional deficits following trauma in brain and spinal cord injuries (Smith and Meaney, 2000). During a traumatic event, tissue-scale loads are transferred to the constituent cells and cellular processes at the microscale of the central nervous system (CNS) tissue. Tissue level deformation can be measured directly in vitro with imaging techniques, and can be quantitatively estimated with computational models, but a comprehensive understanding of the transfer of these strains to the cells in situ has been challenging. It is understood that the white matter microstructure in CNS tissue influences this transfer, and indeed inferences can be made by probing the individual microstructural elements (Arbogast and Margulies, 1999; Prange and Margulies, 2002).

Unlike most soft tissues, where extracellular matrix proteins provide mechanical integrity, the constitutive elements that define the structure of the microscale in CNS white matter are primarily axons and oligodendrocytes (Prange and Margulies, 2002). Characteristics such as axon diameter (Chomiak and Hu, 2009; Nilsson et al., 2012), orientation (Cloots et al., 2011; Rutgers et al., 2008), tortuosity (Hao and Shreiber, 2007), and kinematics vary microscopically, but affect macroscopic behavior. Oligodendrocytes myelinate axons resulting in the interconnections of these two structural elements at nodes of Ranvier through adhesion complexes (Hao and Shreiber, 2007). At paranodal junctions, the axonal cytoskeleton is anchored to the oligodendrocyte through interactions of contactin and contactin-associated protein (on the axon side) with neurofascin 155 (on the oligodendrocyte side) in what has been described as the largest adhesion complex in vertebrate biology (Sherman and Brophy, 2005).

In previous work, axon kinematic behavior following tissue-level deformation of white matter was characterized, first in the adult, guinea pig optic nerve (Bain et al., 2000), and subsequently in the developing chick embryo spinal cord (Hao and Shreiber, 2007; Singh et al., 2015) during a period of rapid myelination from embryonic day (E) 12 to 18. Collectively, these studies demonstrated that axon-to-axon coupling is strongly correlated to the degree of myelination. In E12 chick embryos, before myelination, axons predominantly demonstrated non-affine, uncoupled behavior. With myelination, axons demonstrated increasingly affine, coupled behavior. When myelination was inhibited *in ovo*, the tensile stiffness of the E18 chick embryo spinal cord significantly decreased to levels comparable to tissue harvested early in the myelination process. Together, these results indicate that cellular coupling of axons by oligodendrocytes affects the kinematic behavior of axons as well as the tissue-level mechanical properties. This in turn would influence the strain transfer which occurs from the macroscopic to individual axons. Finite element models of the brain and spinal cord have been used extensively in predicting microstructural strains due to bulk tissue deformation. Cloots et al. (2010) employed computational simulations to determine the relation between tissue-scale and cellular-scale mechanical states, finding that axonal strains are higher than the applied tissue strain (Cloots et al., 2013a). Pan et al. (2011) included kinematic properties in their model, improving fidelity to experimentally observed changes in microkinematics with macroscopic stretch. Zhu et al. generated a finite element simulation to examine how strain distributions along the axon varied with changes in myelin composition (Zhu et al., 2015). Model predictions of strain have been validated using *in vitro* cultures of axons (Tang-Schomer et al., 2010). However, these preparations differ significantly from what

is observed *in vivo* or even *in situ*, using isolated axon cultures, or partial co-culture systems.

In this study, we present a novel approach to experimentally determining axonal strains *in situ* by utilizing the regular incidence of Caspr at the axon paranode to measure changes in axon segment length following macroscopic stretch. We then use these measurements to estimate average strain as a function of tissue-level loading. Additionally, we determine the proportion of irrevocably damaged axons at a given developmental stage and stretch level. Finally, we use this data to make predictions of *in situ* strain thresholds for axonal injury in an adaptation of our phenomenological model from a previous study (Singh et al. 2015).

Methods:

Chick embryo spinal cord isolation: Spinal cord tissue was prepared in a manner similar to our previous study (Singh et al. 2015). Briefly, chick embryonic spinal cords at different stages of development were carefully measured in situ, excised, pre-stretched to their in situ length, quasistatically stretched to a defined level, and fixed in their deformed state. Pieces of reflective plastic (glitter) were carefully placed on the unstretched spinal cord tissue, and their displacements measured following deformation to ensure stretch was uniformly applied. Following overnight fixation, cords were transferred to a 20% sucrose-saline cryoprotectant solution.

Immunohistochemistry: Spinal cords were removed from cryoprotectant solution and divided into cervical, thoracic, and lumbar regions with a razor blade. Regions were embedded in O.C.T. compound (Electron Microscopy Services). Frozen longitudinal sections of 20 μ m or 40 μ m thickness were cut on a cryostat (Thermo Electron) and placed on pre-treated glass slides (Fisher).

Sections were washed four times in immunobuffer (1% bovine serum albumin, and 0.5% Triton X-100 in phosphate buffered saline) (Sigma-Aldrich St. Louis, MO), then incubated in 10% goat serum blocking buffer for 1h. Sections were incubated overnight at 4°C with a primary antibody mixture of 1:500 mouse monoclonal α -neurofilament 166kD (Sigma-Aldrich), and a 1:1000 dilution of rabbit polyclonal α -caspr (Abcam). Sections were rinsed again with immunobuffer six times for 10 minutes each and then incubated in a 1:250 dilution of Alexa 647 goat-anti-mouse secondary antibody and a 1:1000 dilution of Alexa 488 goat-anti-rabbit secondary antibody for 1h at room temperature. Finally, sections were washed with immunobuffer six times for 10 minutes

each and allowed to air-dry in the dark. Slides were then coverslipped with mounting solution (Vector Labs Burlingame, CA).

Imaging: Confocal images of immunostained spinal cord sections were captured with an Olympus IX81 inverted epifluorescent microscope equipped with a spinning disk confocal unit and a Hamamatsu ImagEM digital camera (Middlesex, NJ). Images were taken with an 100x objective with filters at 488nm, 568nm, and 647nm to visualize the different secondary antibody labels. Images of optical sections at increments of 0.2 μ m were captured through the thickness of the slices. Montages were taken across the length of the longitudinal section to determine lengths across multiple internodal segments.

Measurements: End-to-end lengths were measured for internodal and paranodal segments. Pathlengths were measured for internodal segments. The internodal region was defined as the axon segment between two Caspr pairs while the paranodal region was defined as the segment between individual Caspr proteins in a single pair.

Two criteria were used to maintain consistency and minimize ambiguity in measurements: 1) neurofilament staining was consistent through the slice, ensuring the trajectory of the axon was within the thickness of the section, and 2) at least 3 Caspr pairs were present along the same axon. The 3-D trajectory of an axon was traced using ImageJ. Starting at a Caspr pair, the nearest region of high neurofilament intensity in adjacent images in the stack was selected and its path measured until the next Caspr pair was found ([Figure 3-1](#)). Lengths were compiled and averaged. Average lengths for stretched tissue were compared to the average length of unstretched tissue to determine the average percentage change in length as a function of macroscopic stretch.

In 20 μ m sections, axons frequently traversed outside of the thickness of an individual slice. In 40 μ m sections, the majority of axons could be followed continuously from one end of the slice to the other. In these sections, for axons where a discontinuity was observed through the thickness of the slice, the axon was recorded as broken. Length measurements were continued at the beginning of the next nearest pair of nodal proteins on a similarly “broken” axon. The proportion of broken axons was computed for each stage of development and stretch level and further split into non-affine and affine axons based on their measured tortuosity (Singh et al., 2015). Axon segments that had all slack removed and appeared perfectly straight with a tortuosity < 1.002 were classified as non-affine. . The remaining, wavy, broken segments were classified as affine.

Mathematical Model: An axon kinematic model from our previous study (Singh et al., 2015) was adapted to predict strain thresholds. The model used a Levenberg-Marquardt multi-parameter, nonlinear regression scheme to predict transition parameters for axon kinematic behavior at each developmental stage (Singh et al., 2015). Modifications were made to use similar principles to predict strain thresholds. For this study, unstretched tortuosity, end-to-end internodal length, and internodal pathlength data were extracted and used as input data at each development stage. New tortuosities were then calculated for each axon at different stretch levels. Internodal end-to-end and pathlength were calculated at different stretch levels. The equations used to calculate an axon’s new length was dependent on predicted kinematic behavior and are described below:

Kinematic Model: Full derivations for our axon kinematic model with regards to how tortuosity is calculated can be found in Singh et al. 2015.

Non-affine model: In non-affine kinematics, we postulate that stretch is initially applied to straighten the tortuous axon. Thus, the end-to-end length increases with stretch normally, but the pathlength remains constant until the axon is fully straight:

$$L_{E-E} = \lambda l_{E-E} \quad (\text{Eq 3-1})$$

$$\begin{cases} L_{PL} = l_{PL}, & T_0 > \lambda \\ L_{PL} = (\lambda - T_0)l_{PL}, & T_0 \leq \lambda \end{cases} \quad (\text{Eq 3-2})$$

Affine Model: In affine behavior, axons are assumed to be interconnected with each other via the glial matrix, such that individual axons experience the same geometric transformations as the macroscopic tissue. Due to the continuum-like nature, pathlength increases even when the axon is tortuous. The change in end-to-end length varies along the undulated axon and integrating along the length gives us the following equations for internodal lengths:

$$L_{E-E} = [2\sqrt{\lambda} - 1]l_{E-E} \quad (\text{Eq 3-3})$$

$$L_{PL} = \lambda l_{PL} \quad (\text{Eq 3-4})$$

Switching Model: In a similar fashion, the equations used to calculate the new internodal length with stretch vary with kinematics. When the axon's current tortuosity is greater than the switching tortuosity, T , the non-affine equations (Eq 3-1) & (Eq 3-2) are used to calculate the new length. Otherwise, equations (Eq 3-3) & (Eq 3-4) are used.

To predict the number of broken axons, each unstretched axon was individually assigned a strain threshold from a probability distribution. Strain was defined as the percentage change in pathlength of the axon. When the strain in the axon exceeded its strain threshold, the axon was recorded as broken. Three different probability distributions were

tested: normal, uniform, and gamma. A single value “constant” threshold was also tested. Parameters for each distribution were determined using the Levenberg-Marquardt multi-parameter, nonlinear regression scheme, which attempted to fit the predicted proportion of broken axons to the experimentally-derived proportion of broken axons. The model was executed 100 times for each development stage, from which the mean values and standard deviations for the distribution parameters and regression coefficients for each fit were determined. Separate simulations were executed where two thresholds were identified – one for affine axons and one for non-affine axons.

Results:

Spinal cord tissue and axon morphology: Average spinal cord length increased from $11.7 \pm 2.1\text{mm}$ at E12 to $23.8 \pm 3.4\text{mm}$ at E18. Mean 3-D tortuosity for unstretched spinal cords was observed to decrease slightly with development stage, decreasing from 1.161 ± 0.093 to 1.141 ± 0.075 between E12 to E18. These data and statistics were similar to our findings in Singh et al. (2015) for spinal cord length and axon tortuosity (Singh et al., 2015).

Average internodal and paranodal lengths: Average internodal end-to-end length increased from $85.8 \pm 9.4\mu\text{m}$ at E12 to $136.1 \pm 8.7\mu\text{m}$ for E18 spinal cords (59% increase) (Figure 3-2). Internodal pathlength increased significantly as well from $99.2 \pm 8.3\mu\text{m}$ to $150.8 \pm 10.2\mu\text{m}$, increasing 52% with development. For both cases, the increases in internodal length were significantly smaller than the increase in tissue length with development (~103% increase from E12 to E18). Average paranodal length increased less dramatically than internodal length from $1.8 \pm 0.6\mu\text{m}$ at E12 to $3.3 \pm 1.1\mu\text{m}$ at E18.

Similar trends were observed for stretched spinal cords. Average end-to-end internodal and paranodal lengths increased with stretch for each developmental stage (Figures 3-3A and 3-3B respectively). Earlier development stages demonstrated a sharper increase compared to later stages. The percentage change in E12 and E14 internodal lengths were similar to the increase in tissue length due to macroscopic stretch (Figure 3-3A). At later stages of development (E16 and E18), we observed a deviation from this trend.

Application of 20% macroscopic stretch resulted in an average end-to-end internodal length change of ~13% and ~8% for E16 and E18 spinal cords, respectively. Statistical

significance was found across all stretch levels in both internodal and paranodal length changes using Kolmogorov-Smirnov tests ($P_{\max} < 0.01$).

In calculating the average change for internodal pathlength ([Figure 3-3C](#)), we observed that earlier stages of development showed little to no change in average pathlength with stretch until 15-20% macroscopic stretch. Later stages of development showed gradual increases in mean internodal pathlength with macroscopic stretch but changes were still significantly smaller than the changes observed for end-to-end length. No statistical significance was found in relative changes in pathlength.

Characterization of broken axons: The unusual deviation in trends we observed regarding changes in end-to-end length in E16 and E18 samples provided impetus to better understand the root cause in this change in relationship between microscopic and macroscopic stretch. Internodal end-to-end lengths and tortuosity distributions were examined for E16 and E18 samples for any indications as to why trends diverge. Histograms for internodal end-to-end and pathlengths demonstrated increasing shifts to the right with macroscopic stretch. Figure 3-4 shows a representative histogram for E12 and E18 samples ([Figure 3-4](#)). Interestingly, the number of observations for the bins corresponding to lower lengths in E16 and E18 histograms increased with greater macroscopic stretch. From this, it was surmised that broken axons were being included in tracings which provided impetus to examine thicker slices.

Increasing our tissue slice thickness from 20 to 40 μ m allowed tracing and characterization of broken axons. Percentages of broken axons for each stretch level and development stage were calculated. To increase confidence in determining whether an axon was broken, we started 10 μ m into the thickness of the tissue slice in our confocal

images. Using that plane as a starting point, we continued to look into the depth of the tissue and recorded voids in neurofilament intensity as breaks, as the likelihood of the axon's trajectory leaving the thickness of the tissue was minimal at our starting depth (Figure 3-5A). Consolidating all traced axons from all developmental stages and stretch levels, we observed the majority of breaks occurred at the internode region (96.1%).

The proportion of broken axons increased with stretch and development stage (Figure 3-8). More axons broke with increasing macroscopic stretch for a given development stage. About 11% of axons were broken when E12 spinal cords were stretched to 20% macroscopic stretch, which increased to 22.5% broken at E18 with the same macroscopic stretch. Axons were observed to break throughout the spinal cord. In general, no distinguishing patterns of breakages seemed to occur in the cervical, thoracic, or lumbar regions which supported observations made in a similar study (Tang-Schomer et al., 2012). The exception to this was in the case of E12 and E18 developmental stages, where we noticed at 10% stretch there were greater numbers of break observed at the cervical and lumbar regions, which leveled out at the highest degree of macroscopic stretch.

In E12 and E14 spinal cords, the majority of axons were perfectly straight prior to breaking, with tortuosities equal to or close to 1. We observed more tortuous broken axons at later development stages. Interestingly, the internodal length range for broken axons was smaller for axons at later versus earlier development stages. The highest internodal segment length for a broken axon was observed in E18 spinal cords ($L_{e-e} = 230.4\mu\text{m}$) in comparison to E12 spinal cords ($L_{e-e} = 141.4\mu\text{m}$). Both these instances occurred in 20% stretched spinal cords, and in cases where the axon was close to

perfectly straight. While fewer broken axons were observed at earlier development stages, the axons that did break were closer to the mean internodal end-to-end lengths. Following our analysis of the thicker spinal cord slices, we omitted broken axons and proceeded to replot changes in end-to-end internodal length as a function of macroscopic stretch. Figure 3-5B shows a similar plot to Figure 3-3A where the percentage change in internodal end-to-end lengths were plotted when broken axons from 40 μ m thick slices were included or excluded from the calculation. While the results for E12 and E14 did not change significantly given that the small percentage of axons which broke at earlier stage cases were relatively close to the mean internodal end-to-end length, trends for E16 and E18 improved somewhat, shifting closer to the 1:1 line that corresponds to equivalent macroscopic-microscopic transfer.

Estimating in situ axon failure thresholds: The possession of quantitative data for proportions of broken axons allowed us to adapt kinematic models from our previous study to predict distribution parameters for injury thresholds. Each unstretched axon was assigned a strain threshold selected from a normal distribution, and the new end-to-end and pathlength was calculated for given macroscopic stretch. The proportion of broken axons predicted by the model was fit to the proportion of broken axons measured from stretch experiments, and the probability distribution parameters were adjusted accordingly until convergence was achieved. In general, the mean breaking threshold decreased with development stage from 1.24 at E12 to 1.17 at E18, suggesting axons are more susceptible to damage with increasing development. Standard deviation also decreased slightly from 0.12 to 0.08 (Table 3-1).

Comparisons between single thresholds and separate thresholds for non-affine and affine kinematic axons were made. The larger proportion of broken axons at later stages of development suggested that axons exhibiting affine behavior have a greater likelihood of breaking, and therefore a lower macroscopic stretch threshold than the single threshold. A broken axon was classified as non-affine if the tortuosity was 1 (perfectly straight), and affine if tortuosity was greater than 1. At all developmental stages, low levels of stretch resulted in primarily affine axons breaking (Figure 3-9). The proportion of broken non-affine axons increased with higher levels of stretch. Predicted thresholds for non-affine and affine axons differed from the single threshold. In all cases, non-affine thresholds were greater than the single threshold, and affine thresholds were less than the single threshold (Table 3-2). While the non-affine thresholds remained relatively constant with development ($P_{\min} = 0.14$), we observed affine thresholds slightly decreased from 1.19 to 1.14 in E12 and E18 specimens respectively.

Discussion:

The goals of this study were to evaluate the efficacy of using Caspr as a fiducial marker for measuring axonal strain as a function of tissue stretch, and use these measurements to estimate axonal failure strain thresholds. By measuring how distances between Caspr expressed at the nodes of Ranvier changed with macroscopic stretch relative to unstretched tissue, we were able to quantitatively estimate the average strain individual axons experience: an elusive measure to obtain for axons in their natural state. In our measurements, we also recorded the number of broken axons and predicted the propensity for injury by adapting our kinematic models to calculate the proportion of broken axons based on predicted injury thresholds. These thresholds were determined by fitting the proportion of broken axons calculated by the model to the proportion experimentally measured at each stretch level.

Expression of Caspr at the nodes of Ranvier occurs early in neural development, and primarily in CNS tissue (Einheber et al., 1997). Evidence has also been provided that Caspr expression is necessary for normal degrees of myelination (Anderson et al., 2000). The motivation to use Caspr came from our attempts to distinguish the role of myelin and axo-glial adhesions as the primary cause of coupling behavior predicted to occur in axon kinematics (Hao and Shreiber, 2007; Singh et al., 2015). When we observed changes in Caspr distances in stretched samples, our objective shifted to investigating the use of Caspr as a fiduciary marker for measuring axonal strains.

Previous work suggests the transfer of macroscopic stretch to microscopic strain is not a straightforward one-to-one translation (Bain and Meaney, 2000; Karami et al., 2009; Smith and Meaney, 2000). This was verified by comparisons of internodal length changes

to macroscopic stretch. The greatest deviation in this trend occurred at later stages of development, during which spinal cord axons experience significant changes in their morphology and kinematic behavior (Hamburger and Hamilton, 1951; Keirstead et al., 1997; Singh et al., 2015). In general, features of the microstructure dictate the macro-to-microscopic transfer, and probing these characteristics can provide insight into the multi-scale behavior of axons exposed to controlled tissue-level stretch.

In the previous chapter, we inferred the macro-to-micro transfer by characterizing 3-D axon kinematic behavior. Axons were modeled to exhibit one of three types of behavior: non-affine, affine, or switching (Hao and Shreiber, 2007; Singh et al., 2015). Non-affine axons are predicted to be uncoupled to surrounding axons, and it is believed that macroscopic stretch is initially applied in straightening tortuous axons. Analogous to a string being unraveled, while the direct end-to-end distance increases, the pathlength remains constant, as under non-affine modes, the string would not experience true strain until it has completely straightened. In contrast, affine axons increase in both end-to-end length and pathlength as they experience the same geometric transformation as the tissue, experiencing strain even at low levels stretch. In this model, axons initially behave non-affinely until they reach a unique transition tortuosity based on the level of physical connectivity to glia, after which they switch to affine behavior. Our observations concerning the change in internodal end-to-end and pathlength with macroscopic stretch seem to support this kinematic model. At earlier stages of development, pathlength was seen to increase much less dramatically at lower levels of stretch, while end-to-end length increased normally. Based on our fitted kinematic parameters for switching, approximately 50% of axons were predicted to behave with purely non-affine kinematics.

Furthermore, at lower macroscopic stretch, a very small proportion of axons would achieve their respective switching tortuosities that would cause them to exhibit affine behavior with stretch.

There was strong agreement between tissue-level stretch and the change in end-to-end internodal length at earlier stages of development (E12 and E14, average $R^2 = 0.971$). This trend shifted with increasing development where we observed spinal cord tissue roughly doubling in length from E12 to E18, while the average internodal end-to-end length only increased by 60%. For all development stages, tissue growth did not equate to end-to-end length increases, with tissue growth consistently being larger than the change in average internodal lengths ([Figure 3-6](#)). Interestingly we observed a linear relationship between tissue growth and increases in internodal length from E14 to E18. This suggests that effects of growth-induced stretch on axons are easier to predict at later stages, while the effects of artificially-induced stretch on axons are easier to predict at earlier stages. To elucidate reasons for these patterns, we examined distributions of internodal and paranodal lengths for different developmental stages and stretch levels. Histograms of end-to-end lengths at later stages of development ([Figure 3-4](#)) showed uncharacteristically high frequencies of internodal lengths at lower bins for stretched samples, and did not shift as much to the right as expected. We hypothesized three reasons for this: 1) new axons or new Caspr pairs were being expressed on existing axonal segments, which would decrease mean segment length; 2) broken axons were being captured in our analysis, which would decrease the mean length or; 3) non-uniform kinematic behavior along single axons that would vary trends.

First we re-examined internodal length distributions to determine the likelihood of new axons or newly expressed Caspr pairs artificially affecting length distributions. Nascent axons continue to form throughout the stages of development we studied, as evidenced by the continuous expression of neurofilament (Sherman and Brophy, 2005). Similar studies on the developing morphology have shown Caspr is expressed as early as E10 in the chick embryo (El-Eishi, 1967). Increased numbers of oligodendrocytes are also observed (Dobbing et al., 1957), correlating to the increased Caspr signal we observed in developed specimens. Based on these findings, it is likely a combination of both these factors that contribute to the decreasing changes in average internodal length. In comparing changes in length distributions against analytically calculated distributions ([Figure 3-7](#)), we inferred that regions of overlap between the analytically calculated distribution and empirical distribution to belong to the original population of segments which increased in length due to tissue growth. This implies the remaining area corresponding to the proportion of newly formed segments (axons), or new segments due to new pairs.

Possessing quantitative data on broken axons caused by macroscopic stretch enabled us to apply similar principles from our previous study to predict axonal failure thresholds in *ex vivo* preparations (Singh et al., 2015). Each axon was assigned a strain threshold from a probability distribution, and parameters were determined by fitting model and experimental proportions of broken axons. Thresholds selected from normal distributions resulted in the best fit, followed by gamma, uniform, and constant threshold distribution ([Figure 3-9](#)). Most biological phenomenological models exhibit statistics associated with normal or log-normal distributions, especially in large populations (Limpert et al., 2001),

which corroborated our findings. The poor fit associated with the constant threshold indicates that each axon likely has a unique injury threshold, which substantiates the idea of individual microstructural features influencing behavior. However, we emphasize the importance of testing a constant threshold as a self-check for the fitting scheme's accuracy. Setting a constant threshold enabled us to confirm and validate algorithm performance. For instance, when we set a constant threshold of 1.10 (10% increase in pathlength), we can calculate the proportion of axons whose pathlength will increase by 10% by hand. We then executed the program and ascertained that the model predicted proportion matched our calculation.

Decreasing thresholds with further development suggested that injury thresholds were, at least partially dictated by kinematics and changes in morphology. The most significant change with development is the increase in myelination, and connectivity to surrounding glia which correlates to the greater propensity for switching behavior. By splitting our proportion of broken axons into those assumed to be exhibiting non-affine and affine kinematics, we could determine individual thresholds. Indeed, we consistently observed affine thresholds to be consistently lower than the values we obtained for single thresholds ([Table 3-2](#)). This is further reflected in the switching parameters for these data: when failed axons are omitted, we see a decrease in upper bound parameters, providing additional evidence that axons predicted to behave with affine kinematics are prone to failure ([Figure 3-11](#)).

Even after omitting broken axons from our analysis, we still observed a deviation in trend between macroscopic and microscopic stretch at later stages of development. In E16 specimens, there was still a significant deviation from the 1:1 line we plotted ([Figure 3-](#)

5B). This was even more pronounced in E18 specimens, where 20% macroscopic stretch only resulted in an 8% increase in mean end-to-end internodal length, which increased to 12% once broken axons were omitted. We believe that there are two possible explanations. In our kinematic model, we assumed that a single segment exclusively exhibited non-affine or affine kinematics at any given time. It is possible kinematics are non-uniform along the single segment. Depending on the axonal segment's connectivity to surrounding glia, some regions may be prone to affine behavior, which would influence how the axon strains with macroscopic stretch. This is applicable for E16 and E18 specimens, where 55-70% of axonal segments are predicted to demonstrate affine or switching behavior (Singh et al., 2015), implying connectivity between axons. Another possibility is that a single axon with multiple segments may have broken further along the spinal cord. For instance, an axon fiber which we observed intact in the cervical region (i.e. no segments were broken), may have broken further along the white matter tract, in the thoracic or lumbar regions. This could theoretically influence kinematic behavior of the intact segments, causing these segments to switch from affine to non-affine behavior, or retract and become tortuous.

As described above, it is unclear what happens to axon morphology and kinematics following immediate breaking. To elucidate this, we executed the model undergoing one of two scenarios: 1) axons break at a random point in an internodal segment, and length and tortuosity remain fixed following injury, and 2) axons break at a random point in an internodal segment but continue to deform according to their kinematic mode prior to damage. We then evaluated the goodness-of-fit for each scenario to determine the most likely scenario.

When axons were modeled to retain their morphology following damage, we observed a slight shift in length distributions towards the left when compared to the scenario where the model predicted broken axons to continue to exhibit non-affine behavior. Overall, mean internodal end-to-end decreased slightly but there were no statistically significant changes when compared to experimental results. When axons were modeled to deform based on their kinematic behavior, mean end-to-end length decreased significantly, while pathlength increased significantly. This was unsurprising as we observed a larger proportion of broken axons exhibiting affine behavior, which would suggest that with increasing stretch, pathlength would increase even if the broken axon was still tortuous. Overall, we observed the strongest fit in the condition where axons retained their morphology following breaking (mean $R^2 = 0.79$).

To validate the results we predicted from our model, we characterized axonal segments along the full length of the white matter tract in the spinal cord. The biggest challenge we encountered was ensuring the same axon was traced through the different regions of the spinal cord. As described in the methods, excised spinal cords were divided into cervical, thoracic, and lumbar regions and sectioned in a serial manner. Each of these regions was sectioned individually, which resulted in cases where a fiber from one region could not be confidently connected to the fiber in the adjacent region. To this end, we analyzed axons where the calculated tortuosity was consistent with the axon between sections (i.e. if the segment tortuosities differed no more than 0.02). This increased confidence that the trajectories between two adjacent sections corresponded to each other.

We examined full length white matter tracts of E12 and E18 specimens that were unstretched, or stretched 10% or 20% ([Figure 3-14](#)). To ensure axons we captured were

from the white matter tract, we stained for myelin. Unsurprisingly, examining the entire length of the cord increased the number of broken axons recorded when compared to those found in individual slices as we noted some segments along a single axon experienced breaks further along the fiber length. With this spatial information, we looked for patterns in broken axons. Axons broke primarily in the cervical and lumbar regions at 10% stretch in each development stage but broke equally in all three regions of the spinal cord at 20% stretch. Notably, in E18 10% and 20% cords we observed small “pockets” of broken axons. Our definition of a pocket was where more than 3 separate axons had broken within 30 μ m of each other. We observed no pockets in any of the E12 cords examined. Figure 3-13B shows the profile of 328 axons measured across the full length of a single E18 20% spinal cord ([Figure 3-13](#)). While there were no discernable patterns or differences between the numbers of axons that broke in each region, we noticed that pockets occurred primarily in the cervical and lumbar regions of the cord. These pockets were confirmed with cluster analysis in MATLAB, where we observed the center point of the algorithmically designated cluster corresponded with the spatial position based on images (i.e. the cluster center calculated from the script matches where the pocket is in images). It is likely that there is an unequal stress concentration generated at the far edges of the cord close to where the cord was fixed during macroscopic stretch, which would explain the high concentration of breaks found in those regions.

Tracing axons along the entirety of the white matter tract also enabled us to determine when multiple segments along a single axon broke. Again, this behavior was most prevalent in E18 cords, where some axons broken twice or three times along their segments. No axons broke in more than three segments along the entire length of spinal

cord. Additionally when we extended our dataset to include segments captured from our full-length analysis, thresholds decreased further in response to the greater proportions of broken axons we captured. For instance, the E18 composite failure threshold decreased from 1.17 to 1.14 when full-length measurements were included. The decrease in the affine threshold from 1.14 to 1.11 contributed most significantly to the fall in the composite threshold, as most of the broken axons captured were primarily affine. E12 thresholds also decreased though not as significantly as what we observed in E18 samples. This further corroborates our assessment that E12 axons primarily exhibit non-affine kinematics.

These variations in threshold introduce the question of what properties of axons influences the propensity to break. Previous studies from our group demonstrate that myelin and connectivity to glia not only directly influence kinematic behavior, but also indirectly affect the axon's ability to resist tensile loading, where axon connectivity via these elements enables "sharing" of the macroscopic load and transmission of stress to surrounding axons. Other studies have established that axonal fibers are significantly stiffer (Ouyang et al., 2013) than the neuronal cell body (Spedden and Staii, 2013), myelin, and the surrounding glia (Shreiber et al., 2009). The occurrence of pockets also suggests that an axon's propensity to break might be dependent on the behavior and resilience of nearby segments. We hypothesize that a single axon's failure redistributes the stresses caused by tissue-level stretch to remaining intact axons, causing these axons to "take up the slack".

Direct measurements of axonal strain are possible in *in vitro* preparations. In these studies, axons are cultured and exposed to stretch injury both quasistatically and

dynamically. In *in vitro* preparations with unmyelinated axons, axons were able to be stretched 50-75% their original length without experiencing irrevocable damage (Smith et al., 1999). As this preparation would consist of axons behaving non-affinely, it lends support to the elevated thresholds we observed for axons predicted to exhibit non-affine kinematics. *In vivo* studies of the guinea pig optic nerve determined conservative strain thresholds of 14% for axonal injury (Bain and Meaney, 2000). The guinea pig optic nerve is highly myelinated which implies affine kinematics, and therefore supports the thresholds we predicted for affine behavior. We are still limited by the phenomenological nature of our model, where we rely on “snapshots” of fixed tissue at discrete levels of stretch. True validation cannot be achieved until methods have improved to trace these markers in real time, *in vivo* preparations undergoing continuous stretch.

Our analysis is further limited by the quasi-static approach we used to injure tissue samples. Understandably, almost all cases of CNS trauma occur due to dynamic injury, and plenty of evidence has been put forward that strain rate is correlated to injury severity (Smith and Meaney, 2000; Smith et al., 1999; Wright and Ramesh, 2012). We are currently investigating approaches to dynamically injure and snap-freeze tissue immediately after trauma, to better capture the primary injury response. Snap-freezing provides the advantage that it captures any immediate changes to cell morphology unlike fixation, which requires time for the fixative to diffuse through the tissue. Even in the small scales of time required for complete fixation, axon morphology undergoes visible changes following dynamic injury (Tang-Schomer et al., 2010). Preliminary results from our group suggest that axon morphology is not adversely affected by snap-freezing when compared to axons that are fixed via 4% paraformaldehyde. It will be interesting to

examine if changes in internodal lengths following dynamic injury differ when compared to quasistatic stretch injury.

Our work presents predictions on thresholds for axonal injury in spinal cord tissue. It is very likely that functional and morphological damage thresholds are lower than breaking thresholds. Scenarios such as mild TBI and diffuse axonal injury suggest that failure can occur even if an axon is not completely broken (Kilinc et al., 2009; Smith and Meaney, 2000), and so the parameters obtained in model predictions represent the worst-case scenario in a traumatic event. Still, the injury parameters we've gleaned, along with the kinematic parameters from our previous study can work towards improving finite element modeling of multi-scale white matter behavior. These models can be applied to improving the design of protective equipment, and better predicting instances of TBI and SCI following the initial injury event. Future studies would work towards examining this phenomenon in dynamic injuries.

Conclusions:

In this chapter we addressed two questions with regards to elucidating the translation from macroscopic to axonal level deformation: 1) is Caspr an effective fiducial marker for estimating strains at the axonal level, and 2) using this information and empirical data of broken axons, can we estimate *in situ* thresholds for axonal failure?

Caspr is an ideal candidate for use as a fiducial marker due to its regular expression at the nodes of Ranvier in axons. By measuring how individual Caspr proteins and Caspr pairs are displaced with macroscopic stretch, we can estimate the average strain populations of axons experience as a function of macroscopic stretch. We determined that the transfer of macroscopic stretch to axonal strain is close to 1:1 at earlier stages of development, and that these trends deviate significantly at later stages of development. We formulated two hypotheses for the shift in behavior: shifts in kinematic behavior between axonal segments; and the capture of broken axons which diminished the change in average internodal lengths. By examining thicker slices of tissue we could record proportions of broken axons and provide estimates of failure thresholds for different classifications of kinematic behavior.

Although the thresholds we predicted are based on a phenomenological model, the experimental results from changes in internodal lengths still provide estimates of strain at the individual axon level. *In situ* estimation of axon strain provides utility in validating computer simulations of multi-scale kinematics of white matter. Additionally, the failure thresholds we have gleaned could be used as parameters to further refine multi-scale simulations for understanding the mechanisms of white matter injury. Ultimately, information from models can be utilized to improve prevention methods for white matter

primary injury. In the next two chapters however, we shift focus to another area in the CNS injury and rehabilitation process. We now inquire on the role of different design parameters in neural electrodes that dictate its success in tissue insertion and long-term signal acquisition, with the hopes of improving patient outcomes following CNS injury.

References:

- Anderson, E.S., Bjartmar, C., Hildebrand, C., 2000. Myelination of prospective large fibres in chicken ventral funiculus. *J. Neurocytol.* 29, 755–64.
- Arbogast, K.B., Margulies, S.S., 1999. A fiber-reinforced composite model of the viscoelastic behavior of the brainstem in shear. *J. Biomech.* 32, 865–70.
- Bain, A., Meaney, D., 2000. Tissue-level thresholds for axonal damage in an experimental model of central nervous system white matter injury. *J. Biomech. Eng.* 122, 615–22.
- Bain, A.C., Meaney, D.F., Hall, H., 2000. Tissue-Level Thresholds for Axonal Damage in an Nervous System White Matter Injury 122.
- Chomiak, T., Hu, B., 2009. What is the optimal value of the g-ratio for myelinated fibers in the rat CNS? A theoretical approach. *PLoS One* 4, e7754. doi:10.1371/journal.pone.0007754
- Cloots, R.J.H., van Dommelen, J. a W., Kleiven, S., Geers, M.G.D., 2013. Multi-scale mechanics of traumatic brain injury: predicting axonal strains from head loads. *Biomech. Model. Mechanobiol.* 12, 137–50. doi:10.1007/s10237-012-0387-6
- Cloots, R.J.H., van Dommelen, J. a W., Nyberg, T., Kleiven, S., Geers, M.G.D., 2011. Micromechanics of diffuse axonal injury: influence of axonal orientation and anisotropy. *Biomech. Model. Mechanobiol.* 10, 413–22. doi:10.1007/s10237-010-0243-5
- Dobbing, J., Morgan, R.S., Reid, R.T.W., Wright, G.P., 1957. Neuroglial Development and Myelination in the Spinal Cord of the Chick Embryo 5, 428–437.
- Einheber, S., Zanazzi, G., Ching, W., 1997. The axonal membrane protein Caspr, a homologue of neuexin IV, is a component of the septate-like paranodal junctions that assemble during myelination. *J. Cell Biol.* 139, 1495–1506.
- El-Eishi, H.I., 1967. Biochemical and Histochemical Studies on Myelination in the Chick Embryo Spinal Cord. *J. Neurochem.* 14, 405–412. doi:10.1111/j.1471-4159.1967.tb09538.x
- Hamburger, V., Hamilton, H., 1951. A series of normal stages in the development of the chick embryo. *J. Morphol.*
- Hao, H., Shreiber, D.I., 2007. Axon kinematics change during growth and development. *J. Biomech. Eng.* 129, 511–22. doi:10.1115/1.2746372

- Karami, G., Grundman, N., Abolfathi, N., Naik, a, Ziejewski, M., 2009. A micromechanical hyperelastic modeling of brain white matter under large deformation. *J. Mech. Behav. Biomed. Mater.* 2, 243–54. doi:10.1016/j.jmbbm.2008.08.003
- Keirstead, H., Pataky, D., McGraw, J., Steeves, J., 1997. In Vivo Immunological Suppression of Spinal Cord Myelin Development. *Brain Res. Bull.* 44, 727–734. doi:10.1016/S0361-9230(97)00374-2
- Kilinc, D., Gallo, G., Barbee, K., 2009. Mechanical membrane injury induces axonal beading through localized activation of calpain. *Exp. Neurol.* 219, 553–561. doi:10.1016/j.expneurol.2009.07.014.Mechanical
- Limpert, E., Stahel, W., Abbt, M., 2001. Log-normal Distributions across the Sciences: Keys and Clues. *Bioscience* 51, 341–352.
- Nilsson, M., Lätt, J., Ståhlberg, F., van Westen, D., Hagslätt, H., 2012. The importance of axonal undulation in diffusion MR measurements: a Monte Carlo simulation study. *NMR Biomed.* 25, 795–805. doi:10.1002/nbm.1795
- Ouyang, H., Nauman, E., Shi, R., 2013. Contribution of cytoskeletal elements to the axonal mechanical properties. *J. Biol. Eng.* 7, 21. doi:10.1186/1754-1611-7-21
- Prange, M.T., Margulies, S.S., 2002. Regional, Directional, and Age-Dependent Properties of the Brain Undergoing Large Deformation. *J. Biomech. Eng.* 124, 244. doi:10.1115/1.1449907
- Rutgers, D.R., Toulgoat, F., Cazejust, J., Fillard, P., Lasjaunias, P., Ducreux, D., 2008. White matter abnormalities in mild traumatic brain injury: a diffusion tensor imaging study. *AJNR. Am. J. Neuroradiol.* 29, 514–9. doi:10.3174/ajnr.A0856
- Sherman, D.L., Brophy, P.J., 2005. Mechanisms of axon ensheathment and myelin growth. *Nat. Rev. Neurosci.* 6, 683–90. doi:10.1038/nrn1743
- Shreiber, D.I., Hao, H., Elias, R. a I., 2009. Probing the influence of myelin and glia on the tensile properties of the spinal cord. *Biomech. Model. Mechanobiol.* 8, 311–21. doi:10.1007/s10237-008-0137-y
- Singh, S., Pelegri, A. a, Shreiber, D.I., 2015. Characterization of the three-dimensional kinematic behavior of axons in central nervous system white matter. *Biomech. Model. Mechanobiol.* 1303–1315. doi:10.1007/s10237-015-0675-z
- Smith, D.H., Meaney, D.F., 2000. Axonal Damage in Traumatic Brain Injury. *Neurosci.* 6, 483–495. doi:10.1177/107385840000600611

Smith, D.H., Wolf, J. a, Lusardi, T. a, Lee, V.M., Meaney, D.F., 1999. High tolerance and delayed elastic response of cultured axons to dynamic stretch injury. *J. Neurosci.* 19, 4263–9.

Spedden, E., Staii, C., 2013. Neuron biomechanics probed by atomic force microscopy. *Int. J. Mol. Sci.* 14, 16124–40. doi:10.3390/ijms140816124

Tang-Schomer, M.D., Johnson, V.E., Baas, P.W., Stewart, W., Smith, D.H., 2012. Partial interruption of axonal transport due to microtubule breakage accounts for the formation of periodic varicosities after traumatic axonal injury. *Exp. Neurol.* 233, 364–72. doi:10.1016/j.expneurol.2011.10.030

Tang-Schomer, M.D., Patel, A.R., Baas, P.W., Smith, D.H., 2010. Mechanical breaking of microtubules in axons during dynamic stretch injury underlies delayed elasticity, microtubule disassembly, and axon degeneration. *FASEB J.* 24, 1401–10. doi:10.1096/fj.09-142844

Wright, R.M., Ramesh, K.T., 2012. An axonal strain injury criterion for traumatic brain injury. *Biomech. Model. Mechanobiol.* 11, 245–60. doi:10.1007/s10237-011-0307-1

Zhu, F., Gatti, D.L., Yang, K., 2015. Nodal versus Total Axonal Strain and the Role of Cholesterol in Traumatic Brain Injury. *J. Neurotrauma.*

Figures:

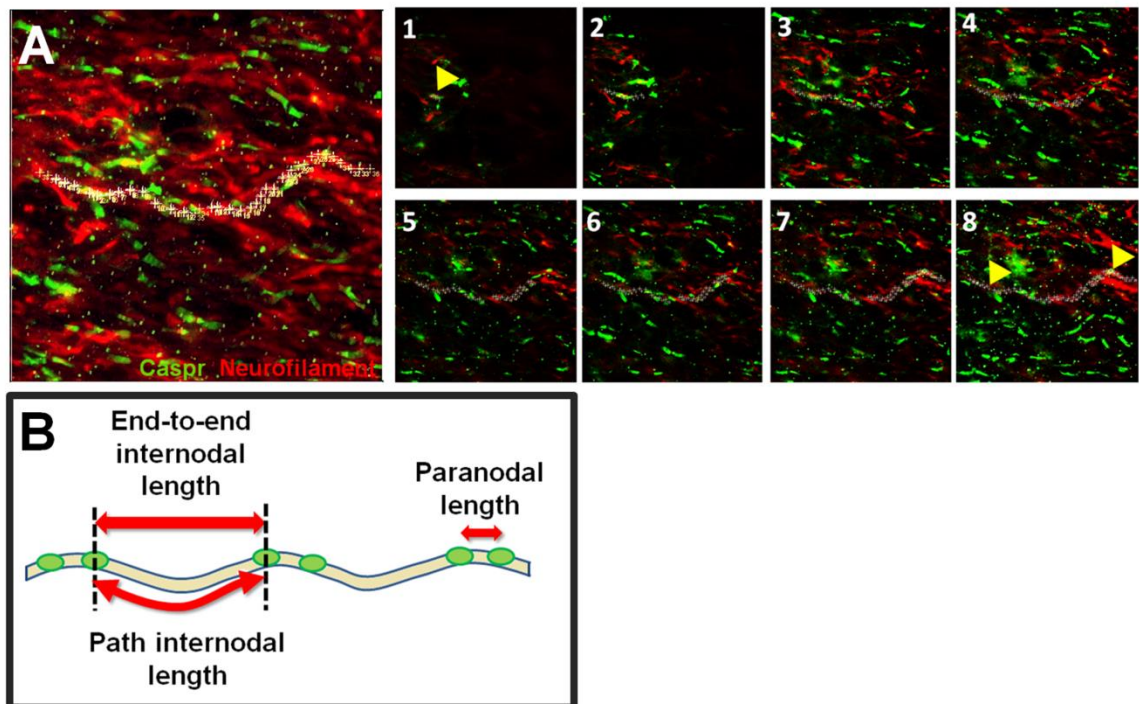


Figure 3-1: Internodal and paranodal lengths were measured by hand from longitudinally sliced spinal cord tissue, stained for Caspr (green) and Neurofilament (red). (A) Illustrates a z-projected image stack of an E16 spinal cord taken at 100X. To measure lengths, a Caspr pair was selected and the image in the stack with the highest intensity of neurofilament was designated the starting point (Image 1). Images (2-8) in the stack were then examined to find the adjacent region of highest neurofilament staining and these regions were then marked to determine the trajectory of the axon. Upon marking the entire axon length, path and end-to-end lengths were measured between pairs. (B) Schematic delineating the definitions of internodal end-to-end, pathlength, and paranodal lengths.

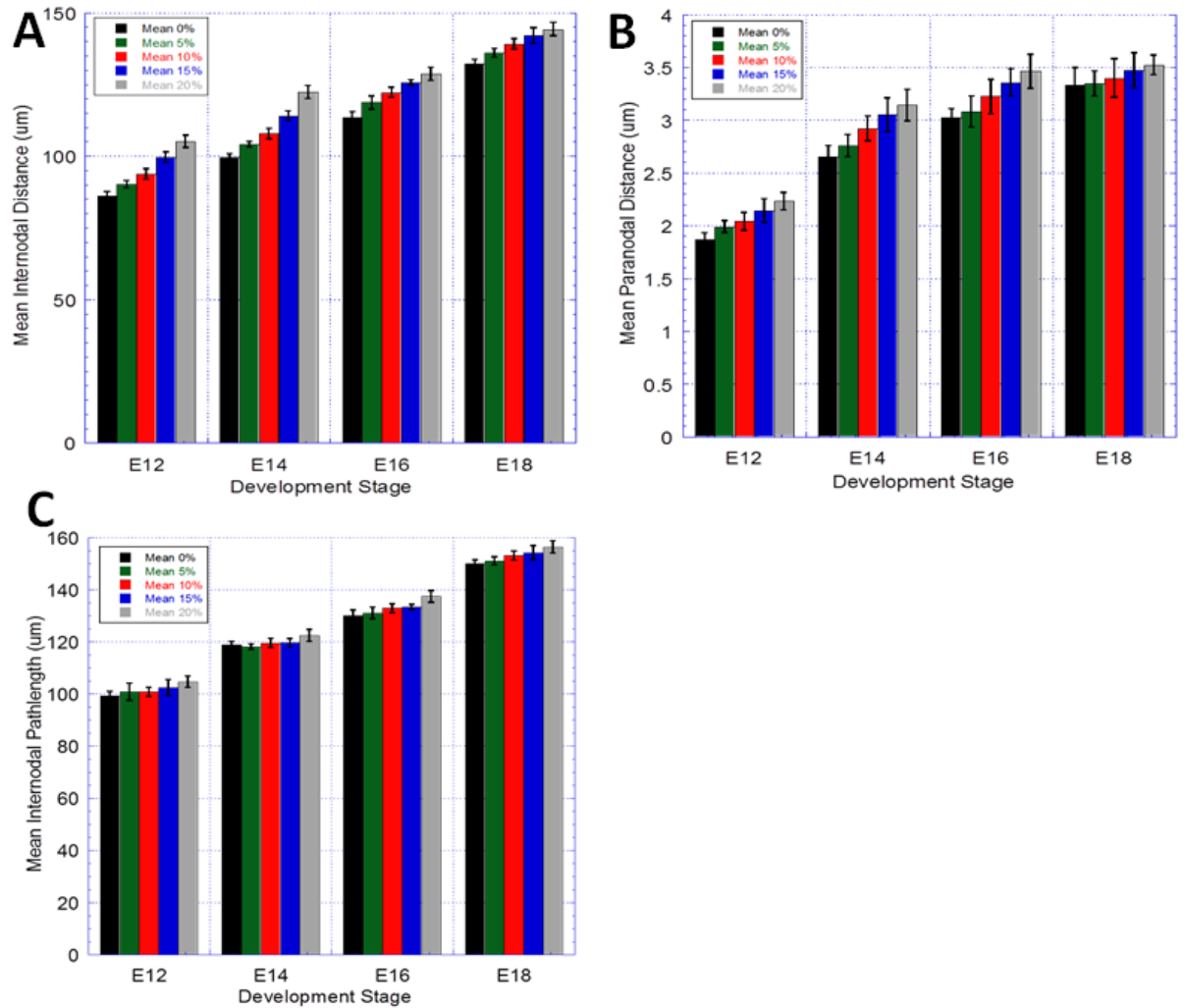


Figure 3-2: Bar graphs of (A) average internodal end-to-end length, (B) average paranodal length, and (C) average internodal pathlength. The percentage changes in length depicted in Figure 3-3 are calculated by dividing the average length for a given stretch against the average unstretched length.

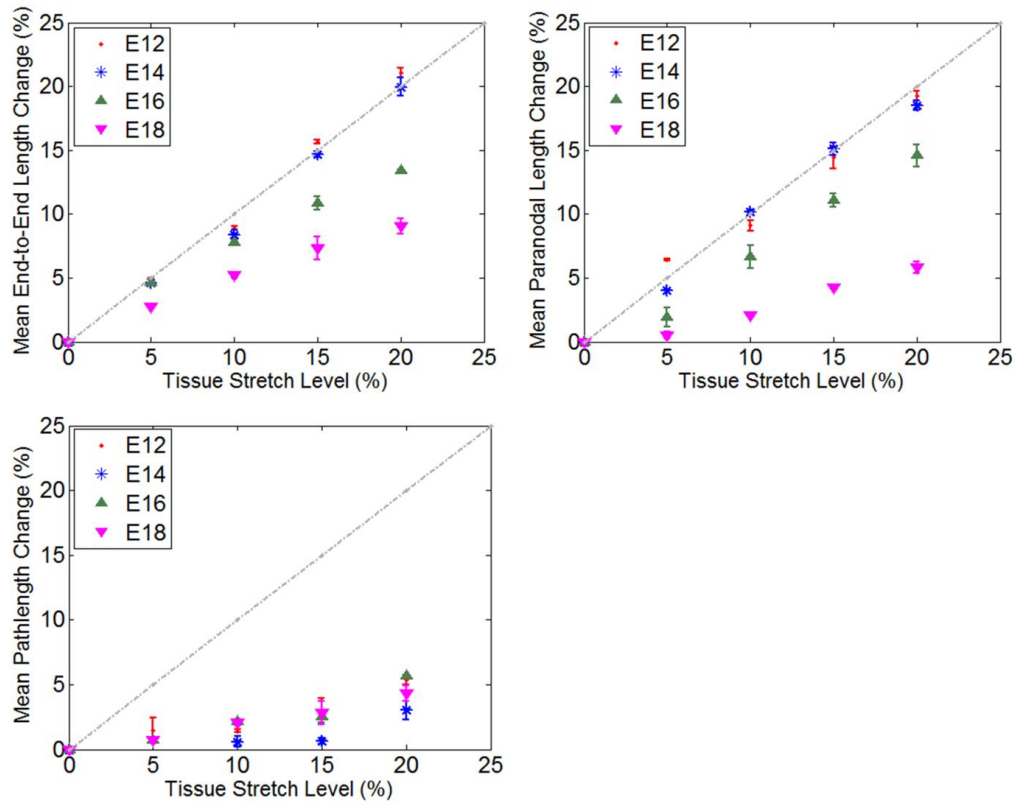


Figure 3-3: Plots for mean percentage length changes in 20 μ m thick slices observed for (A) end-to-end internodal, (B) paranodal, and (C) internodal pathlength. Mean percentage length change was computed by: $100 * (\text{Mean Stretched Length} - \text{Mean Unstretched Length}) / \text{Mean Unstretched Length}$. At earlier stages, there is almost a 1:1 transfer (represented by grey dashed line) of tissue-level to micro-level stretch for internodal end-to-end and paranodal length changes. This trend deviates towards later stages. For pathlength changes, at earlier stages there is little change to distances, which is the true measure of strain applied to the axon. This is surmised to be due to a larger proportion of non-affine axons, which require the axon to unfold completely prior to straining. There is a small but gradual change experienced by axons at later stages of development.

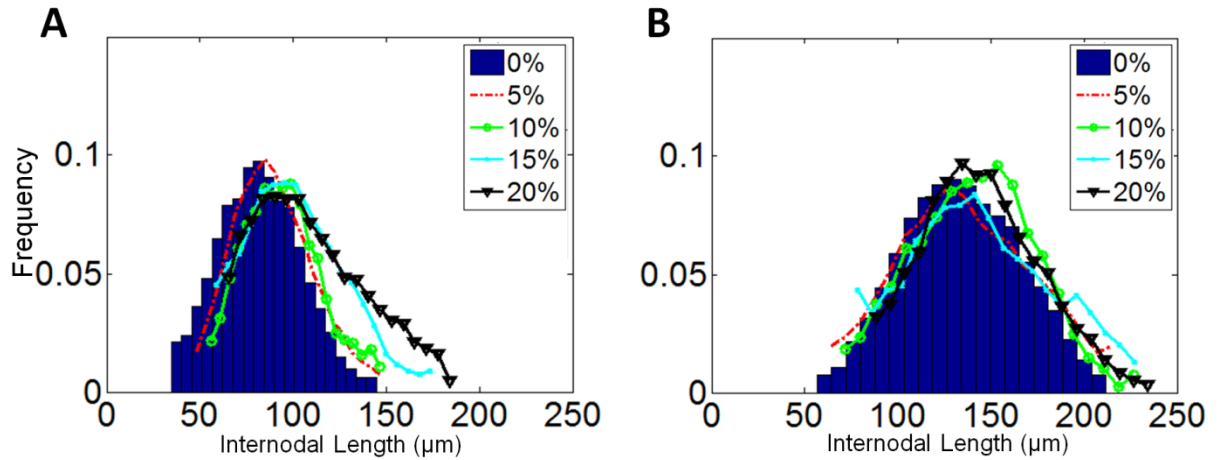


Figure 3-4: Histograms for end-to-end internodal lengths for (A) E12, and (B) E18 at different stretch levels. The lower-end bins for E18 at all stretch levels (5-20%) stretch show a dramatic increase in frequency when compared to similar lower-end bins for 0%. This dramatic increase is also present in E12 specimens but only at 15% and 20% macroscopic stretch.

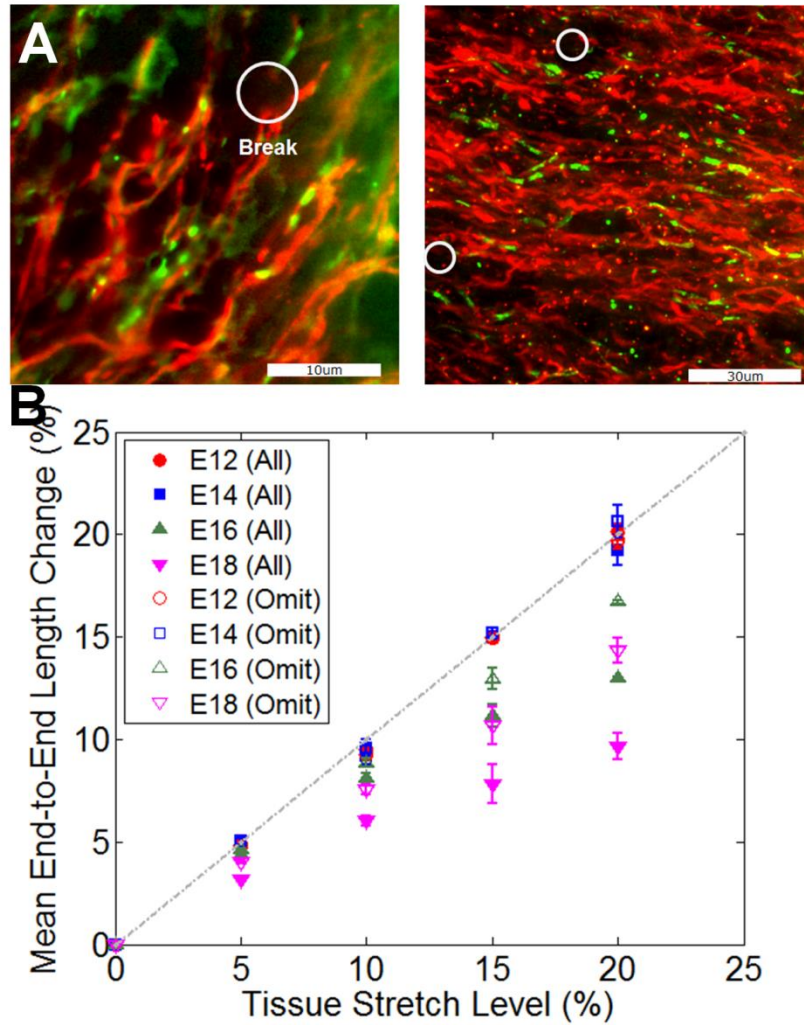


Figure 3-5: (A) Thicker (40µm) slices were taken to determine where axons had broken with greater certainty. Axons were labeled as broken when a void region was found in the z-projected image, and no continuous path could be found in the image stack, as shown in the E18 representative images above. (B) When lengths from broken axons were omitted, trends in end-to-end internodal length changes were observed to improve somewhat, moving closer to the dashed grey 1:1 line.

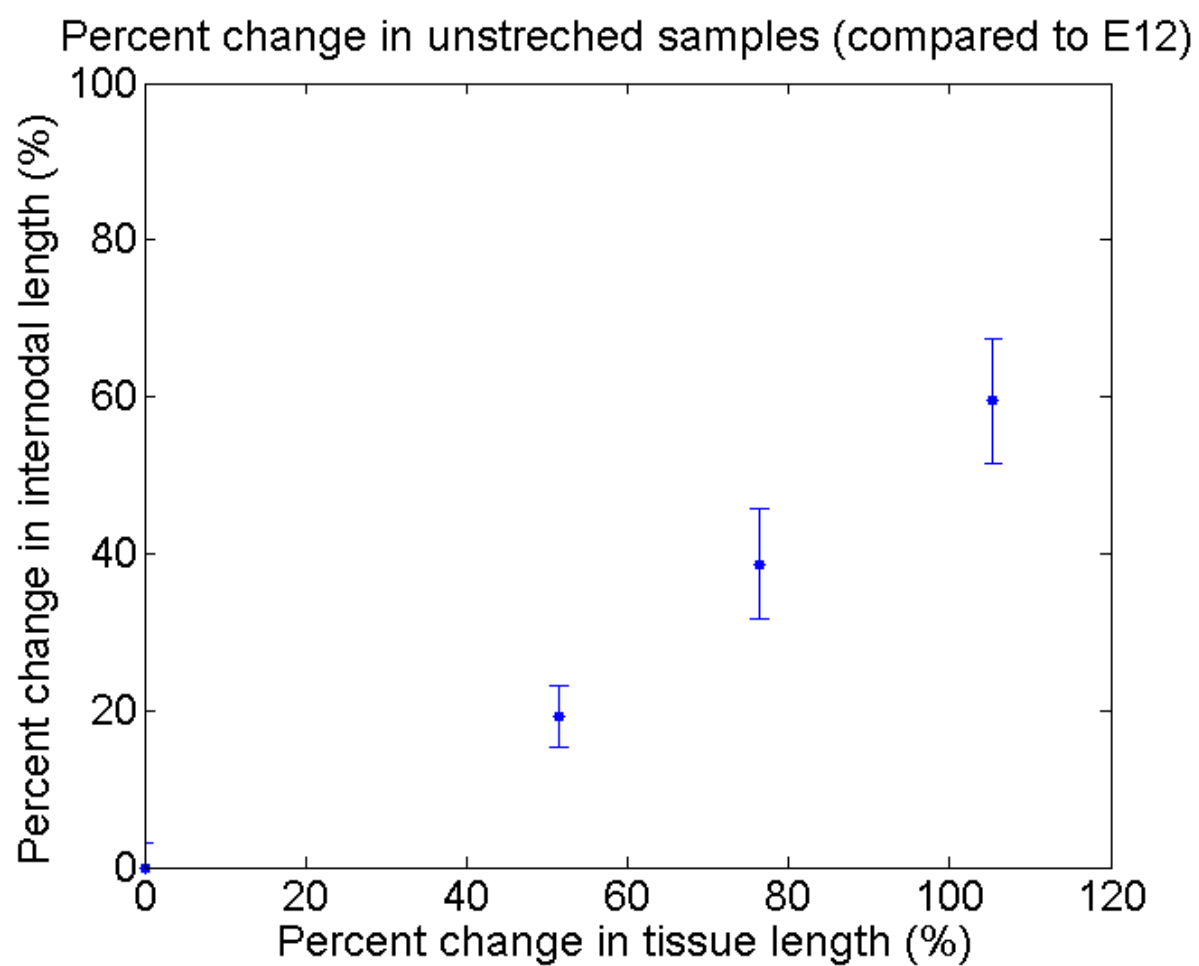


Figure 3-6: Percentage change in internodal length compared to percentage change in tissue length.

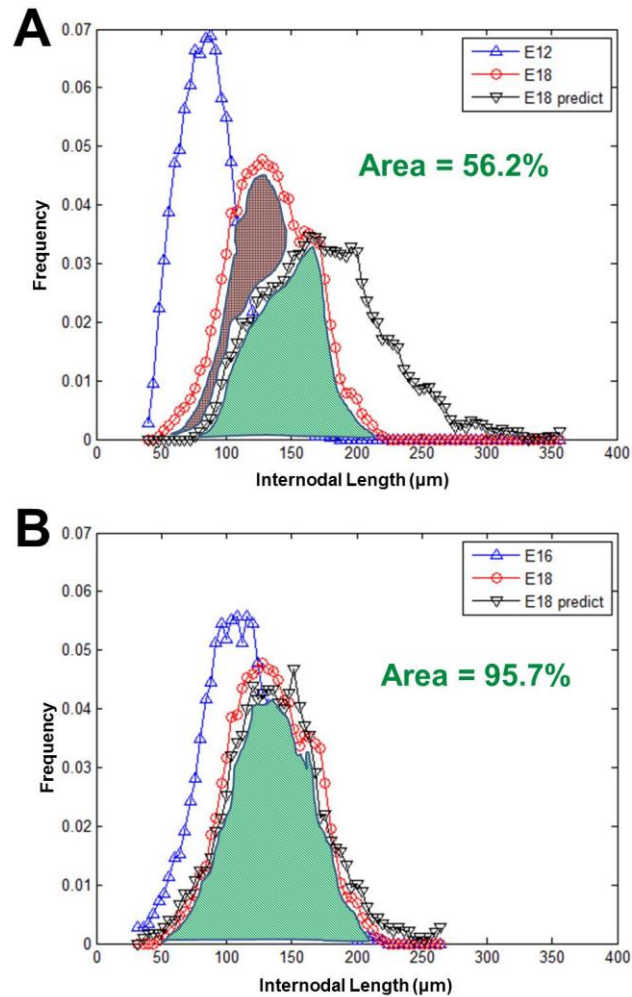


Figure 3-7: End-to-end length distributions were plotted for (A) E12 (blue) and (B) E16 (blue). To determine what proportion of segment lengths were likely to be due to developmental-induced tissue growth in E18 results (red), the original E12 and E16 distributions were multiplied by the percentage growth in tissue length ($E12 \rightarrow E18 = 103.4\%$ increase; $E16 \rightarrow E18 = 21.3\%$) to produce the predicted length distribution (black), and the overlapping area as a percentage of the area underneath the empirical data curve was calculated. This area corresponds to the proportion of segments that rise from the original population following growth-induced stretch. The remaining proportion

is likely to be new segments being formed via morphogenesis or newly expressed Caspr pairs.

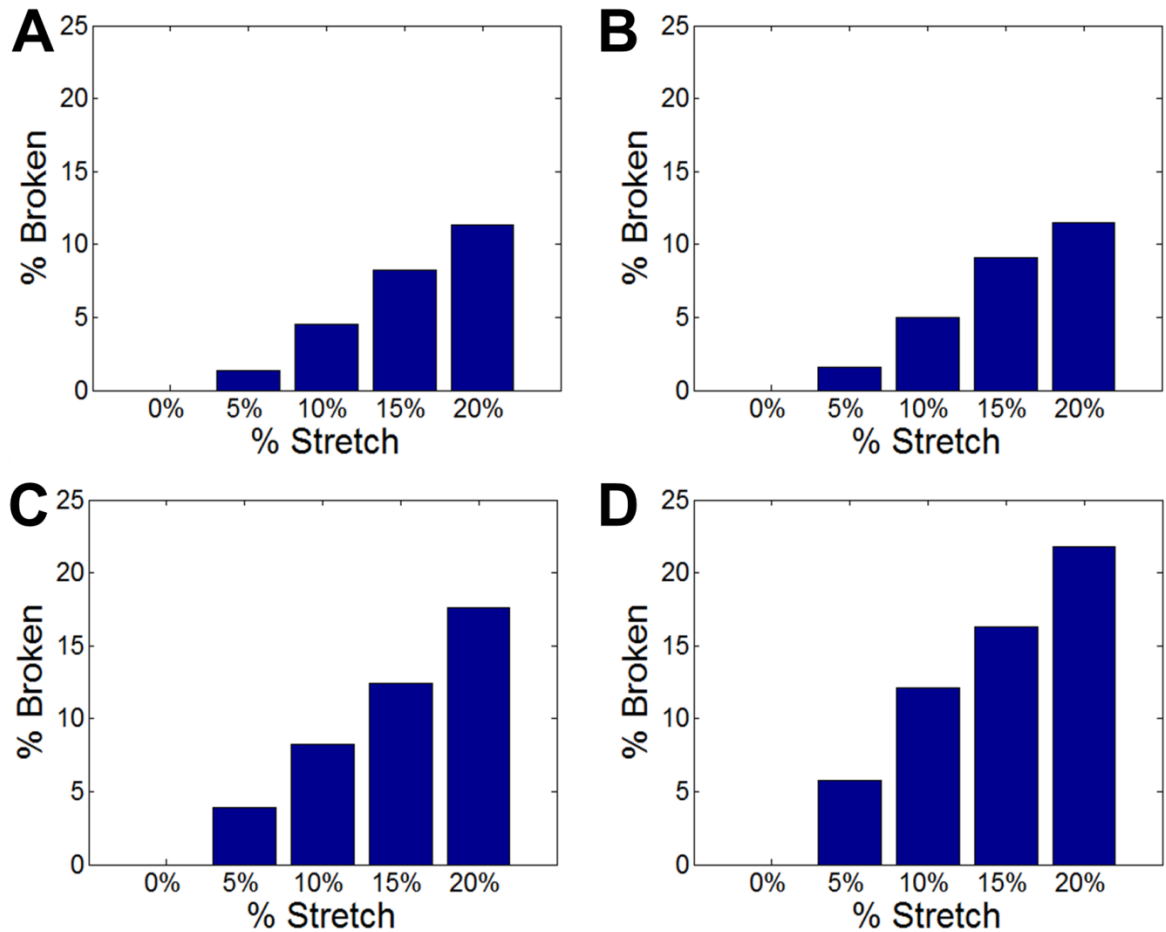


Figure 3-8: Proportion of broken segments from 40 μ m thick slices was tabulated for (A) E12, (B) E14, (C) E16, and (D) E18 spinal cords. More broken segments were observed at later stages of development, correlating with increased myelination and affine behavior (Singh et al. 2015).

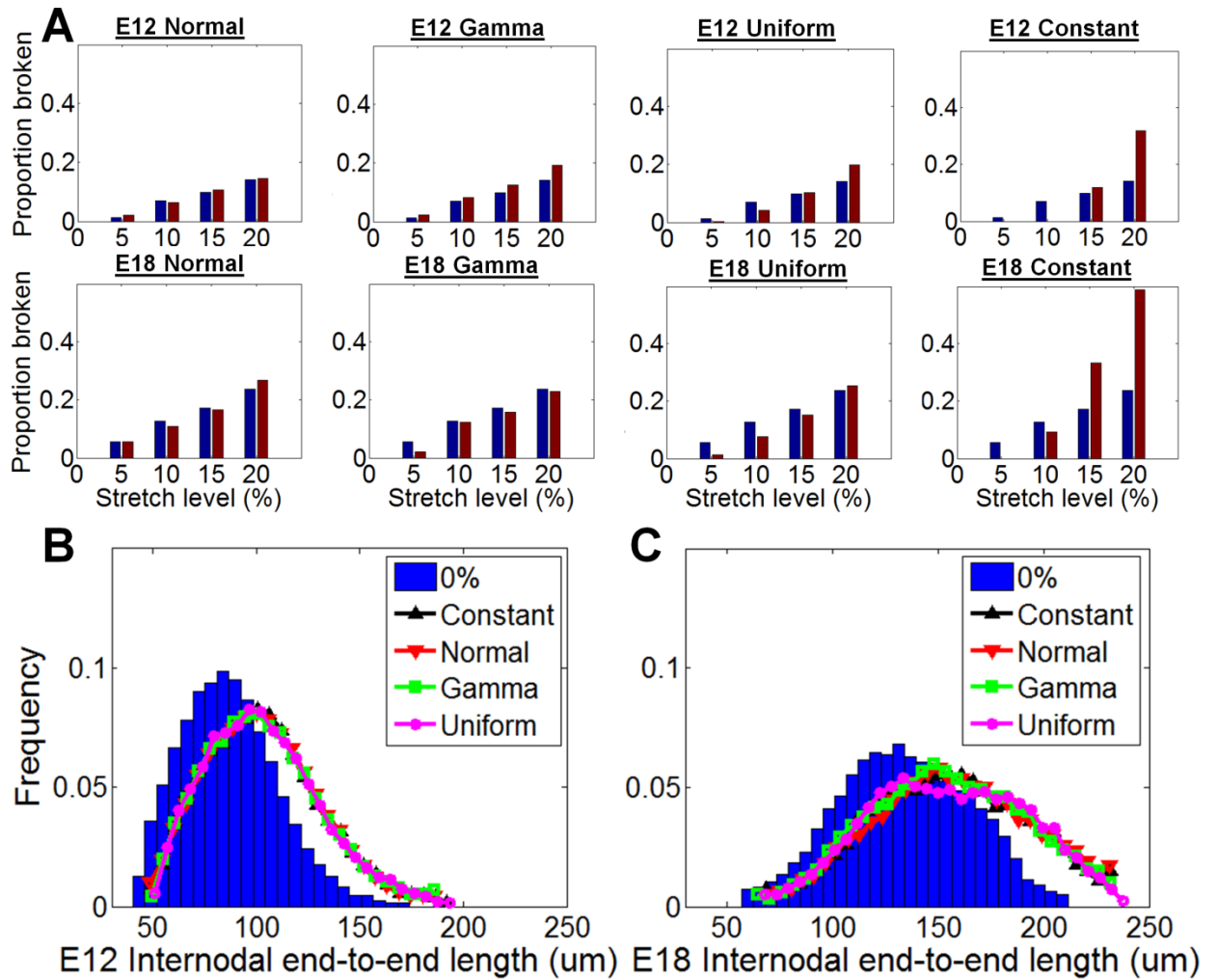


Figure 3-9: Model predictions for E12 and E18 compared to experimental results where the strain threshold was picked from (A) normal distribution, gamma distribution, uniform distribution, and a constant value. The best fit was determined to be from strain thresholds picked from a normal distribution (see Table 2). When histograms of predicted internodal end-to-end lengths for (B) E12, and (C) E18 after unstretched and 20% stretch were plotted, deviations were observed at the later development stage, corresponding to the greater proportion of broken axons predicted for constant and uniform distributions.

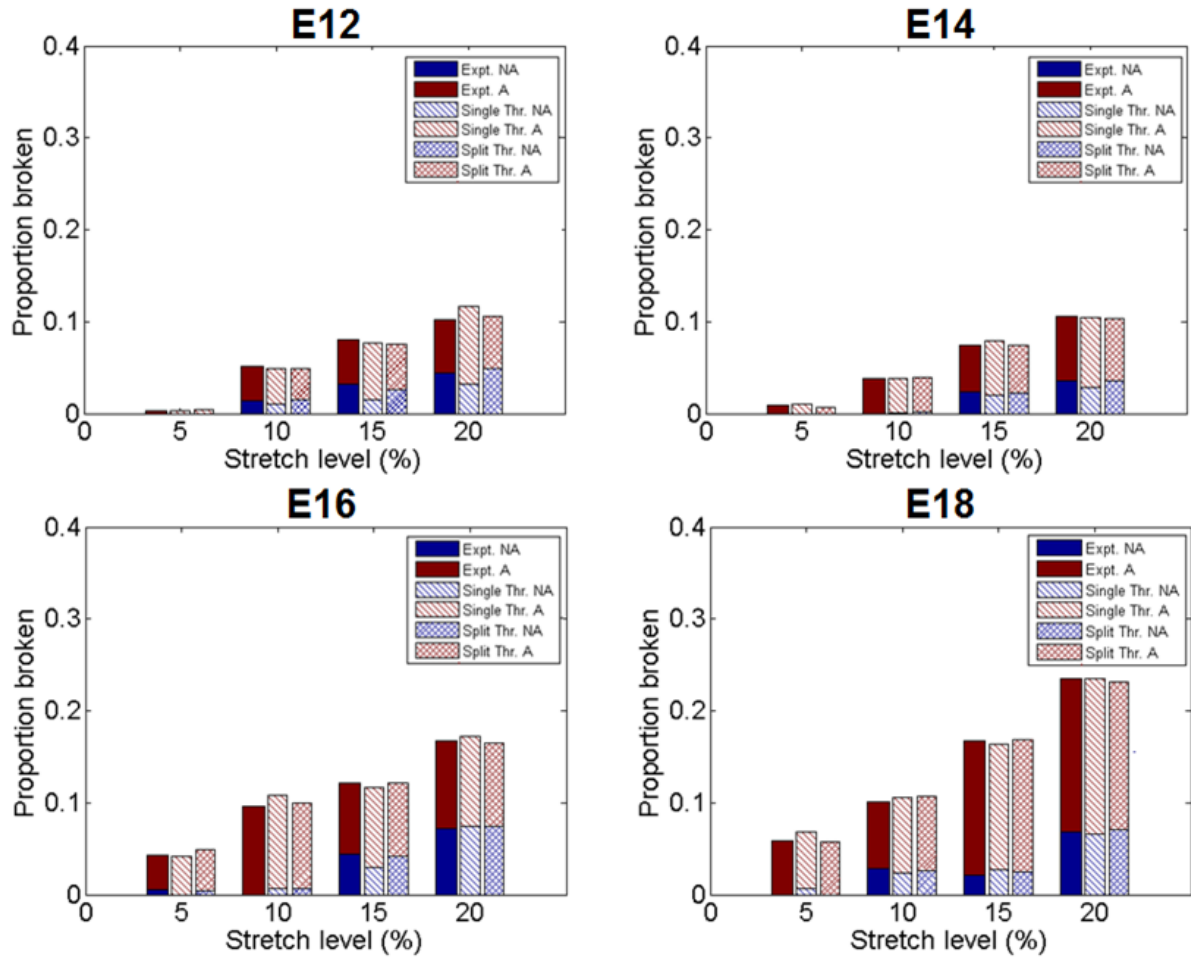


Figure 3-10: Proportion of broken axons for different development stages split between non-affine and affine kinematics when thresholds were selected from a normal distribution. Model predictions for a single threshold for both non-affine/affine behavior (inclined), and individual thresholds for non-affine/affine behavior (hashed) using a normal distribution fitting are also plotted. There is greater agreement observed between experimental results and model results when individual thresholds for non-affine/affine fitting are used. At all developmental stages, the individual non-affine threshold was greater than the single threshold. Conversely, individual affine thresholds were always less than the single threshold.

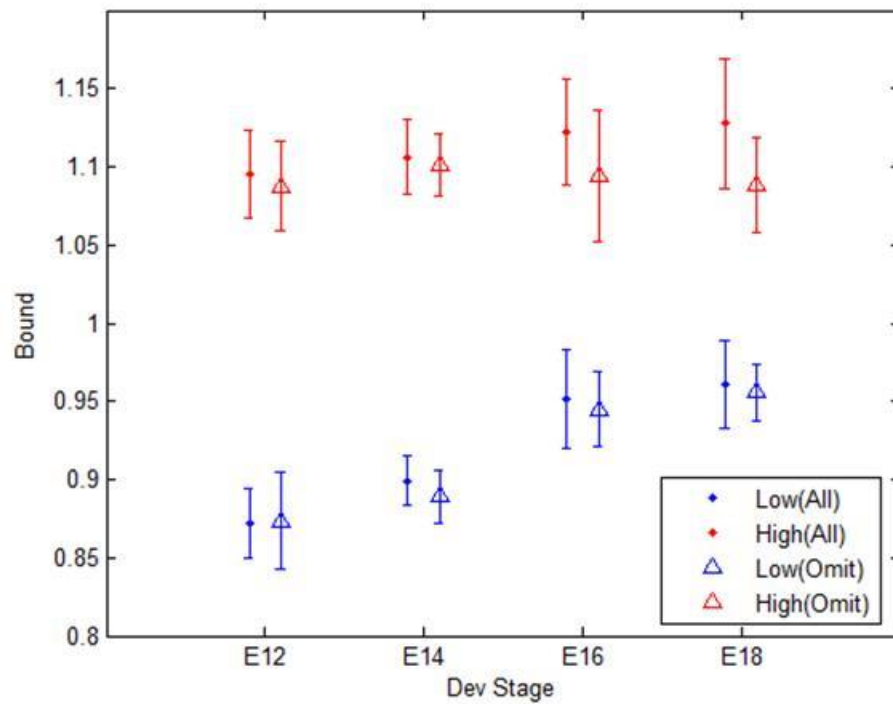


Figure 3-11: Kinematic parameters derived from testing distributions consisting of the complete population of axons, and the population when broken axons were omitted.

When broken axons are omitted from kinematic analysis, little change is seen in the lower bounds (T_1) tortuosity parameter for switching behavior. More substantial change (but still statistically insignificant) is predicted for the upper bound tortuosity for switching behavior- which decreases relative to the bounds when all axons are counted. This decrease in (T_2) suggests that it is indeed affine axons that are failing following macroscopic stretch.

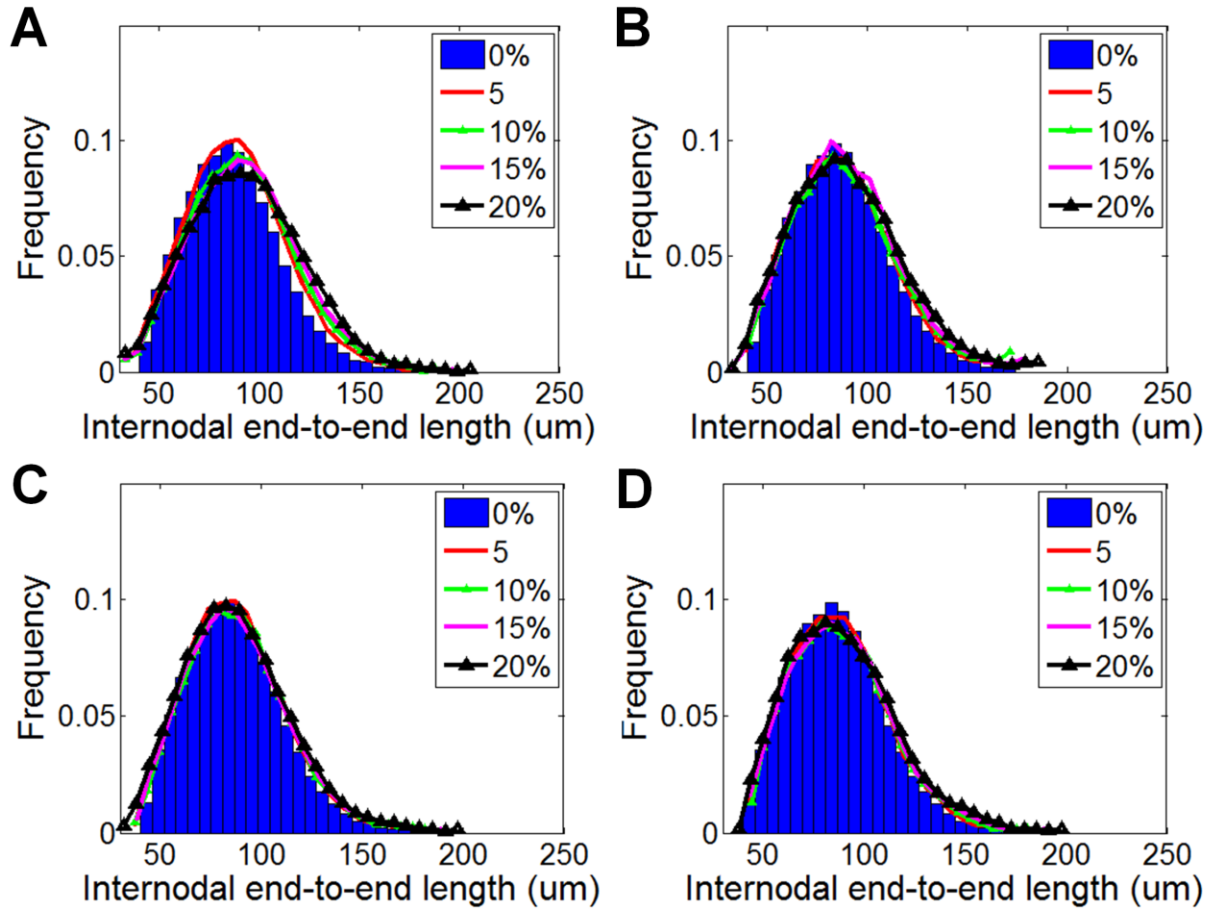


Figure 3-12: Histograms for the predicted changes in internodal end-to-end lengths as determined by model executions. In this case, new lengths were calculated using the formulae presented in methods. If an axon was simulated to fail, it broke at a random position along the length of the axon, and no longer experienced any increase in length.

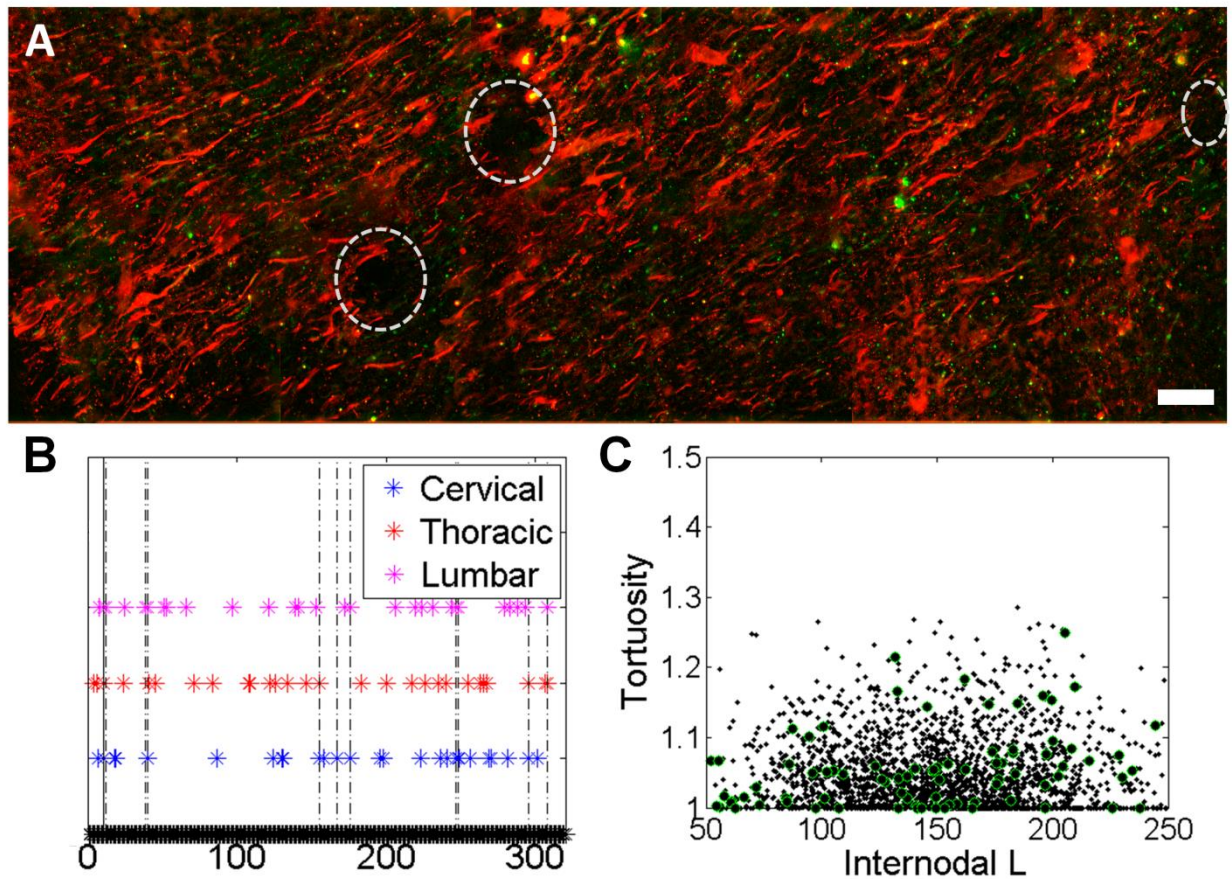


Figure 3-13: E18 20% spinal cords were partitioned into the cervical, thoracic, and lumbar regions and sectioned into 40 μ m slices. Starting at the cervical region, axons were traced through the length of the spinal cord. Broken axons were found through the section and their location along the cord was recorded. (A) shows the thoracic region of the cord where several pockets of broken axons (dashed circles) were found (Scale bar = 50 μ m). (B) Broken axons plotted by region. Dashed lines correspond to pockets of broken axons where 3-5 axons broken within a single pocket (defined as axons which broke within 30 μ m of each other). Full lines correspond to 5 or more axons broken in a single point. (C) Axon tortuosity against internodal length was plotted for E18 20% to find patterns in broken axons.

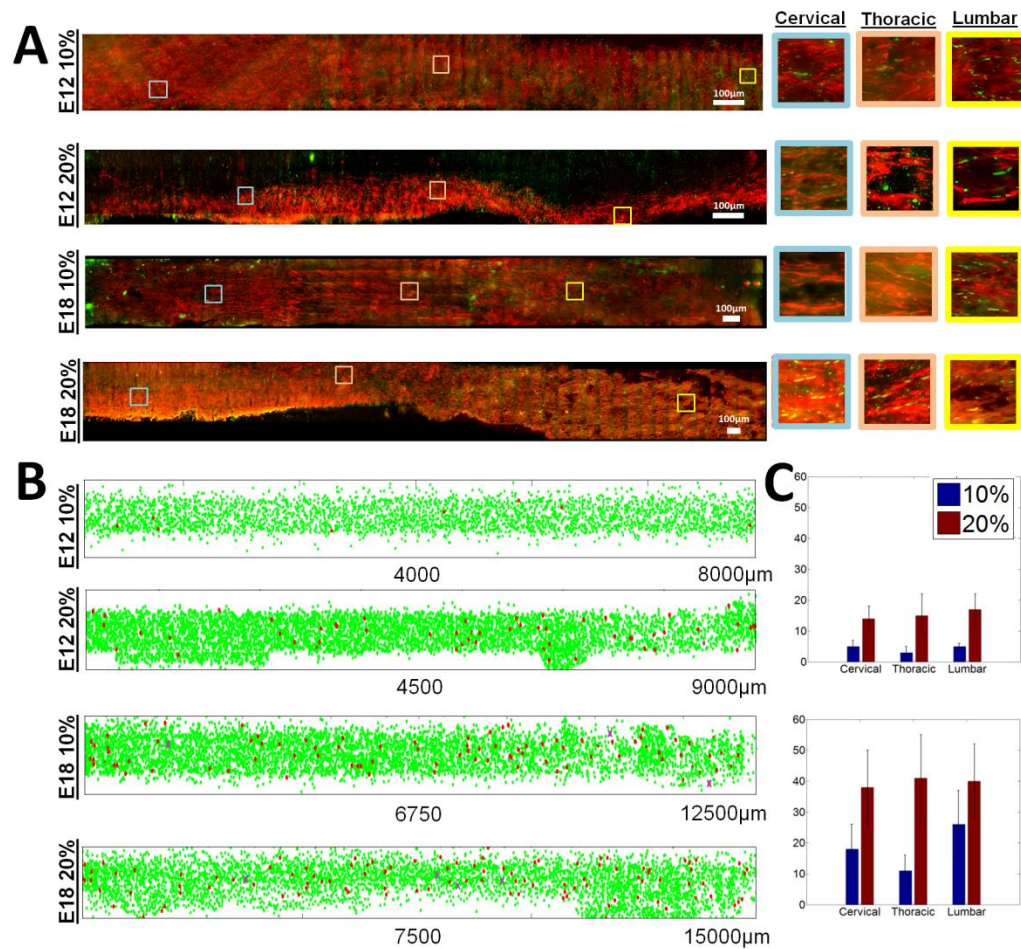


Figure 3-14: (A) Representative images for full-lengths of spinal cords. Unstretched and stretched E12 and E18 specimens were reconstructed from tissue-sections and processed to identify broken axons. The images in the right show selected zoomed-in regions for cervical, thoracic, and lumbar regions to delineate differences in axon morphology, nodal distances and occurrences of breaks. (B) From full-length profiles, spatial positions of nodes (green) were extracted along with positions of breaks (red for internodal breaks, purple for paranodal breaks). Pockets of breaks were noticeably present in E18 20% samples. (C) Numbers of broken segments classified by region in 10% and 20% stretched spinal cords (N = 3). Broken segments were relatively prevalent in the cervical and lumbar regions of spinal cords in 10% samples, but relatively equal across all regions in 20% samples.

Distribution	E12			E14			E16			E18		
Normal	Mean	SD	R^2	Mean	SD	R^2	Mean	SD	R^2	Mean	SD	R^2
	1.25	0.12	0.87	1.23	0.11	0.85	1.20	0.09	0.90	1.17	0.08	0.92
Gamma	a	b	R^2	a	b	R^2	a	b	R^2	a	b	R^2
	1.21	0.35	0.81	1.20	0.33	0.75	1.14	0.28	0.78	1.12	0.29	0.82
Uniform	U_1	U_2	R^2	U_1	U_2	R^2	U_1	U_2	R^2	U_1	U_2	R^2
	1.07	1.44	0.79	1.10	1.39	0.82	1.06	1.38	0.74	1.09	1.32	0.76
Constant	ϵ		R^2	ϵ		R^2	ϵ		R^2	ϵ		R^2
	1.21		0.45	1.19		0.43	1.16		0.36	1.14		0.34

Table 3-1: Predicted parameters for axonal failure strain probability distributions for the four distribution types tested. The modified model was executed through 100 iterations until parameter values converged. Normal distributions generated the best fit between experimental and model results, followed by gamma, uniform, and constant thresholds.

Development Stage	Non-affine Thresholds	Affine Threshold	Single Threshold
E12	1.29 ± 0.12	1.19 ± 0.13	1.25 ± 0.12
E14	1.28 ± 0.13	1.18 ± 0.14	1.23 ± 0.11
E16	1.27 ± 0.14	1.17 ± 0.09	1.20 ± 0.09
E18	1.27 ± 0.15	1.14 ± 0.10	1.17 ± 0.08

Table 3-2: Predicted parameters (mean \pm standard deviation) for breaking strain

classified by predicted kinematic behavior. In all cases, non-affine thresholds were higher than affine and single thresholds.

Chapter 4: Modeling the insertion mechanics of coated flexible neural probes for optimizing probe performance

Major sections of this chapter have been excerpted from the following publication: Singh,

S., Lo, M.-C., Damodaran, V.B., Kaplan, H.M., Kohn, J., Zahn, J.D., Shreiber, D.I.,

2016.

“Modeling the insertion mechanics of flexible neural probes coated with sacrificial polymers for optimizing probe design”, Sensors (Basel). 16, 1–18. I have received

permission from the publishers to utilize this and all the work presented herein is my

own.

Abstract:

Single-unit recording neural probes have significant advantages towards improving signal-to-noise ratio and specificity for signal acquisition in brain-to-computer interface devices. Long-term effectiveness is unfortunately limited by the chronic injury response, which has been linked to the mechanical mismatch between rigid probes and compliant brain tissue. Small, flexible microelectrodes may overcome this limitation, but insertion of these probes without buckling requires supporting elements such as a stiff coating with a biodegradable polymer. For these coated probes, there is a design trade-off between the potential for successful insertion into brain tissue and the degree of trauma generated by the insertion. In this chapter, I outline the process in developing and validating a finite element model (FEM) to simulate insertion of coated neural probes of varying dimensions and material properties into brain tissue. Simulations were performed to predict the buckling and insertion forces during insertion of coated probes into a tissue

phantom with material properties of brain. The simulations were validated with parallel experimental studies where probes were inserted into agarose tissue phantom, ex vivo chick embryonic brain tissue, and ex vivo rat brain tissue. Experiments were performed with uncoated copper wire, and both uncoated and coated SU-8 photoresist, and parylene C probes. Model predictions were found to strongly ($<10\%$) agree with experimental results ($<10\%$ error). The ratio of the predicted buckling force-to-predicted insertion force, where a value greater than one would ideally be expected to result in successful insertion, was plotted against the actual success rate from experiments. A sigmoidal relationship was observed, with a ratio of 1.35 corresponding to equal probability of insertion and failure, and a ratio of 3.5 corresponding to a 100% success rate. This ratio was dubbed the “safety factor”, as it indicated the degree to which the coating should be over-designed to ensure successful insertion. Probability color maps were generated to visually compare the influence of design parameters. Statistical metrics derived from the color maps and multi-variable regression analysis confirmed that coating thickness and probe length were the most important features in influencing insertion potential. The model also revealed the effects of manufacturing flaws on insertion potential.

Background & Significance:

Brain-to-Computer interface (BCI) devices have been gaining traction towards clinical usage (Mak and Wolpaw, 2009; Nicolas-Alonso and Gomez-Gil, 2012), particularly for rehabilitation following central nervous system (CNS) injury. BCI devices generally operate by acquiring a volition signal, processing the acquired signal, and translating the processed signal into the operation of an extra-corporeal device. Successful operation of a BCI device is foremost dependent on accurate signal acquisition (Amiri et al., 2013). The three most common modalities of acquiring volition signal, in order of least-to-most invasive, accurate, and resolved are: (1) Electroencephalograms (EEGs), (2) Electrocorticographs (ECOGs), and (3) Single-Unit Recordings (SURs) from neural probes. Neural probes in particular have been widely used in research as evidenced by the popularity of the Utah Array (Maynard et al. 1997; Cheung 2007) and the Michigan Array (Hoogerwerf & Wise 1994; Bareket-Keren & Hanein 2012).

However, current neural probes are limited by their inability to maintain signal fidelity for long-term acquisition of SURs. Probe insertion into brain tissue injures cells and the surrounding microvasculature. A wound healing response is initiated that includes microglia and astrocyte activation, which can hinder signal acquisition (Biran et al., 2005; Polikov et al., 2005; Turner et al., 1999). Moreover, a chronic response to the implanted probe is also observed. Reactive astrogliosis persists long-term from shear stresses at the probe-tissue interface, which ultimately leads to glial scarring (Aregueta-Robles et al., 2014; Rousche et al., 2001). Astrocytes comprising the glial scar encapsulate the recording electrode, which increases the local impedance and limits electrode contact with surrounding neurons. As a result, current probes, which are successful in obtaining accurate signals in the short-term, fail to maintain adequate

signal-to-noise ratio in long-term use (N. Hamzavi et al., 2013; Stice and Muthuswamy, 2009; Subbaroyan et al., 2005).

Among the many features believed to influence the magnitude of this foreign body response, two factors are particularly relevant from the perspective of probe design: probe geometry and probe material properties. Previous studies have shown that larger probes induce a greater magnitude of primary injury and a greater degree of long-term gliosis (Szarowski et al., 2003; Zhu et al., 2011). Probe material properties have a more significant effect on the chronic response than the acute injury. Stiffer probes have been linked to larger chronic responses in comparison to probes that have mechanical properties similar to CNS tissue (Lind et al., 2013; Turner et al., 1999; Zhu et al., 2011). These observations suggest that a smaller, more flexible microelectrode will minimize primary trauma and the subsequent chronic response (Lind et al., 2010).

However, small, flexible probes may be too weak to insert into brain tissue and must be assisted by a stiffer and/or larger device. For example, flexible probes have been inserted through insertion shuttles that confer temporary mechanical strength to the probe. Once the probe is successfully in place, the shuttle or coating is removed surgically.

Unfortunately, these shuttles induce significant primary trauma (Felix et al., 2013).

Another approach to providing temporary mechanical strength is coating or supporting a flexible probe with a sacrificial, protective polymer, which degrades following insertion. Previous groups have utilized polymer coatings made of nitrocellulose-based materials (Zhong and Bellamkonda, 2007), poly(DL-lactide-co-glycolide) (Foley et al., 2009), polyethylene glycol (PEG) (Chen C-H et al. 2010), and tyrosine-based compounds (Lewitus et al. 2011). Each of these has shown promise as a temporary coating, and the

tyrosine-based compounds have the added benefit of ultrafast degradation, which removes the insulating coating layer within hours to allow for earlier neural recordings. Given the properties of the coating or supportive material and the properties of the probe, it is possible to design the probe to optimize mechanical performance. From a mechanical perspective, the ideal coating would have the minimum coating thickness necessary to allow successful insertion, which would minimize tissue trauma during insertion and leave a flexible probe that would reduce interfacial stresses. An ideal coating would also degrade rapidly into non-cytotoxic byproducts, and leave the intact probe exposed to nearby neurons for signal acquisition as early as possible after implantation. Given the wide range of probe and coating specifications, experimentally finding an acceptable range of designs which fit these criteria can be a costly and time-consuming task.

In general, computational modeling can be an effective approach to evaluate the effects of different specifications on probe insertion and mechanical performance in soft tissue. Finite element models that simulate needle insertion into soft tissues have been employed in prosthesis design (Abolhassani & Patel 2006; Okamura & Simone 2004). Similar principles have been applied to neural microelectrodes, particularly to understand how probe geometry (Subbaroyan et al., 2005) and material properties (Polanco et al., 2014) influence probe-tissue interfacial stresses. Other groups have concentrated on modeling the mechanical trauma exerted on the brain during and post-insertion to ascertain the probe's 'neural kill zone' (Hamzavi et al. 2013), but none have focused on design criteria for insertion mechanics.

We have developed an approach for the reproducible manufacture of polymer-supported microprobes using microfabrication techniques (Lo et al., 2015). We have used our

approach to make microprobes from parylene C, a class VI polymer used in many medical devices, and from SU-8 photoresist. The probes are coated with an ultra-fast degrading tyrosine-based polymer that is rigid during insertion but is hydrolytically degraded within hours following insertion (Lewitus et al. 2011). The goal of this study was to develop and validate a finite element model that predicted coated probe performance during insertion into brain tissue. We first developed finite element simulations to model buckling and penetration into tissue, and validated predictions made by each model by testing varying sizes of copper wire. Next, we compared the model predictions to results from experimental tests of uncoated and coated SU-8 and parylene probes to validate the model for softer materials. Finally, we used the model to predict the performance of uncoated and coated parylene over a range of design specifications, employing a number of metrics to assess which features of the probe and coating design influence insertion and tissue damage, as well as the design regime of coated probes that will insert and minimize insertion trauma.

Materials and Methods:

Buckling and Insertion Tests: Buckling and insertion testing was performed with an Enduratec ELF 3200 uniaxial mechanical testing device (Bose) (Figure 4-1). Probes or probe mimics were secured to an actuator, which lowered the probe into an agarose tissue phantom, chick embryonic brain tissue, or adult, rat brain tissue. These tissues or tissue phantoms were set on a rigid surface, which was connected to a 0.5 N cantilever-type load cell (Entran Sensors and Electronics, Fairfield NJ, USA). For tests with an agarose phantom, a 0.6% by weight solution of low-temperature melting agarose (Sigma-Aldrich, St Louis MO, USA) was prepared. This concentration of agarose has mechanical properties similar to brain tissue and has previously been used as a tissue surrogate (Lewitus et al. 2011, Chen et al. 2004). For tests with chick embryonic brain tissue, which provided an inexpensive and convenient source of model tissue, fresh fertilized chicken eggs (Charles River Labs, North Franklin CT, USA) were incubated for 18 days. The embryo was extracted from the egg, and brain tissue was excised. Finally, for tests with rat brain tissue, rat brains were extracted from female Sprague-Dawley rats (Charles River Labs, North Franklin CT, USA) following euthanasia via asphyxiation in 100% CO₂ environment following an approved IUCAC protocol. Preliminary experiments showed that the presence of the dura layer had negligible effect on insertion force and thus was left intact. Brains were transferred to 37 °C saline and used immediately following removal.

Probes or probe mimics were lowered at a rate of 0.1 mm/s into the agarose phantom or brain tissue. A humidifier was used to ensure tissue remained hydrated during testing.

The probe either buckled after contact with the tissue/phantom, or it penetrated the

tissue/phantom, traveled through the entirety of the tissue or phantom, came in contact with the rigid surface underneath the tissue/phantom, and then buckled. No probes that penetrated the surface of the tissue or phantom failed to reach the rigid underlying surface. The insertion force was defined as the peak force in the recorded profile during penetration of the tissue but before contact with the rigid surface. Buckling force was defined as the peak force generated once the sample came in contact with the rigid surface. In general, forces for probes that buckled during penetration of the agarose phantom and/or brain tissue were below the limit of detection for the transducer (0.1 mN).

The insertion and buckling tests were performed with either uncoated copper wire, coated or uncoated SU-8 probes, or coated or uncoated parylene C probes. Initial tests were performed with copper wire with the sole intent of providing data to validate simulation results. Three different diameters (320, 750, and 875 μm) of copper wire were first tested with agarose phantoms. A number of SU-8 and parylene C probes (Table 4-1) were tested in embryonic chick brain tissue. Eight probes were tested in each cohort, and the number of successful insertions was recorded. Four probes were tested in each brain, with a minimum distance of ~ 1 mm between insertion locations to prevent the possibility of insertion in damaged tissue.

Finally, select parylene C and SU-8 probe designs were tested in rat brain tissue (Table 4-2). We purposely selected a range of probe and coating designs for insertion into rat tissue that were expected to all fail (all fabricated probes fail to insert), all succeed (all fabricated probes successfully insert), or demonstrate a mixture of failure and success (some but not all fabricated probes successfully insert). These expectations were based on

model predictions for insertion and buckling forces following model validation against the agarose and chick tissue experimental data. Twelve probes were tested in each cohort, and the number of successful insertions was recorded. All tests were completed within an hour post sacrifice to prevent any substantial change to the *ex vivo* brain's material properties (Prange & Margulies, 2002). The minimum distance between insertion locations within the same brain was ~1 mm.

Finite Element Analysis: Probe mechanics were simulated in ABAQUS 6.10 (Simulia).

Two models were developed: one to simulate buckling of uncoated and coated probes, and the other to simulate insertion into a tissue phantom.

Probes and coatings with varying design parameters (see Table 4-3 for a full list) were generated and meshed with 8-node, reduced-integration (C3D8R) elements. Mesh size was uniform for the probe (10 μ m), and coating (5 μ m). The probes were completely coupled to the coating by specifying a tied constraint between contacting surfaces. To validate the model, probes were modeled as one of three different materials to match buckling and insertion experiments: copper, SU-8 photoresist, and parylene C. For each material, we used the flexural modulus. With the exception of the flexural moduli for SU-8 and parylene C, values for material properties were obtained from the literature: copper ($E = 110$ GPa, $\rho = 8960$ kg/m³, $\nu = 0.36$), SU-8 photoresist ($E = 2.4$ GPa, $\rho = 1190$ kg/m³, $\nu = 0.32$), or parylene C ($E = 5.6$ MPa, $\rho = 1289$ kg/m³, $\nu = 0.45$) (Spratley et al. 2007, Hopcroft et al. 2003, Rizzi et al. 2013, Chung & Allan 2005, Sim et al. 2005, Kalpakjian & Schmid 2006). The tyrosine polycarbonate coating was modeled using material properties from previous characterizations ($E = 1.9$ GPa, $\rho = 1290$ kg/m³, $\nu = 0.42$) (Lewitus et al. 2011).

To determine the flexural modulus experimentally for SU-8 photoresist and parylene C, strips of varying dimensions for SU-8 ($0.5\text{--}2\text{ cm} \times 500\text{ }\mu\text{m} \times 20\text{ }\mu\text{m}$), and parylene C ($1\text{--}3\text{ cm} \times 1\text{ cm} \times 20\text{ }\mu\text{m}$) were clamped at one end and allowed to deform under their own weight in cantilever bending. Digital microcalipers were used to measure the maximum deflection. Stiffness was calculated by using the beam deflection equation (Goldstein & Salcman 1973):

$$E = \frac{qL^4}{8I\delta_{max}}$$

where q is the weight per unit length of the strip; L is the length of the strip; δ_{max} is the maximum deflection of the strip; I is the area moment of inertia of the cross-section of the strip; and E is the flexural modulus. Images of the bending profile were captured and examined to ensure that appropriate bending behavior was observed (Figure 4-2).

Buckling Model: A linear buckling analysis was performed in ABAQUS to identify the force required to initiate buckling. Contour maps were generated to evaluate force distributions along the probe and coating. The buckling force for each model execution was determined by calculating the mean maximum force of the nodes in the probe and coating.

Insertion Model: Probe insertion into brain tissue was modeled with a dynamic, explicit analysis in ABAQUS. Agarose and brain tissue were modeled as hyperelastic materials using Ogden material parameters adapted from the literature (Normand et al. 2000, El Saeyd et al. 2008) with C3D8R elements and adaptive meshing. To emulate probe penetration, elements that exceeded a shear strain of 0.05 were deleted from the mesh

prior to the next increment in time. This value was selected based on preliminary results of insertion tests, where the threshold value for element deletion in our simulation was modified until predicted insertion forces matched experimental results in insertion tests with the agarose phantom and brain tissue. The influence of this value was evaluated with a sensitivity analysis (described below). Infinite elements were used at the edges of the tissue to simulate the significantly larger size of the tissue with respect to the size of the probe (Figure 4-3A). A convergence study was performed to determine the smallest element size for the region of insertion in the tissue (Figure 4-4). Coated probes were inserted at a rate of 0.1 mm/s into the substrate. The bottom of the tissue was fixed (Figure 4-3A). The top of the probe and coating was only permitted to move in the z-direction. Similar to the buckling case, contour maps were generated to visualize force distributions along the probe and coating. An average insertion force was calculated as the average peak force for the nodes in the coating and probe identified from force vs. time plots.

Sensitivity Analysis: In addition to varying probe geometry, a sensitivity analysis was performed to determine the influence of the parameters used to define material properties and failure thresholds of the hyperelastic brain tissue on the predicted insertion forces. Material properties were adjusted to a maximum of $\pm 10\%$ (Perrson et al. 2010), the coefficient of friction between tissue and coating/probe was varied from 0 to 0.5, and strain thresholds for element deletion were varied from 0.01 (extreme) to 0.25 (conservative) based on information in the literature (Zhang et al. 2004, Cater et al. 2006, Bjornnson et al. 2006). A surface–surface contact algorithm was specified.

To assess sensitivity to coating flaws, a cylindrical void region was introduced in the coating. The radius of the void region was varied by proportion of the coating thickness, from 5% to 100% of the coating thickness. Four coating thicknesses were modeled (50, 75, 100, and 200 μm). The percentage change in insertion and buckling forces relative to simulations with a non-defective coating was calculated.

Each model was executed on a *Lenovo Z580* (Intel[®] Core[™] i5-3210M CPU @ 2.50 GHz; 6 GB RAM) or a *Lenovo Y510* (Intel[®] Dual Core[™] 2.81 GHz; 4 GB RAM). A single design simulation took approximately 7–12 min to execute depending on the size of probe/coating. Simulations were run in parallel. A total of about 28,000 simulations were executed.

Data Interpretation: To provide a performance metric for the simulation results, the ratio of the predicted buckling force to the predicted insertion force was determined for each simulation. We termed this ratio the “safety factor” for that particular design. A probe design would have a safety factor of 1 if the predicted buckling force equaled the predicted insertion force. To assess the influence of each parameter on performance, we designed a graphical user interface in MATLAB to generate safety factor probability maps. Model results for varying parameters (outlined in Table 4-3, column: “Range modeled”) were tabulated and read by the script. Interpolation methods were used to compute gaps in values, and color maps that plotted two parameters against each other were generated.

In addition to providing a visual assessment of performance, the color maps were also quantitatively assessed using three statistical measures—kurtosis, variance, and

skewness—to draw numerical comparisons between pairs of parameters. Kurtosis indicates the “peakedness”, or sharpness of the peak in the distribution. Color maps with high kurtosis indicate that there is a small optimal design region for successful insertion that falls rapidly when deviated from in either direction. Lower values of kurtosis suggest that the peak is more spread, and there is no clear delineation between failure and guaranteed insertion. Variance provides a measure of how quickly the likelihood of insertion increases or decreases along changes in a design parameter, which loosely allows comparisons of the importance between the two parameters from the map on insertion potential. Skewness measures whether a parameter positively or negatively influences insertion potential. Distributions with a positive skew (right-tailed) suggest that increasing the design parameter negatively influences insertion potential. Conversely, a negative skew (left-tailed) implies increasing the value of the parameter improves insertion capability. In addition, multi-variable regression analysis was used to quantitatively assess the influence of each parameter on the safety factor.

Results

Model and Fabrication Comparisons: Figure 4-3B, and Figure 4-3C shows a side-by-side comparison of the simulated coated probe and a scanning electron microscope image of a representative coated probe. Mechanical similarities between simulated and fabricated coated probes were corroborated by the comparable insertion profiles we observed, as indicated in Figure 4-5A. Convergence studies shown in Figure 4-4 demonstrated that a minimum element size of 10 μ m was necessary for insertion force values to converge.

Insertion and Buckling Tests: Insertion tests with copper wire in agarose were used to validate the FE models of buckling and insertion. Figures 4-6A and 4-6B demonstrates the correlations between measured and model-predicted forces for the insertion and buckling cases, respectively. There was strong agreement between model and experimental results ($R^2_{\text{insertion}} = 0.975$, $R^2_{\text{buckling}} = 0.878$).

The next sets of tests were conducted with a selection of coated and uncoated SU-8 and parylene C probes in embryonic chick brain tissue. Figures 4-6C, and 4-6D shows similar plots of measured force against model predicted forces, demonstrating strong agreement between model and experimental results ($R^2_{\text{insertion}} = 0.967$, $R^2_{\text{buckling}} = 0.883$). Uncoated SU-8 probes successfully inserted for both of the dimensions tested (320 μ m \times 5 μ m and 320 μ m \times 20 μ m). None of the uncoated parylene C probes successfully inserted. When parylene C probes were coated, there was a significant reduction in the failure rates. For example, a 50 μ m \times 50 μ m coating on the 20 μ m \times 5 μ m parylene C probe reduced the

failure rate by 50%, and a larger, $50\ \mu\text{m} \times 100\ \mu\text{m}$ coating reduced it by another 37.5%.

Every coated SU-8 probe inserted successfully without buckling.

Following tests on embryonic chick brain tissue, we selected probe designs for insertion tests in *ex vivo* rat brain based on their likelihood of failure as predicted by simulation results. Figure 4-6B shows a plot of buckling force vs. insertion force for the selection of coated and uncoated probes tested. Similar to the chick brain tests, all of the uncoated parylene C probes buckled during insertion. A $100\ \mu\text{m} \times 100\ \mu\text{m}$ coating was the minimum needed to ensure a 100% successful insertion rate, with varying degrees of success with smaller coatings. A $50\ \mu\text{m} \times 100\ \mu\text{m}$, which was the smallest coating tested for the parylene C probes, amounted to a 62.5% success rate.

Model Results: Figure 4-5 displays a representative plot of force during insertion for a $75\ \mu\text{m} \times 100\ \mu\text{m}$ coated SU-8 probe from experiment and simulation. Overall, predicted values for insertion forces were within 10.4% of experimental values. Simulated force profiles strongly matched experimental results for insertion tests. Force distributions for each of the models showed that the coating experienced the majority of the load during insertion. Force was primarily distributed on the bottom of the probe and coating once the sample penetrated the tissue. Based on contour plots, the sides of the coating in contact with the tissue experienced frictional forces about an order of magnitude smaller than that experienced at the bottom of the probe and coating. To assess the effect of friction on insertion forces, we adjusted the coefficient of friction from 0 to 0.5 (Wu et al 2004). While there was no appreciable effect on the insertion force ($\Delta F_{\text{max}} = +6.2\%$), frictional force experienced by the sides of the coating increased by 36%. In all cases, the

maximum frictional force was still an order of magnitude below the measured insertion force (Frictional force = $\sim 10^{-4}$ N).

We performed a sensitivity analysis on the hyperelastic parameters that defined the mechanical properties of the tissue in our model by measuring the change in insertion force with each varied parameter. A 10% change in the bulk modulus, κ , resulted in the most drastic change to predicted insertion force (from 1.19 mN to 5.54 mN for the $75 \mu\text{m} \times 100 \mu\text{m}$ coating). We also evaluated the influence of our shear strain threshold for element deletion by varying the threshold from 0.01 to 0.25. Our default threshold value was 0.05. With this range of strain threshold values, the insertion forces varied from -4% to +12% of the insertion force from simulations with the default threshold value (Figure 4-5C).

Model Predictions for Probe Performance: Model predictions for insertion and

buckling force were tabulated and processed. Maximum buckling force predicted was 1140N when coating dimensions of 2mm x 350 μm were modeled. Minimum predicted buckling force was

1.66×10^{-7} N for the uncoated parylene C probes (20 x 5 μm). Buckling force was consistently lowest for uncoated probes. Largest insertion force predicted was 0.198N for a 350x350 μm coated probe. Insertion force was consistently lowest for uncoated probes. Our model predicted little change in insertion force when angle of insertion and length of the probe/coating combination was changed

Parallel examination of the insertion and buckling forces from the parametric simulations allowed predictions of probe performance for various conditions. In ideal circumstances,

a safety factor above one—*i.e.*, the predicted force required for insertion is less than that required for buckling—would correspond to successful insertion experimentally.

As shown in Figure 4-7A, we found a strong sigmoidal relationship between probe success rate and the safety factor. We fit a logistic equation to estimate the expected success rate as a function of safety factor, which allowed us to directly link model predictions to the probe performance in an experimental setting.

$$\text{Percent of inserted probes} = \frac{1}{1 + 16e^{-2(S_f)}}$$

Using this relationship, we assessed the impact of each of the probe specifications on insertion potential with parametric simulations. The range of values for each parameter was based on design constraints of the physical probe and coating procedure: probes could be fabricated with lengths from 0.5 mm to 5 mm, and coated with polymer to a thickness of 0 μm (uncoated) to 350 μm on each side, defining this range as our design space with respect to length and coating thickness, respectively. The safety factor for individual pairs of parameters (defined as ρ_1 and ρ_2) was then plotted against each other to map out how the insertion probability changes with design. Figures 4-8, 4-9, and 4-10 depict probability color maps of how changing coating thickness, probe thickness, and cross-sectional profile with other geometric and material parameters affect insertion potential respectively.

The color maps provided a visual representation of insertion probability. To evaluate the importance of the different design parameters and other variables, we calculated the bivariate kurtosis, variance, and skewness of each probability distribution map. Each

color map generated a three-dimensional array of values, which prevented the calculation of a single statistic per color map. To determine a single value for each statistic for a given color map, we calculated the kurtosis, variance, and skewness for each 2-D distribution generated along ρ_1 , for a fixed value of ρ_2 . This was repeated for all the values of ρ_2 , and the results were averaged to give a single statistic for a given pair of design parameters. For the regime of coated probes, our comparison of coating aspect ratio vs. coating thickness generated the highest kurtosis ($\beta_{kurt} = 8.73$), and skewness ($\alpha_{skew} = -2.71$). The color map for this pair of parameters is shown in Figure 4-7E.

Visually, the high kurtosis is represented by the marked delineation between probe failure and successful insertion, which occurs at approximately 20 μm coating thickness. The relatively large value for skewness is represented by the 100% probable insertion predicted in the regions to the right of the narrow transition region. The highest variance calculated was for the comparison of probe length and coating size ($\sigma^2 = 0.1089$).

When we included uncoated probes in our analysis, the highest kurtosis and skewness were found to be exhibited with uncoated probe width vs. probe length ($\beta_{kurt} = 38.9$, $\alpha_{skew} = 7.13$). The minimum length for an uncoated parylene C probe to reach a reasonable probability of successful insertion was 200 μm , which would not penetrate deep enough into tissue to obtain useful signal. Similar results were seen for other pairs of parameters we plotted, as seen in Figure 7, demonstrating that uncoated probe designs that were predicted to insert into tissue were either outside of the fabrication limits, or surmised to be too big to mitigate the chronic response.

Multi-variable linear regression was used to quantitatively determine the individual effect of each parameter on the safety factor. Results are provided in Table 4-4 with the design

parameters listed in descending order of significance based on the p value calculated in our regression model. The safety factor was most dependent on probe length and coating thickness.

Discussion

We developed and validated a finite element model to design and evaluate the mechanical performance of flexible neural probes that are coated with a polymer to enable insertion into brain tissue without buckling. For a given probe design under ideal, theoretical conditions, when the insertion force exceeds the buckling force, we expect that design to fail. By correlating actual failure rates to the ratio of buckling-to-insertion force, we defined a safety factor that was related to the probability of successful insertion. We are using this design tool to assist in our development of smaller, ultra-flexible probes to minimize trauma but maximize recording area (Lo et al. 2015).

Experimentally, we used three materials that provided a wide range of mechanical properties and insertion potential to assist in model design: copper, SU-8 photoresist, and parylene C. Copper is 100 times stiffer than SU-8 and SU-8 is about 1000 times stiffer than parylene C. Copper specimens inserted successfully at all diameters tested.

Uncoated SU-8 probes inserted successfully for sizes as small as $320\text{ }\mu\text{m} \times 5\text{ }\mu\text{m}$.

Uncoated parylene C probes failed to insert at the lengths we experimentally tested.

When a stiff coating was added to the flexible parylene C probe, the coating effectively shielded the probe and, if thick enough, allowed insertion before buckling. We observed that a minimum of $75\text{ }\mu\text{m}$ was necessary for 100% successful insertion for the probe lengths and geometries we were targeting. Varying coating stiffness in our model resulted in changes to the buckling force, but little change to insertion force. As our polymer coating is water-resorbable, there is potential for the polymer stiffness to decrease during insertion. We examined a smaller range of stiffnesses (0.5-2GPa) to account for this possible degradation during insertion. The polymer stiffness under dry conditions is about

1.8GPa. With exposure to a high moisture environment, stiffness decreases 20%, and coating thickness decreases, eventually being completely degraded in 8 hours (D.

Lewitus et al., 2011) Model results suggested that while a 75 μ m thick coating would allow successful insertion given that the probe is immediately inserted, a wiser course of action would be to employ a slightly thicker coating to account for possible degradation during the insertion process.

The peak force experienced by the probe occurred immediately before penetrating the brain or brain surrogate, assuming that the probe did not buckle, which was captured in our FEM of penetration into brain tissue. Modeling tissue mechanics due to penetration is inherently complex due to soft tissue's non-linear, anisotropic nature, and the initiation of failure within the tissue, which often results in non-convergent solutions (Abolhassani et al. 2007). To model probe penetration into brain tissue, we used element deletion, which removes elements after a user-specified stress or strain threshold is reached. To estimate this threshold, we used results from our experimental validation in the agarose phantom and chick embryo brain tissue to define a preliminary strain threshold. We then adjusted the threshold strain in our simulations until the predicted insertion force generally agreed with experimental values. Our final threshold value fell with the range of failure strains reported in the literature (Zhang et al. 2004, Cater et al. 2006), including strains measured during insertion of neural electrodes (Bjornsson et al. 2006).

The insertion force is thus directly dependent on this element deletion criterion, and consequently, so is the safety factor. Using our criterion for element deletion, we found that a safety factor of 3–3.5 corresponded to a probe design which inserted successfully 100% of the time. Lower safety factors corresponded to a lower success rate, and a safety

factor of 1.35 indicated a 50/50 ratio of success and failure. Failure properties for CNS tissue vary across the literature (Zhang et al. 2004, Bain et al. 2000, LaPlaca et al. 2007), and our adoption of a threshold of 0.05 should not be viewed as a prediction of the failure properties, but rather a means to an end. If we used a different value for element deletion, the shape of the relationship between the computationally derived safety factor and the experimentally determined probability of successful insertion would not change significantly, although the value for an appropriate safety factor would change.

Our model results were validated against experimental results, with the predicted insertion and buckling forces within 10% of their experimental values for the designs we tested. Values for insertion force from our experiments were in the same order of magnitude as those seen in the Sridharan study (Sridharan et al. 2015), which used probes of similar dimensions. The dependence of the buckling on probe properties and dimensions were consistent with Euler's equation for buckling. As such, for simple geometries under ideal conditions, the insertion force could potentially be estimated analytically by, for instance, modeling a point force on an elastic half space, and then incorporating a stress or strain threshold based on experimental data.

However, the likelihood of probe insertion success can be influenced by stress concentrations, positioning errors, and non-uniform geometries. These features can all be easily implemented into the FEM to assess their role in influencing insertion likelihood. For example, we examined the influence of bevel angle on insertion and buckling. The model predicted that a bevel angle of at least 60° is required to appreciably reduce the insertion force. The FEM also allows investigations of design and manufacturing concerns. During testing, some of the coated parylene C probes that were predicted to

succeed based on our model failed to insert. Among the possibilities for this failure include defects in the probe, non-uniform coating distribution, or swelling in the coating due to water resorption. Using our model, we introduced a cylindrical void into the coating to simulate a coating defect and determined the changes to safety factor as a result. Simulation results showed that with a void diameter of 50 μm , the maximum decrease in safety factor was about 15% (Figure 4-11) when the defect occurred at the beveled tip of the coating. We observed a clear trend where the change in safety factor increased with growing void size. The variation in safety factor with defect size indicates that even at a safety factor of 1.35, where the logistic curve between insertion likelihood and safety factor is steepest, the probability of insertion changes at most ~5%.

Ultimately, we believe that the safety factor provides a useful metric driving design decisions especially in light of other variables. For example, increasing the stiffness of the tissue increased the insertion force required to reach the strain threshold for penetration. From a designer standpoint, a thicker coating or smaller length would be necessary to meet the necessary safety factor.

Probability color maps, which denoted how the likelihood of insertion varied with changes in pairs of parameters, allowed us to qualitatively assess the influence of each device feature on insertion success. We analyzed eight design parameters in this study, which corresponded to 56 pairs, or 28 color maps. Figure 4-8 shows probability color maps for a number of parameters compared with coating thickness. Including features such as coating non-uniformity, or different probe geometries would serve to exponentially increase the number of color maps electrode designers would need to review. This provided the rationale to determine how to quantitatively rank the role of

each design parameter on safety factor. To quantitatively make this assessment, we used two sets of measures: (1) pair-wise statistical comparisons between parameters; and (2) multi-variable regression. We compared pairs of parameters by calculating the bivariate kurtosis, variance, and skewness of our generated probability surface maps. Designers can use the values from each statistic to rank which design features to focus on, as well as which pair of features generates the greatest “tradeoff” in insertion capability.

We consistently observed that kurtosis was highest for pairs of parameters in uncoated probes compared to coated probes. Figure 4-9 shows color maps and respective statistics for uncoated probe width plotted against various design parameters. Uncoated and coated probes, which had a high kurtosis, delineated a more sudden transition from a region of failure to success. For instance, in the case of probe length *vs.* uncoated probe width (Figure 4-9A), there is a clear boundary between 0.2 and 0.8 mm where insertion potential quickly dropped as length increased. This ‘threshold’ length remained through the range of probe widths that were modeled (up to 350 μ m). In contrast, a low kurtosis, such as Figure 4-9C (probe stiffness *vs.* coating thickness), indicates a broader “peak”, where the transition from failure to success was gradual. Variance measured how quickly insertion potential increased (or decreased) with parameter change. Coating thickness *vs.* probe length was calculated to produce the highest variance (Figure 4-8A for color map). This matched expectations as both these variables directly influenced buckling force, and coating thickness in particular, directly influenced insertion force as suggested by theoretical calculations and previous indentation studies (Sharp et al. 2011). This is reflected in the color map by the wide variation in insertion potential, where the upper left quadrant of the color map is primarily red (failure), and the remainder of the map is

blue (success). Skewness measured whether the potential for insertion increased or decreased with changes in the pair of parameters. We found skewness was most negative for probe width *vs.* probe length (Figure 4-9A), suggesting increasing width increased insertion potential.

Individually, each statistic does not reflect the general shape of the color probability map. The high kurtosis we observed for probe length *vs.* probe width, for example, does not indicate whether increasing probe width would increase or decrease insertion capability, nor does it indicate how quickly it would change. When these statistics are taken collectively, however, we can quantify the influence between the pair of parameters on each other, as well as whether the pair has a positive or negative impact on each other, offering the means to rank pairs of design parameters. High kurtosis values calculated for coating aspect ratio *vs.* coating thickness tell designers that past a coating thickness of 30 μm , any increases in aspect ratio will marginally increase the probability of insertion (until it reaches a probability of 1 after which it remains there). The corresponding variance, which was calculated to be lowest in the cohort of coated probes, informs designers that there are no sudden rises or drops in probability, and the strongly negative skew suggests that increasing thickness favors insertion potential.

In contrast to the statistical measures above, which can only be used for pairs of parameters, multi-variable regressions provide a method to assess the role of each design parameter individually against all other parameters. Multi-variable regressions confirmed that probe length and coating thickness have the most significant effects on safety factor (Table 4-3), and thus should be the first features to consider in design. This was confirmed by color maps where probe length was modified against coating geometry and

coating material properties (Figure 4-10). It is important to note that these regressions and color map analyses are limited to the range of the parameters we examined. We selected the range based on both the limits of the fabrication process for our coated ultra-flexible probes (Lo et al. 2015), as well as the feasibility of their use. Although an uncoated parylene C probe 200 μm in length is predicted to insert successfully, it will not be effective in recording because it will not be able to reach target tissues. Increasing the range of values our parameters can take would inevitably change the values predicted by our regression, though we expect trends to be similar (e.g., probe length and coating thickness would still impact safety factor the most).

Although our model successfully simulates and captures insertion potential for different designs of coated probes, it does not predict the specific effects on the chronic response. We are extending our model to predict the interfacial stresses between the already-inserted probe and tissue and how that changes with probe geometry and material, in order to equate stress values with astrocyte activation. With that said, there is good evidence that smaller, flexible neural implants mitigate the acute and chronic injury, and thus, are able to record signals for an extended period of time. Smaller probes reduce the insertion force generated, which theory and our model confirms, and smaller probes have been equated to less tissue damage, and less acute reactive tissue (Szarowski et al. 2003). Flexible probes are predicted to reduce strains experienced by surrounding brain tissue due to micromotions, which have been implicated in the long-term chronic response (Zhu et al. 2011). Decreasing probe size and stiffness increases the likelihood of probe mechanical failure. However, clinicians may accept the increased chance of failure if it improves the probe's long-term recording capability. As a hypothetical example, it may

be prudent to accept an 80% success rate if it enables the probe to maintain recording fidelity for twice the length of time as the 100% success rate probe. Neural probe designers can utilize our model to design and fabricate probes that fit the criteria, eliminating the guesswork and lengthy fabrication time required to pinpoint those designs which would achieve the necessary result.

References

- Abolhassani, N., Patel, R. V., 2006. Deflection of a flexible needle during insertion into soft tissue. *Conf. Proc. IEEE Eng. Med. Biol. Soc.* 1, 3858–61.
doi:10.1109/IEMBS.2006.259519
- Amiri, S., Fazel-Rezai, R., Asadpour, V., 2013. A review of hybrid brain-computer interface systems. *Adv. Human-Computer ...* 2013.
- Aregueta-Robles, U. a, Woolley, A.J., Poole-Warren, L. a, Lovell, N.H., Green, R. a, 2014. Organic electrode coatings for next-generation neural interfaces. *Front. Neuroeng.* 7, 15. doi:10.3389/fneng.2014.00015
- Bareket-Keren, L., Hanein, Y., 2012. Carbon nanotube-based multi electrode arrays for neuronal interfacing: progress and prospects. *Front. Neural Circuits* 6, 122.
doi:10.3389/fncir.2012.00122
- Biran, R., Martin, D.C., Tresco, P. a, 2005. Neuronal cell loss accompanies the brain tissue response to chronically implanted silicon microelectrode arrays. *Exp. Neurol.* 195, 115–26. doi:10.1016/j.expneurol.2005.04.020
- Cheung, K.C., 2007. Implantable microscale neural interfaces. *Biomed. Microdevices* 9, 923–38. doi:10.1007/s10544-006-9045-z
- Felix, S.H., Shah, K.G., Tolosa, V.M., Sheth, H.J., Tooker, A.C., Delima, T.L., Jadhav, S.P., Frank, L.M., Pannu, S.S., 2013. Insertion of flexible neural probes using rigid stiffeners attached with biodissolvable adhesive. *J. Vis. Exp.* e50609. doi:10.3791/50609
- Foley, C.P., Nishimura, N., Neeves, K.B., Schaffer, C.B., Olbricht, W.L., 2009. Flexible microfluidic devices supported by biodegradable insertion scaffolds for convection-enhanced neural drug delivery. *Biomed. Microdevices* 11, 915–24. doi:10.1007/s10544-009-9308-6
- Hamzavi, N., Tsang, W.M., Shim, V.P.W., 2013. Nonlinear elastic brain tissue model for neural probe-tissue mechanical interaction. 2013 6th Int. IEEE/EMBS Conf. Neural Eng. 1119–1122. doi:10.1109/NER.2013.6696134
- Hamzavi, N., Tsang, W.M., Shim, V.P.W., 2013. Nonlinear Elastic Brain Tissue Model for Neural Probe-Tissue Mechanical Interaction 6–8.
- Hoogerwerf, a C., Wise, K.D., 1994. A three-dimensional microelectrode array for chronic neural recording. *IEEE Trans. Biomed. Eng.* 41, 1136–46.
doi:10.1109/10.335862

- Lewitus, D., Smith, K.L., Shain, W., Kohn, J., 2011. Ultrafast resorbing polymers for use as carriers for cortical neural probes. *Acta Biomater.* 7, 2483–91. doi:10.1016/j.actbio.2011.02.027
- Lewitus, D.Y., Smith, K.L., Shain, W., Bolikal, D., Kohn, J., 2011. The fate of ultrafast degrading polymeric implants in the brain. *Biomaterials* 32, 5543–50. doi:10.1016/j.biomaterials.2011.04.052
- Lind, G., Linsmeier, C.E., Schouenborg, J., 2013. The density difference between tissue and neural probes is a key factor for glial scarring. *Sci. Rep.* 3, 2942. doi:10.1038/srep02942
- Lind, G., Linsmeier, C.E., Thelin, J., Schouenborg, J., 2010. Gelatine-embedded electrodes--a novel biocompatible vehicle allowing implantation of highly flexible microelectrodes. *J. Neural Eng.* 7, 046005. doi:10.1088/1741-2560/7/4/046005
- Lo, M., Wang, S., Singh, S., Damodaran, V.B., Kaplan, H.M., Kohn, J., Shreiber, D.I., Zahn, J.D., 2015. Coating flexible probes with an ultra fast degrading polymer to aid in tissue insertion. *Biomed. Microdevices* 17, 34. doi:10.1007/s10544-015-9927-z
- Mak, J., Wolpaw, J., 2009. Clinical applications of brain-computer interfaces: current state and future prospects. *Biomed. Eng. IEEE Rev.* ... 187–199. doi:10.1109/RBME.2009.2035356.Clinical
- Maynard, E.M., Nordhausen, C.T., Normann, R. a., 1997. The Utah Intracortical Electrode Array: A recording structure for potential brain-computer interfaces. *Electroencephalogr. Clin. Neurophysiol.* 102, 228–239. doi:10.1016/S0013-4694(96)95176-0
- Nicolas-Alonso, L.F., Gomez-Gil, J., 2012. Brain computer interfaces, a review. *Sensors (Basel)*. 12, 1211–79. doi:10.3390/s120201211
- Okamura, AM, Simone C, O.M., 2004. Force modeling for needle insertion into soft tissue. ... , *IEEE Trans.* 51, 1707–1716.
- Polanco, M., Yoon, H., Bawab, S., 2014. Micromotion-induced dynamic effects from a neural probe and brain tissue interface. *J. Micro/Nanolithography, MEMS, MOEMS* 13, 023009. doi:10.1117/1.JMM.13.2.023009
- Polikov, V.S., Tresco, P. a, Reichert, W.M., 2005. Response of brain tissue to chronically implanted neural electrodes. *J. Neurosci. Methods* 148, 1–18. doi:10.1016/j.jneumeth.2005.08.015
- Rousche, P.J., Pellinen, D.S., Member, S., Pivin, D.P., Williams, J.C., Vetter, R.J., Kipke, D.R., 2001. Flexible Polyimide-Based Intracortical Electrode Arrays with Bioactive Capability 48, 361–371.

Stice, P., Muthuswamy, J., 2009. Assessment of gliosis around moveable implants in the brain. *J. Neural Eng.* 6, 046004. doi:10.1088/1741-2560/6/4/046004

Subbaroyan, J., Martin, D.C., Kipke, D.R., 2005. A finite-element model of the mechanical effects of implantable microelectrodes in the cerebral cortex. *J. Neural Eng.* 2, 103–13. doi:10.1088/1741-2560/2/4/006

Szarowski, D., Andersen, M., Retterer, S., 2003. Brain responses to micro-machined silicon devices. *Brain Res.* 983, 23–35.

Turner, J.N., Shain, W., Szarowski, D.H., Andersen, M., Martins, S., Isaacson, M., Craighead, H., 1999. Cerebral astrocyte response to micromachined silicon implants. *Exp. Neurol.* 156, 33–49. doi:10.1006/exnr.1998.6983

Zhong, Y., Bellamkonda, R., 2007. Dexamethasone-coated neural probes elicit attenuated inflammatory response and neuronal loss compared to uncoated neural probes. *Brain Res.* 15–27.

Zhu, R., Huang, G.L., Yoon, H., Smith, C.S., Varadan, V.K., 2011. Biomechanical Strain Analysis at the Interface of Brain and Nanowire Electrodes on a Neural Probe. *J. Nanotechnol. Eng. Med.* 2, 031001. doi:10.1115/1.4005484

Figures:

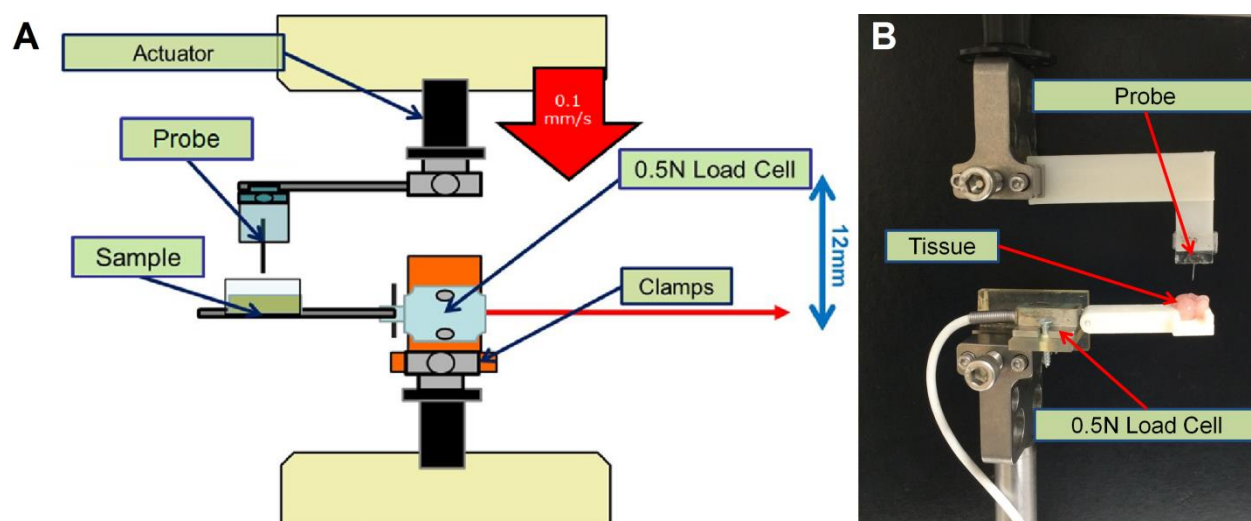


Figure 4-1: (A) Mechanical testing setup to experimentally characterize probe and coating behavior. Probes were fixed on a glass slide and clamped to a rapid-prototype piece, which was clamped to an actuator on a Bose ELF 3200. A 0.5 N load cell was threaded onto a rapid-prototyped piece, which was clamped to the reaction plate of the testing device. A third piece containing a well for the sample (agarose or brain tissue) was pinned to the load cell. (B) Zoomed-in image of the fixed probe and sample of embryonic chick brain tissue.

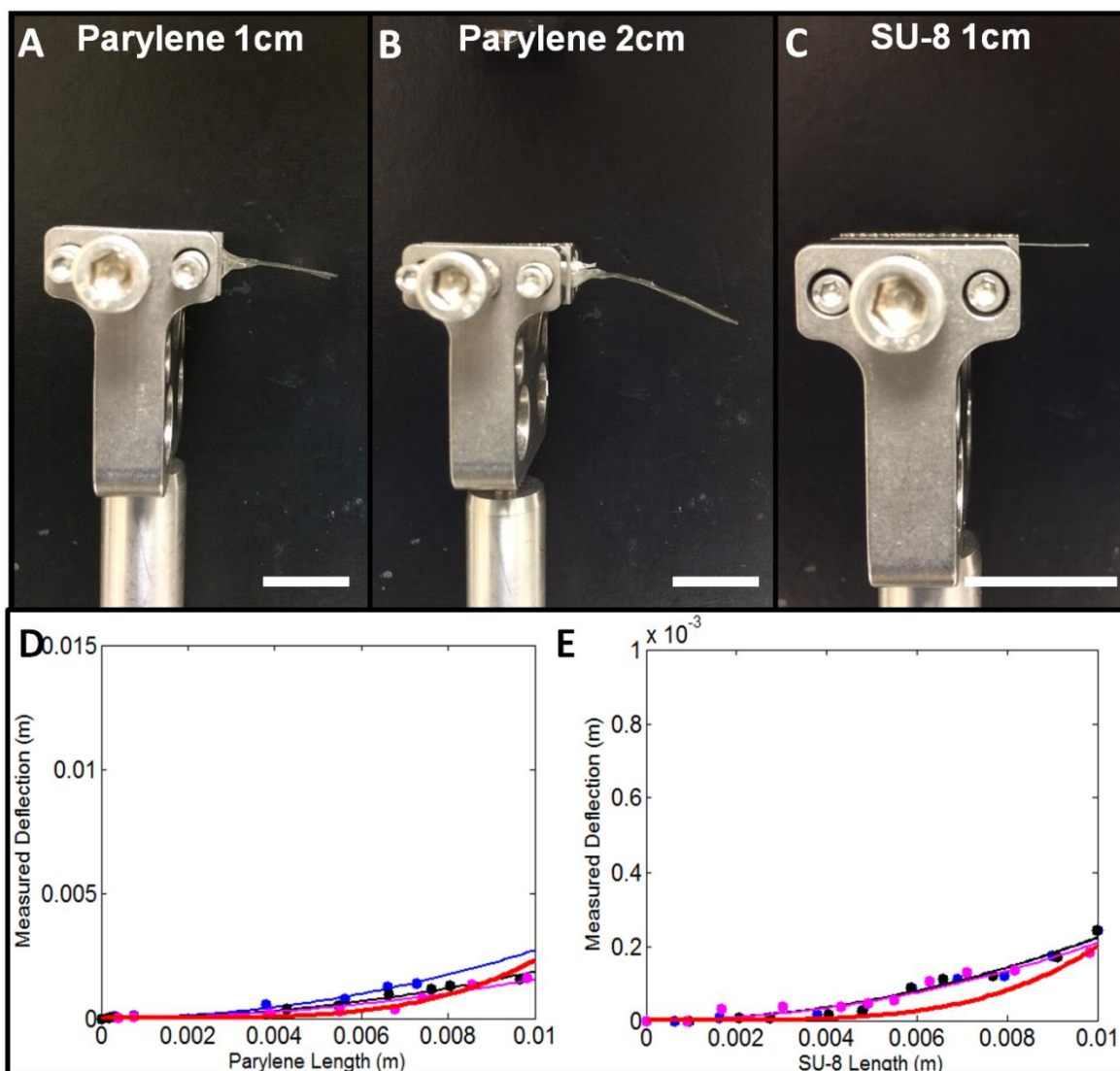


Figure 4-2: (A-C) Representative images of deflection profiles of parylene C and SU-8.

(D&E) Deflection profiles for (D) parylene C and (E) SU-8. Curve fitting was used to fit the image-acquired data to the complete beam deflection equation to extract the flexural Young's modulus. The red curve is the resultant fit when the maximum deflection and corresponding flexural modulus ($E_{\text{Parylene}} = 5.6 \text{ MPa}$, $E_{\text{SU-8}} = 2.4 \text{ GPa}$) were used.

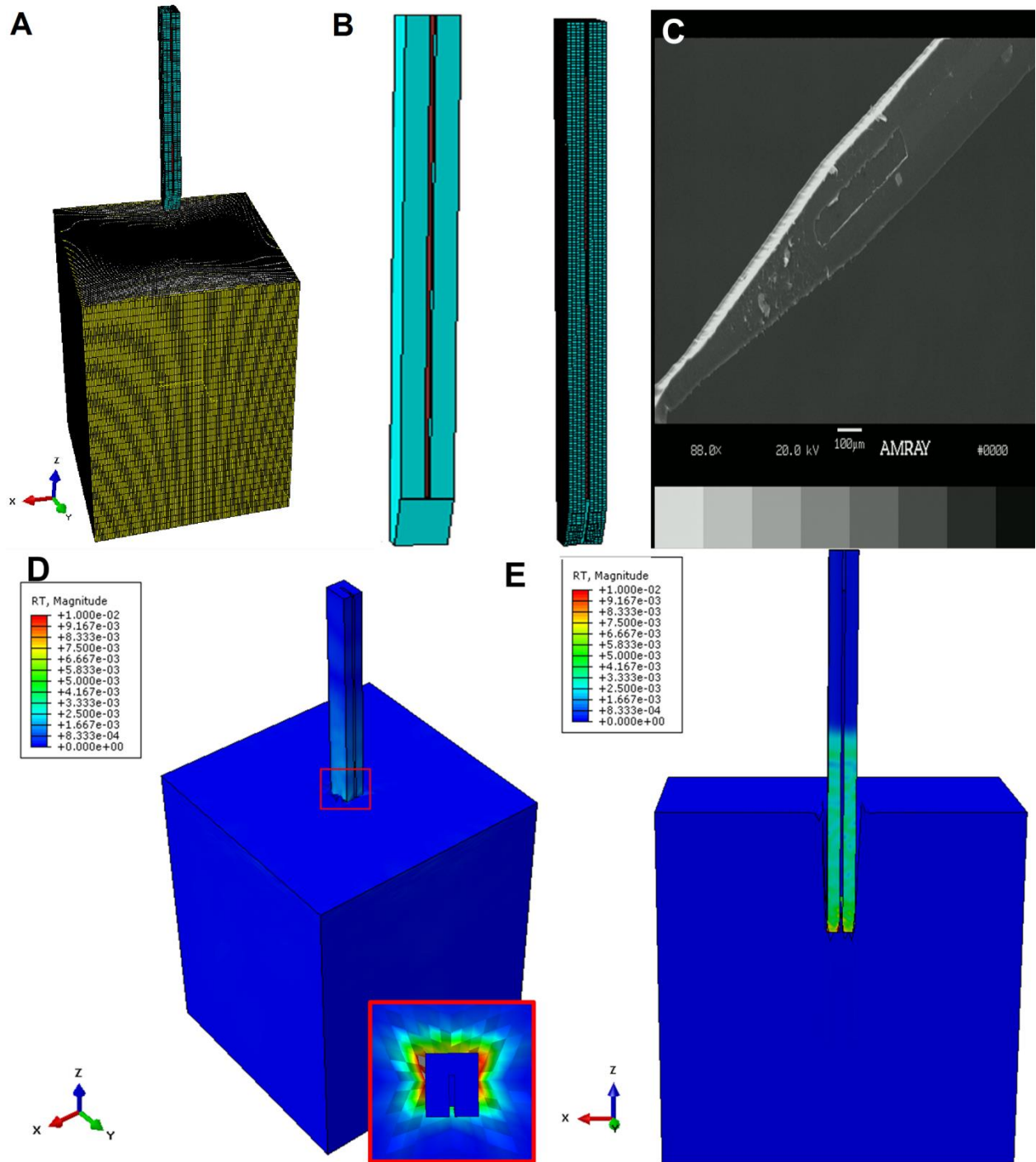


Figure 4-3: (A) Screenshot of Finite Element (FE) model. Stiffness, dimensions, and geometries were varied for the probe (red), beveled coating (light blue), and brain tissue (grey/yellow). The model was executed to simulate insertion of the coated probe into brain tissue. Infinite elements (CIN3D8—yellow) were defined around the edges of the

brain instance to reflect the significantly larger size of the brain relative to the coated probe. The bottom of the instance was fixed with a zero-displacement and zero-rotation constraint. **(B)** A close up of the simulated coated probe before and after meshing; **(C)** a scanning electron microscope image of the coated probe; and **(D)** a screenshot of the inserted probe shortly after penetration. Nodes that experienced force at this step had their maximum force averaged to determine insertion force. The zoomed-in region depicted in the red box shows the contour map of strains experienced on the surface of the brain instance. Elements in grey have reached the failure threshold (0.05) and are deleted in the next step. **(E)** Cut-away of the coated probe one second later than shown in **(D)** insertion, showing that only the coating experiences force during insertion.

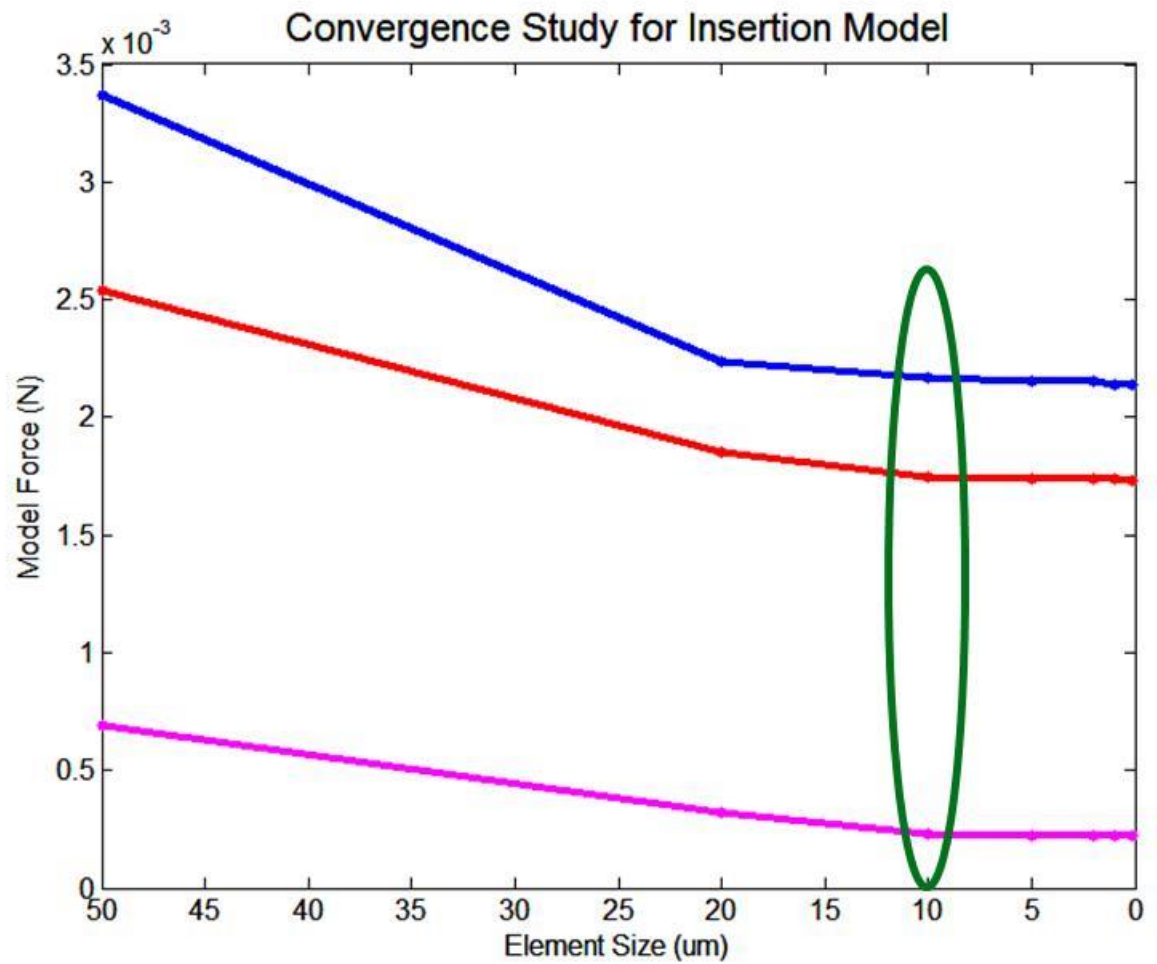


Figure 4-4: Convergence studies were conducted to determine the ideal mesh size that would maintain accuracy while minimizing computational time. An element size of 10 μm was determined to reflect these criteria.

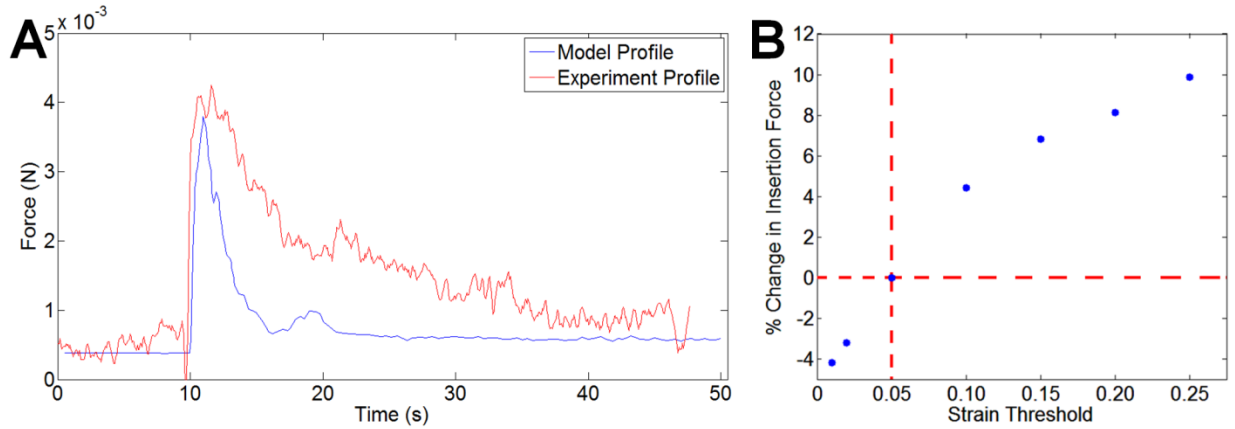


Figure 4-5: Force profile for insertion phase from (A) a representative experiment, and a simulation for a $20\ \mu\text{m} \times 5\ \mu\text{m}$ SU-8 probe with a $75\ \mu\text{m} \times 100\ \mu\text{m}$ coating inserted in agarose phantom. Profiles showed the characteristic peak when the probe first penetrates the tissue phantom. (B) Changing the strain threshold criterion for element deletion changed the resultant predicted insertion force by up to 10% from the chosen value of 0.05.

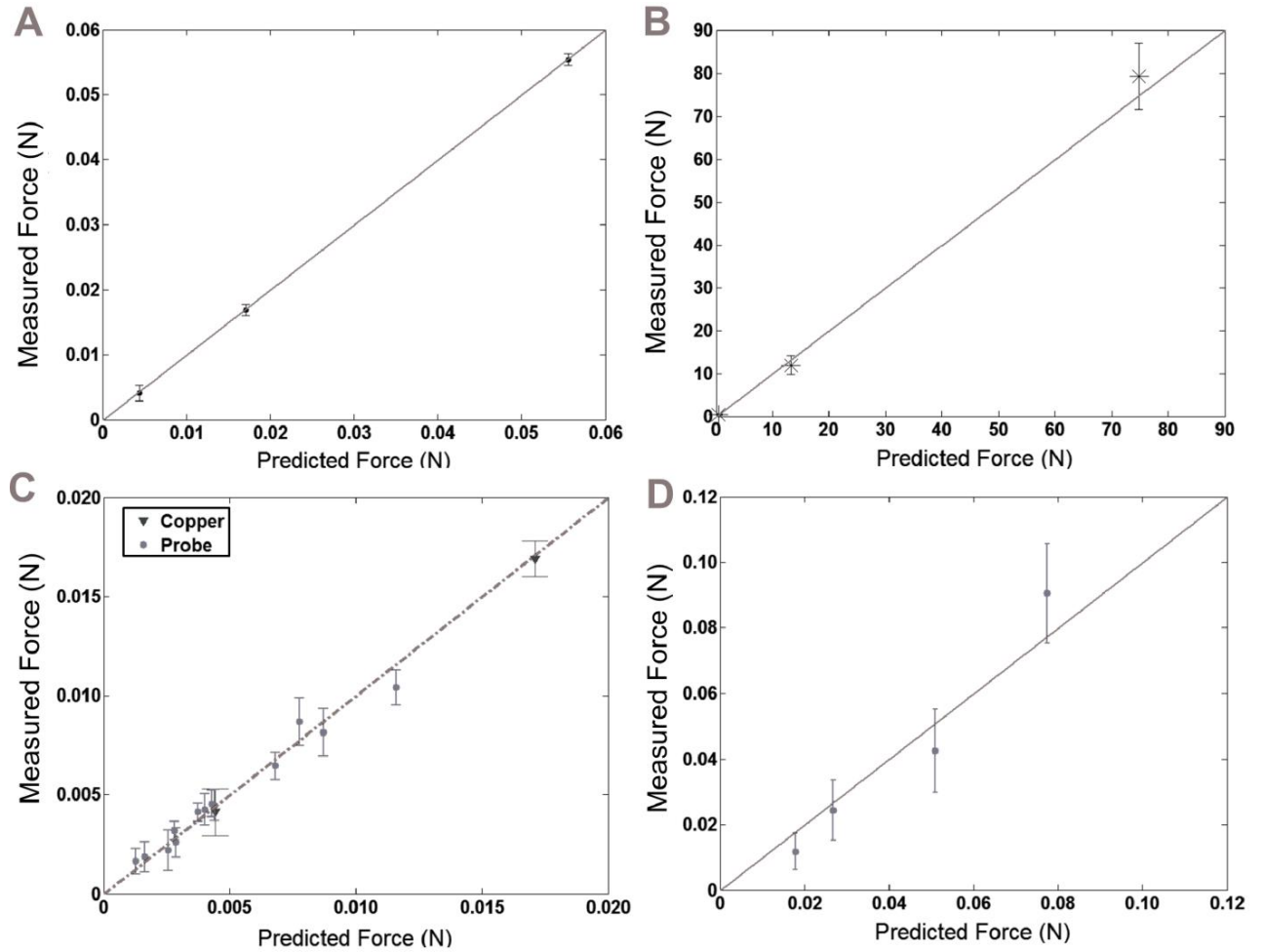


Figure 4-6: Model accuracy was verified by comparing experimental results to model

predictions in same conditions for (A) copper wire insertion into 0.6% agarose gel

($R^2_{\text{insertion}} = 0.967$); (B) copper wire buckling ($R^2_{\text{buckling}} = 0.883$); (C) probe insertion into

E18 embryonic chick brain tissue ($R^2_{\text{insertion}} = 0.975$); and (D) probe buckling ($R^2_{\text{buckling}} =$

0.878).

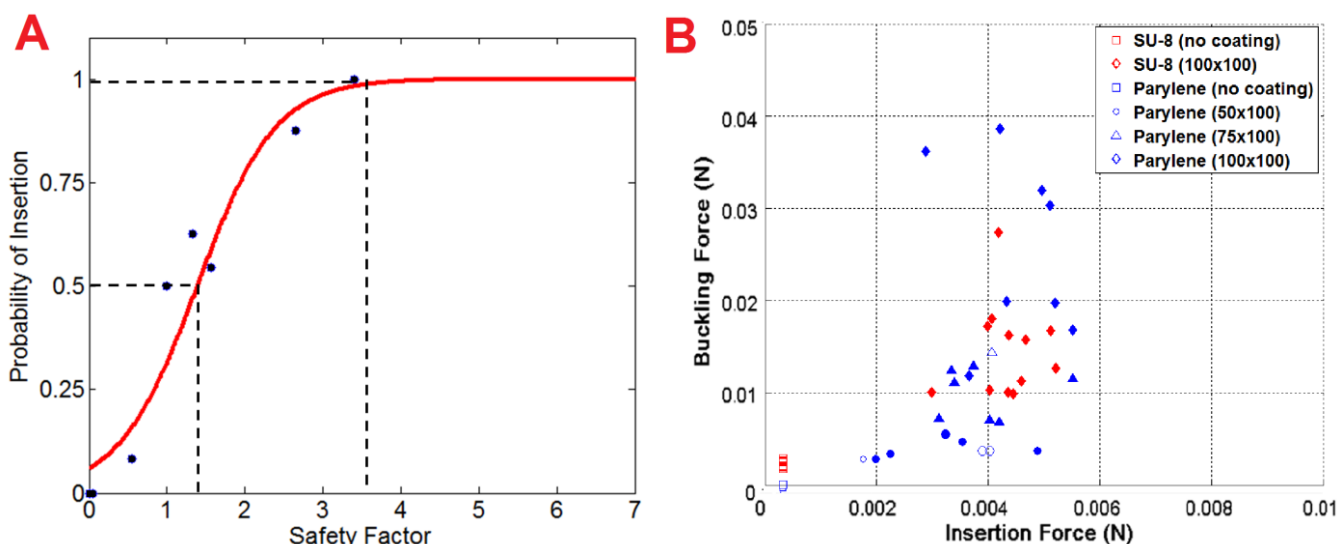


Figure 4-7: (A) Empirical probability of successful insertion vs. the “Safety Factor”.

Each data point represents the number of successfully inserted probes divided by the total number of probes tested in that particular cohort. The data were fit with a sigmoidal function. A safety factor of ~ 1.35 corresponds to a 50% likelihood of insertion. A safety factor of ~ 3.5 corresponds to 100% success rate. (B) Buckling force vs. insertion force for experiments with rat brain tissue. Filled data points correspond to coated probes that inserted successfully, while empty points correspond to probes that failed (lengths in legend in μm).

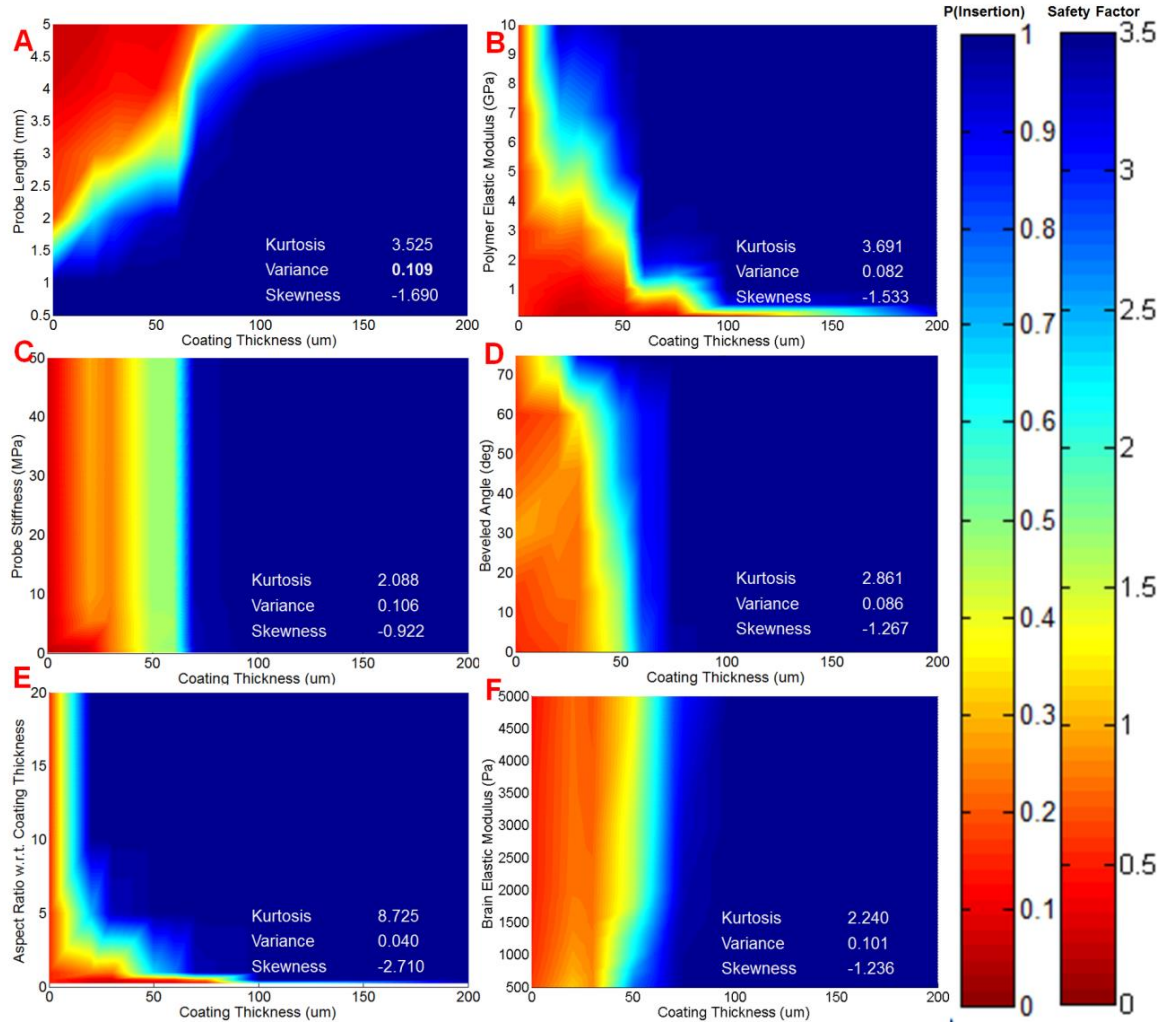


Figure 4-8: Color maps of the probability of successful insertion of coated probes

(Coating Width = $50\mu\text{m}$) for six different parameters with respect to coating thickness (0–200 μm): (A) probe length; (B) polymer stiffness; (C) probe stiffness; (D) bevel angle of coating tip; (E) coating aspect ratio; and (F) brain stiffness. To quantitatively assess and compare pairs of parameters in each color map, we calculated the kurtosis, variance, and skewness of each distribution. The largest variance was calculated for probe length vs. coating thickness. The largest kurtosis and skewness were calculated for aspect ratio vs. coating thickness.

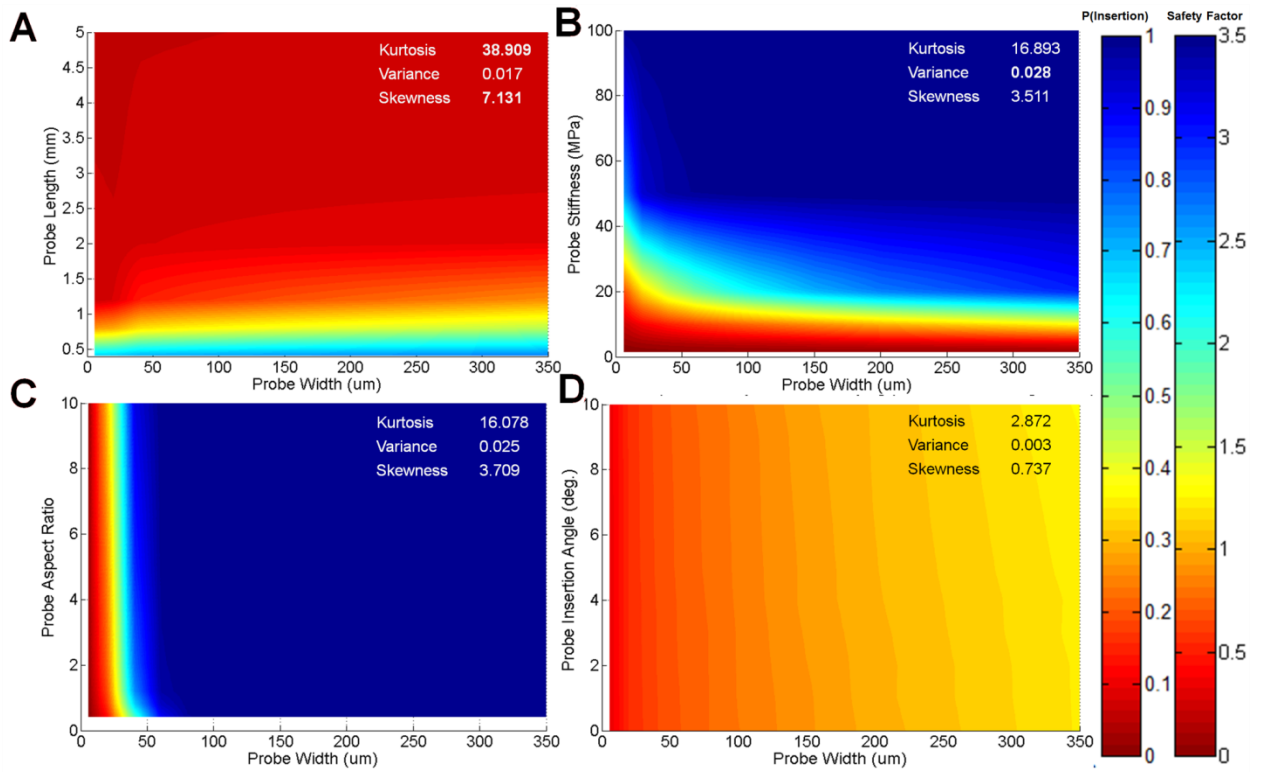


Figure 4-9: Color maps of the probability of successful insertion of uncoated probes for four different parameters with respect to probe width (0–350 μm): **(A)** probe length; **(B)** probe stiffness; **(C)** probe aspect ratio; and **(D)** probe insertion angle. Color maps demonstrated that the regime of successful insertion fell within unfeasible or ineffectual design ranges, confirming the necessity of the coating for probe insertion into brain tissue. Generally, values for kurtosis and skewness calculated from color maps were greater for uncoated probes than coated probes.

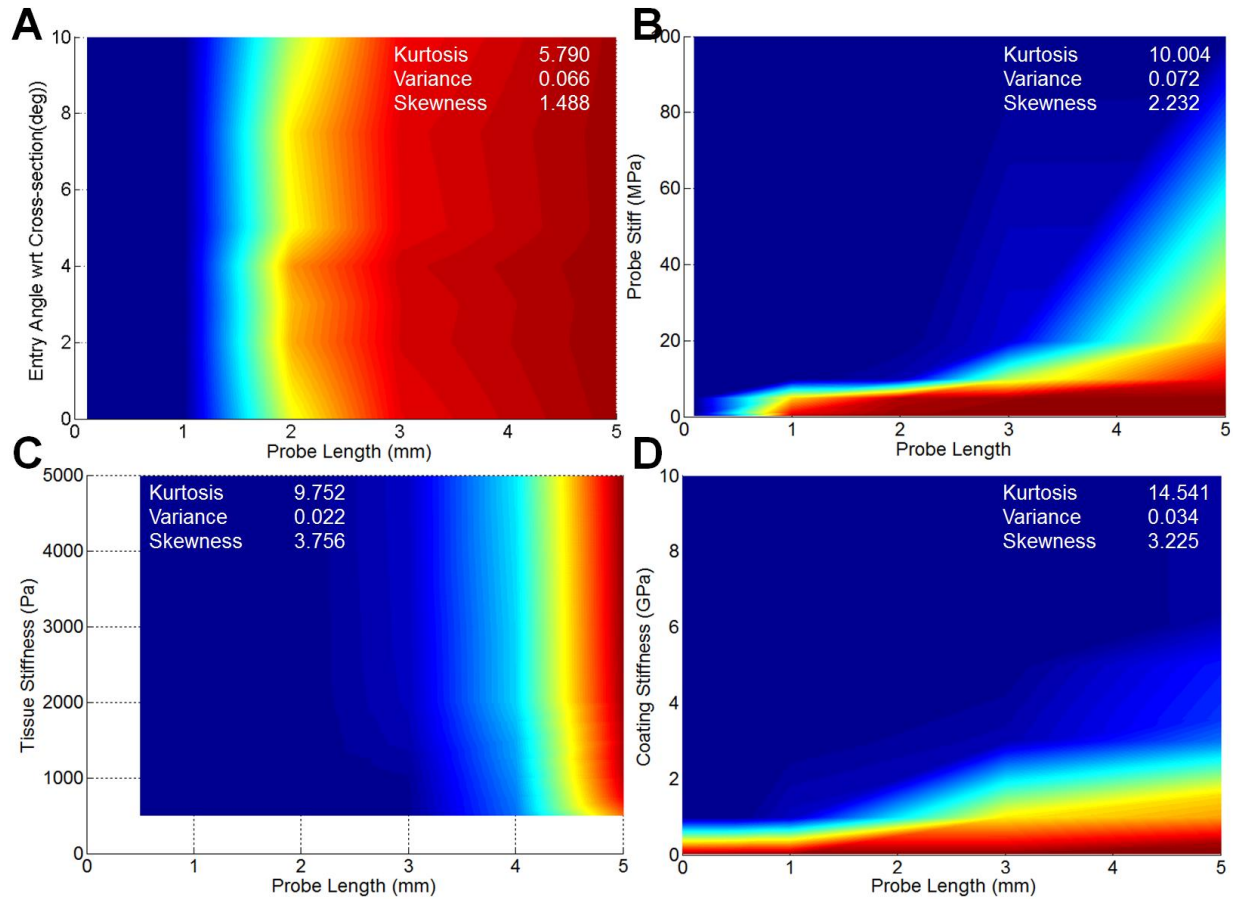


Figure 4-10: Color maps of the probability of successful insertion of (A&B) uncoated and (C&D) coated probes for four different parameters with respect to probe length (0–5 mm): (A) insertion angle for uncoated probes; (B) probe stiffness for uncoated probes; (C) tissue stiffness for coated probes; and (D) coating stiffness for coated probes. In the case of uncoated probes

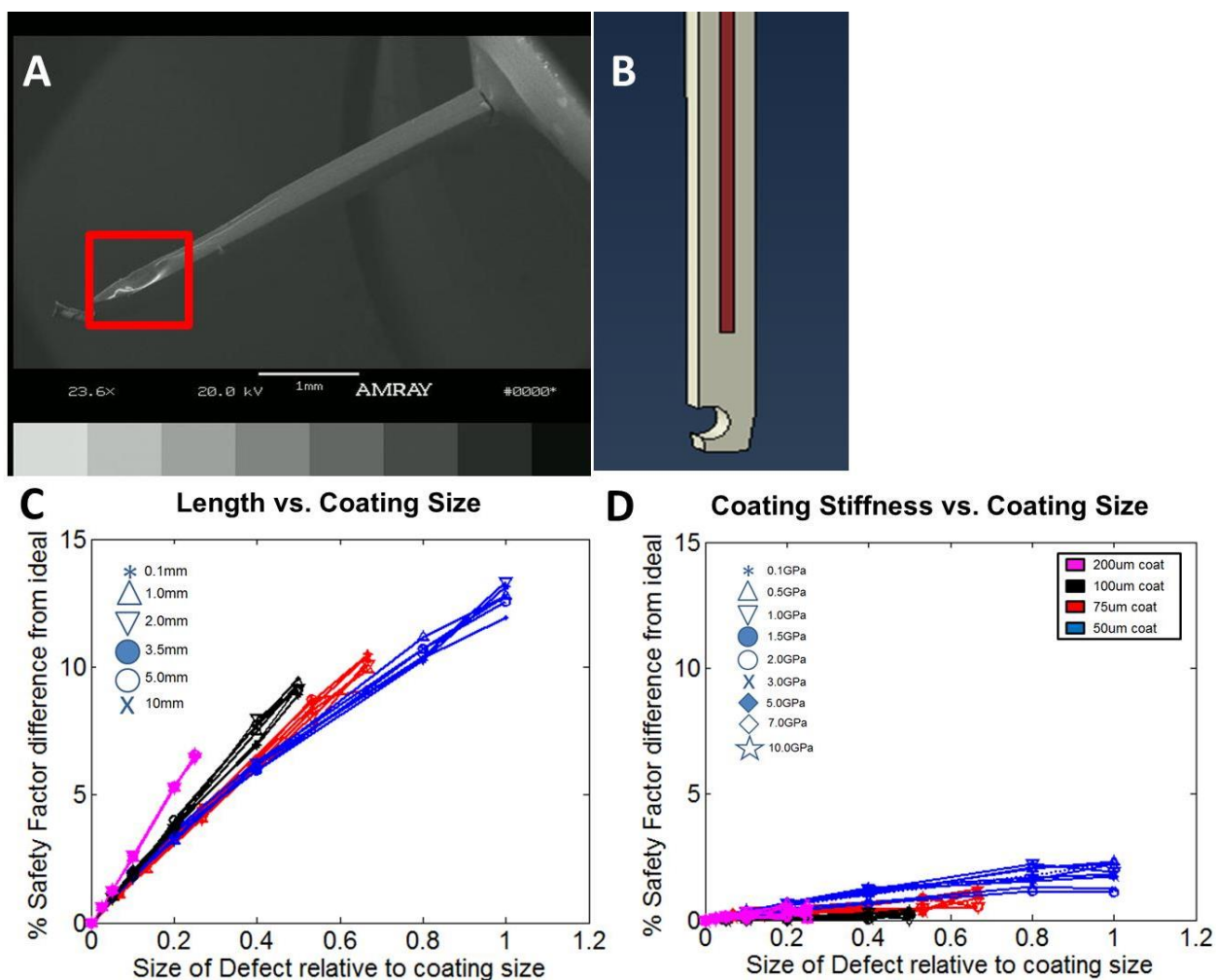


Figure 4-11: (A) Scanning electron microscope (SEM) images of a flawed probe with non-uniform coating. The red box highlights the presence of a divot in the coating. In general, most of these defects occurred at the tip of the probe. (B) The FE simulation was modified to mimic the defect we observed in SEM images. The position and size of the defect was varied to determine changes to safety factor. In general, changes in defect size had a greater impact on safety factor than defect position. (C,D) The percentage difference in safety factor from the ideal (no defect) case with changes in parameter and defect size. The percentage difference in safety factor was plotted against the size of the defect relative to coating size (e.g., $0.25 = 50 \mu\text{m}/200 \mu\text{m}$).

Cohort	Probe Material	Probe Dimensions (μm)	Coating Dimensions (μm)	Total	Pass	Fail	% Success Rate
1	SU-8	$320 \times 5 \times 3500$	-	8	8	0	100.0
2	SU-8	$320 \times 20 \times 3500$	-	8	8	0	100.0
3	SU-8	$320 \times 20 \times 3500$	$50 \times 50 \times 4000$	8	8	0	100.0
4	SU-8	$320 \times 20 \times 3500$	$75 \times 100 \times 4000$	8	8	0	100.0
5	SU-8	$320 \times 20 \times 3500$	$100 \times 100 \times 4000$	8	8	0	100.0
6	Parylene C	$20 \times 5 \times 3500$	-	8	0	8	0.0
7	Parylene C	$100 \times 5 \times 3500$	-	8	0	8	0.0
8	Parylene C	$320 \times 5 \times 3500$	-	8	0	8	0.0
9	Parylene C	$320 \times 20 \times 3500$	-	8	0	8	0.0
10	Parylene C	$20 \times 5 \times 3500$	$50 \times 50 \times 4000$	8	4	4	50.0
11	Parylene C	$20 \times 5 \times 3500$	$50 \times 100 \times 4000$	8	7	1	87.5
12	Parylene C	$20 \times 5 \times 3500$	$75 \times 100 \times 4000$	8	8	0	100.0
13	Parylene C	$20 \times 5 \times 3500$	$100 \times 100 \times 4000$	8	8	0	100.0
14	Parylene C	$20 \times 5 \times 3500$	$250 \times 100 \times 4000$	8	8	0	100.0
15	Parylene C	$20 \times 5 \times 3500$	$350 \times 100 \times 4000$	8	8	0	100.0

Table 4-1: Cohorts of probes tested in *ex vivo* chick embryonic brain tissue.

Cohort	Probe Material	Probe Dimensions (μm)	Coating Dimensions (μm)	Total	Pass	Fail	% Success Rate
1	SU-8	$40 \times 10 \times 3500$	-	11	6	5	54.5
2	SU-8	$40 \times 10 \times 3500$	$100 \times 100 \times 4000$	12	12	0	100.0
3	Parylene C	$40 \times 2.5 \times 3500$	-	8	0	8	0.0
4	Parylene C	$40 \times 2.5 \times 3500$	$50 \times 100 \times 4000$	8	5	3	62.5
5	Parylene C	$40 \times 2.5 \times 3500$	$75 \times 100 \times 4000$	8	7	1	87.5
6	Parylene C	$40 \times 2.5 \times 3500$	$100 \times 100 \times 4000$	12	12	0	100.0
7	Polymer Shank	-	$100 \times 100 \times 4000$	8	8	0	100.0

Table 4-2: Cohorts of probes tested in *ex vivo* rat brain tissue.

Parameter	Range Modeled	Coefficient Value	95% Confidence Interval	p Value
Coating Thickness	0–200 μm	15,513 μm^{-1}	[11928, 19113]	<0.0001
Probe Length	0.01–10 mm	–33,037 mm^{-1}	[–41029, –26755]	<0.0001
Coating Stiffness	0.001–100 GPa	1857 (GPa) $^{-1}$	[1322, 2274]	<0.0001
Coating Aspect Ratio	0.1–10	5480	[3922, 7034]	<0.0001
Probe Width	5–350 μm	62 μm^{-1}	[54, 69]	<0.0001
Beveled Angle	0–75°	1398	[515, 2236]	0.0043
Probe Stiffness	1–5000 MPa	434 (MPa) $^{-1}$	[131, 768]	0.0056
Brain Stiffness	0.5–5 kPa	–25 (kPa) $^{-1}$	[–39, –11]	0.0114

Table 4-3: Multi-variable regression results for the different parameters modeled in probe designs *versus* safety factor sorted in order of ascending p Value. Ranges modeled were selected based on limits of the fabrication process (for geometries), and potential selection of probe materials.

Chapter 5: An *in vitro* approach to correlating *in silico* predictions regarding the long term performance of flexible neural implants

Abstract:

Single-unit recording neural probes have significant advantages in signal-to-noise ratio and specificity for signal acquisition in Brain-to-Computer interface devices. Following insertion, micromotions in the brain lead to deformation at the probe-tissue interface, frequently leading to chronic gliosis, which results in encapsulation of the probe and limits long-term signal acquisition. To assess the features of the inserted probe that influence this chronic response, simulations were designed and executed in ABAQUS 6.10 FEA software (Simulia) to model probe displacement in brain tissue. Interfacial stress and tissue strain contour maps were generated, and average stress and strain was calculated by averaging the non-zero maximum stresses and strains for the probe and tissue elements, respectively. To validate model predictions, a polydimethylsiloxane (PDMS) well was fabricated and bonded to a glass slide. The displacements of 14 μ m diameter fluorescent polystyrene beads entrapped in a 0.6% agarose gel resulting from the lateral movement of a microprobe within the gel were measured. A MATLAB script was employed to track bead displacements and plot strain maps. To link strain predictions to gliosis, rat-derived primary astrocytes were cultured in collagen gels that were cast around a fixed probe in a 12 well-plate. Micromotion was then simulated by exposing the 12 well-plate to controlled motion via orbital shaker. Experimental values for average maximum strain agreed within 13.6% with model predictions for tungsten microwires. Simulations predicted average tissue strains of 6.7×10^{-3} for parylene probes, 0.048 for

polymer shanks, and 0.13 for tungsten microwires. Correlations between the average maximum principal strain along the tissue and GFAP intensities were found, enabling us to estimate maximum strain values allowed to avoid astrocyte activation. Future studies will employ the model to predict how probe geometry affects these measures and their correlations to the degree of gliosis induced. Ultimately, this model can be used as a tool to improve neural electrode design and to provide insight into the micromechanical features that contribute to inducing the inflammatory response.

Introduction:

Brain-to-computer interface devices provide a means for rehabilitation following functional injury to central nervous system tissue (Aregueta-Robles et al., 2014; Cheung, 2007; Grill et al., 2009; Hoogerwerf and Wise, 1994). Of most value is the ability to acquire accurate signals from firing neurons and translate these signals into a proportionate physical output from an extracorporeal device. Among acquisition approaches, single-unit recording neural probes have significant advantages in signal-to-noise ratio and specificity for signal acquisition (Nicolas-Alonso and Gomez-Gil, 2012). Unlike less invasive approaches such as electroencephalography and electrocorticograms (Cheung, 2007; Mak and Wolpaw, 2009; Nicolas-Alonso and Gomez-Gil, 2012), neural probes can obtain signal from single neurons. While most neural probes can acquire signals with high fidelity in the short term, their long term efficacy is hindered by a foreign body response.

Following insertion, a series of events occur at the probe implantation site that ultimately limits signal acquisition. These can be distinguished by their time scale of effect: immediate, acute responses, and the longer-term, chronic response. The acute injury is caused by mechanical trauma to the tissue due to insertion. The electrode damages extracellular matrix, capillaries, and glial and neuronal cells, inciting migration and inflammation of nearby microglia. Within the next few days, astrocytes increase their expression of glial fibrillary acidic protein (GFAP), corresponding to activation and the first steps in glial scarring (Lind et al., 2013; Yiu and He, 2006). Previous studies have demonstrated that magnitude of the acute response is a function of probe size (Retterer et al., 2004). For instance, silicon-machined probes with greater surface area resulted in

greater microglia activation than probes with less surface area (Polikov et al., 2005; Thelin et al., 2011). Probe geometry and methods of probe fixation also have an impact on the acute and chronic responses (Karumbaiah et al., 2013).

The chronic response that takes place weeks following insertion is initiated by surrounding astrocytes, resulting in formation of a glial scar. The scar sequesters the probe from surrounding neurons, limiting recording capability. Material mismatch between the probe and brain tissue has been demonstrated to be largely responsible for the chronic response (Aregueta-Robles et al., 2014; Cheung, 2007; Polanco et al., 2014). Probe displacement induced by tissue pulsation from cerebrospinal fluid (CSF) or blood flow and rotational accelerations due to head movement can cause differential movement of the probe and surrounding tissue, which produces shear and disrupts tissue. Probes made of metals or semi-conductor materials have stiffnesses hundreds of thousands times greater than brain tissue (Hamzavi et al., 2013). These stiffer probes result in greater interfacial stresses between the substrate and surrounding tissue, which exacerbates the chronic response (Subbaroyan et al., 2005).

To overcome these constraints, our approach was to fabricate flexible neural micro-electrodes made from parylene C (Lo et al., 2015). Parylene C has a flexural stiffness about 1000 times less than silicon, suggesting that chronic inflammation would be reduced compared to silicon-machined probes. However, parylene's flexibility makes it particularly vulnerable to buckling forces, and probes on their own fail to penetrate brain tissue to reach target neurons. In light of this, we coated parylene C probes with an ultra-fast degrading polymer which conferred temporary stiffness to inserted probes (D. Lewitus et al., 2011). With sufficient coating, the probe is able to successfully penetrate

brain tissue. However, there is a balance between the size of the coating and probe, and the conditions necessary for insertion. A larger coating thickness increases the mechanical trauma to tissue (Felix et al., 2013; Lo et al., 2015). Given the vast number of permutations of coating and probe features, designing, fabricating, and testing so many probes becomes a daunting, and expensive task.

Computational models provide a non-destructive means of analyzing probe performance under various conditions, including insertion into soft tissue. It is important to note that modeling as a means for understanding probe performance is not on its own a novel concept. Subbaroyan et al. developed a finite element simulation of probe-tissue mechanics and assessed the effects of material properties, tethering, and tip geometry on tissue strain (Subbaroyan et al., 2005). Hamzavi et al. extended this treatment to examine localized strains in a non-linear elastic model of brain tissue (Hamzavi et al., 2013).

Although these models examine changes in interfacial stress and strain as a function of probe geometry and material properties, they are limited by a lack of experimental validation for strains being predicted by models, and no clear quantitative correlation between the interfacial stresses and strains and the cellular effects observed in the chronic response. The intersection between the mechanical and biological effects would provide useful information to neural electrode designers in evaluating the chronic effects expected following insertion.

In this chapter, we design and validate a finite element simulation to predict the interfacial stresses and tissue strains generated by implanted probes due to micromotion. We then develop and assess the efficacy of an *in vitro* probe-gel-astrocyte system to relate the inflammatory response to the quantitative predictions made by the

aforementioned simulations. Taken with the results from our previous study on modeling probe and tissue insertion mechanics, we use the results herein to determine the parameters that can be optimized for ideal probe performance.

Methods:

To assess the effects of probe material and geometry on chronic damage, we used a combination of modeling and *in vitro* studies. First we developed an *in silico* model of probe micromotion in tissue. Next we performed validating experiments by measuring the displacements of fluorescent beads in agarose and collagen gels and subjected to controlled motion. Finally we developed and characterized an *in vitro* culture system of collagen gels seeded with astrocytes, cast our gels around different probe designs, and measured the degree of glial activity to correlate micromotion mechanics to biological outcomes. Details of each approach are described below.

Finite element simulations: Probe mechanics were simulated with ABAQUS 6.10

(Simulia). Probes with varying geometries and material properties were generated and meshed with 8-node, reduced integration (C3D8R) elements (Figure 5-1). Agarose and brain tissue were modeled as hyperelastic materials using Ogden material parameters adapted from the literature with C3D8R elements and adaptive meshing (El Sayed et al., 2008; Singh et al., 2016; Zhang et al., 2004). To mimic previous studies' observations of brain micromotion (Gilletti and Muthuswamy, 2006), the tissue was moved 10 μ m in a single direction,. Stress and strain fields for each model were extracted, and the following metrics were obtained: average nodal strain, average nodal stress, maximum principal strain, element von Mises stress, and radius of effect, which we defined as the distance from the probe to the last element that had a strain above 1×10^{-6} .

Separate simulations were performed that mimicked the experimental model of tissue displacement (see *Strain measurement validation* below). The tissue block was displaced similarly to the motion experienced by the gel when placed on a digital microtiter shaker (Ika TM, Wilmington NC), set to rotate at 150rpm. This was achieved by moving the tissue and probe instance by 50 μ m to the right, followed by a deceleration step, and movement 50 μ m perpendicular to the previous direction followed by another deceleration. This range of motion was repeated until the tissue-probe returned to its initial position. Two conditions were tested, one where the top of the probe was affixed to the top surface and coupled to the surrounding tissue, and a second condition where the probe was unfixed and coupled to the surrounding tissue.

Strain measurement validation: To validate model predictions, 0.4mg of 14 μ m diameter Fluoro-Max Green Fluorescent Polymer Microspheres (Thermo Scientific) were mixed in 1mL of 0.6% agarose, or 3.75mg/mL collagen to measure their displacements following simulated micromotion. The gel mixture was cast around a polydimethylsiloxane (PDMS) well bonded to a glass slide. Using a marker, several dots were made under the slide to act as fiduciary markers. A probe or probe mimic was either fixed to the PDMS well or was allowed to float freely in the liquid agarose or collagen until the gel had fully cast around the probe. Prior to gelling, the glass slide was carefully moved to the stage of an IX81 inverted epifluorescence microscope (Figure 5-2A for schematic), and a stack of images was taken to determine initial position of the beads. The stage holding the glass slide was then moved 10 μ m at a rate of 250 μ m/s before being shifted back to its original position at the same rate. The slide was imaged once more to ensure the fiduciary

markers were aligned to their initial positions, before images of the new bead positions were taken.

Images of the bead positions before and after motion were then overlaid and processed through an in-house built MATLAB script to generate strain contour maps as a function of bead displacement (Figure 5-2 B-C). Briefly, the script determined the center points of beads in both images. Using Delaunay triangulation, a strain mapping function was generated based on displacements of triangle sides. From the mapping function, strain tensors were calculated and assigned to the center point of each triangle, and the maximum principal strain was extracted for each triangle. A mesh grid of 512 x 512 pixels with 1 pixel resolution was generated and strain magnitudes were interpolated. Color maps were generated to visualize strain in bead images and determine the maximum value of 2-D strain and the average 2-D strain for use as metrics to compare to the *in silico* results.

In vitro model development: PDMS rings with an outer diameter of 22mm and an inner diameter of 9.5mm were punched out using a hollow punch kit (Mayhew Tools, Turners Fall MA). Rings were fitted with one of the following: 1) 50-500 μ m diameter tungsten microwires; 2) parylene strips 50-500 x 20 μ m in cross-sectional area or; 3) nothing (control). Rings with probe or probe mimic inserts were placed into 12 well plates and plates were sterilized with 95% ethanol, followed by 10 minute treatment in a UV-microwave. This was followed by oxygen-plasma treatment at 100W power, 250cm³ O₂ at 700mTorr for 60 seconds to ensure rings remained bound to the bottom surface of each well.

Culture preparation: Primary astrocytes were obtained from dissociated brain tissue from P8 rats. Cells were cultured in T-75 Falcon flasks for 7 days, reaching ~90% confluence. Cells were then trypsinized until detachment, and cold astrocyte culture media comprised of 10% fetal calf serum (CO), 1% L-Glutamine, 1% Penicillin-Streptomycin, in Dulbesco's Minimal Essential Media (Sigma-Aldrich, St Louis MO), was added to quench the reaction. Cells and media were centrifuged at 2000rpm for two minutes. Media supernatant was removed and the resultant pellet of cells was dissolved in 1mL astrocyte media warmed to 37°C. A small (45µL) volume was aliquoted and placed on a glass slide to determine the total number of cells, as well as stain for GFAP (1:500) and DAPI (1:5000) to visually assess the purity of astrocyte cultures. Only cultures with 80% or greater purity were used.

Collagen gels were prepared by mixing 20µL HEPES buffer, 140µL 0.1N NaOH, 100µL Minimum Essential Media (MEM), 52µL M199 Supplemental Media, 10µL L-Glutamine, 10µL Penicillin-Streptomycin, and 677µL reconstituted bovine collagen at 3.75mg/mL per 1mL of collagen gel. The collagen mixture was then supplemented with a volume of astrocyte media containing cells (31,250 cells/mL), and mixed thoroughly to ensure cells were distributed evenly. 400µL (12,500 cells/well) of the cell-collagen mixture were placed in each well. Preliminary studies demonstrated this concentration of cells was found to minimize gel compaction. The well plate was placed in a 37°C, 5% CO₂ incubator for 45 minutes to allow gels to form. Once gelled, 400µL of warm astrocyte culture media was added to each well.

Inducing micromotion: In each experiment, two plates were prepared. Control plates were not exposed to motion and stored in a 37°C, 5% CO₂ incubator. Plates for the injury

condition were also stored in a stored in a 37°C, 5% CO₂ incubator and placed on one end of a digital microtiter shaker (Ika™, Wilmington NC); set to rotate at 150rpm. We calculated this setting to equate to an angular acceleration of 0.26rad/s. Literature studies on micromotion as well as model executions with these parameters suggested the relative motion between gel and substrate would be equivalent to the lateral translation experienced by a stationary probe in tissue (Salek et al., 2011; Subbaroyan et al., 2005). At days 1, 3, and 5, 200µL of supernatant from each well was extracted and stored in 0.5mL microcentrifuge tubes at -20°C for further processing.

Immunohistochemistry and supernatant analysis: After 5 days, plates were removed from the incubator, and cells were fixed in 4% paraformaldehyde for 45 minutes.

Paraformaldehyde was removed and replaced with an immunobuffer solution comprised of 1% Bovine Serum Albumin (Sigma-Aldrich, St Louis MO), and 0.5% Triton X-100 (Sigma-Aldrich, St Louis MO) in Phosphate Buffered Saline. A series of 4 washes with immunobuffer were performed before blocking buffer of 10% goat serum in immunobuffer was added and allowed to remain for 1 hour. Following this blocking step, blocking buffer was replaced with a cocktail of 1:500 dilution of polyclonal rabbit primary antibody of GFAP (Dako Pharmaceuticals), and a 1:1000 dilution of a monoclonal mouse primary antibody of Iba1 (Millipore). Plates were allowed to incubate overnight at 4°C. The primary antibody cocktail was then removed and four more washing steps were performed before a cocktail of secondary antibodies was introduced. This secondary cocktail was comprised of a 1:500 dilution of goat-anti-rabbit Alexa Fluor 488 (Invitrogen), a 1:500 dilution of goat-anti-mouse Alexa Fluor 647 (Invitrogen), and 1:1000 DAPI (Fisher Scientific).

Following immunostaining, plates were imaged on an IX81 inverted epifluorescent microscope, using filters (410nm, 488nm, and 647nm) to capture all three sets of stains used. A spinning disc unit attached to a Hamamatsu ImagEM digital camera (Middlesex NJ) was used to capture images through the depth of the collagen gel. Image stacks were processed, and GFAP and Iba1 intensity and shape were analyzed for each of the different conditions. Ramified (branching) astrocytes were characterized and their GFAP staining intensities were recorded as an additional indicator of activation. Astrocytes were considered activated if more than two extensions could be seen (Burda and Sofroniew, 2014).

To assess the acute response and as a metric to indicate the capability of the *in vitro* assay, supernatant samples from days 1, 3, and 5 were assayed for Tumor Necrosis Factor alpha (TNF- α) produced by cell-collagen mixtures, through use of a rat-specific TNF- α sandwich enzyme-linked immunosorbent assay (ELISA) (Biolegend) to quantitatively assess cytokine production. Cultures stimulated with lipopolysaccharide (LPS) (1 μ g/mL) were used as a positive control.

Results

Model predictions: We modified two features of probes in the model: probe geometry and probe material properties. The geometric features we changed were the shape and dimensions of the probe. Figure 5-3 shows a representative set of contour maps for probes made of three different materials with the same dimensions ($320\mu\text{m} \times 20\mu\text{m} \times 3.5\text{mm}$ & $100\mu\text{m} \times 20\mu\text{m} \times 3.5\text{mm}$). Von mises stress (stress), and the principal maximum strains were plotted using contour maps. Generally, we observed that larger probes resulted in a substantially larger radius of non-trivial ($\epsilon > 1 \times 10^{-6}$) strains, and consequently stress, which we termed “radius of effect”. The material properties of the simulated probe influenced the magnitude of stress and strain, and had a marginal impact on radius of effect.

When probe width was increased, we observed non-linear increases in radius of effect (Figure 5-4). Average principal strains, and radius of effect both increased with probe width similarly to a power law (Figure 5-5). Maximum stress occurred at the top of the probe, which was fixed at the boundary. A second stress concentration occurred at the bottom end of the probe. When probes with beveled tips were simulated, the magnitude of stress at the elements at the bottom of the tip roughly tripled in comparison to smooth probes.

$350\mu\text{m}$ tungsten (270GPa) microwires generated a maximum Von Mises stress of 14.72kPa. This was significantly higher than similarly sized parylene C (5.6MPa, $\sigma_{\text{max}} = 0.11\text{kPa}$), and SU-8 photoresist (2.1GPa, $\sigma_{\text{max}} = 3.3\text{kPa}$). Qualitatively speaking, stiffer materials resulted in larger maximum Von Mises stress. No quantitative relationship could be discerned between the probe stiffness and the maximum stress and strain. The

magnitude of stress decreased inversely with the square root of distance ($1/\sqrt{\text{distance}}$), which was consistent with a previous study by Subbaroyan et al. (Subbaroyan et al., 2005). Simulations also predicted average tissue strains (calculated from the maximum principal strains of non-trivial elements) of from 6.7×10^{-3} for parylene probes, 0.048 for photoresist, and 0.13 for tungsten microwires. Representative strain profiles can be seen in Figure 5-6.

Model Validation: In validating experiments, we compared strain maps from bead experiments to simulations that replicate the same geometries and material properties used for the tested probe design. Figure 5-7 shows representative comparisons between simulations and bead movement experiments for agarose phantoms. Overall, there was strong agreement between strain magnitudes predicted by simulations and those calculated in bead experiments (difference in average maximum principal strain = 13.6%). Agreement was strongest in stiffer probes, where bead movement was more noticeable, and strain could be calculated with greater certainty.

Next we performed validating experiments with the goal of replicating the conditions used in the *in vitro* assay. 24 well plates containing collagen gels and fluorescent beads were cast around protruding probes in a PDMS ring as described in the methods. Samples without probes showed no bead movement which matched model predictions of average strains of 2×10^{-6} (implying movement was present but negligible) (Figure 5-8). When probe specimens were included with the PDMS ring, simulation average strains matched experimental strains to a maximum of 21%. This gave us confidence that our simulation predictions reflect the deformations experienced by the tissue surrogate.

Assessing efficacy of *in vitro* model: We employed three metrics to assess the utility of our astrocyte-collagen *in vitro* system in modeling the effects of micromotion on chronic injury: 1) live-dead assays to ensure cell death did not occur and to normalize ELISA results; 2) TNF- α ELISAs to demonstrate the acute response matches the expectations of what is observed in *in vivo* studies; and 3) intensity of GFAP staining over 5 days to assess astrocyte activity. TNF- α was selected as a primary marker as its expression is characteristic of a pro-inflammatory response (Biran et al., 2005). Concurrently, live-dead staining analysis was conducted and concentrations of TNF- α were normalized by the average number of living cells measured in each of the time points.

Live-dead staining confirmed astrocytes were viable. Viability was above 85% for all conditions (Figure 5-9). In all conditions, TNF- α expression was highest following one day after plating. In almost all conditions, concentrations dropped off in day 3, followed by day 5 (Figure 5-10). The exception to this was the samples that were stimulated with LPS, which remained constant at about 1000pg/mL. For comparisons, cohorts were broken down by materials, followed by size. Astrocytes cultured with microwires generated the greatest concentrations of TNF- α , followed by parylene C and control cases (no probe). Larger probes generated more TNF- α than smaller probes in all cases, though statistical significance was only found in some cases (Table 5-1). Finally, probe-gel conditions subjected to motion generated more TNF- α than their stationary counterparts, where statistical significance was seen in all cases ($P < 0.02$).

Comparing GFAP intensities between conditions showed similar patterns to that of the TNF- α expression (Figure 5-11). Stiffer probes generated higher intensities of GFAP staining as well as more ramified astrocytes. Larger probes generated higher intensities as

well, though the differences were not as profound as material differences. In all cases, motion resulted in greater GFAP intensities compared to equivalent conditions without motion. These results correspond strongly with the TNF- α data we obtained from ELISA analyses, where higher TNF- α expression corresponds with higher GFAP intensities.

Direct comparisons between *in silico* and *in vitro* results: For selections of designs, we overlaid the strain profiles predicted by simulation results with GFAP intensity profiles from stained samples of astrocyte-collagen gels cast around probe samples. Figure 5-12 and 5-13 shows representative sets of profiles for parylene probes and tungsten microwires undergoing no motion (Figure 5-12A, 5-13A) and motion (Figure 5-12B, 5-13B), respectively. GFAP intensity decreased with distance from the probe as does predicted stress. For each condition, the intensities from GFAP signal were averaged. This composite signal was compared against the predicted strain.

We determined correlation coefficients between the images of immunostained astrocytes and the model predictions for replicate conditions as a measure of the model's means of reflecting strains on the cell-gel mixture. Two metrics were used to assess the minimal conditions to induce astrocytosis: element strain, and normalized GFAP intensity, relative to the negative control (no probe, no movement). We compared each metric and assessed its relative ability to predict the likelihood of astrocyte activation.

Correlations were strong between the stress/strain predictions and the averaged GFAP intensity. These correlations were higher in stiffer probes, followed by SU-8 probes, and finally parylene probes. We plotted contour maps of von Mises stress and maximum principal strain, and determined strong correlation between stress (strain) and GFAP intensity ($R^2_{\text{avg}} = 0.83$). To normalize intensities across conditions, we divided the

GFAP intensities for each condition against the average intensity of the control case where cell-collagen gels that were not cast around probes nor exposed to motion. This negative control condition generated the lowest average intensities of GFAP expression, as well as the lowest concentrations of TNF- α determined through ELISA analysis.

Next, we estimated a strain threshold for astrocyte activation. To accomplish this, we plotted strain predictions from simulations against the corresponding average intensities of GFAP expression from *in vitro* results. Next, data points were classified by whether the cell at the location exhibited ramified morphology. The 50th percentile of intensities of ramified astrocytes was determined, and this value for the intensity was used to indicate “activation”. Using this activation value, we applied this threshold to our GFAP-predicted strain profiles to determine the strain threshold associated with activation, and averaged the result from all data sets. The average strain threshold was found to be 0.098, with a conservative estimate of 0.026 and a more tolerant estimate of 0.133 (Figure 5-14).

Discussion

The goals of the work in this chapter were to: 1) develop and validate a finite element model to predict the interfacial stresses and strains generated with probe micromotion; 2) develop and validate a simple *in vitro* model of astrocytes in collagen gel subjected to similar conditions as a probe in brain tissue; and 3) quantitatively correlate simulation predictions to the effects seen in the *in vitro* model, and determine the likelihood of astrocyte activation as a function of interfacial stress and tissue strain. Combined, these results would provide a means of quantitatively assessing how variations in probe design affect the chronic response, and provide insight on steps that can be taken to mitigate probe-induced chronic injury.

Micromotion has been implicated as a likely cause of chronic reactivity following neural probe implantation (Felix et al., 2013; Gilletti and Muthuswamy, 2006; Karumbaiah et al., 2012; Polanco et al., 2014). Normal physiological activity such as pulsatile flow in vasculature, flow of cerebrospinal fluid (CSF), and breathing causes tissue to move and experience additional deformation upon interacting with the implanted electrode. Functional imaging studies suggest that this motion generates the equivalent of lateral translation of the probe (Gilletti and Muthuswamy, 2006), supporting our model methodology of translating tissue in a single direction in simulations. The magnitude of this motion can vary in different animal species. For instance, in mouse studies, micromotion of the brain tissue during normal physiological conditions varies by about 30-40 μ m. In experimental setups, the probe is commonly fixed to the skull, resulting in a large interfacial stress between the probe and surrounding tissue, which exacerbates the chronic response (Cheung, 2007).

The salient concern in the design of neural implants is their long-term efficacy given the occurrence of gliosis. Previous work implicates probe geometry and probe stiffness as features that modulate the degree of scarring (Polikov et al., 2005; Potter et al., 2012; Stice and Muthuswamy, 2009). By utilizing parylene as our probe substrate, probes would be flexible enough to minimize interfacial stresses between electrode and tissue, and therefore minimize scarring (Lo et al., 2015). To distinguish the design properties that drive this response, a model was required to quantify the stresses and strains caused by the implant. To this end, we adapted the model from Singh et al. to quantify the interfacial stresses and strains generated between probe and tissue following brain micromotion (Singh et al., 2016). In contrast to our previous study, the coating was omitted from analysis, as the time scale for chronic damage is days and weeks following insertion; which is well after the hours need to degrade the ultrafast degrading polymer utilized to coat neural electrodes (D. Y. Lewitus et al., 2011).

More importantly, finite element simulations allowed us to quantitatively predict the strains being generated at the probe-tissue interface for conditions where experimental observations are infeasible. This is important for two reasons. As described in previous chapters, measuring microscopic strains in situ is still a challenge. Equally important, whereas stiffer probes generated relatively large magnitude strains that allowed for measurement of bead displacements in our validation experiments, the softer parylene probes did not produce appreciable movement in beads, making it impossible to reliably quantify strain in parylene probes. Simulations of parylene probes predicted strains that were two orders of magnitude smaller than stiffer probes of similar dimensions. We were unable to capture bead displacements with certainty when we imaged agarose gels cast

around parylene probes, which was commensurate with the very small strains we predicted were being generated by the more flexible probes.

The relationship between probe width and tissue strain and probe width and radius of effect could be fit with a power law. However, the relationship between probe stiffness and tissue strain and radius of effect is more difficult to discern. We did observe that both strain and radius of effect increased with stiffness in a non-linear fashion. For instance, when parylene probes were compared to tungsten microwire, strain increased 500%, and radius of effect increased 67%, implying that probe stiffness has a more substantial effect on tissue strain than geometry. These findings justify the emphasis our group had on selecting a flexible material over minimizing size, as even by using a substantially large probe (>500 μ m in width), the strains in the expanded radius of effect may be too small to elicit the chronic injury response (Grill et al., 2009). Furthermore, larger probes can accommodate more recording traces, improving recording resolution.

After developing and validating the finite element simulation, our next step was to develop an *in vitro* model to assess design impacts on gliosis. The *in vitro* model served as a surrogate to in vivo studies and organotypic cultures. Organotypic models are inherently more biomimetic than the cell-gel culture system we utilized, but also more complex, comprising cell-cell interactions, architecture, etc (Cater et al., 2006). The advantage to our approach is the ability to isolate the components that are implicated in chronic injury. Brain tissue is comprised of a complex network of astrocytes, microglia, oligodendrocytes, neurons, and epithelial cells that interact with one another during injury and inflammatory cascades (Burda and Sofroniew, 2014; Uno et al., 1997; Werner and Engelhard, 2007). As astrocytes are responsible for glial scarring that limits the

electrode's long-term ability to measure signal, we found it prudent to quantify their expression of pro-inflammatory markers as a function of probe material and geometry (Lind et al., 2013; Polikov et al., 2005). Thus, our *in vitro* model sought to isolate astrocytes in cell cultures. Iba1 staining for microglia demonstrated the presence of no microglia in our cultures, confirming that the downstream inflammatory effects we observed were primarily due to astrocytes.

ELISA was used to evaluate the *in vitro* model's authenticity to similar organotypic and *in vivo* models. TNF- α is a cytokine and its expression is a hallmark of inflammation. ELISA results showed similar trends across all probe conditions. We were surprised at the steady decline in concentration over days 1 to 5. To elucidate reasons for this change, we first tested whether cell viability was severely impacted by the probe material or the rotational motion using a live-dead staining. If cell death increased, this would explain the decrease in TNF- α expression. Cell viability was not adversely affected by probe material or motion, being between 85-98% across samples. Cell count did not change considerably in the period as well ($P_{\min} = 0.22$). As cell count and viability did not change in this time period, it followed that TNF- α expression per cell was decreasing, and that TNF- α is a representative marker of the acute response, but not as effective a metric for assessing chronic damage. Evaluation of brain tissue in a parallel *in vivo* study performed by our group, where electrodes made of copper and parylene C were inserted for 1, 4 and 12 weeks, support this finding (Lo et al. 2016, in preparation).

We used GFAP expression as an indicator for astrocyte activation. Along with TNF- α , GFAP is a component in the inflammatory cascade (Chung and Benveniste, 1990). Unlike GFAP which is specifically expressed by astrocytes, TNF- α is expressed

by astrocytes, microglia, activated macrophages, and oligodendrocytes (Uno et al., 1997). The same parallel *in vivo* studies our group has performed demonstrated elevated levels of GFAP with stiffer probes, further supporting the observations we made in our *in vitro* study (Lo et al. 2016, in preparation).

Finally, we explored the link between the stress and strain predictions and the corresponding astrocyte markers in our *in vitro* model. Profiles of astrocyte activation reflect the stress and strain predictions from simulations. We correlated predictions to the GFAP intensities in prepared gels and found strong agreement between the two metrics ($R^2 > 0.72$). We then determined an element strain threshold that corresponds to astrocyte activation. Our conservative estimate for astrocyte activation was a strain of 2.6%. Thresholds near this value were most prevalent in parylene C GFAP profiles. The only other study we encountered that performed a similar assessment of strain-induced gliosis was by Karumbaiah et al., where they reported a cyclic strain of 3% induces upregulation of IL-6 and IL-36Ra (Karumbaiah et al., 2012). Admittedly, the method we used to define “activated” astrocytes as the upper 50% of normalized intensity of ramified (branching) astrocytes is somewhat crude. These criteria could be further refined by selecting a more discerning intensity threshold, or correlating these results to qPCR results (Brahmachari et al., 2006).

Our results confirm the general wisdom that larger, stiffer probes result in a greater magnitude of gliosis. These same properties also improve the likelihood of insertion. Our group has fabricated small, flexible probes made of parylene and coated these probes with a tyrosine-based polymer that confers temporary stiffness to the probe. In the previous chapter, we developed an approach to model insertion of coated probes into soft

tissue. Combining the metrics we elucidate with the safety factor values we extracted for our designs allow for the design of optimized probes that minimize both the acute and chronic injury response, while still inserting successfully.

Conclusions:

In this chapter, we sought to quantitatively link the interfacial stresses between probes and surrounding tissue with degree of chronic damage using an *in vitro* model. We first developed an extension to the model in chapter 4 to predict interfacial stresses between the probe and tissue interface and validated these predictions with corresponding strain mapping experiments. Next, to assess chronic damage, we developed a culture system of astrocytes seeded in 3-dimensions in collagen gels, cast the hydrogel-cell mixture in liquid form around different probe specimens, and exposed the gel-cell-probe system to controlled motion meant to mimic probe micromotion experienced by *in vivo* brain tissue. Finally, we compared stress and strain predictions from our finite element simulations to GFAP expression, an astrocyte marker that corresponds to increased chronic damage.

Taken with the simulation we developed and validated in chapter 4, we have a fully encompassing model to assess probe designs and their expected mechanical outcomes during and following insertion. As expected, there is a balancing act between minimizing the acute damage (minimizing insertion force), maximizing the recording space for probes (increased size), and minimizing the chronic response for continual measurements. Depending on the probe's features, it is possible to optimize design or materials in such a way to ensure ideal recording potential.

Equally importantly, we developed a methodology to link stress and strain on astrocytes in collagen gels, to the likelihood of astrocyte activation. Similar to the work in chapter 3 where we elucidated strain thresholds for axonal failure, the strains predicted by our finite element simulations reflect regions of astrocyte activation and chronic damage.

References:

- Aregueta-Robles, U. a, Woolley, A.J., Poole-Warren, L. a, Lovell, N.H., Green, R. a, 2014. Organic electrode coatings for next-generation neural interfaces. *Front. Neuroeng.* 7, 15. doi:10.3389/fneng.2014.00015
- Biran, R., Martin, D.C., Tresco, P. a, 2005. Neuronal cell loss accompanies the brain tissue response to chronically implanted silicon microelectrode arrays. *Exp. Neurol.* 195, 115–26. doi:10.1016/j.expneurol.2005.04.020
- Brahmachari, S., Fung, Y.K., Pahan, K., 2006. Induction of glial fibrillary acidic protein expression in astrocytes by nitric oxide. *J. Neurosci.* 26, 4930–9. doi:10.1523/JNEUROSCI.5480-05.2006
- Burda, J.E., Sofroniew, M. V, 2014. Reactive gliosis and the multicellular response to CNS damage and disease. *Neuron* 81, 229–48. doi:10.1016/j.neuron.2013.12.034
- Cater, H.L., Sundstrom, L.E., Morrison, B., 2006. Temporal development of hippocampal cell death is dependent on tissue strain but not strain rate. *J. Biomech.* 39, 2810–8. doi:10.1016/j.jbiomech.2005.09.023
- Cheung, K.C., 2007. Implantable microscale neural interfaces. *Biomed. Microdevices* 9, 923–38. doi:10.1007/s10544-006-9045-z
- Chung, I., Benveniste, E., 1990. Tumor necrosis factor- α production by astrocytes. Induction by lipopolysaccharide, IFN- γ , and IL-1 β . *J. Immunol.*
- El Sayed, T., Mota, A., Fraternali, F., Ortiz, M., 2008. Biomechanics of traumatic brain injury. *Comput. Methods Appl. Mech. Eng.* 197, 4692–4701. doi:10.1016/j.cma.2008.06.006
- Felix, S.H., Shah, K.G., Tolosa, V.M., Sheth, H.J., Tooker, A.C., Delima, T.L., Jadhav, S.P., Frank, L.M., Pannu, S.S., 2013. Insertion of flexible neural probes using rigid stiffeners attached with biodissolvable adhesive. *J. Vis. Exp.* e50609. doi:10.3791/50609
- Gilletti, A., Muthuswamy, J., 2006. Brain micromotion around implants in the rodent somatosensory cortex. *J. Neural Eng.* 3, 189–95. doi:10.1088/1741-2560/3/3/001
- Grill, W.M., Norman, S.E., Bellamkonda, R. V, 2009. Implanted neural interfaces: biochallenges and engineered solutions. *Annu. Rev. Biomed. Eng.* 11, 1–24. doi:10.1146/annurev-bioeng-061008-124927
- Hamzavi, N., Tsang, W.M., Shim, V.P.W., 2013. Nonlinear elastic brain tissue model for neural probe-tissue mechanical interaction. 2013 6th Int. IEEE/EMBS Conf. Neural Eng. 1119–1122. doi:10.1109/NER.2013.6696134

Hoogerwerf, a C., Wise, K.D., 1994. A three-dimensional microelectrode array for chronic neural recording. *IEEE Trans. Biomed. Eng.* 41, 1136–46. doi:10.1109/10.335862

Karumbaiah, L., Norman, S.E., Rajan, N.B., Anand, S., Saxena, T., Betancur, M., Patkar, R., Bellamkonda, R. V, 2012. The upregulation of specific interleukin (IL) receptor antagonists and paradoxical enhancement of neuronal apoptosis due to electrode induced strain and brain micromotion. *Biomaterials* 33, 5983–96. doi:10.1016/j.biomaterials.2012.05.021

Karumbaiah, L., Saxena, T., Carlson, D., Patil, K., Patkar, R., Gaupp, E. a, Betancur, M., Stanley, G.B., Carin, L., Bellamkonda, R. V, 2013. Relationship between intracortical electrode design and chronic recording function. *Biomaterials* 34, 8061–74. doi:10.1016/j.biomaterials.2013.07.016

Lewitus, D., Smith, K.L., Shain, W., Kohn, J., 2011. Ultrafast resorbing polymers for use as carriers for cortical neural probes. *Acta Biomater.* 7, 2483–91. doi:10.1016/j.actbio.2011.02.027

Lewitus, D.Y., Smith, K.L., Shain, W., Bolikal, D., Kohn, J., 2011. The fate of ultrafast degrading polymeric implants in the brain. *Biomaterials* 32, 5543–50. doi:10.1016/j.biomaterials.2011.04.052

Lind, G., Linsmeier, C.E., Schouenborg, J., 2013. The density difference between tissue and neural probes is a key factor for glial scarring. *Sci. Rep.* 3, 2942. doi:10.1038/srep02942

Lo, M., Wang, S., Singh, S., Damodaran, V.B., Kaplan, H.M., Kohn, J., Shreiber, D.I., Zahn, J.D., 2015. Coating flexible probes with an ultra fast degrading polymer to aid in tissue insertion. *Biomed. Microdevices* 17, 34. doi:10.1007/s10544-015-9927-z

Mak, J., Wolpaw, J., 2009. Clinical applications of brain-computer interfaces: current state and future prospects. *Biomed. Eng. IEEE Rev.* ... 187–199. doi:10.1109/RBME.2009.2035356.Clinical

Nicolas-Alonso, L.F., Gomez-Gil, J., 2012. Brain computer interfaces, a review. *Sensors (Basel)*. 12, 1211–79. doi:10.3390/s120201211

Polanco, M., Yoon, H., Bawab, S., 2014. Micromotion-induced dynamic effects from a neural probe and brain tissue interface. *J. Micro/Nanolithography, MEMS, MOEMS* 13, 023009. doi:10.1117/1.JMM.13.2.023009

Polikov, V.S., Tresco, P. a, Reichert, W.M., 2005. Response of brain tissue to chronically implanted neural electrodes. *J. Neurosci. Methods* 148, 1–18. doi:10.1016/j.jneumeth.2005.08.015

Potter, K. a, Buck, A.C., Self, W.K., Capadona, J.R., 2012. Stab injury and device implantation within the brain results in inversely multiphasic neuroinflammatory and neurodegenerative responses. *J. Neural Eng.* 9, 046020. doi:10.1088/1741-2560/9/4/046020

Retterer, S.T., Smith, K.L., Bjornsson, C.S., Neeves, K.B., Spence, A.J.H., Turner, J.N., Shain, W., Isaacson, M.S., 2004. Microfluidics : A Potential Intervention Strategy for Controlling Reactive Cell and Tissue Responses 51, 2063–2073.

- Salek, M.M., Sattari, P., Martinuzzi, R.J., 2011. Analysis of Fluid Flow and Wall Shear Stress Patterns Inside Partially Filled Agitated Culture Well Plates. *Ann. Biomed. Eng.* 40, 707–728. doi:10.1007/s10439-011-0444-9
- Singh, S., Lo, M.-C., Damodaran, V.B., Kaplan, H.M., Kohn, J., Zahn, J.D., Shreiber, D.I., 2016. Modeling the Insertion Mechanics of Flexible Neural Probes Coated with Sacrificial Polymers for Optimizing Probe Design. *Sensors (Basel)*. 16, 1–18. doi:10.3390/s16030330
- Stice, P., Muthuswamy, J., 2009. Assessment of gliosis around moveable implants in the brain. *J. Neural Eng.* 6, 046004. doi:10.1088/1741-2560/6/4/046004
- Subbaroyan, J., Martin, D.C., Kipke, D.R., 2005. A finite-element model of the mechanical effects of implantable microelectrodes in the cerebral cortex. *J. Neural Eng.* 2, 103–13. doi:10.1088/1741-2560/2/4/006
- Thelin, J., Jörmtehl, H., Psouni, E., Garwicz, M., Schouenborg, J., Danielsen, N., Linsmeier, C.E., 2011. Implant size and fixation mode strongly influence tissue reactions in the CNS. *PLoS One* 6, e16267. doi:10.1371/journal.pone.0016267
- Uno, H., Matsuyama, T., Akita, H., Nishimura, H., Sugita, M., 1997. Induction of tumor necrosis factor-alpha in the mouse hippocampus following transient forebrain ischemia. *J. Cereb. Blood Flow Metab.* 17, 491–9. doi:10.1097/00004647-199705000-00002
- Werner, C., Engelhard, K., 2007. Pathophysiology of traumatic brain injury. *Br. J. Anaesth.* 99, 4–9. doi:10.1093/bja/aem131
- Yiu, G., He, Z., 2006. Glial inhibition of CNS axon regeneration. *Nat. Rev. Neurosci.* 7, 617–627. doi:10.1038/nrn1956.Glia
- Zhang, L., Yang, K.H., King, A.I., 2004. A Proposed Injury Threshold for Mild Traumatic Brain Injury. *J. Biomech. Eng.* 126, 226. doi:10.1115/1.1691446

Figures:

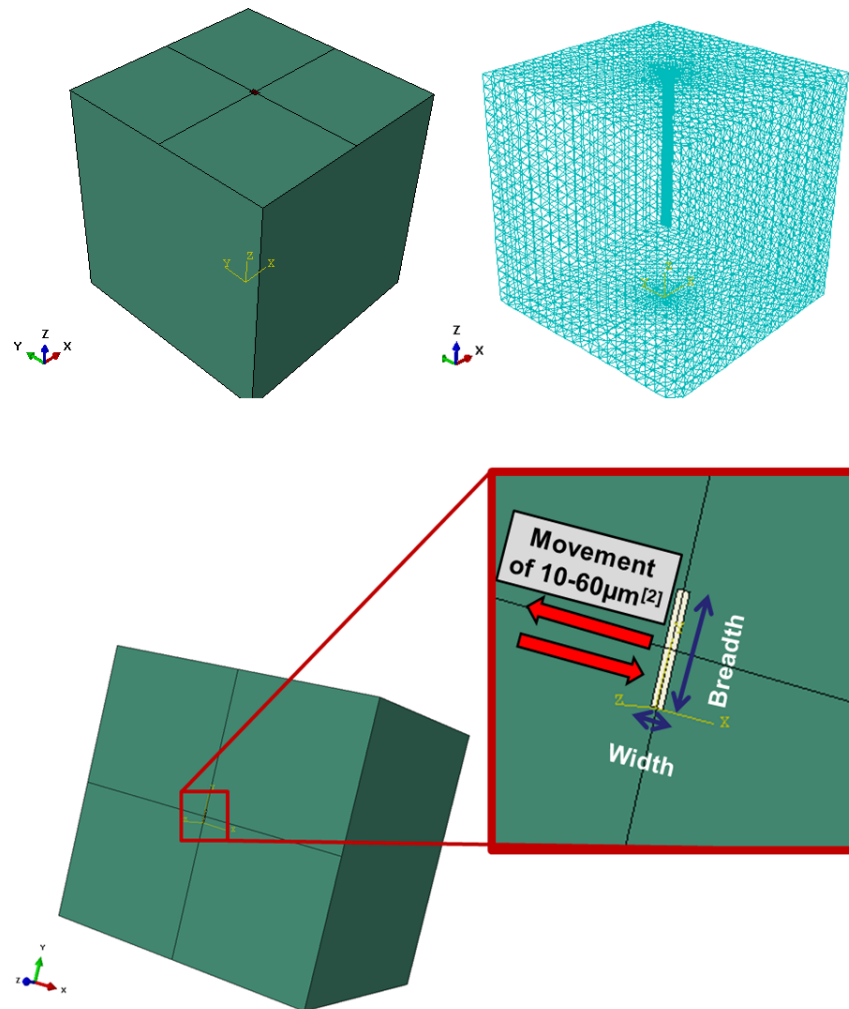


Figure 5-1: Schematic of Finite Element (FE) model for the embedded probe. Stiffness, dimensions, and geometries were varied for the probe. To simulate the micromotion experienced by the probe due to the brain's resting conditions, the probe was moved 10 to 60 μm while the tissue remained stationary.

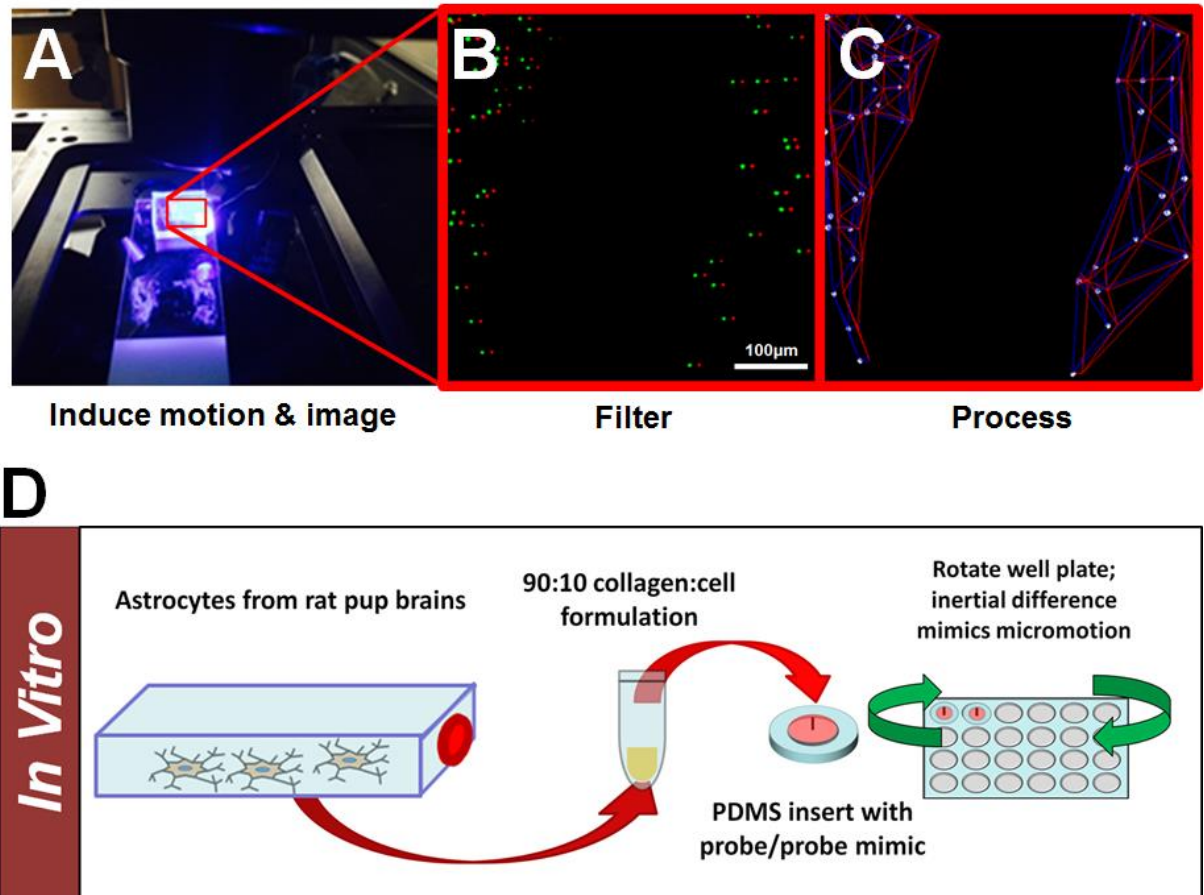


Figure 5-2: Images of the experimental setup used to validate strain predictions from FE simulations. (A) Agarose (or collagen) gels were cast around a fixed probe. A PDMS well was bound to a glass slide and placed on an inverted epifluorescent microscope. The slide was imaged, moved a certain distance, moved back to its original position, and imaged again. (B) shows the initial position of beads (red) prior to motion, and final position (green) following motion. (C) shows post-processed images and the outcome of Delaunay triangulation to calculate the strain mapping function. (D) is a schematic of the *in vitro* approach used to evaluate astrocytosis in probe designs.

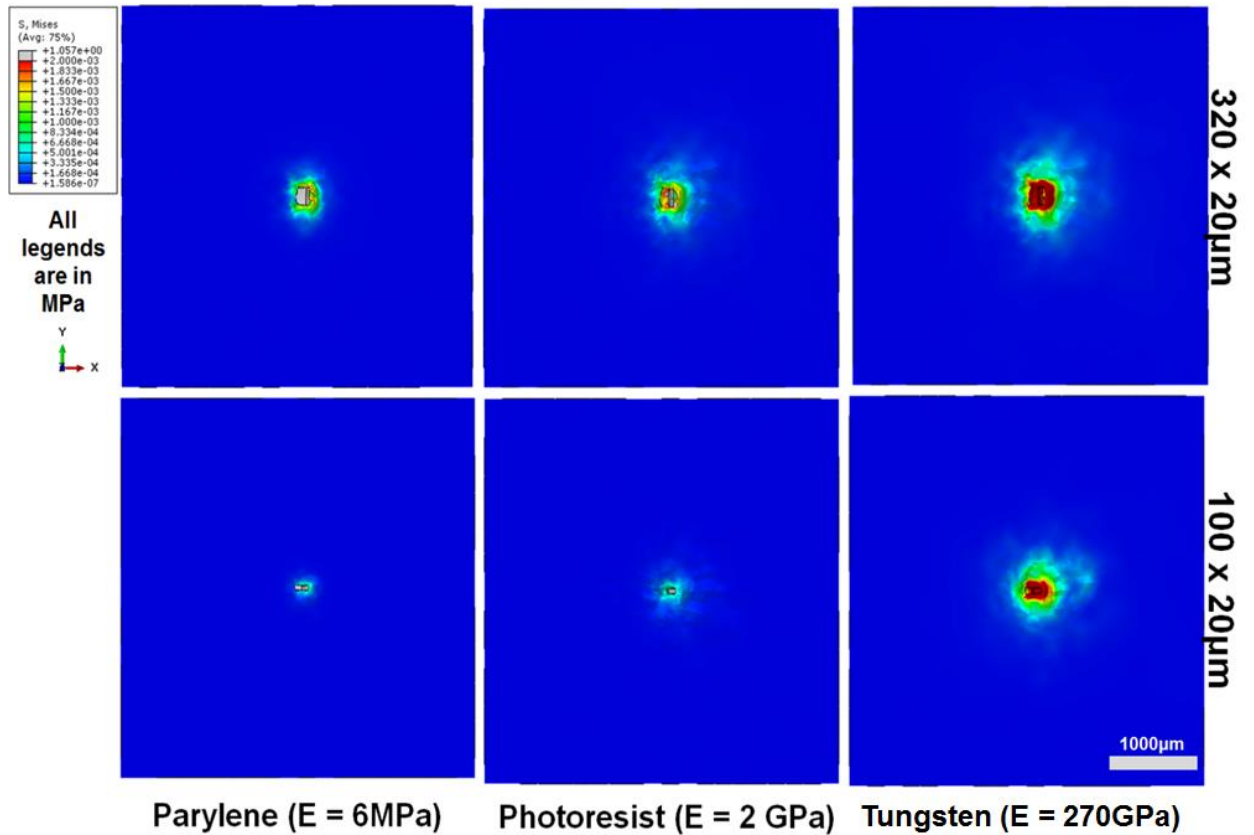


Figure 5-3: Representative screenshots of model executions and contour maps (von Mises stress) for the three materials tested as viewed following a view cut through the z-axis.

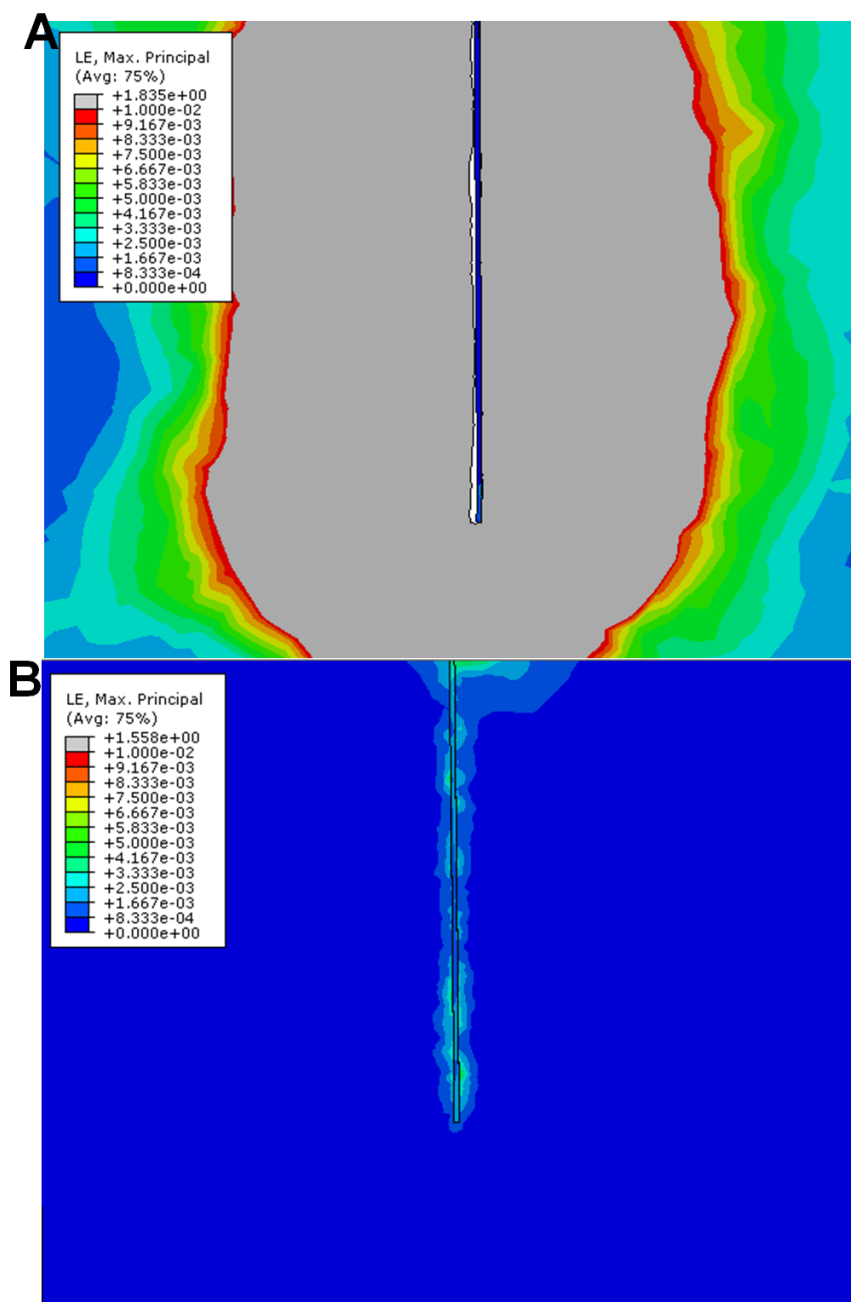


Figure 5-4: Representative contour plots for a (A) microwire and (B) parylene probe model execution with the view cut through the x-axis. Each had dimensions of $100\mu\text{m} \times 20\mu\text{m} \times 4\text{mm}$. The differences in contour maps are noticeable when results are visualized under the same scale.

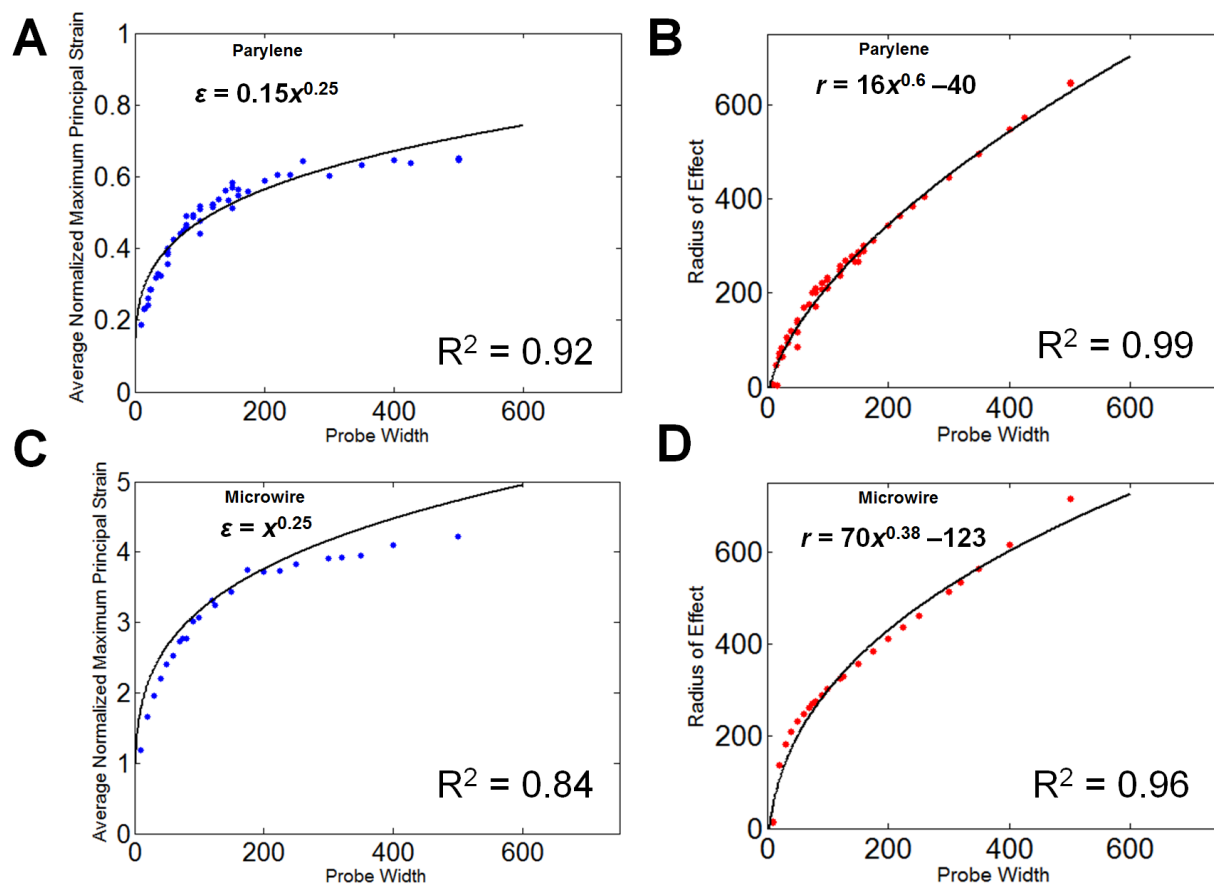


Figure 5-5: Plots of predicted strain and radius of effect as a function of probe width.

Curve fitting analysis was used to fit power laws to the simulation data. (A) and (C) compare the highest principal strain obtained for parylene and tungsten microwire respectively. (B) and (D) perform the same material comparisons in the context of radius of effect. We note that material properties make a difference to the maximum strain but not to the radius of effect.

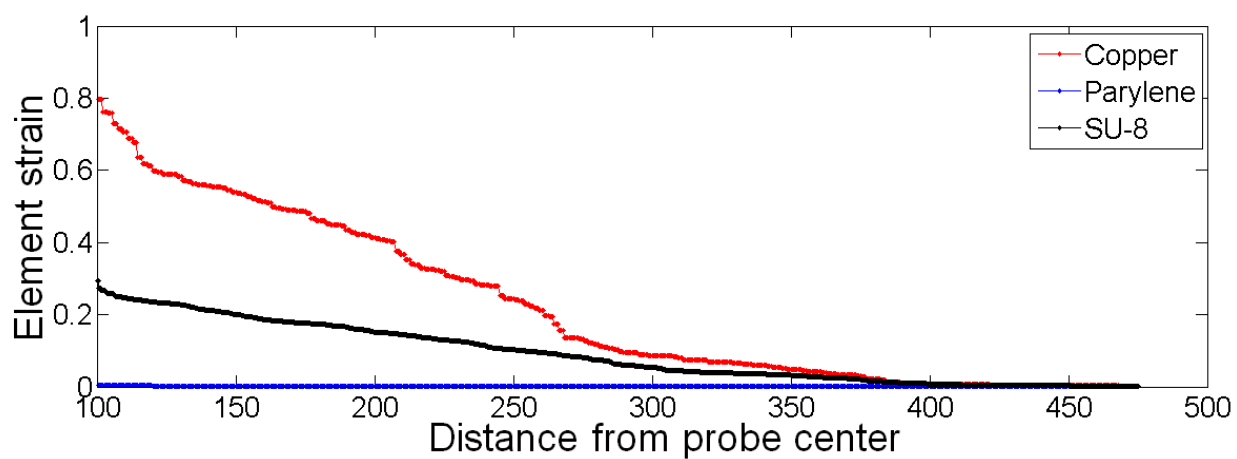


Figure 5-6: Representative output of 2-D normalized strain profiles of copper wire, parylene probes, and SU-8 probes ($350\mu\text{m} \times 20\mu\text{m} \times 4\text{mm}$) for micromotion simulations. Tissue was displaced $10\mu\text{m}$ while the probe was fixed at the top.

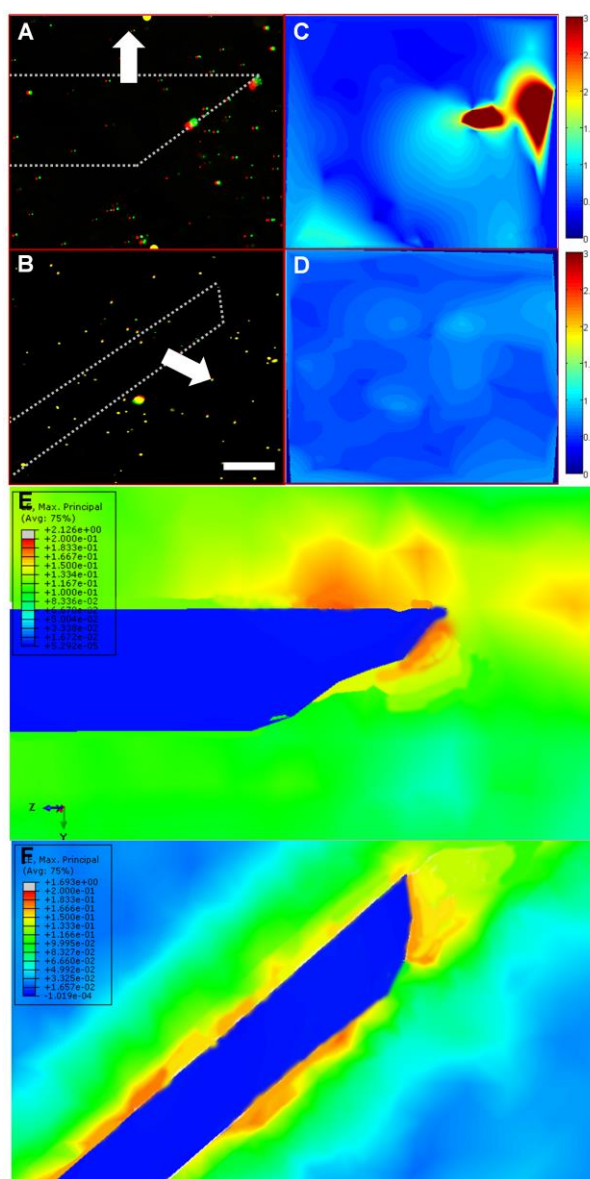


Figure 5-7: Representative images of microwires: (A) is a beveled tungsten microwire with diameter of 500µm; (B) and diameter of 200µm. Smaller microwires (Figures 5-3B and 5-3D) cause smaller bead movement, resulting in lower magnitude strain density. While parylene probes were also tested for strain mapping, beads did not move appreciably for the mapping to produce results (Scale bar = 200µm). (E & F) show the corresponding model results for the probes shown in (A) and (B).

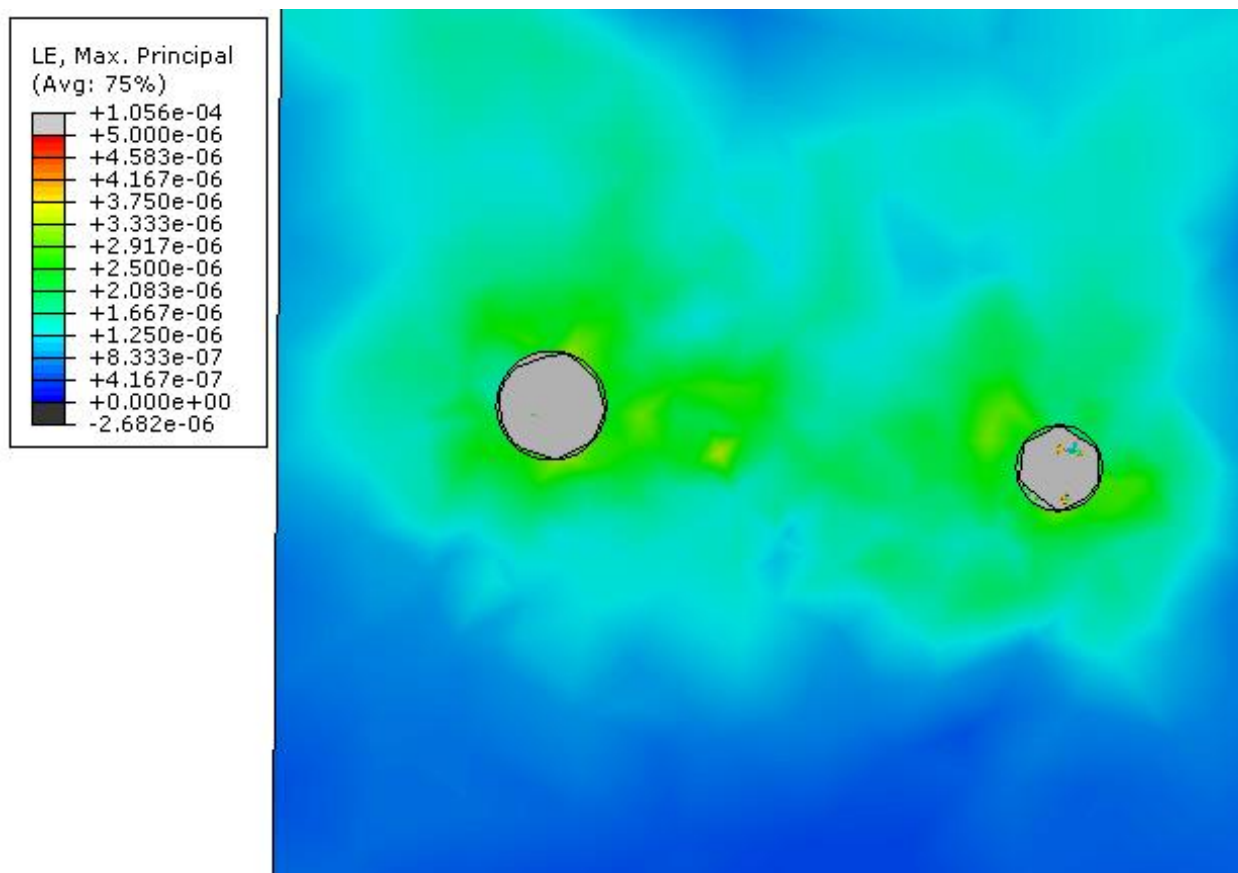


Figure 5-8: Simulations of beads embedded in the agarose system when experiencing motion similar to the orbital shaker used to mimic micromotion resulted in negligible element strains ($\epsilon < 10^{-5}$).

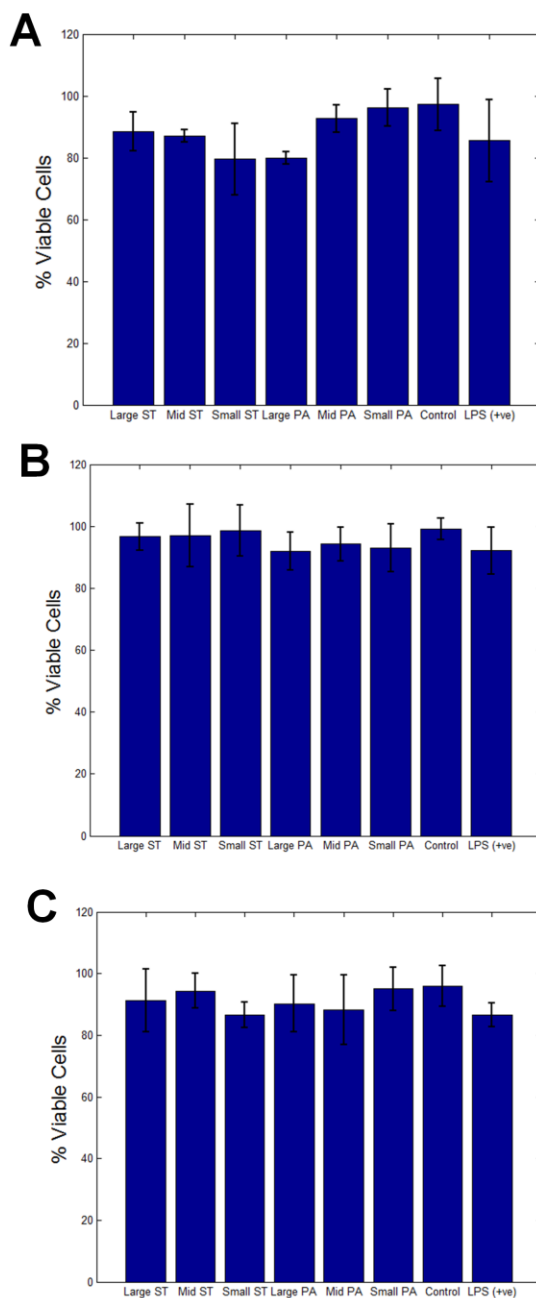


Figure 5-9: Cell viability results from live-dead stains performed on (A) 1 day, (B) 3 day, and (C) 5 day samples experiencing motion via orbital shaker. Viability was used to normalize the TNF- α concentration extracted from ELISAs to confirm that the concentration changes with time were not due to cell death.

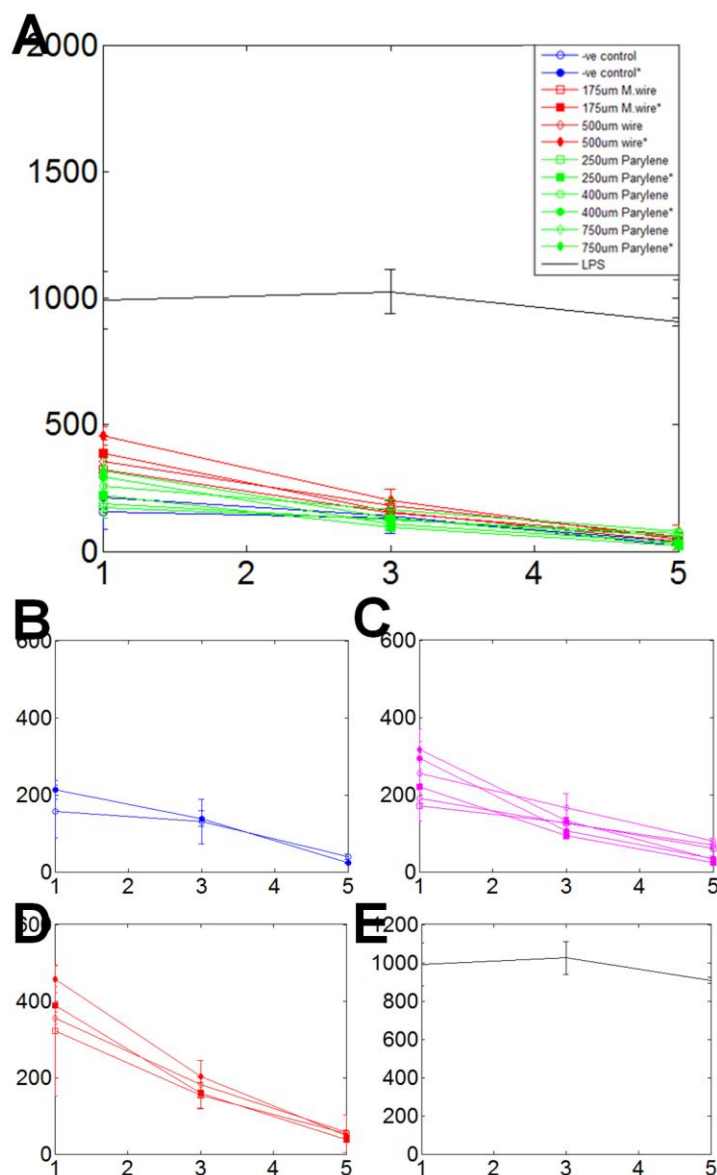


Figure 5-10: (A) Composite plots of TNF- α concentrations (given in pg/mL, y-axis) over 5 days (x-axis) as determined by ELISA run in triplicate (N = 4) for varieties of microwires and parylene probes exposed to movement (marked with *) or no movement. (B-E) are isolated plots of TNF- α concentrations for (B) negative controls; (C) parylene probes; (D) microwires; and (E) LPS positive control.

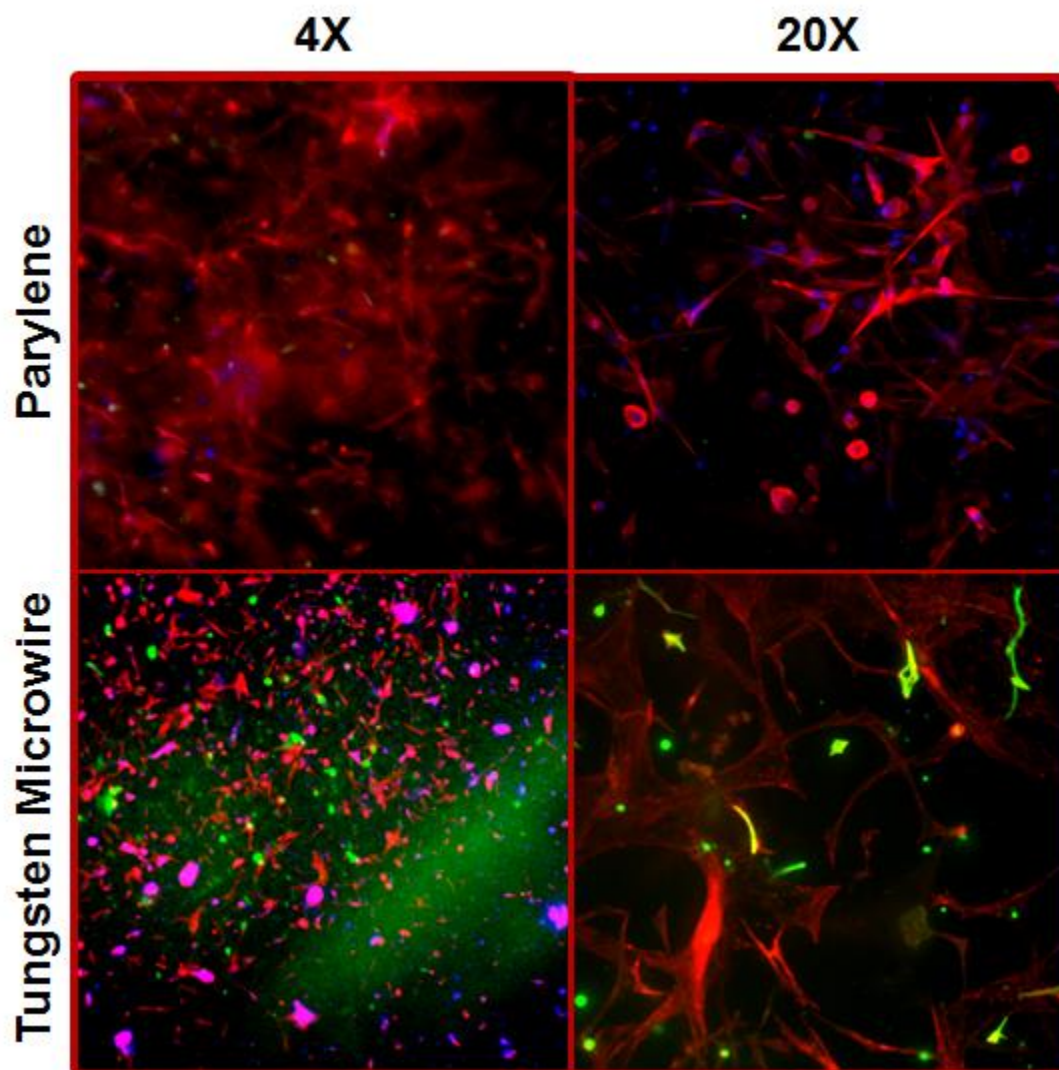


Figure 5-11: Representative images of DAPI (blue), Phalloidin (red), and GFAP (green) staining for cell-gel samples left stationary. GFAP intensity was noticeably higher in the stiffer tungsten microwire samples than the flexible parylene samples

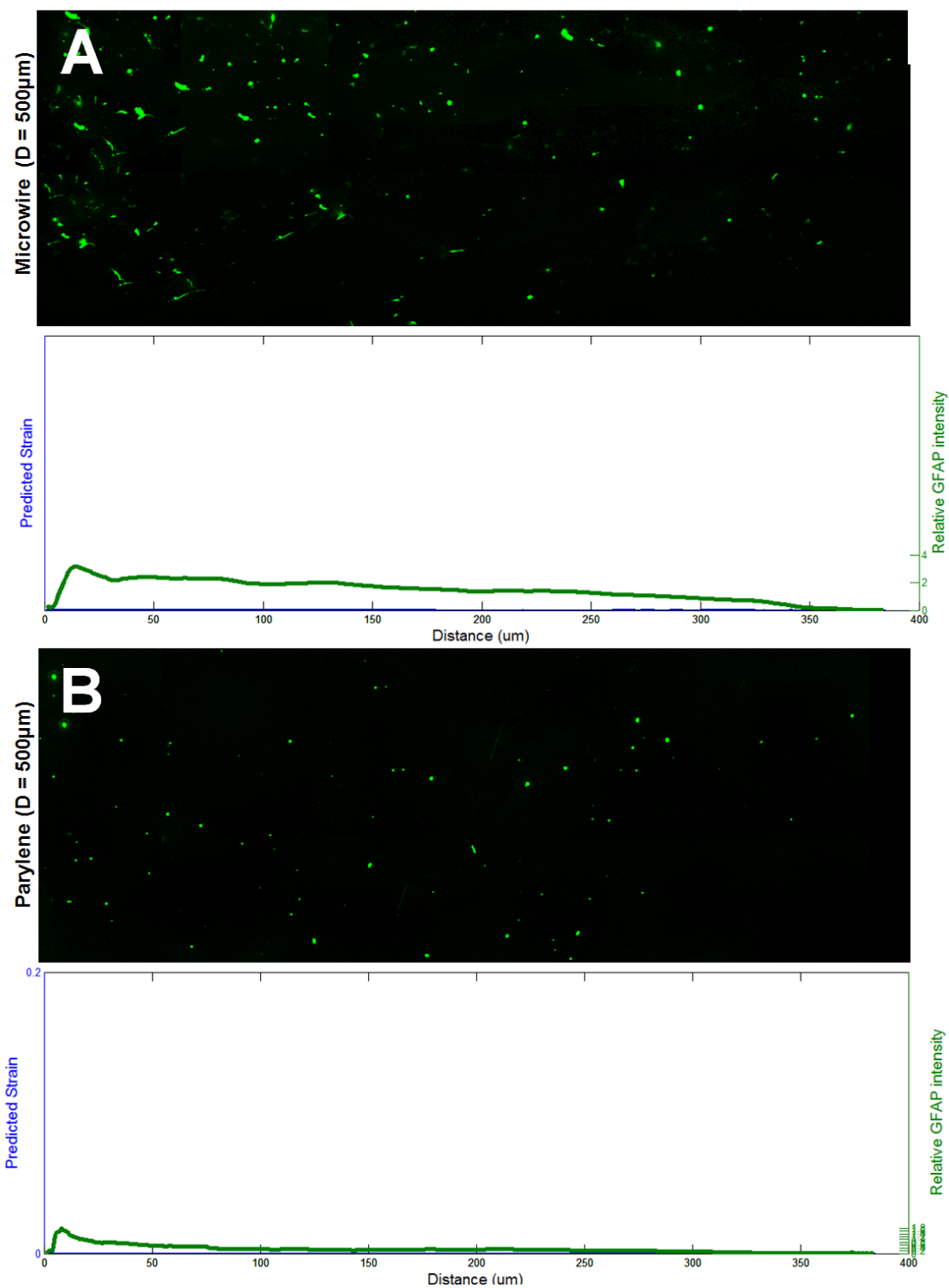
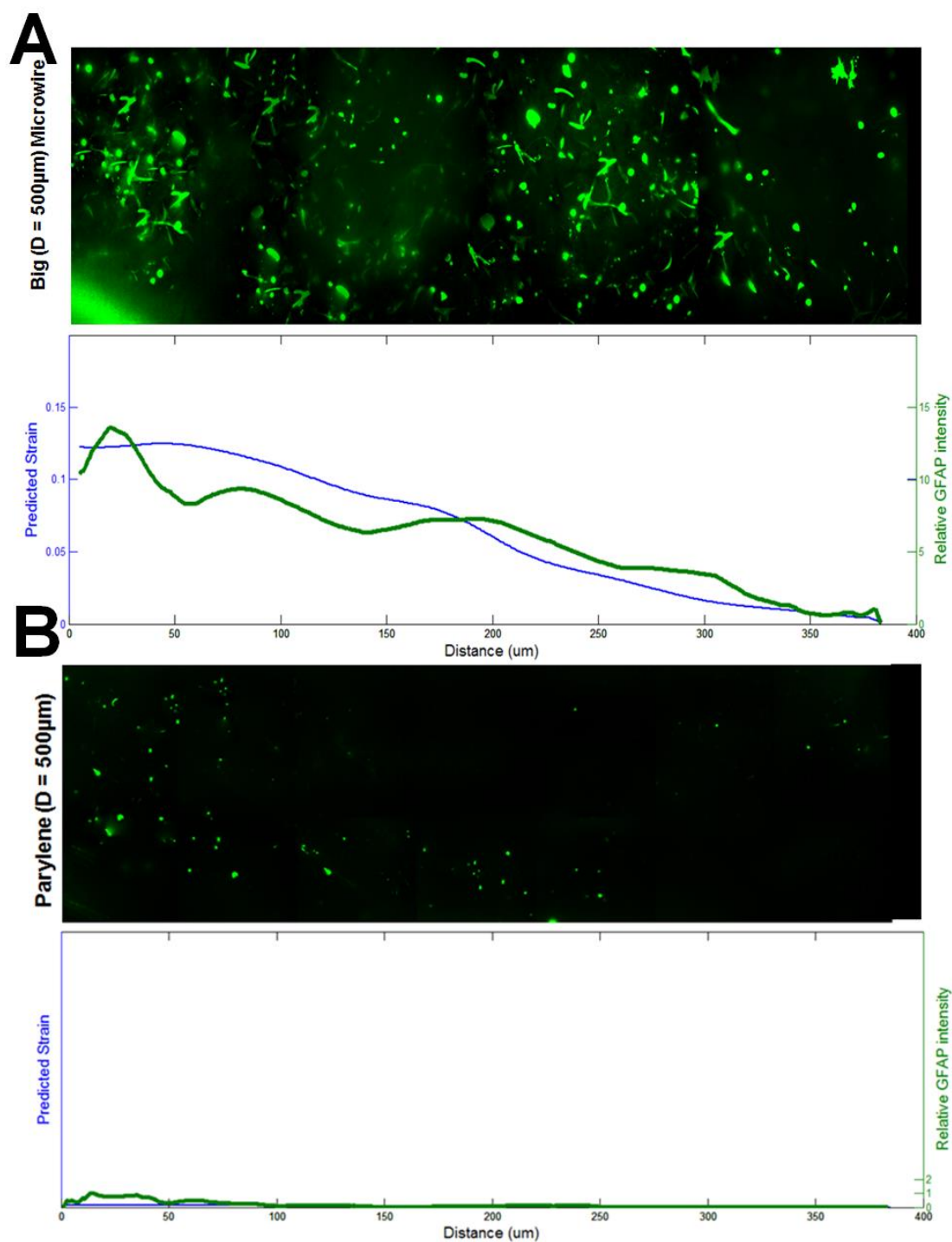


Figure 5-12: GFAP images and probe profiles for 500μm diameter (A) microwires, and (B) parylene sections for cell-probe-hydrogel conditions that were stationary.



normalized element strains predicted by simulations that replicate the experimental conditions imaged above.

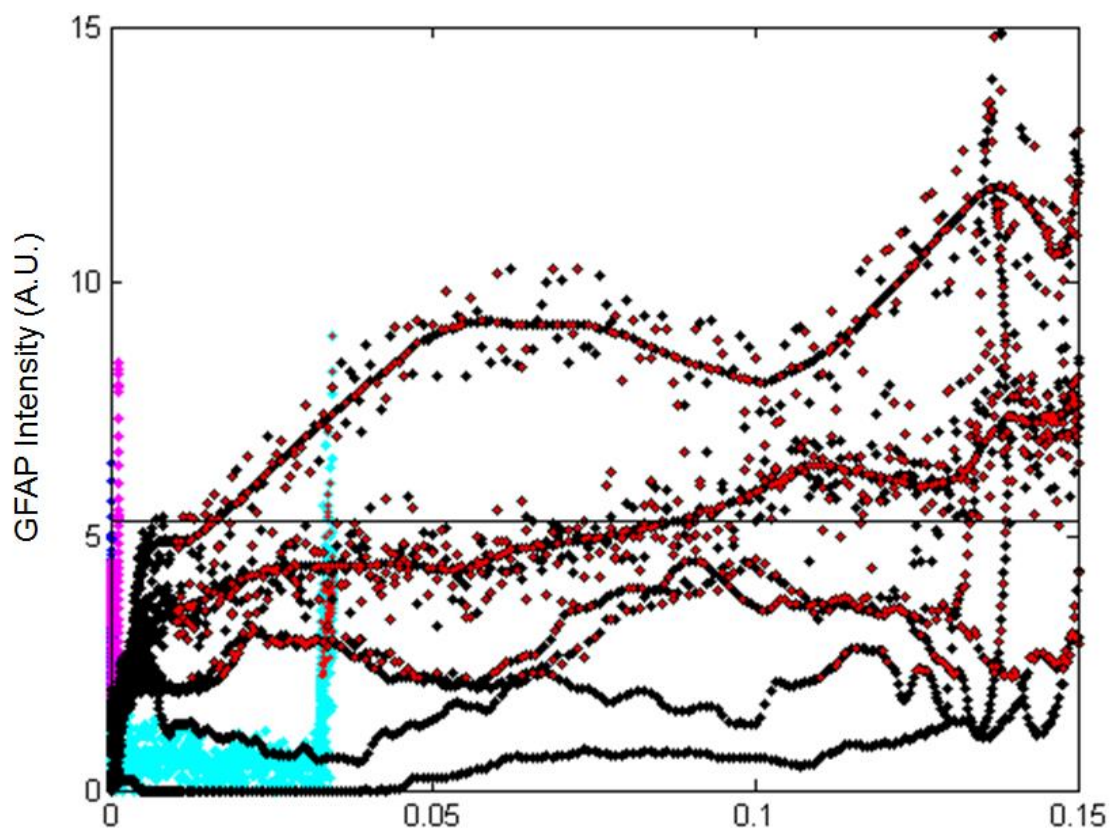


Figure 5-14: GFAP intensities for astrocyte cultures for 100 x 20µm parylene probes (blue), 350 x 20µm parylene probes (green), 500 x 20µm parylene probes (purple), 150µm diameter microwire (cyan), and 750µm diameter microwire (black) as a function of predicted element strain. Ramified astrocytes (two or more extensions) are recorded in red. A horizontal line was drawn representing the 50th percentile of ramified astrocytes to estimate an intensity threshold corresponding to activation. The x-axis intercept for each intensity-strain profile was determined and used to estimate strain thresholds for activation.

Condition	Day 1	Day 3	Day 5
Negative Control	157.15 \pm 68.16	130.05 \pm 57.89	39.45 \pm 6.39
Negative Control**	213.09 \pm 24.97	138.13 \pm 20.03	22.88 \pm 0.75
Microwire (D = 200 μ m)	322.50 \pm 171.50	154.02 \pm 33.10	53.72 \pm 49.02
Microwire (D = 200 μ m)**	389.28 \pm 49.00	158.52 \pm 10.67	37.34 \pm 5.41
Microwire (D = 500 μ m)	355.98 \pm 16.77	182.75 \pm 63.22	57.91 \pm 6.04
Microwire (D = 500 μ m)**	456.60 \pm 35.25	202.16 \pm 32.12	48.23 \pm 5.77
Parylene (W = 200 μ m)	171.36 \pm 26.42	128.09 \pm 34.13	60.05 \pm 11.39
Parylene (W = 200 μ m)**	389.28 \pm 108.10	182.67 \pm 38.45	47.18 \pm 5.52
Parylene (W = 500 μ m)	190.37 \pm 34.70	125.10 \pm 15.33	70.01 \pm 10.86
Parylene (W = 500 μ m)**	293.22 \pm 64.23	106.46 \pm 25.15	35.16 \pm 7.8
Parylene (W = 1000 μ m)	256.06 \pm 45.05	165.22 \pm 38.29	79.16 \pm 36.20
Parylene (W = 1000 μ m)**	317.96 \pm 82.88	133.81 \pm 54.71	32.57 \pm 26.42
Positive Control (LPS)	992.56 \pm 112.03	1025.29 \pm 87.75	908.44 \pm 162.23

Table 5-1: Mean concentrations of TNF- α determined by ELISA analysis. Statistical significance was found between samples exposed to movement when compared to stationary samples in almost all cases in Day 1 and Day 3 timepoints.

Chapter 6: Thesis Discussion and Concluding Remarks:

Thesis Summary:

In this thesis, we assessed several ways in which microscale features affect the bulk tissue-level response and vice versa, in the context of injury and flexible neural electrodes. We examined two facets of central nervous system injury and rehabilitation: approaches to better understand and model how tissue-scale deformations are translated to the cellular scale; and how neural probe stiffness and geometry can be modulated to mitigate acute and chronic trauma. We investigated both of these disparate elements by using a methodology that combined computational methods with experimental validation. The validated models were then probed to make predictions of scenarios that could not be experimentally measured or analyzed, in order to study the two aspects above.

To better understand how macroscale deformations in white matter tissue translate to axonal strain, we modeled axon kinematic behavior as it changes with development and stretch in chick embryonic spinal cords. We first extended the 2-D kinematic models presented by Bain et al. and Hao & Shreiber to 3-D (Bain et al., 2003; Hao and Shreiber, 2007). We characterized 3-dimensional tortuosity in axons and determined how tortuosity changed with stretch as a means of predicting kinematic behavior and inferring the strain populations of axons experience. Our findings suggested that accounting for the additional dimension would predict a smaller proportion of axons to exhibit discrete, or non-affine kinematics when compared to 2-D (Singh et al., 2015). This implied that greater proportions of axons exhibit affine or switching kinematics, which means greater proportions of axons are experiencing strain at lower levels of stretch than previously thought in the 2-D case.

To verify these inferences, we then explored methods of determining strain at the axonal level. Traditional measurements of strain are performed with fiducial markers, which provided the motivation to search for an analogous marker present in axons. We determined contactin-associated protein or Caspr as an ideal candidate for use as a fiducial marker. Caspr displacements were measured for different levels of tissue-scale stretch and the results demonstrated that while there is an equivalent transfer of macroscopic to microscopic stretch at earlier stages of development, this trend deviated at later stages. Through analyzing length distributions, we determined one possible cause for this discrepancy was axon failure. Examining thicker tissue sections confirmed this hypothesis, and we captured the proportion of broken segments. Adapting the kinematic models we developed in chapter 2, we were able to computationally estimate failure thresholds for axons in situ. Thresholds were predicted to decrease with development stage, in concert with increasing affine behavior. Moreover, when thresholds were categorized by kinematic behavior, we determined that non-affine axons have higher thresholds and are more resilient to stretch.

We then examined the next facet of the CNS injury and rehabilitation system: probe design and performance. We split the problem into two parts: insertion, and post-insertion mechanics. To model insertion mechanics, we developed a finite element simulation that utilized element deletion methods to simulate probe insertion. The model predicted three metrics: insertion force, buckling force, and safety factor of the design. Safety factor was defined as the ratio of buckling to insertion force. These predictions were validated with parallel insertion and buckling tests on probes and coatings of varying dimensions and material properties. Experimental results demonstrated a logistic relationship between

safety factor and likelihood of insertion. We conducted a parameter sweep of design features and constructed probability heat maps to ascertain the range of acceptable designs. Analyzing heat maps and utilizing nonlinear regression methods: we determined that coating thickness, and probe length were the biggest determinants to successful insertion. Furthermore, there is a tradeoff between ensuring successful insertion and minimizing acute damage, which is correlated to the magnitude of insertion force (Sharp et al., 2009).

Next, we sought to understand the probe features that affect the chronic response, and correlate probe-induced microstrains with gliosis with the goal of predicting the necessary strain to activate astrocytes. By simulating probe micromotion as a proximal cause of chronic injury (Polanco et al., 2014), we predicted tissue strain as a function of probe geometry and stiffness in a modified form of our probe insertion model. The model was validated by measuring bead displacements in an agarose tissue phantom subjected to conditions being modeled. We then developed an in vitro model to correlate the predicted strains to gliosis comprised of astrocyte-collagen-gels cast around probe specimens. Through simulations, it was determined that stiffness contributes most to micromotion-induced strains. We also determined strain thresholds for astrocyte activation vary between 2.6-13%.

The necessity of modeling:

One common thread between the questions we sought to answer in this thesis was the use of computational and experimental approaches to gain a greater understanding of each system (injury and effects of probe design). At the start of this work, we first addressed the reasons as to why we could not employ experimental methods on their own

to answer these questions. What were the obstacles associated with characterizing CNS injury, and designing neural probes, that made modeling a necessary approach?

The mechanisms of primary injury are inherently complex. Brain and spinal cord tissue demonstrates regional-dependent material properties that are defined by the microstructure. Moreover, CNS tissue is a complex environment of cellular components comprised of neurons, glia, oligodendrocytes, astrocytes, and myelin, which interact with one another upon experiencing mechanical stimulation (Burda and Sofroniew, 2014). These two features combined ensure that during primary trauma, axonal injury occurs non-uniformly, and that certain regions will be more prone to injury than others. The lack of a consistent, accurate animal model for studying white matter injury, as well as the difficulties in scaling the model to reflect what happens in humans with fidelity is one issue (Goldstein et al., 2014). Porcine models have made progress with regards to the latter, but biological variability is still a problem (Gefen and Margulies, 2004). Imaging capabilities are also limited in distinguishing the occurrence of injury (Carlsen and Daphalapurkar, 2015). We are hampered by the fact that axons are so small, and imaging cannot be performed in real-time during the injury event, which takes place at the millisecond level (Meaney, 2015). Thus, much of our understanding of primary injury mechanisms is through analysis of post mortem tissue (Tang-Schomer et al., 2012). We are also limited by the inability to measure strain at the microscopic level. Micromotion induced strains in probe studies cannot be visualized or directly measured in brain tissue. Even when we utilized tissue phantoms made of agarose and collagen, the flexible parylene probes did not produce measurable strain.

In response to the experimental limitations we encountered in characterizing axonal and chronic injury, we developed models that used measurable metrics as inputs (e.g. macroscopic stretch, probe size), and predicted immeasurable outcomes. Axonal strain and failure in situ cannot be observed in real time. However, we can devise a methodology of how axons experience strains based on the way axon undulation changes with tissue-level stretch. By examining features at the microscale, we could also standardize across species differences. Similarly, we can experimentally obtain information on proportions of axons that fail for given levels of macroscopic stretch, and then use models to predict what occurs in the timespan between no deformation and failure.

Novelty:

The contributions of this thesis are the new approaches in connecting macroscopic-scale events to microscopic effects in the context of CNS primary injury and neural probe biomechanics. In this work we offered an additional perspective to understanding axonal injury by characterizing 3-D kinematic behavior, extending the framework introduced by Bain et al. and Hao & Shreiber. As a means to validate some of these findings, we demonstrated that contactin-associated protein (Caspr) can be utilized as a fiducial marker for means of estimating axonal level strains in the spinal cord. To our knowledge, this is the first time Caspr has been used in this manner, and the first time that axonal strain has been estimated in situ. Moreover, this work is the first to classify and predict axonal failure thresholds by kinematic properties.

In our discussions of the neural probe model, we mention that the concept of modeling mechanical performance is not novel on its own. Indeed, computational models

for predicting probe-tissue interfacial stresses as a function of design (Polanco et al., 2014; Subbaroyan et al., 2005), as well as in vitro organotypic culture systems for assessing probe performance have been developed and utilized (Polikov et al., 2005). The innovative nature of our work can be described in four ways: 1) we presented a model that simulated probe insertion through hyperelastic tissue by way of element deletion; 2) we validated this model with experimental evidence and demonstrated a direct link between the probability of successful insertion, and the probe's mechanical features; 3) we developed and validated a separate simulation of probe micromotion that predicts local tissue strain; and 4) we quantitatively assessed and correlated the predicted strains to gliosis and estimated a range of strain values required for astrocyte activation. Taken collectively, our model for probe mechanical performance is an invaluable design tool for neural electrode fabrication as it addresses the concern of mitigating injury in both the acute and chronic timescales in a quantitative manner.

Philosophy of Engineering:

Distinguishing this work as an engineering thesis was difficult but necessary. The question of “how to understand the multiscale transfer” in white matter primary injury is nebulous with an equally nebulous outcome. Similarly, in the goal of “optimizing neural probes”, there is no pre-defined or objective definition of when the optimal state is achieved. Buleit et al. defines engineering as the reconceptualization of a complex system into an analytical problem with a definable solution (Buleit et al., 2015). With that definition in mind, we were able to formulate the right questions and ensure this thesis fits these criteria as an engineering study.

We examined the open ended problems of understanding CNS trauma, and designing improved rehabilitative devices and pinpointed two areas to focus on: the multiscale transfer of tissue-level stresses to axons, and the design of a tool to model flexible neural probe mechanics. The rationale in examining the context of multiscale injury is that axonal injury is a proximal cause of functional damage in CNS injuries. By better understanding this transfer, we could devise better ways of preventing axonal injury. The problem is conceptualized when we consider this transfer cannot be observed directly for the reasons described earlier in this chapter. Thus, we were able to transform our initial problem statement into an engineering problem by focusing on asking what approaches can we develop to predict what is happening at the axonal scale. From that point forward, there is a clearly defined question that facilitates an analytical approach, and a measurable outcome.

The questions addressed in the neural probe work of the thesis are easier to conceptualize as an engineering problem. Ultimately, the goal was to determine the best design of a coated, flexible neural probe that would mitigate insertion trauma, and long-term injury, which in essence is an optimization problem. There were two approaches available in formulating an acceptable problem statement to fit Bulleit et al.'s definitions of an engineering problem: 1) design the model to predict insertion force/tissue strain and arbitrarily define a threshold or critical value for insertion force/tissue strain that corresponds to success, or 2) design the model to predict the same features and thoroughly assess its efficacy as a design tool for designers and clinicians to use. We opted for the latter as the design space for the end user of these flexible electrodes can

vary depending on target tissue (probe length), acceptable insertion rate, or period of implantation.

Evaluating this work from the broader scale of biomedical engineering, the findings of this thesis contribute significantly to the areas of tissue and cellular biomechanics (axon kinematics and white matter tissue behavior due to stretch), tissue engineering (development of an in vitro approach for evaluating gliosis due to probe micromotion), image processing (axon tracing through transverse sections), neural engineering (design of flexible neural electrodes), and continuum mechanics. The multi-disciplinary approach presented in this work provides a suitable paradigm for engineering studies.

Future Work:

The work in this thesis has provided greater insight into the biomechanics of CNS injury and axonal strain as a function of macroscopic stretch. In our studies, we utilized the chick embryonic spinal cord as a model for stretch injury. Future work can focus on characterizing kinematics in other regions of white matter. Although, our characterizations of kinematics and failure thresholds are at the constituent (axon) level, different regional properties and other features such as axon orientation, axon diameter, and coupling potential can lead to differences in this multiscale transfer.

Furthermore, this work has generated useful data regarding kinematics and failure thresholds at the axon level. These features can be implemented into finite element models such as those developed by Cloots et al. and Pan et al., where axons are modeled as representative volume elements (Cloots et al., 2013b; Pan et al., 2013). Each axon is assigned their individual definitions of tortuosity, kinematic behavior, and connectivity to

surrounding glia. Groups of representative volume elements are initialized and arranged in a manner similar to white matter tissue, and the entire construct is deformed to predict stresses and strains on individual axons. Failure strain would be an additional parameter assigned to each volume element, and from that, we can predict certain outcomes, such as mild TBI, with greater accuracy (Johnson et al., 2013; Wright and Ramesh, 2012).

One area for future studies is in probing the influence that Caspr has on coupling behavior. In chapter 3, we described the role of Caspr as a protein component of axo-glial linkages that connect axons to the surrounding glia by means of contactin and neurofascin 155. Bain et al. and Hao & Shreiber also demonstrated a correlation between myelin and predicted affine behavior (Bain et al., 2003; Hao and Shreiber, 2007). The next step would be to distinguish the role Caspr has in coupling as opposed to myelination. Some possible approaches of determining the roles of Caspr are using a transgenic knockout models, or through antibody attenuation (Asano et al., 2000). Similarly to the kinematic features we gleaned, we can implement

Additionally, we developed a design tool that can be used to predict the mechanical performance, and effects on gliosis of neural probes coated with an ultrafast degrading polymer (D. Y. Lewitus et al., 2011). There are three avenues of future work we identified. One area of further study is refining the model, especially with regards to the material properties and behavior of the brain tissue. We modeled brain tissue as a homogeneous, isotropic, hyperelastic material, as these properties were suitable for obtaining a reasonable estimate for the insertion force (El Sayed et al., 2008). As discussed earlier, brain tissue properties are highly region dependent and some of the assumptions, in particular our assumption of isotropy, do not reflect the microstructure of

the tissue at all (Meaney, 2015, 2003). The model could be refined further, and perhaps even be combined with the representative volume element methodology used by Pan et al. to simulate the bulk tissue at the resolution of individual axons (Pan et al., 2013).

Another area of future studies is in further assessment of the role of probe design using our model. As a proof of concept, we demonstrated the effect that beveled geometries, and coating defects have on the insertion and buckling forces. We simulated these features as they directly influenced our group's fabrication and decision making process, as simulation results were used in a parallel in vivo study. Other features could be investigated, such as the influence of adjacent probes in multi-electrode arrays; heterogeneous coating schemes; or the effects of insertion rate.

This work also introduced a new system for assessing probe design on gliosis. By isolating astrocytes in our system, we could quickly and cost-effectively correlate micromotion-induced strains to astrocyte activation. One idea we have discussed is developing a co-culture system of astrocytes, and neurons that would enable both mechanical and functional testing. It is important to note that while introducing additional cell types makes the system more biomimetic, we would still want to distinguish it from an organotypic model, and adding components such as microglia, oligodendrocytes, etc. would introduce the complexities and difficulties associated with an organotypic or in vivo model

References:

- Asano, K., Kubo, O., Tajika, Y., Takakura, K., Suzuki, S., 2000. Expression of cadherin and CSF dissemination in malignant astrocytic tumors. *Neurosurg. Rev.* 23, 39–44.
- Bain, A.C., Shreiber, D.I., Meaney, D.F., 2003. Modeling of Microstructural Kinematics During Simple Elongation of Central Nervous System Tissue. *J. Biomech. Eng.* 125, 798. doi:10.1115/1.1632627
- Bulleit, W., Schmidt, J., Alvi, I., Nelson, E., Rodriguez-Nikl, T., 2015. Philosophy of Engineering: What It Is and Why It Matters. *J. Prof. Issues Eng. Educ. Pract.* 141, 02514003. doi:10.1061/(ASCE)EI.1943-5541.0000205
- Burda, J.E., Sofroniew, M. V, 2014. Reactive gliosis and the multicellular response to CNS damage and disease. *Neuron* 81, 229–48. doi:10.1016/j.neuron.2013.12.034
- Carlsen, R.W., Daphalapurkar, N.P., 2015. The importance of structural anisotropy in computational models of traumatic brain injury. *Front. Neurol.* 6, 28. doi:10.3389/fneur.2015.00028
- Cloots, R.J.H., van Dommelen, J. a W., Kleiven, S., Geers, M.G.D., 2013. Multi-scale mechanics of traumatic brain injury: predicting axonal strains from head loads. *Biomech. Model. Mechanobiol.* 12, 137–50. doi:10.1007/s10237-012-0387-6
- El Sayed, T., Mota, A., Fraternali, F., Ortiz, M., 2008. Biomechanics of traumatic brain injury. *Comput. Methods Appl. Mech. Eng.* 197, 4692–4701. doi:10.1016/j.cma.2008.06.006
- Gefen, A., Margulies, S.S., 2004. Are in vivo and in situ brain tissues mechanically similar? *J. Biomech.* 37, 1339–52. doi:10.1016/j.jbiomech.2003.12.032
- Goldstein, L.E., McKee, A.C., Stanton, P.K., 2014. Considerations for animal models of blast-related traumatic brain injury and chronic traumatic encephalopathy. *Alzheimers. Res. Ther.* 6, 64. doi:10.1186/s13195-014-0064-3
- Hao, H., Shreiber, D.I., 2007. Axon kinematics change during growth and development. *J. Biomech. Eng.* 129, 511–22. doi:10.1115/1.2746372
- Johnson, V.E., Stewart, W., Smith, D.H., 2013. Axonal pathology in traumatic brain injury. *Exp. Neurol.* 246, 35–43. doi:10.1016/j.expneurol.2012.01.013
- Lewitus, D.Y., Smith, K.L., Shain, W., Bolikal, D., Kohn, J., 2011. The fate of ultrafast degrading polymeric implants in the brain. *Biomaterials* 32, 5543–50. doi:10.1016/j.biomaterials.2011.04.052

Meaney, D.F., 2015. Accidental Injury. doi:10.1007/978-1-4939-1732-7

Meaney, D.F., 2003. Relationship between structural modeling and hyperelastic material behavior: application to CNS white matter. *Biomech. Model. Mechanobiol.* 1, 279–93. doi:10.1007/s10237-002-0020-1

Pan, Y., Sullivan, D., Shreiber, D.I., Pelegri, A. a, 2013. Finite Element Modeling of CNS White Matter Kinematics: Use of a 3D RVE to Determine Material Properties. *Front. Bioeng. Biotechnol.* 1, 19. doi:10.3389/fbioe.2013.00019

Polanco, M., Yoon, H., Bawab, S., 2014. Micromotion-induced dynamic effects from a neural probe and brain tissue interface. *J. Micro/Nanolithography, MEMS, MOEMS* 13, 023009. doi:10.1117/1.JMM.13.2.023009

Polikov, V.S., Tresco, P. a, Reichert, W.M., 2005. Response of brain tissue to chronically implanted neural electrodes. *J. Neurosci. Methods* 148, 1–18. doi:10.1016/j.jneumeth.2005.08.015

Sharp, A. a, Ortega, A.M., Restrepo, D., Curran-Everett, D., Gall, K., 2009. In vivo penetration mechanics and mechanical properties of mouse brain tissue at micrometer scales. *IEEE Trans. Biomed. Eng.* 56, 45–53. doi:10.1109/TBME.2008.2003261

Singh, S., Pelegri, A. a, Shreiber, D.I., 2015. Characterization of the three-dimensional kinematic behavior of axons in central nervous system white matter. *Biomech. Model. Mechanobiol.* 1303–1315. doi:10.1007/s10237-015-0675-z

Subbaroyan, J., Martin, D.C., Kipke, D.R., 2005. A finite-element model of the mechanical effects of implantable microelectrodes in the cerebral cortex. *J. Neural Eng.* 2, 103–13. doi:10.1088/1741-2560/2/4/006

Tang-Schomer, M.D., Johnson, V.E., Baas, P.W., Stewart, W., Smith, D.H., 2012. Partial interruption of axonal transport due to microtubule breakage accounts for the formation of periodic varicosities after traumatic axonal injury. *Exp. Neurol.* 233, 364–72. doi:10.1016/j.expneurol.2011.10.030

Wright, R.M., Ramesh, K.T., 2012. An axonal strain injury criterion for traumatic brain injury. *Biomech. Model. Mechanobiol.* 11, 245–60. doi:10.1007/s10237-011-0307-1